Imperial College London

Under-deposit Localised Dissolution in Simulated Sour Environments

Ahmed Shamso

November 2019

A thesis submitted to Imperial College London in fulfilment of the requirements for the award of degree of Doctor of Philosophy (PhD)

Department of Materials

Imperial College London

Abstract

Sour (H_2S –containing) environments present a major problem for oil and gas industries; of particular concern, is Underdeposit Corrosion (UDC), which is a type of accelerated localised corrosion observed under deposits, creating a risk to the asset integrity. Iron sulfides, a typical deposit in the sour environment, are considered critical due to their complex nature. The kinetics and controlling factors of sour UDC are not fully understood and there is no consensus on the methods used to evaluate it in pipelines. The efficacy of inhibitors may vary in such a scenario and so the amounts and efficiencies required cannot be *a priori* decided. There is, therefore, an urgent need for a protocol that addresses the characteristics of deposits to provide kinetic and mechanistic information on UDC phenomena.

In this work, both the general and localised corrosion kinetics of steel were studied in a simulated sour environment under 'inert' (sand) and 'active' (iron sulfide) deposits. Our multiscale investigation involved electrochemically measuring planar electrodes and 1-dimensional artificial pits to simulate actively dissolving interfaces with different geometries, followed by *ex-situ* surface analyses. In addition, the interfacial salt layer responsible for defining the stability of pits propagation was further investigated *in-situ* using synchrotron microfocus X-ray analyses.

The study showed that deposits stabilise a pitting-like corrosion in mild steel by altering the ionic diffusion process, which perturbs the local environment in a way that maintains an active chemistry for pit propagation. The salt films on the active interface have properties that are found to be dependent on the deposit type and the environment medium: sulfur-containing species, such as H_2S or iron sulfide deposits, form an additional sulfide film at the metal interface, stabilising the kinetics for a further continued, yet slow pitting corrosion. Troilite presented the most aggressive form of deposit under the studied conditions. Therefore, based on the mechanistic understanding of UDC developed in this work, a protocol for the development of representative deposits for in-line corrosion sensing can be established, opening avenues towards researching effective and reliable inhibition protocols.

Dedication

”وَأَنْزَلْنَا الْحَدِيدَ فِيهِ بَأْسٌ شَدِيدٌ وَمَنَافِعُ لِلنَّاسِ“
“We sent iron, with its mighty strength and many uses for mankind”
Quran (QS 57: 25)

الربانية في العلم أن تعلم أنه من الله مصدرا وإلى الله غاية
The divinity in knowing is to believe that God is its source, and that seeking ways to come closer to God is its objective.

Declaration of Originality

I declare that this work is my own and that any references to other work are appropriately referenced. Some of the work presented in this thesis has been published in the following journal articles:

- **A. N. Shamso**, A. M. Abdullah, N. J. Laycock and M. P. Ryan, (2018) "Under-deposit Corrosion (UDC): Investigating Dissolution Kinetics Using Artificial Pits," (Houston, TX: NACE, 2018), C2018-11055

- **Ahmed N. Shamso**, James Hesketh, Gareth Hinds, Aboubakr M. Abdullah, Nicholas J. Laycock and Mary P. Ryan, (2020) "Using Artificial Pits to Elucidate the Mechanisms of Under-Deposit Corrosion in Mild Steel," Electrochim. Acta, ***Manuscript submitted.***

- **A. N. Shamso,** A. M. Abdullah, N. J. Laycock and M. P. Ryan, "*In Situ* X-Ray Microprobe Study of Dissolution and Interfacial Characteristics of Steel within Occluded Geometries in Sour Environments," ***Manuscript ready for submission.***

- **A. N. Shamso, A**. M. Abdullah, N. J. Laycock and M. P. Ryan, "The Interdependent Deposit-Steel Interaction during Underdeposit Corrosion (UDC)," ***Manuscript ready for submission.***

Copyright Declaration

Acknowledgment

I am deeply grateful to my supervisors, Professor Mary Ryan and Professor Abubakr Abdullah for their guidance, patient support, and all the knowledge I gained from their expertise. Mary's passion for *in-situ* synchrotron radiation experiments and organised approach to high-quality scientific inquiry, and Bakr's diligent and keen eye for important details have greatly inspired me. I am also lucky to have had the mentorship of Shell's Dr Nick Laycock who expanded my knowledge and inspired my development as a research engineer.

I owe a debt of gratitude to Imperial College London, Qatar University, and Shell Qatar, who not only funded my studentship, but also made this journey an enriching and enjoyable experience. It has been my immense pleasure to witness the establishment of the collaboration during my time here and be part of the flourishing laboratories. Thank you Dr Marwa Al-Ansary, Dr Dhruv Arora, Dr Abitha Ramesh, and the rest of Shell Qatar team for all the activities. I believe my PhD experience was made much more comprehensive and fulfilling by being part of the Shell-AIMS centre, and for that, I will be forever grateful. Thank you, Dr Milly, Aigerim, Eden, Jim, Dafni, Sarah and Milla – the brilliant Shell-AIMS Cohort.

I am also thankful to my collaborators on this project Dr Jiahui Qi and Ms Noora Al-Qahtani, as well as my beamtime partners Dr's Mak, Miguel and Milly. Not only did I learn a lot from them, but they made my experiments enjoyable, something I will truly miss. My H_2S experiments have run smoothly with the help of the NPL team, Prof Gareth Hinds, Dr James Hesketh and Mr Phil Cooling. Thanks for the experience and for the friendly lunches. I am thankful to Dr Mahmoud Ardakani and Dr Ecaterina Ware, for the training and kind support on electron microscopes.

I will forever be indebted and grateful for Mum, and Dad in Heaven, who taught me my first word, and for the constant care, love, and inspiration. I am also truly lucky to have had the support of my inspirational brother Mohamed and his wife Jasmine, who also gifted the family with baby Hana, whose contribution to my thesis was also significant through some sneaky Hieroglyphic typos. I am grateful for my sisters Walaa and Doaa for their loving support, and the joy they brought to the family by gifting us my nephews Dawood, Murad, Yasin, Mohamed and Ahmed, and my beautiful niece Hayat, the newest member of the family.

Karim, Mak, Omar, Adamu, Motaz, Osama, Amir, M. Ouda, Tarek and Yasin. I do not see Imperial without you; you have really made my days very enjoyable. Thanks for being sincere friends, and also for all the out-of-my-box technical help.

Finally, a special thank you to the SchoolX team who have been adding a great purpose to my life and keeping my soul flourishing during the hard times.

Contents

List of Figures

List of Tables

List of Abbreviations

1D	One Dimensional
2D	Two Dimensional
A	Area of electrode surface
AFM	Atomic force microscopy
C	Metal ion concentration
C_{sat}	Saturation concentration of metal ions
CV	Cyclic voltammetry/voltammogram
ΔC	Difference of metal ion concentration between pit bottom and pit mouth
CE	Counter electrode
D	Diffusion coefficient
EDX	Energy dispersive X-rays
E	Electrode potential
E_{corr}	Free corrosion potential
E_{pit}	Pitting potential
E_{rp}	Repassivation potential
E_T	Transition potential
EIS	Electrochemical impedance spectroscopy
EXAFS	Extended X-ray absorption fine structure
F	Faraday's constant (96485 C/mole)
FEG	Field emission gun
FTIR	Fourier Transform InfraRed spectroscopy
h	Hour
i	Current density
i_{corr}	Corrosion current density
i_{lim}	Diffusion-limited current density
ix	Pit stability product of 1D artificial pit
IR	Product of current and resistance/potential drop
LCF	Linear combination fitting
min	Minute
M_W	Molecular weight
N	Number of electrons produced in metal dissolution
Q	Transferred charge
OCP	Open circuit potential

pH	Level of acidity or alkalinity
RE	Reference electrode
Rs	Solution resistance
s	Second
SCE	Saturated Calomel Electrode
SE	Secondary Electrons
SECM	Scanning Electrochemical Microscopy
SEM	Scanning Electron Microscope
WE	Working electrode
x	Depth of artificial pit
XANES	X-ray absorption near edge structure
XAS	X-ray absorption spectroscopy
XRD	X-Ray diffraction
XRF	X-ray fluorescence
XPS	X-Ray photoelectron spectroscopy

1 Introduction

The global cost of corrosion is estimated to be US$2.5 trillion, which is equivalent to 3.4% of the global GDP (2013).[1] With the continued need for fossil fuels, even as we enter energy transitions, the extraction of oil and gas from significantly abundant sour fields is increasing globally. Sour *i.e.,* H_2S –containing gas environments present several challenges to the fluid handling system equipment, including an accelerated rate of localised corrosion, and potential catastrophic premature failures. This creates a risk to asset integrity, leading to financial losses, and significant risk to both human health and the environment.

As shown in the Schematic in Figure 1.1, a combination of different organic and inorganic deposits is usually present in the pipeline, such as sand from geological formations[2], inorganic scales[3,4], biofilms[5], and wax[6]. Corrosion products compose another form of inorganic deposits, which are formed by the reaction of active components of the oil and gas brines, mainly carbon dioxide (CO_2) and hydrogen sulfide (H_2S), with the steel to give iron carbonate ($FeCO_3$) and various forms of iron sulfide (FeS), along with the oxides.[7–9]

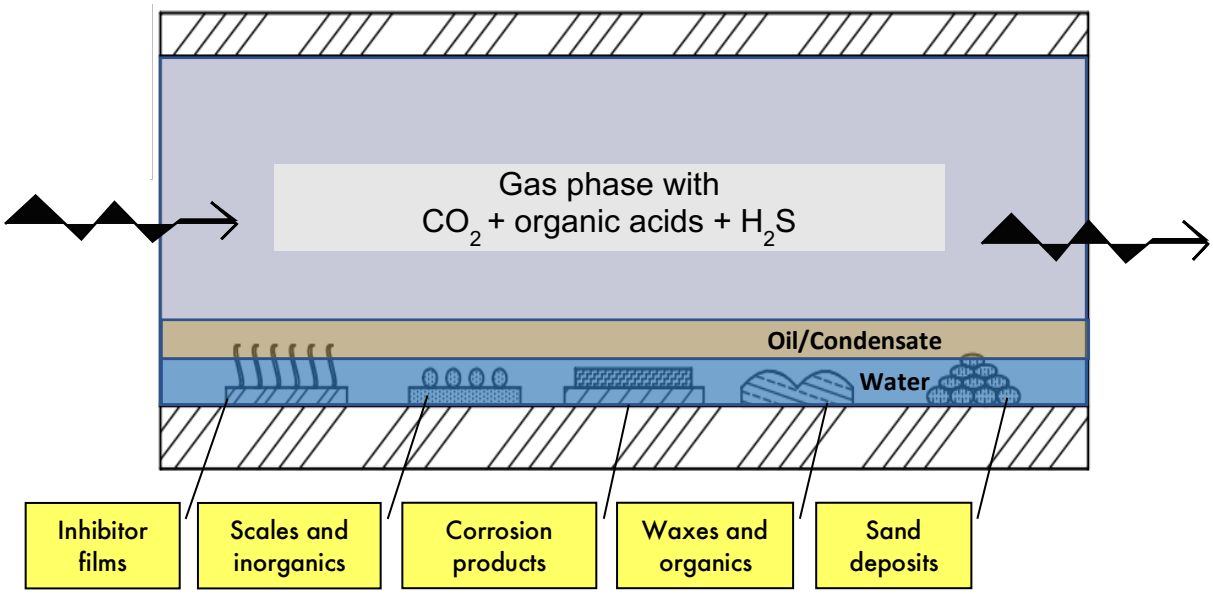

Figure 1-1 A schematic of a pipeline section showing the different deposit types typically present inside oil and gas pipelines.

These solid deposits affect the integrity of the equipment by eroding the base steel, the protective corrosion products, and the film-forming inhibitors at higher velocities or places of high turbulence[10], in addition to decreasing the inhibitor's efficiency by preferential adsorption.[11] A major problem in sour systems, however, is 'Underdeposit Corrosion (UDC)'

which is a type of extremely rapid, localised attack observed *under* deposits (in this case typically iron-sulfides); it is extremely difficult to monitor or predict.[4,6,12,13]

Despite the held view of the protective nature of corrosion products, localised UDC attack is typically observed under iron-sulfide scales in sour gas environments.[9,14] There are possible effects that are speculated to initiate and control pitting under deposits, but mechanistic understanding remains unclear. Due to the rupture of the corrosion product film, in response to erosion effects by other deposits or volumetric stresses during the film growth, a galvanic cell is believed to form between the higher potential passivated surface and the lower potential bare surface leading to the formation of localised corrosion pits.[9,12,15] The coupling between areas of different electrolyte chemistries, such as deposit-covered and bare surfaces or regions under an irregular deposit, is also thought to maintain the pit propagation.[4,6,15,16]

The operational conditions determine the characteristics of the formed deposits, and hence the severity of the UDC attack.[17] Under different conditions of temperature, pressure and reaction time, different phases of iron sulfide may form with different stoichiometric ratios.[18] The typical pipeline deposit is a combination of the different components, and therefore, the solid composition can have a multitude of effects: it may participate directly in the corrosion reaction, act as an electrolyte or be a naturally inhibiting deposit.[15,19] Nonetheless, conductive iron sulfide films, both epitaxially grown at the surface or accumulated in the sludge, can potentially act as new cathodic sites of recently activated pits, which provides the driving force necessary for sustaining pit growth and propagation.[20,21] The mechanism of UDC in pipelines is not fully understood: the complex nature of iron sulfides along with the dynamic changes of their physical and chemical properties during the corrosion process entails that multiscale correlative investigations are needed.

The deposit's surface barrier effect against the transport of the corrosive cathodic species is suggested in previous studies to lower the corrosion. They could not prove, however, a change in the overall corrosion mechanism, especially that is associated with the pit formation and propagation.[6,19] The degree of UDC is also likely affected by the physical and chemical nature of the deposit, making the study of the deposit's characteristics helpful for the development of new corrosion inhibitors and mitigation strategies.[12,22]

There have been several investigations to understand UDC where various electrochemical techniques such as modified three-electrode systems[23], multi-electrode arrays[24,25], and artificial pits[16,26] were used, as summarized in a study by NACE International Task Group (TG) 380 "Underdeposit Corrosion— Testing and Mitigation".[27] The study showed that the test design differs according to the deposit type and the corrosion measuring technique but all designs share a common feature; the behaviour of a bare electrode is compared to another

electrode that is covered with deposit. The multi-electrode systems offer an additional advantage of allowing for the identification of statistical changes in localised corrosion rate without recourse to extensive repetitive testing as compared to conventional methods.[25,28,29] Most of the work, however, investigated the inhibition performance on electrodes covered with deposits, with a lack of systematic studies that address the underpinning mechanism behind UDC.

Artificial pits have been used to elucidate the galvanic coupling mechanism of localised corrosion and the effects of deposits on the galvanic current, but mainly to develop mechanistic models of pitting corrosion. Zero Resistance Ammeter (ZRA) was used to measure the galvanic current from the propagation of pre-corroded pits when coupled to a much larger external cathode.[15,27,30–32] It has also been used to examine the ability of the inhibitor to prevent or reduce the propagation of the pit.[33] In deeper kinematic pitting studies, artificial pits have been used to study mass transport, pit solution chemistry and salt film formation within pits.[34–37] Rapid hydrolysis reactions of the dissolved metal ions at the pit bottom are responsible for maintaining a minimum degree of local acidification expected for stable pitting.[38] Originally formed as a result of supersaturation with metal ions at the pit bottom, the salt film, precipitation and dissolution reactions decide dominantly the localised corrosion kinetics.[34–36] It is not clear, however, whether the presence of deposits will have an effect on these local kinetic reactions by changing the transport mechanism and the pitting stability accordingly, which needs to be experimentally evidenced.

Ex-situ morphological and compositional characterisation are typically used to complement the electrochemical findings of corroded surfaces. Of the different available tools, Scanning Electron Microscopy (SEM), Energy Dispersive X-ray Spectroscopy (EDS)[19,39], Raman spectroscopy[40–42] and X-ray Photoelectron Spectroscopy (XPS)[13,14] have been used most frequently. These characterisation methods, however, lack the spatial and temporal resolution that can provide much details about the real-time physical and chemical alterations at the interface. Therefore, the results cannot be directly correlated to the electrochemical observations.

Recently, *in-situ* techniques using highly advanced synchrotron-light sources have enabled dynamic analysis of corroding systems. Synchrotron radiation is an extremely intense source of X-rays and does not require vacuum: it can penetrate electrodes and electrolytes at reasonable depths,[37,43] and with appropriate kinetics. Therefore, *in-situ* X-ray synchrotron measurements have been used to study the pit chemistry in addition to the transient structures of the newly formed films at actively dissolving interfaces.[36,37,43–46] In order to develop a one-dimensional system, the pit is micron-sized and the solution quantity is very small. The capacity of focusing the beam to a micron-sized spot is, therefore, necessary to detect local

variations in the concentrations of iron complexes. This demonstrates the potential of *in-situ* X-ray synchrotron techniques in studying the kinetics of pit dissolution under deposits.

In conclusion, it is important to study the effect of the deposit particle size, thickness, type and chemical composition on the propagation of pits, and to use such a protocol to provide kinetic and mechanistic information on the different scenarios of Underdeposit Corrosion phenomena. From the available literature, none of the reported techniques has directly related the deposit characteristics to the corroding pit kinetics, and therefore, a systematic study is necessary and is the topic of this dissertation.

2 Literature Review

2.1 Introduction to corrosion

Corrosion has been one of the most critical failure modes in oil and gas assets, costing the industry billions of dollars. A study shows that corrosion accounts for 25% of asset failure in oil and gas companies.[47] The average annual corrosion cost in the United States is estimated to be about $7 billion, including maintenance, prevention, and unexpected closure of equipment.[48]

With the growing demand for energy, oil and gas explorations expanded to super-deep and ultra-deep waters. Furthermore, sour fields, as a naturally abundant resource, were classically excluded from operation because the production process design was not optimised for this type of fields. Recently, however, and with advancements in production design, the interest in sour fields has been *on-rise*. The expansion in exploration and operation has, therefore, triggered extensive research into understanding corrosion and advancing the technology to maintain the assets for both economic and safety reasons.[49,50]

Carbon Steel X65 has been the primary material of transmission pipelines to transfer the Hydrocarbons, for its cost effectiveness. Most pipelines operate under acidic gas environments, *i.e.,* containing CO_2 and/or H_2S at different ratios. These acidic gases dissolve in mixtures of hydrocarbons and aqueous fluids produced from the reservoir, making the environment more corrosive. This renders the pipeline carbon steel highly susceptible to localised corrosion, especially pitting, as well as the typical *general* corrosion problems, which reduces the pipeline resistance to external forces, eventually leading to service failure as a result of leaking.

Some examples of the most commonly faced corrosion in oil and gas industry include H_2S or sour corrosion[7,51], erosion corrosion[2,52,53], microbial influenced corrosion (MIB)[54,55], and stress corrosion cracking (SCC)[56,57]. While corrosion control has significant expenditure, the payoff includes public safety, prolonged asset lifetime, reliable performance and environmental protection. This leads to a more cost effective operation on the long run.[48]

2.1.1 Uniform and localised corrosion

There are numerous types of corrosion categorised according to their visual appearance, special inspection tools, or microscopic examination, as shown in Figure 2.1.[58] Uniform corrosion, or often called general corrosion, attacks the entire or a large fraction of the exposed surface, causing metal thinning. The lifetime of the equipment can be accurately predicted, and this type of corrosion is typically prevented using suitable materials with coatings, inhibitors or cathodic protection.

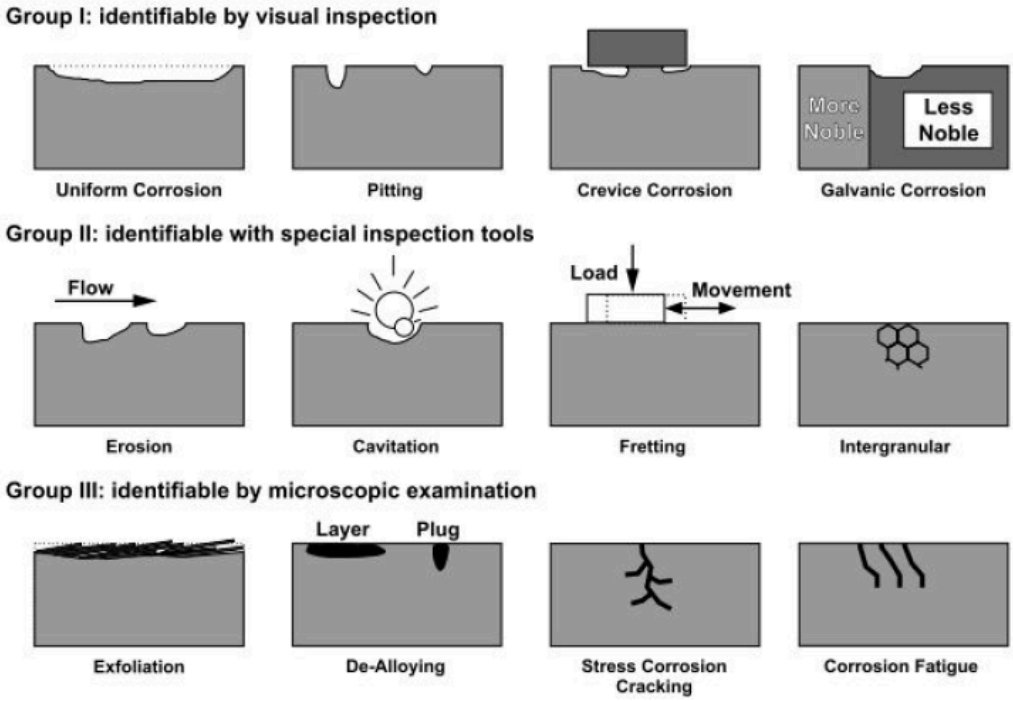

Figure 2-1 Different forms of corrosion grouped by the ease of recognition: (I) visual inspection, (II) special inspection tools, and (III) microscopic examination.[58]

Due to some mechanistic reasons associated with variations in the local chemistry, corrosion can develop preferentially at one part of the metal surface. Localised corrosion, the typical result in its many forms such as pitting and crevice corrosion, implies that a high corrosion rate is associated with a small area of the metal, and hence imposing a critical risk to the asset integrity.

Pitting can take different shapes, *for example,* wide or narrow, shallow or deep, and even or uneven. Pits grow vertically in the direction of gravity and tend to undermine or undercut the surface when they are first initiated.[59,60] Due to complications related to corrosion products covering the pits, pitting is difficult to detect. Operational precautions such as solution velocity and surface finish are usually considered to minimise surface pitting.

Among the different types of localised corrosion, pitting corrosion has been the most destructive as well as common type. Chloride ions generally facilitate the pitting corrosion of the metal, especially at areas or local sites of different chemistries or reactivities such as inclusions, geometrical defects, and where the passive oxide film breaks down. Equation 2.1 represents a simple anodic reaction, where a metal dissolves to form metal cations:

$$M \rightarrow M^{2+} + 2e^{-} \qquad \text{Equation 2.1}$$

Where, M represents a dissolving metal. The produced electrons flow from the corroding anodic sites to a more stable or passive metal surface, a cathode. This leads to the migration of chloride ions from the bulk solution to build up at the anodic sites such as inside the pit, to balance the positive charge of metal cations; a process that leads to further hydrolysis of the metal ions, as represented in Equation 2.2, reducing the pH inside the local areas.

$$M^{2+} + 2H_2O \rightleftharpoons M(OH)^{+} + H^{+} + H_2O \rightleftharpoons M(OH)_2 + 2H^{+} \qquad \text{Equation 2.2}$$

Figure 2.2 shows a schematic polarisation curve of a generic metal exhibiting active-passive behaviour.[61] As the potential is made more positive than the corrosion potential, the metal dissolution may reach a maximum value and then decrease abruptly to a small value due to forming a passive oxide film at peak B.

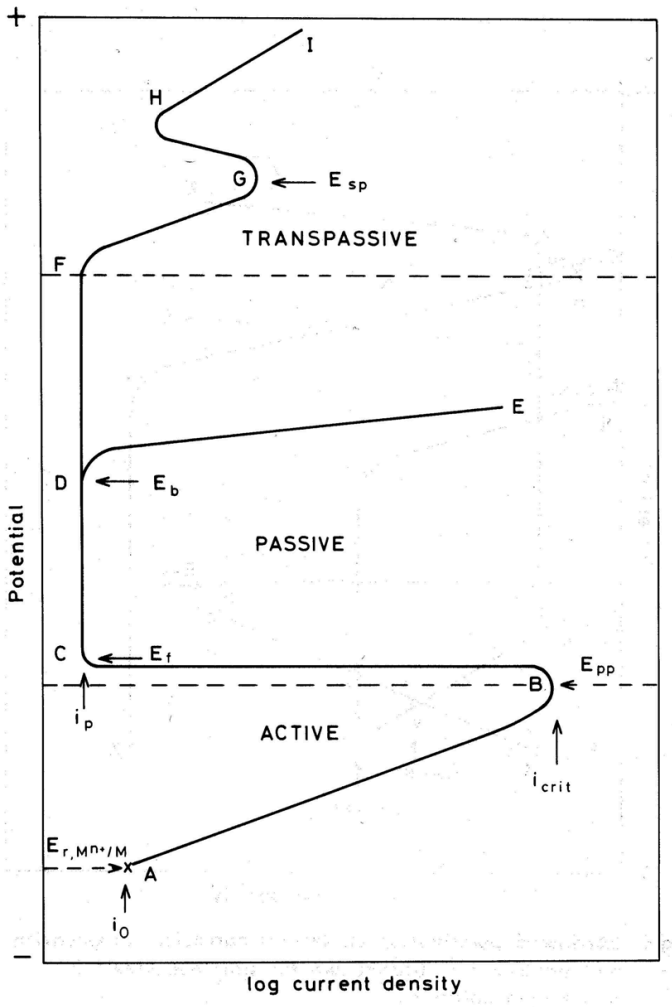

Figure 2-2 Schematic anodic polarisation curve for a metal that shows passive behaviour.[61]

The potential at this point is referred to as the critical (primary) passivation potential E_{PP} and i_{crit} is the critical passivation current density needed to attain E_{PP}; the smaller i_{crit}, the easier is passivation. As the metal surface becomes completely covered with the passive film, the film thickness increases to an equilibrium value and the current is called the passive current density, i_P, which is independent of potential and measures the film's protectiveness. The most negative potential at which this state is attained is called the Flade potential, E_F. As the potential is made more positive in the passive state, i_P remains constant until eventually the current begins to increase, possibly due to localised breakdown of the passive film by anions, particularily chloride ions, at weak points such as dislocations or inclusions in the metal. The breakdown of the oxide by anions with the initiation of pitting occurs at a critical potential called the critical breakdown or pitting potential E_b, and the current then increases rapidly with potential, along DE.[61,62]

For some metals where the passive film is not broken down as a result of the aggressive anions, oxidation of alloying elements, such as Cr in stainless steel, takes place and the current increases with positive displacement of potential, along FG. This process is known as transpassive dissolution. As the potential is made more positive, the rate of transpassive dissolution may decrease due to the onset of secondary passivity at G. Further increase in potential leads to the breakdown of water and current increases with potential (HI) due to oxygen evolution.[61,62]

Pitting corrosion takes place in two main separate stages: pit initiation and propagation. Many theories of pit initiation have evolved focusing on passive film penetration, film breaking, or adsorption.[63] In stainless steel, pitting commonly starts at nucleation sites such as surface defects[64,65], and propagate in two stages: metastable and stable. Initially, pits grow for a limited time before repassivation, which is called metastable pitting. Whereas upon survival from repassivation and where there is an effective perforated cover over the pit mouth, often called lacy cover acting as an effective barrier to diffusion, the pit grows stably.[59] In order for the pit to propagate stably, the solution inside the pit should be maintained at very low pH values, *i.e.,* high anodic dissolution rate, with their potential higher than E_{pit}.

The schematic in Figure 2.3 represents the typical processes taking place during localised corrosion. The chemistry inside the pit is controlled by metal hydrolysis, leading to low pH values. In addition, chloride ions from the solution migrate to balance the charge inside the pit. The high chloride ion concentration and low pH inside corroding pits form an aggressive local chemistry that prevents repassivation of the metal surface, hence accelerating the dissolution. The pit solution pH was measured in Tin pits by Suzuki *et al.*[66] and Wilde *et al*. [67], and for stainless steel, Monkowski[68] reported a less than zero value in some experiments.

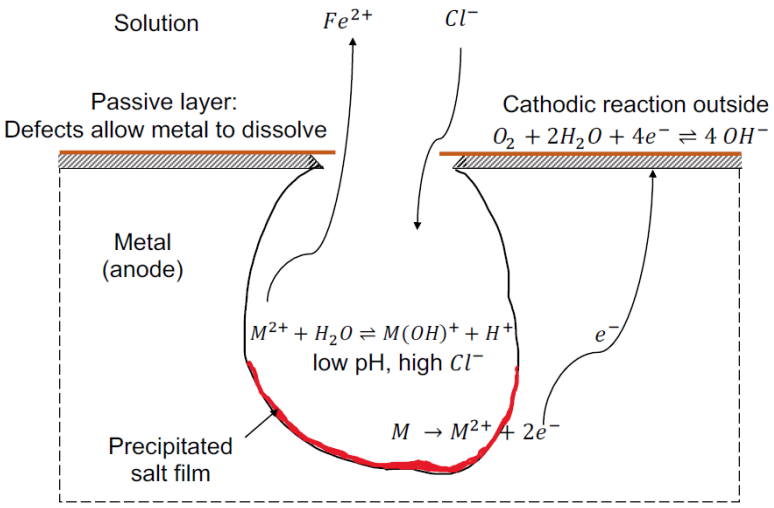

Figure 2-3 A schematic diagram of corrosion processes taking place during localised corrosion, adapted from [69].

If the rate of metal ion production at the pit bottom is lower than the ionic escape rate from the pit, the pit repassivates due to dilution. On the other hand, when the rate of metal dissolution is high, the pit becomes supersaturated and metal salt film precipitates.[70] Tester and Isaacs[35] showed that stainless steel could dissolve under anodic dissolution through an iron rich salt film, and in another study, Isaacs *et al.,*[43] found that the salt film is rich in Fe and depleted in Ni and Cr. The metal cations concentrations were calculated and reported to be 5 *M*.[43]

The process of salt film precipitation and dissolution inside the pit keeps the active chemistry required to sustain pit propagation, and therefore, the salt film structure and chemistry have been of interest in pitting studies. In studies of Fe-Cr alloys by Grimm and Landolt[71,72], the salt layer structure is proposed to have a duplex structure with an inner compact layer showing high field of conduction and an outer porous layer with ohmic conduction, as shown in Figure 2.4.[72] The thickness of the salt layer is a function of potential and the diffusion rate of metal ions from the interface. Several studies suggested that the salt film thickens with increasing the potential or as the pit becomes deeper.[43,73]

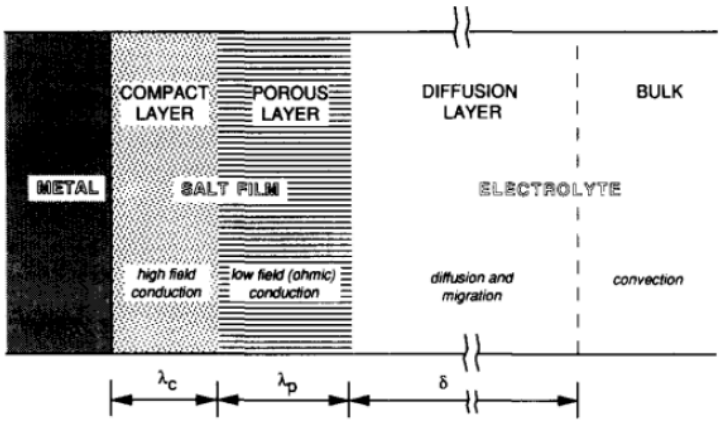

Figure 2-4 A schematic of the salt film above the dissolving metal.[72]

2.1.2 Sour corrosion

Reservoir environments with measurable amounts of H_2S down to 0.5 ppm are classified as sour conditions, whereas sweet conditions indicate the total absence of H_2S.[74] Sour corrosion problems were first reported in the 1940s.[75–77] It is caused by H_2S in the fluids, a highly toxic and corrosive gas that is soluble in hydrocarbons and water.

Hydrogen sulfide reacts with the surface of the pipeline steel to form adherent iron sulfide films that are assumed to be protective to the metal.[9,78] These films, however, can break down due to volumetric stresses, phase transformation, or due to rupture by the effect of other sediments. As a result, the bare steel forms a galvanic couple with the iron sulfide films, in a similar case to passivity breakdown[79], causing a rapid pitting attack. This might cause failure in a time period as short as a few months if not mitigated.[80] Since the pitting mechanism is not fully understood, the service failure can be repetitive. Additionally, pitting corrosion is generally difficult to quantify, both in the field or the laboratory, due to its random nature.[80]

On the other hand, some high sour systems have not experienced a significant number of localised corrosion-related failures since the protectiveness and stability of the iron sulfide films are generally dependent on the operating conditions such as salinity, temperature, and metallographic details.[81]

2.2 Underdeposit Corrosion (UDC)

A major problem in sour gas environments is Underdeposit Corrosion, commonly referred to as UDC, which is a type of localised corrosion observed under deposits, in this case typically iron-sulfide scales.[4,12,13,19] Iron sulfide is formed in different phases and stoichiometries[14] along with other deposit typically present in the pipeline. These deposits are different in their properties and arrangements and can provide different degrees of protection to the bare metal.[9] The study of the chemical and physical characteristics of the solid deposits and their influence on the bare metal are, therefore, helpful to understand UDC, and for the development of new corrosion inhibitors and mitigation strategies.[12,22]

2.2.1 Deposits

In oil and gas pipelines, a combination of different organic and inorganic deposits is usually present. Sand, in the form of inorganic silica from the geological formations, is the most abundant form of deposit.[2] Inorganic scales of carbonates and sulphates from hard water may also form.[82] Organic deposits such as asphalthene and wax naturally exist in crude oil, and this type of deposits typically contains active heteroatoms of oxygen, nitrogen, and sulfur that

are able to inhibit corrosion due to their surface activity.[6] Biofilms formed due to microbial activity are also considered as a form of organic deposits.[5]

Solid deposits are more likely to form at certain locations of the pipeline depending on the flow velocity and viscosity, size and density characteristics of the deposit, and the pipeline topography and dimensions.[17] Deposits affect the integrity of the equipment in different ways. For instance, at higher velocities or places of high turbulence, the solid particles cause erosion of the base steel, the protective corrosion products, and the filming inhibitors. Inhibitors also adsorb on the solid deposits, which decreases the inhibition efficiency. Finally, localised corrosion can be induced beneath or around the deposits as will be discussed in this review.[4,6,12,13]

2.2.2 Iron sulfide films: structure and breakdown

Another interesting form of inorganic deposits is the corrosion products, such as $FeCO_3$ and FeS that form by the reaction of CO_2 and H_2S from the oil and gas brine.[7–9] Corrosion products should be distinguished from other deposits for their ability to form a thin inert film on top of the metal surface protecting it from corrosion. This action is usually referred to as Passivity. It is important here to understand that these passive films do not infinitely protect the metal, however, they do reduce the corrosion rate by several orders of magnitude. Typically, the passive film is structured to have bi- or multi-layers. The inner barrier layer is thin, dense and adherent to the metal surface, while the outer layer is much thicker.[12]

In case of a brine saturated with CO_2 and H_2S, it is widely held view that the protectiveness is mainly decided by the H_2S component as it is an efficient scale-forming agent that forms FeS, a much less soluble scale than $FeCO_3$.[9] The H_2S protectiveness-decisive nature has been confirmed by Kvarekval *et al*.,[9] who conducted a study using a flow loop arrangement under experimental conditions similar to practice. The results of weight loss and linear polarisation resistance measurements showed that the absence of H_2S from the inlet brine has resulted in a much higher corrosion rate; a 30-40 mm/y as opposed to 0.5-2 mm/y when tested with H_2S/CO_2 ratios 0.2-0.6. This clearly shows the effect of FeS corrosion films on the passivity of the surface. The study, however, has not considered the localised corrosion rate despite the observation of localised pits. They argued that iron sulfide precipitation in pits potentially slowed down the pit growth but mentioned no experimental evidence.

The corrosion film layers are different in composition, density, structure and thickness, and have distinct boundaries between them, as shown in the SEM image in Figure 2.5.[9] The three layers are iron oxide (magnetite) as the inner layer, followed by a Sulfur-deficient FeS layer, and finally a Sulfur-rich FeS layer on top. It is believed that the layers form by either

precipitation or solid-state reaction between anionic species of the aqueous media and the metal cations that diffuse through the inner barrier layer. This strongly supports the assumption that corrosion products formation is a mass diffusion-limited process, where Fe^{2+} ions diffusion outward while the Sulfur species diffuse inward to the steel surface.[9,83] Electrical potential and concentration gradients formed due to this ionic diffusion process across the corrosion film makes possible a simultaneous concurrence of various iron sulfides.

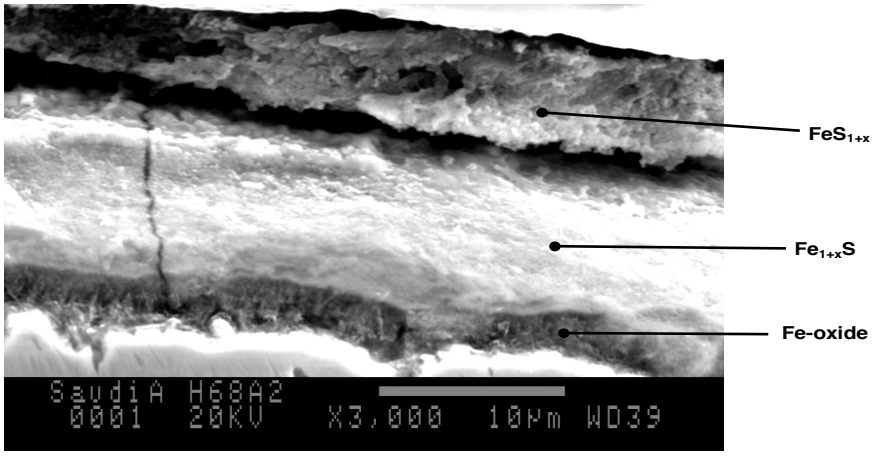

Figure 2-5 An SEM image showing three layers of corrosion products distinct in composition and thickness formed above the steel surface.[9]

Different phases of iron sulfides, with various degrees of protectiveness, are commonly produced during the corrosion process in H_2S environment.[9,18,22,84,85] Bai *et al.,*[18] investigated the corrosion products of steel in aqueous H_2S environment and found that different solid phases were formed with different stoichiometric ratios under different conditions of temperature, pressure, and reaction time. For instance, in an H_2S-H_2O vapor environment, FeS as nanocrystals forms initially and finally troilite (FeS) emerges. When immersed in oxygen-free solutions saturated with H_2S at 50 ^oC and 1 MPa pressure, mackinawite ($Fe_{1+x}S$) and cubic FeS initially form and then transition to troilite at longer times of reaction. Mackinawite was the only FeS phase observed in aqueous brine solution under atmospheric pressure and different temperatures for 168 h.[18] The study, however, did not include the effect of different phases of iron sulfides on the corrosion processes that take place afterwards.

Mackinawite $Fe_{1+x}S$ is an iron rich metastable phase of iron sulfide, and has been reported to be the initial corrosion product under most operating conditions.[18,22,86,87] Sun *et al.,*[14] reported film formation in solutions that are undersaturated with H_2S, and the rate of formation, on the other hand, was not accelerated in a supersaturated solution. Therefore, it has been a hypothesis that the initial iron sulfide layers were formed as a result of a direct solid-state heterogeneous reaction between H_2S and Fe at the steel surface. This was supported by

some pieces of evidence, for instance, the mackinawite is formed extremely fast, which is not a good indication of a precipitation reaction.[22] Nonetheless, the mackinawite layer was not formed in the case of stainless steel and other corrosion resistant alloys, which supports the hypothesis that mackinawite is formed from the iron of the substrate itself rather than the bulk solution.[87]

In Herbert's study using model phases under very controlled conditions of temperature and pressure, the possible processes that can take place at the surface are summarized in Figure 2.6.[12] In this model, mackinawite is formed via a solid state reaction or precipitation. The thin mackinawite film grows rapidly at longer exposure times especially when the environment is highly sour and at higher temperatures, which may be related to either the outward diffusion of ferrous species or the inward diffusion of the sulfide species or both together. In which case, the integrity or stability of the film is weakened because of the voids formed at the surface as Fe^{2+} diffuses outside causing poor adhesion. The inward diffusion of sulfides, on the other hand, generates a new FeS film that is larger than the iron it replaces at the interface of the formed mackinawite film with the steel, causing internal compressive stresses that damage the existing mackinawite film.[87]

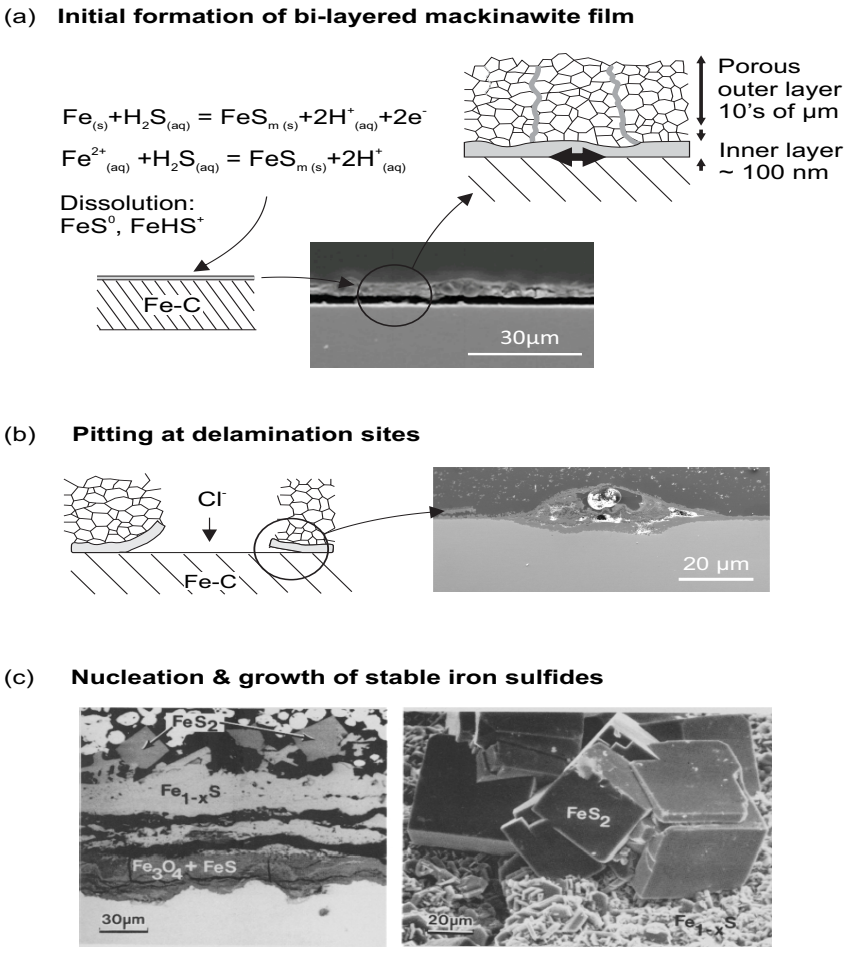

Figure 2-6 Mechanism of iron sulfide formation on steel in H_2S-bearing electrolytes.[9,12,88,89]

Due to the continuous dissolution and re-precipitation of mackinawite,[87] and the volumetric stresses due to the film growth, the thickness becomes bigger until it eventually breaks or delaminates, leading to the formation of bubble-like sulfide deposits as shown in Figure 2.6-b.[12] This causes the formation of localised corrosion pits and the increase in the local concentration of cations, which may lead to nucleation of stable phases of iron sulfides, as in Figure 2.6-c.[12] In practice, however, the operational conditions are more complex due to the introduction of aqueous environment, and hence, the type and characteristics of the formed film phases are expected to be different.

Overall, the non-stoichiometry of mackinawite makes it unstable, and it converts over time to stable iron monosulfide (pyrrhotite) or disulfide (pyrite) phases.[9,12] These phases decide the metal resistance to corrosion. Therefore, there is a need for a study that addresses the characteristics of deposits representative to the different conditions present in the real environment, and the use of such a protocol to provide kinetic and mechanistic information on UDC phenomena.

2.2.3 Towards a representative deposit

In an actual H_2S aqueous environment, iron sulfide layers can be formed by both deposition and corrosion reaction. Therefore, *in-situ* deposition of iron sulfides at the metal surface was adopted in previous studies.[90–92] Achour *et al.*,[90] deposited the film *in-situ* by both pre-corroding the steel surface in uninhibited CO_2/H_2S saturated brine, and by injecting iron chloride ($FeCl_2$) solution into a corrosion cell containing H_2S. SEM analysis of the produced film showed the standard framboid shape of mackinawite, with EDX showing Sulfur deficiency. Particle size analysis showed a range of 10 to 100 microns, and a bigger particle size was observed for the deposited FeS than the one formed by corrosion.

In Menendez experiments[91], mackinawite is produced according to a method previously developed by Butler and Hayes.[92] Stoichiometric mixing of 0.5 M sodium sulfide (Na_2S) dissolved in 0.6 L DI-water and 0.5 M $FeCl_2$ dissolved in 1 L DI-Water was able to produce mackinawite as was confirmed by X-ray diffraction (XRD) analysis. In the same study, purchased reagents of FeS, identified as different mixtures of troilite and pyrrhotite, were also used. It was eventually found that the precipitated mackinawite is more corrosive than the other phases, and non-stoichiometric mackinawite was particularly more corrosive than the stoichiometric one, producing localised corrosion morphology (larger pits) like that in practical sour field conditions. Hence, the study deduced that precipitated non-stoichiometric mackinawite should be chosen as the representative deposit for UDC testing.[91]

In another pitting study, salt deposits were applied using inkjet printing[69], where chloride deposits were applied to stainless steel in an attempt to study the pit growth and propagation *in-situ* under salt deposits using synchrotron X-ray micro-tomography. This method has an advantage that it can control the deposit diameter and the deposition density; the factors that were reported to affect the pit size.[69]

To conclude, the type of deposit and the application process differ according to the scope of the study and the stage of corrosion. Mackinawite is a more suitable representative in studying early stage corrosion and pit initiation. However, since mackinawite transitions into more stable pyrrhotite and pyrite with time, these phases are more suitable to use in the studies of late stage corrosion or pit propagation. As sand is the most abundant deposit, its simultaneous presence may affect the formation of iron sulfides. For this reason, different combinations of deposits components and characteristics should be used to determine the different scenarios when each combination is used.

2.3 Mechanism behind Underdeposit Corrosion

Localised pitting is found to be the critical factor in UDC. Many theories of pit initiation have evolved focusing on passive film penetration, film breaking, or adsorption.[63] Similarly, in UDC, the passive film damage and the corrosion product film rupture can take place due to volumetric stresses, or by the effect of other solid particles present such as sand. These have been assumed as the primary pit initiation sites.[12,93] The pit then propagates due to galvanic effects causing a high rate of attack beneath the deposits. The nature and type of the corrosion films and the external deposits directly affect the pit propagation process.

Three potential scenarios have commonly been assumed for corrosion processes taking place under deposits. Firstly, the area of the metal beneath the deposit is anodically coupled to other uncovered areas which are considered as external cathodes. Here, the driving force for galvanic corrosion is owed to the different chemistry underneath and outside the deposits, and the corrosion preferentially starts at areas close to the edge of the deposit. The second scenario could be visualised as if there is a separation between the anodes and the cathodes beneath the deposit and no external cathode presents. The irregularities of the deposit in this case produce differences in the local chemistry, suitable for pitting corrosion. The last scenario implies that there is no local separation of the anode such that the uncovered steel could not sustain localised corrosion. However, the presence of hygroscopic salts or clays could offer a suitable electrolyte for uniform corrosion.[4,6,16]

It has become important to realise that the corrosive environment under deposits evolves over time such that we should differentiate between the initiation and propagation of the pit. During

initiation, a time may be required for the deposits to nucleate and accumulate suitably enough for corrosion initiation. However, after UDC initiation the corrosion rate may increase, reach a *quasi-steady* state, or slow down and eventually suppressed.[4,26,94,95] In order for the corrosion to proceed under deposits, it is important that corrosive species and products transport through the deposit layer. Corrosion in covered areas is, therefore, expected to be lower than that in uncovered areas. This assumption does not hold in many cases, however, due to the random galvanic coupling reactions that take place according to the scenarios mentioned above.

Since there is a lack of systematic studies of the mechanism of UDC in sour gas environments, sweet gas mechanisms are often used to understand the common concepts of UDC.[4,26,94,95] Despite the numerous studies, they could not explain the origin of galvanic corrosion couples due to the multiscale of complexity, *i.e.,* a combination of corrosion films and other types of deposits, commonly sand, are involved.

Han *et al.,*[30–32] attempted to systematically explore the mechanism of localised corrosion under sweet gas environments. An artificial pit configuration was developed to elucidate the mechanism of localised CO_2 corrosion by measuring the galvanic current from pits' propagation. A potential difference was found to exist between the bare surface in the pit (anode) and the $FeCO_3$-covered surface (cathode) under the same bulk environment during the formation of $FeCO_3$. This potential difference was the driving force for localised corrosion propagation and resulted in the formation of a galvanic cell. A Zero Resistance Ammeter (ZRA) was used to continuously monitor the mixed potential as well as the open circuit potentials (OCP) of the individual electrodes. The covered electrode has higher OCP than the anode, with the coupling potential lying *in-between* closer to the cathode potential due to its large surface area. In Han's artificial pit experiments, a compression fit was used in order to change the pit depth, which overlooks the effect of corrosion history on the material's behaviour.

According to Han's observations, ferrous carbonate scales are formed when the solubility limit is reached, which causes the pH beneath the deposit to increase compared to the bulk pH. As a result, a magnetite, Fe_3O_4, passive film is locally formed and the potential increased. When the scale is locally damaged, the steel surface is locally depassivated and exposed to the bulk solution. A galvanic cell is then established between the higher potential passivated surface and the lower potential bare surface, leading to accelerating the dissolution of the bare steel surface and a change in the local chemistry. In addition, coupling between covered and uncovered areas usually occurs, causing enhancement of the localised corrosion rate.[15] A change in the local chemistry is believed to maintain the pit propagation by sustaining a potential difference between the large $FeCO_3$-covered steel and the smaller-area bare regions. It has also been reported by de Reus *et al.,*[96] that galvanic corrosion was induced by

coupling between sand-covered and uncovered steel in presence of CO_2, *i.e.,* iron carbonate film.

Unlike the typical effect of inhibitors in slowing the corrosion down, inhibitors can have adverse effects under deposits. Due to preferential adsorption on the deposit and the difficulty of the inhibitor to penetrate through to the inner surface of the metal, significant galvanic corrosion currents can be induced, causing severe localised corrosion. Huang[6] examined the effect of silica sand deposits on CO_2 corrosion of mild steel, with and without corrosion inhibitors. As a result of adding the inhibitor, the water chemistry became different between deeply covered areas and adjacent uncovered areas. Inadequate amounts of inhibitor have shown to cause adverse effects.[97]

In the case of sour environments, the corrosion process is mainly decided by the presence of iron sulfide layers and its different phases, which decide the galvanic coupling and the mass transport process of corrosion species. A global Fe-S passive film model has been under development in the Yildiz and Van Vliet groups at MIT.[12] The model proposes a pitting mechanism through the formation of nanocavities at the passive film interface. Figure 2.7 outlines the different processes that can take place at the passive film.[12] Key atomic steps taking place include ionic diffusion, interfacial charge-transfer reactions on the surface, and eventually vacancy formation under reducing conditions, as demonstrated in Figure 2.7-a. Figure 2.7-b shows additional important considerations such as the presence of multiphase films, fluid chemistry and mechanical effects that affect the stability of the passive film. A model under operational conditions of the field, however, has not yet been developed.

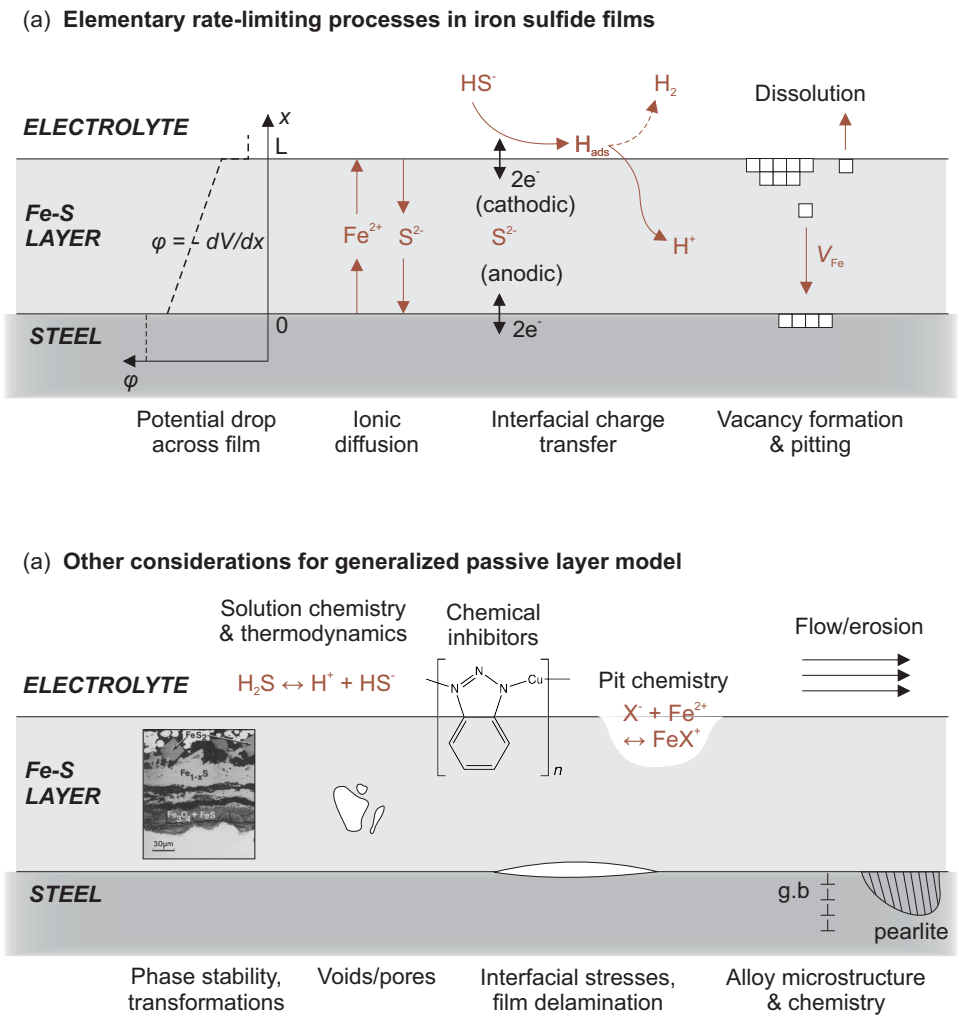

Figure 2-7 A schematic of unit processes in Fe-S passive layers: (a) key atomic steps such as ionic diffusion, interfacial charge-transfer reactions, and vacancy formation under reducing conditions. (b) additional considerations such as multiphase films, fluid chemistry and mechanical effects.[12]

In a typical under-deposit pitting process, as described earlier, deposits initiate pits that then propagate. Galvele[38] proposed an ionic transport model that calculates the conditions required for stable propagation of unidirectional pits. In this model, a one-dimensional pit geometry was used to simplify the dissolution reactions, and the transport equations for all species were solved for a stable pit in a steady state condition. The critical quantity of the stability product ix was calculated, where i is the pit current density and x is the pit depth. The model concluded that the pit will propagate in a stable way when ix reaches a high enough pH value lower than the critical value required for corrosion.

One-dimensional artificial pit electrodes have, therefore, been experimentally used to study mass transport, pit solution chemistry, and corrosion film formation within pits.[34–36] The dissolution kinetics, as per Galvele's study[38], can be simulated by dissolving a metal inside

epoxy to give a uniform one-dimensional cavity, while avoiding the possibility of forming multiple pits. In this case, only the top surface is exposed to the electrolyte, with the pit connected as the working electrode (WE) in an electrochemical cell composed of a reference electrode (RE) and a counter electrode (CE). This method can provide one-dimensional geometry, which allows including the effects of diffusion and resistance during the electrochemical measurements on pits. This model, however, was based on the case of uncovered pits, with no deposits existing above the pit cavity. Adding deposits on the pit mouth can possibly affect the diffusion and resistance during the process of pit propagation; this area is not being thoroughly understood. Figure 2.8 shows a schematic of the corrosion processes taking place during localised corrosion and the model pit of Galvele[38]; both adapted with a deposit applied on top of the pit cavity.

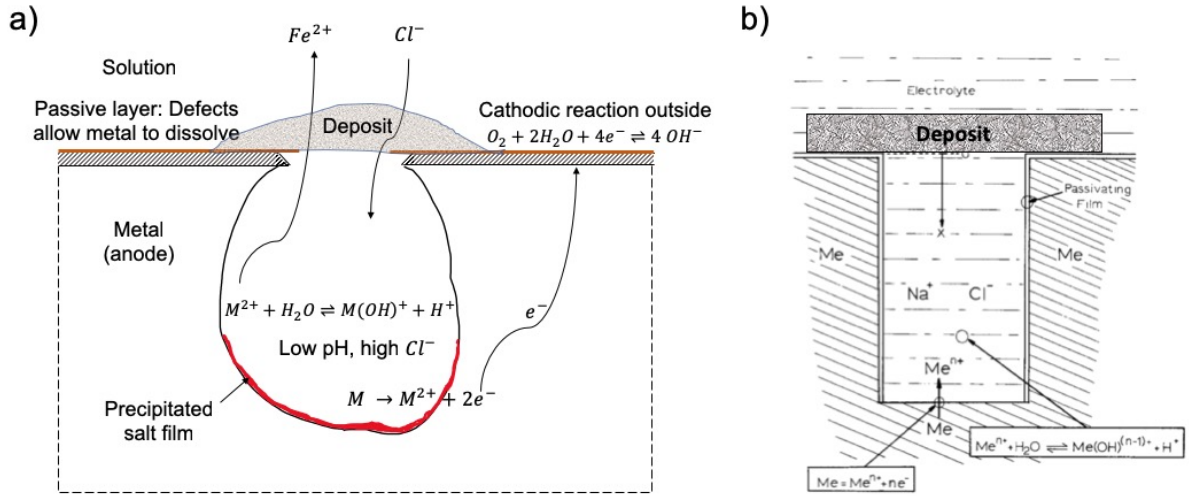

Figure 2-8 A schematic of corrosion processes taking place during localised corrosion (a), and Galvele's model (b), adapted with a deposit on top of the pit cavity. [38]

Iron sulfides are semi-conductive and can act as a large-area cathode that galvanically couples with the underlying steel, causing severe localised corrosion.[93,98] Therefore, understanding the electrochemical behaviour of iron sulfides is also essential in the investigation of UDC. A wide variety of Iron sulfides are formed in the pipeline whose phases and properties depend strongly on the formation conditions of temperature, pH, pressure, time, and the presence of Oxygen.[9,18,22] Therefore, the galvanic interaction is expected to be different; practically, an electrode displaying a large cathodic activity will have a large driving force for galvanic coupling, and hence the most detrimental effect. This explains that UDC is a multiscale phenomenon that needs a multitude of techniques to fully understand and model. Despite this, only a limited number of studies have investigated galvanic coupling of different iron sulfides to steel.

2.4 On the parameters affecting Underdeposit Corrosion

Under-deposit localised corrosion is usually affected by the characteristics of the solid deposit, the fluid, and the environment.[15,19] For instance, the solid composition may participate directly in the corrosion reaction, act as an electrolyte, or be a naturally inhibiting deposit. The size, shape, thickness, and porosity of the deposit affect the localised UDC in various ways. The flow characteristics and the pipeline topography decide in a great way the locations most susceptible to localised corrosion. The pH, gas type and oil-to-water ratio can also greatly affect the fluid corrosiveness, and hence the UDC rate.[15,19]

2.4.1 Deposit-related parameters

In addition to the corrosion products, it is important to investigate the role of other solid deposits that are commonly present in the real environment. Sand, as the most abundant inert deposit, creates a tortuous path for corrosive species and imposes a resistance to their diffusion towards the steel surface, typically lowering the corrosion rate. Therefore, different grain and particle size can result in different porosities when particles are packed and layered. This hypothesis was evidenced, according to Huang,[6] when lower corrosion rates accompanied by higher resistance values were observed with the more packed and thicker deposits. These observations, however, investigated the uniform corrosion rate, but have not provided conclusive remarks about the localised corrosion kinetics.

The conductive nature of the pipeline's iron sulfides, both newly formed and from the sludge, can also increase the high galvanic corrosion rate, leading to severe localised corrosion attacks.[20] Iron sulfides can act as new cathodic sites for recently activated pits which provides the driving force necessary for sustaining pits growth and propagation. In addition, during electrical resistance measurements in sour environment, the conductive FeS is reported to cause false readings due to electron-bridging, which causes changes in the measured resistance.[21] Normally, ionic species purely provide the conductivity between two electrodes without interference from the measured/supplied electrons. The conductive deposit, however, provides an additional channel for a portion of electrons to be transferred between electrodes. This number of electrons is unknown and does not take part in the corrosion reaction at the metal-solution interface, which in turn severely affects the performance of the resistance measurments.[21]

2.4.2 Environment-related parameters

The temperature and pH of the environment greatly influence both the corrosion rate and the corrosion product film formation. Generally, the rise of temperature has a positive influence

on the rate constant of corrosion reactions as well as the diffusion of the species involved, leading to increased corrosion rates. Concentrations of such species and the solubility of H_2S also differ according to the temperature; H_2S concentration is reported to be lower at high temperature while H^+ concentrations initially increase before decreasing again.[99]

Additionally, there is an established knowledge, previously investigated by Qi *et al*.,[99] that temperature affects the formation and transformation of corrosion products, for instance, mackinawite transforms into mackinawite/cubic FeS at higher temperatures. The study provided evidence that the temperature directly influences the physicochemical properties of the corrosion films such as density and composition. It was concluded that corrosion films play a dominant role in decreasing the corrosion rate in a greater way than the H^+ concentration. The study tends to overlook, however, the fact that pH is a major thermodynamic factor that affects the formation of corrosion products in the first place, as can be deduced from Pourbaix diagrams.

While the pH and temperature affect the initial stages of film formation, and hence its protectiveness, Huang's experiments proved no significant effect between 25 °C and 80 °C when sand deposits were present in a CO_2 saturated solution. This suggests that the effect of temperature and pH is more dominant during the formation stage of the corrosion product layer that, when formed, may become the dominant parameter to consider most in evaluating UDC. Therefore, studying a combination of factors such as corrosion film resistance, H^+ concentration, and the diffusion of corrosion species can allow the film protectiveness to be assessed.

2.5 Methods of investigating Underdeposit Corrosion

The previous discussion of the UDC mechanism and the deposit film formation process shows that a combination of analyses is necessary to explore the different aspects of this phenomenon. This section details various electrochemical and non-electrochemical methods that have been used or seem relevant to study UDC.

2.5.1 Electrochemical testing of UDC kinetics

Based on electrochemical methodologies, various techniques have been used to investigate UDC as summarized in a study by NACE International Task Group (TG) 380 "Underdeposit Corrosion— Testing and Mitigation".[27] The electrochemical techniques include, but not limited to, modified three-electrode systems[23], multi-electrode arrays[24,25], artificial pits[16,26], galvanic cells via Zero Resistance Ammeter (ZRA) and Electrochemical Noise, and Electrochemical Impedance Spectroscopy. Most of the efforts done on UDC, however, were aimed to assess

the inhibition performance of certain inhibitors without great attention to the real mechanism of UDC.[4]

2.5.1.1 Three-electrode electrochemical cells

Bubble test methods are considered the simplest UDC tests since it is used at ambient stagnant conditions and can accommodate any type of solids.[27] Although the test design differs according to the deposit type and the corrosion measurement technique, the system typically consists of two standard three-electrode test cells: one with solids and one without. The working electrode is suspended and not directly covered or immersed in the solid deposits bed, but it rather comes in contact with the deposit particles by bubbling the solution. The corrosion rate can be measured by Linear Polarisation Resistance (LPR), Electrical Resistance Probes (ERP), or the weight-loss methods. Upon injecting the inhibitor, the corrosion rate changes, likely due to the loss of the inhibitor to the solids. This process can give an estimate of the inhibitor's performance in presence of solids, but it is not viable for studying the mechanism of corrosion underneath the deposit.

In sour gas pipelines, it is important to evaluate the inhibition efficiency under iron sulfide deposits in a sour gas environment. Iron sulfide films can be grown on steel by the reaction between H_2S and iron chloride or by pre-corroding the steel probes in an aqueous H_2S environment.[27,90,91] The corrosion measurements using ERP start after transferring the solution and the gas to the test cell. When the corrosion reaction is stopped, by rinsing the ERPs with de-Ionised water and solvents, followed by drying and stabilising at room temperature for 24 h, the FeS layer remains intact and the dial reading of the EPR is recorded. Once again, the ERP is recorded after cleaning with inhibited HCl and the typical post-test cleaning procedures, and then sitting for 2 days to allow H_2 to evolve from the elements. Any significant change in both readings means that the iron sulfide has potentially affected the measurement.[90]

2.5.1.2 High throughput coupled multi-electrode array systems (CMAS)

Multi-electrode corrosion testing systems have been widely used as they provide the advantage of arranging the electrodes in any given pattern and each of the electrodes can be separately addressable.[24,28,29,100,101] They have been recently used as online and real-time corrosion sensors, allowing for quantitative measures of both the localised and general corrosion in many different environments, including under coatings and deposits. Additionally, it has been proven that an array of very close electrodes corrodes the same way as a one-piece electrode of the same shape and total surface area.[100] As a result, it can be able to

determine the corrosion current and potential spatial patterns and how the active-passive electron oscillations travel on a large iron electrode.

Deposits often cause mass transfer restrictions and the average corrosion rate measurements are inappropriate for testing the inhibitor performance against localised attacks. However, in the case of CMAS, all the individual electrodes are coupled to a much larger external electrode and the measured coupling current flowing to each electrode is measured. The coupling current does not effectively represent the corrosion rate, however, knowing that the inhibitor significantly reduces this coupling current could be a sufficient indication of the inhibition performance**.** The multi-electrode system also allows identifying any statistical changes in the localised corrosion rate without recourse to extensive repetitive testing as compared to conventional methods. Figure 2.9 shows a schematic diagram that explains the principle of CMAS in monitoring the localised corrosion rates.[28]

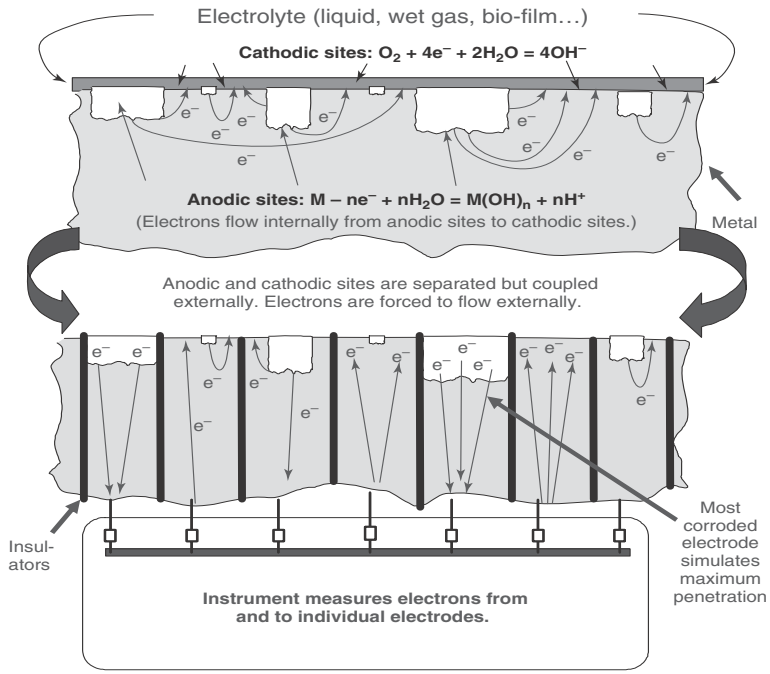

Figure 2-9 A schematic diagram showing the working principle of CMAS to monitor localised corrosion.[28]

Micro-electrode systems were used by Turnbull *et al.,*[25,29] to evaluate the local variation of the under-deposit corrosion activity of carbon steel. Nevertheless, since the inhibitor performance is affected by the history of the metal and the prior existence of corrosion products, CMAS offers the advantage of simultaneous assessment of the effect of the pre-corrosion degree on UDC inhibition. This can be accomplished by corroding individual electrodes to different depths in the test solution whilst located under the deposit and before adding inhibitors.

However, the potential oxidation of H_2S in sour environments, and hence a difficult pre-corrosion process, makes it necessary to pre-corrode the electrode and the test gas shall only be inserted after the pre-corrosion is complete.

2.5.1.3 Artificial pit test method

As explained earlier, real pits have different shapes with complex geometry, which also change with time: the active surface area increases as the pit grows.[58] In addition, pits with different shapes and depths can grow simultaneously making it difficult to predict. Therefore, artificial pits in one-dimensional geometry have been used to simplify the pit geometry to allow studying the mass transport and the pit solution chemistry within pits.[34–36] The ability of the inhibitor to prevent or reduce pit propagation in areas partially covered by a semi-protective layer of corrosion products, has also been addressed using artificial pits.[15,27]

The setup is typically comprised of a pencil electrode, *i.e.,* a metal wire or film mounted in insulating epoxy resin, that is subjected to pre-corrosion. Artificial pits are conventionally coupled with a much larger piece of the same metal, all immersed in the same environment, as shown in Figure 2.10.[15,27] A ZRA is used to measure the coupling current and potential. The coupling current is usually related to the rate of pit propagation, and the change before and after adding the inhibitor is an indication of the inhibitor's ability to fight pitting corrosion. The localised coupled corrosion rate can be added to the uncoupling current measured from polarisation resistance measurements to give the total corrosion rate of the pit.[33]

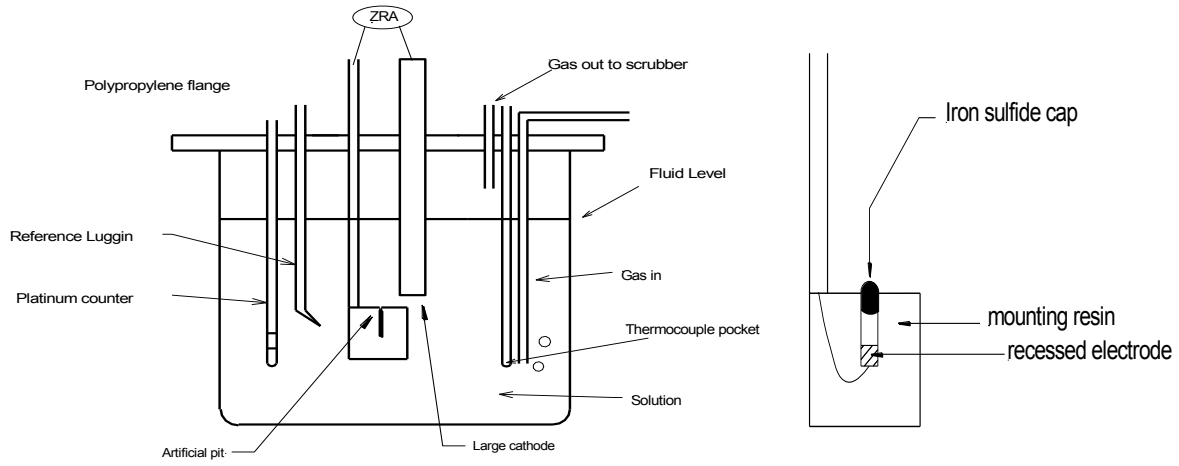

Figure 2-10 A schematic artificial pit ZRA test cell (left), and a pit probe (right): a steel electrode embedded in epoxy with iron sulfide deposits build-up at the pit mouth during the test.[27]

As stated earlier, salt films precipitate inside dissolving pits when the rate of metal cations production at the metal/solution interface exceeds the rate of escape, and this salt film is

responsible for maintaining a stable pit propagation.[70] Therefore, it was a point of interest in several studies to understand the salt film structure and chemistry. Synchrotron X-ray characterisation techniques have used electrochemically active artificial pits to *in-situ* analyse the salt film properties, as will be described later in this review.[35,59,60,102–105]

Cyclic voltammetry (CV) is a common electrochemical measurement used to obtain the dissolution kinetics inside pits. The schematic current-voltage characteristics of artificial pits is shown in Figure 2.11, demonstrating the diffusion-controlled region at high potentials and the effect of supersaturation in extending the film-free (ohmic) dissolution region.[34,106] Starting from the salt-free region, far left at the curve, the pit growth is under ohmic control, *i.e.,* the current increases with potential. The salt film precipitates when a supersaturation state is reached inside the pit, and the steady-state thickness of the salt film increases with increasing the potential or the pit depth. The system is then known to be under diffusion control, where the current density stays at constant value known as the limiting current density i_{lim}. As the potential is decreased further, the current decreases again below i_{lim} and the system transitions from diffusion control into an activation/ohmic-controlled mode at a potential called the transition potential E_T.

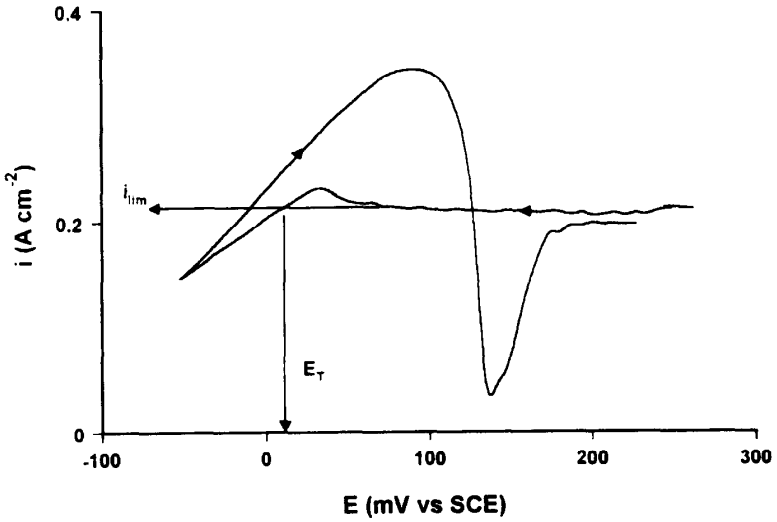

Figure 2-11 Current-voltage characteristics of a stainless steel artificial pit during Cyclic Voltammetry measurements, showing the definitions of i_{lim} and E_T.[34]

2.5.1.4 Galvanic coupling cell

A much higher corrosion rate was exhibited by steel samples covered with iron sulfides compared to sand.[107] This was attributed to the difference in deposit conductivity; sand is inert while iron sulfide is semi-conductive and more electrochemically active, which raises the galvanic effects between the steel and the deposit. Typically, galvanic coupling measurements

were used to couple two electrodes of steel under different conditions of deposit or environment.[108] Despite its importance in deciding the effect of external variables such as inhibitors, it could not provide helpful insights into the deposit-metal interactions during UDC.

Tjelta *et al.*,[93] investigated the galvanic coupling between steel electrodes and different iron sulfide polymorphs, for example troilite, pyrrhotite, and pyrite, in 0.5 M NaCl base electrolyte at 1 atm. H_2S. In these experiments, both the steel and iron sulfide electrodes are connected via ZRA as working electrodes in presence of a reference electrode, in a setup similar to that in Figure 2.10. Pyrrhotite was shown to produce the largest galvanic effect due to its large ability to polarise steel: it displayed a large cathodic activity during potentiodynamic polarisation. Pyrite, on the other hand, despite its reported large ability to polarise steel, was not very active, while troilite was quite active but could not polarise the steel significantly.

2.5.1.5 UDC Autoclave testing

To test UDC under operating conditions of high temperature and partial pressure of the corrosive gases, the same electrochemical test methods can be used in an autoclave. Both electrically conductive and non-conductive deposits can be used. However, when used for testing conductive solid deposits such as iron sulfides, some modifications are required regarding the insulating setting. It is favoured to replace the electrochemical techniques by weight-loss and surface profilometry techniques to monitor the general corrosion rate and the pitting rate, respectively.[27,39,96]

2.5.2 Non-electrochemical techniques to study UDC

Since only a limited number of studies were reported in the literature on under-deposit localised corrosion, techniques used in studying normal pitting are surveyed here as well.

2.5.2.1 *Ex-situ* techniques

The UDC phenomena are directly related to understanding the nature of the corrosion films and the surface morphology. Therefore, *ex-situ* surface analysis was typically involved to complement the findings of the electrochemical measurements. Advanced tools such as SEM, EDS[19,39], XRD[39,42,99], X-ray photoelectron Spectroscopy (XPS)[13,14], and Raman spectroscopy[40–42] have all been used to assess both the morphological and chemical transformations of the produced films during the corrosion process. These techniques enable the identification of corrosion products more precisely, however, since they are mostly planar analytical analyses, only the outer layer of corrosion product is analysed. Without further development to analyse the cross section of the multi-layered corrosion product, the ability of the *ex-situ* techniques to understand the corrosion mechanism remains limited.

Optical microscopy and SEM studies have been the primary tools used to establish the occurrence and severity level of localised corrosion attacks, and to observe the morphology of the corrosion products.[109,110] Subsequently, complementary EDX analysis is often used to analyse the chemical composition of the corrosion product films, and to study the microstructure and inclusions of the test metals after being polished and etched.[110] During sour corrosion, Liu *et al*.,[110] observed a non-homogeneous distribution of elements through the corrosion film cross-section. The corrosion film had two layers: an inner fine-grained layer rich in iron and depleted in sulfur, and an outer columnar-grained layer depleted of iron and rich in sulfur.[85] With increasing the immersion time, the main corrosion product changed from iron-rich mackinawite to sulfur-rich pyrrhotite.[85] Despite the insights that EDX observations provide, comparison of Fe to S ratios is not adequate to understand the film formation mechanism due to the complex combination of the outward diffusion of ferrous ions and the inward diffusion of HS^- ions.

Additional analyses such as TEM and XRD have also been used to analyse the corrosion product type and structure.[30,110] For instance, in Lui *et al.*'s study, the corrosion film formed after immersion for 2 h was scraped from the sample surface, cleaned in ethanol, and eventually collected at a copper net for TEM analysis.[85,110] The analysis detected amorphous iron sulfides, as well as crystalline troilite and mackinawite. It has been previously acknowledged that amorphous iron sulfide forms initially before it can easily transform to mackinawite.[111] In the same study, XRD analysis reported 4 types of corrosion products: mackinawite ($Fe_{1+x}S$), troilite (FeS), cubic ferrous sulfide (FeS), and pyrrhotite ($Fe_{1-X}S$).

Spectroscopic techniques such as Fourier Transform Infrared spectroscopy (FTIR), Raman spectroscopy and XPS have also been used in the study of corrosion films and pitting.[40–42,112–116] XPS analysis showed differences in the binding energy between the surface and subsurface regions, which was attributed to the variation of the chemical environments.[117] FTIR and Raman spectroscopy use laser to detect molecular level changes at the metal-electrolyte interface. FTIR is often used to study the mechanism of inhibition, and to identify the adsorption of inhibitors on the surface.[118] Various iron sulfide species have also been characterised using FTIR in various studies, for instance, Romero *et al.,*[119] characterised iron sulfide peaks at 1400, 2700, 2900 cm^{-1}. In an attempt to understand the pitting mechanism, Sridhar and Dunn[114] used Raman Spectroscopy to characterise the salt film inside nickel pits, but it failed to distinguish between the dissolved metal ion species and the precipitated salt film.

Similarly, the above-mentioned techniques were used to study UDC, but at a limited scale. The reacted metal is typically cleaned off the applied deposits after electrochemical testing and the surface is subjected to analysis. Menendez *et al.,*[91] assessed corrosion of steel under

in-situ synthesised and purchased iron sulfides. Due to the high capacitance and diffusion effects encountered by the thick iron sulfide layer, Vertical Scanning Interferometry (VSI) was used. Data were processed using an image analysis software to assess both the general and localised corrosion attacks. VSI images for mass coupons deduced that the *in-situ* precipitated mackinawite exhibited significant localised attacks, more representative to the sour environment.

The *ex-situ* morphological and compositional characterisation methods, however, lack the spatial and temporal resolution that can provide much details about real-time physical and chemical alterations at the interface. In addition, applying these techniques is limited for post-test analysis, which makes it difficult to directly correlate the results to the electrochemical observations. As a result, more complicated *in-situ* analytical tools have been developed and can be utilised.

2.5.2.2 *In-situ* techniques

Surface analysis of electrochemical systems often encounters some complexities due to the complex charge transfer processes that occur over a depth of few Angstroms on the electrode surface.[120] In addition, pitting is a dynamic process that involves different stages, such as initiation and propagation or termination, and different reactions such as ionic diffusion, electric migration, and interaction with the bulk environment. The difference in the molecular structure between the bulk and the interface regions adds another complexity. As a result, *in-situ* characterisation of electrochemical systems is necessary to reduce the effects of uncontrollable structural changes that may occur during analysis in *ex-situ* environments.

Initial attempts to *in-situ* investigate the steel corrosion were carried out using electrochemical measurements and *in-situ* optical microscopy. This method has made possible the observation of sequential images of corrosive processes such as grain boundary corrosion and sulfide film growth and transformation.[121] Nyborg[122] has shown that a mesa attack in carbon steel was formed by the coalescence of small pits that grow together in a large mesa attack.

Other techniques such as *in-situ* Scanning Reference Electrode (SRE) and *in-situ* Scanning Vibrating Electrode (SVE) techniques have been used to study pitting, but the presence of deposits in the case of UDC limits the applicability of these techniques.[123] Thermal Atomic Force Microscopy (AFM) has also been used to analyse pitting by mapping a thermal image showing the temperature difference between the localised areas, and then using a linear thermal program to measure the critical pitting temperature.[124] Pit depth readings were also

obtained *in-situ* using ultrasound sensors, which is a common practice to monitor pitting depths in service pipelines.[125]

In-situ techniques have recently been developed and equipped with high resolution and penetration powers allowing to detect micro- or even nanoscale processes. *In-situ* probing is enabled by using highly advanced synchrotron-light sources, which enables reliable measurements without significant loss of the intensity of the probing light. The synchrotron radiation is a very high flux X-ray beam, many orders of magnitude stronger than the micro-focus X-ray tube, originated from the deflection of charged electrons or positrons in a magnetic field.[45] Additionally, vacuum is not required, so it can penetrate electrodes and electrolytes at reasonable depths, to allow for high resolution imaging with enhanced signal-to-noise ratio and time-resolved studies using sophisticated detectors.

The synchrotron beam requires short acquisition times that could be shorter than the time of any microstructural alteration. In corrosion research, since the time of acquisition is so short, synchrotron techniques can be more suitable for characterising the corrosion process before the corrosion rate is fairly changed. The corrosion and film precipitation processes take place at the same time, and therefore, it is essential to characterise the film's composition and structure in real-time. In addition, the salt film is an important feature of localised dissolution since the initiation and growth of pits and crevices are closely associated to their presence.

Introduced by Isaacs and Tester in 1975 [35,102], *in-situ* X-ray studies of localised corrosion were carried out on anodically dissolving stainless steel artificial pits to study the behaviour, resistance and thickness of the salt films. The study concluded that the salt film has approximately 100 Å thickness with a resistivity of about 108 Ω.cm. To analyse the concentration of metal ions, Isaacs[43] used *in-situ* X-ray fluorescence (XRF) to analyse the concentration of metal ions, which showed a salt layer composed mostly of iron, however, the fluorescence technique can not directly detect the presence of salt films.[69] This method was later used by Hunkeler and Bohni[103] to study the mass transport control of stainless steel and nickel wires.

Recently, *in-situ* synchrotron X-ray diffraction (XRD) was used to determine the phases of the formed films that influence the transport properties, where it has provided information about the salt structure and crystallite sizes at the interface.[37,46] X-ray tomography can also, non-destructively, provide 3D information about the interior structure of the material, for example during pitting.[69,126]

In-situ X-ray Absorption Near-Edge Structure (XANES) analysis is very sensitive to the oxidation state.[46,70,127] The passivity of iron was investigated in alkaline solutions by Schmuki *et al*.[128] It was found that the ferric passive film has converted completely into ferrous film upon

reduction of the iron passive film, and anodic polarisation resulted in the growth of a new passive film. The addition of ethylenediaminetetraacetic acid (EDTA) prevented the formation of the porous oxide-hydroxide layer as the ferrous layer dissolved during reduction in presence of EDTA. Oblonsky *et al.*[129] studied the formation and dissolution behaviours of passive films formed on iron in acetate solution. Polarisation kinetics of iron were found to control the process that occurs, either repassivation, or active dissolution that leads to autocatalytic reduction by providing electrons for the reduction of the passive layer.

Using *in-situ* XRD and XANES analyses, Rayment *et al.*[46] found that a salt layer of $FeCl_2.4H_2O$ is formed on dissolving iron and stainless-steel pits, but the crystallites size was much smaller in the case of Fe than on stainless steel.[37,130] The XANES spectra of the pit solution showed an overall shape very similar to Fe^{2+}, and the edge energy has not shifted due to a change in the distance above the pit interface. Chloro-complexes were found inside the pit close to the dissolving interface, but not near the pit mouth.[70] When $NaNO_3$ was added during *in-situ* XRD, the salt layer thickness increased slightly. The XRD rings were continuous in absence of nitrate, indicating that the crystallites have random orientation.[37,130]

Most of the work carried out by Newman[59,60,104], Issacs[104] and Steinsmo's[105] groups have studied the pit chemistry and dissolution and passivation kinetics of stainless steel and Fe-Cr alloys using artificial pits in chloride environments. Limited studies, however, were carried out on mild steel pitting, and no similar study was reported on sour environment conditions or in the presence of externally applied deposits.

2.6 Underdeposit Corrosion mitigation

The mechanism by which UDC is taking place and the various production-related issues define the mitigation strategy. As discussed earlier, the anode/cathode separation between covered and uncovered areas or areas beneath non-uniformly packed deposits is responsible for accelerating pitting corrosion under deposits. There is no general consensus, however, on the mechanism of UDC as it depends in the first place on the deposit nature, such as conductivity, porosity or hygroscopicity, and the corrosive fluid, such as composition, water content and inhibitors' presence.

Initially, the equipment design and operating conditions should be optimised to prevent solids from accumulating: this is normally done by avoiding stagnant locations and using higher flow rates. Corrosion resistance alloys (CRA) can be used where critical parts are not able to receive effective mitigation treatment, but they are not economically favourable. Where solids frequently accumulate, localised internal coating can provide temporary corrosion protection, however, it was found unfeasible as it delaminates and needs to be excessively monitored.[27]

Eliminating the solid deposit build-ups has been the main mitigation effort, however, some limitations exist due to the presence of non-piggable systems, which limits the pigging value. Mechanical pigging is usually combined with batch treatment of corrosion inhibitors. The batch inhibited treatment is usually involved as some scales such as mackinawite might have deposited inside the pit re-passivating the pit bottom, and the brush pig usually removes such protecting films.[27] The chemical treatment, however, is limited by the adsorption of inhibitors on the deposit and the restricted transport to the metal surface. The inhibition performance is, therefore, strongly associated to the physical nature of the deposit as well as the field conditions.

A recent study by Alanazi *et al.,*[20] investigated the inhibition of UDC of steel X-60 under field-collected sludge in a simulated sour environment. Two types of inhibitors, fatty acid imidazoline-based and benzyl chloride quaternary, were tested for inhibition performance. Initially, it was thought that higher amounts of inhibitor are necessary to prevent corrosion under deposits and that the adsorbed inhibitor could be quantified. However, it was found that a greater localised rate was achieved with the presence of inhibitors in an under-deposit system. Therefore, lab evaluation of the chemical's effects such as inhibition, solubility, surfactancy, and dispersibility, as well as monitoring its performance in service are necessary parts of the mitigation process.

2.7 Objectives and layout of the thesis

The aim of this work is to elucidate the localised dissolution kinetics of pitting corrosion in steel whilst under deposits, representing a basic case of sour environment pipeline corrosion. To achieve this, several fundamental questions have to be answered: Is the galvanic mechanism enough to interpret Underdeposit Corrosion? How would changing the deposit properties change both the general and localised corrosion behaviours of steel? How are salt films associated with pitting under deposits, and will the salt film properties change, especially when reactive deposits are present? Finally, how would the answers to these questions change if a reactive H_2S gas is introduced in the media?

In this study, a blended electrochemical approach is used, where both general and localised corrosion are assessed and correlated, to provide a comprehensive understanding of the overall performance of steel under deposits. A multitude of complementary microscopy and spectroscopy techniques then detect the dynamic physicochemical variations in both the metal and the deposit, in correlation to the electrochemical response. These variations were studied both *ex-situ* and *in-situ* under different simulated deposit arrangements.

The results of this work are presented in chapters four, five and six. Firstly, in chapter four, the influence of the solid deposit on the general corrosion behaviour of bare steel was studied. Both inert sand and reactive iron sulfides, troilite and pyrite, were used as representative cases of the typical sour environments.[9,18,22,91,131] Open circuit potentials, potentiodynamic polarisation profiles, and potentiostatic currents are measured using a three-electrode electrochemical cell. Additionally, an interesting insight into the galvanic corrosion mechanism is gained by coupling steel coupons with iron sulfide electrodes to measure the galvanic currents via a Zero Resistance Ammeter. SEM, EDX and Raman spectroscopy techniques are used to correlate the morphological and chemical composition changes of both the metal and deposit to the electrochemical responses. The findings of this chapter are presented in terms of the deposit-metal interdependent changes in the physical and chemical characteristics as a function of the different properties of the applied deposit, such as morphology, packing, and chemistry.

In chapter five, artificial pit electrodes are studied to elucidate the role of the deposit morphology and chemistry in changing the localised pit propagation kinetics. The artificial pit acts as an anode in a three-electrode electrochemical cell, simulating an actively dissolving pit, but with reduced dimensionality. Using the same set of deposits involved in chapter 4, cyclic voltammetry measurements[34,106] enable a quantitative extraction of the kinetic data as a function of the various system parameters- essentially the deposit physical and chemical properties. Data are discussed in terms of a transport-controlled model for pit propagation. In

addition to the typically used *ex-situ* morphological and compositional analyses of the artificial pit wire surface, *in-situ* synchrotron X-ray analyses are performed on the salt film of actively dissolving artificial pits. Understanding the salt film chemistry and structure provides essential information about the Fe dissolution behaviour under deposits, as well as the intermediate species. X-ray fluorescence (XRF), X-ray diffraction (XRD) and X-ray absorption near-edge spectroscopy (XANES) are the *in-situ* methods used in the present study.

The experiments presented in chapters four and five are used to establish a fundamental understanding of the effect of deposits on the dissolution kinetics of both planar coupons and artificial pits in aerated and N_2 environments prior to introducing the sour gas variable. In chapter six, Hydrogen Sulfide, as an active gas, is introduced into the same systems, and both the general and localised corrosion kinetics are investigated using the same characterisation tools.

Using this electrochemistry blended approach and the support of various *ex-situ* and *in-situ* analyses, both general and localised corrosion can be assessed, and a correlative argument can be established to provide a comprehensive understanding of the overall performance of steel under deposits. The findings of the study pave the way towards innovating experimental methods and potential protocols to develop *in-line* monitoring probes for industrial application.

3 Experimental methods

In a typical UDC test, working electrodes (WEs) of different geometries are covered with deposits of different physical and chemical properties. In our study, sand and iron sulfides were used as representatives of the sour gas pipeline typical conditions, and to provide contrast between the steel behaviour under insoluble inert and soluble active deposits. Artificial pit electrodes, both in the form of one-dimensional wire and two-dimensional foil, were used to study the localised corrosion phenomenon, whereas the general corrosion was investigated using planar coupons. Both artificial pits and planar coupons were connected as WEs in these electrochemical setups: 3-electrode and ZRA galvanic electrochemical cells. The corroded surfaces were subsequently examined using SEM-EDX and Raman spectroscopy. *In-situ* synchrotron X-ray measurements namely XRF, XRD, and XANES, were also performed on actively dissolving artificial pits.

In this chapter, the general methodology and parameters used in this work are reported, supported by some theoretical aspects of the experimental methods and characterisation techniques used.

3.1 Deposits

Technical grade sand (Sigma Aldrich, UK) with a particle size of -325 mesh (less than 44 μm) and 50-150 mesh (~100-300 μm) were used to examine the effect of inert deposits. Iron sulfide, as a mixture of troilite and pyrrhotite (FeS, Alfa Aeser, UK), and iron disulfide, pyrite (FeS_2, Sigma Aldrich, UK) were used to investigate the influence of chemically reactive deposits. FeS, in powder form, and naturally occurring geological FeS_2, in mineral form (Alfa Aeser, UK), were used in the ZRA experiments. All deposits are commercially available and used in the experiments as received.

3.2 *Ex-situ* electrochemical tests

3.2.1 Three-electrode electrochemical cells

Three-electrode electrochemical cells were used in our work to study the dissolution kinetics of steel planar coupons and artificial pits whilst under deposits. The typical configuration of the cell is explained in Figure 3.1. The cell typically consists of 3 electrodes namely, working electrode (WE), reference electrode (RE) and counter electrode (CE).

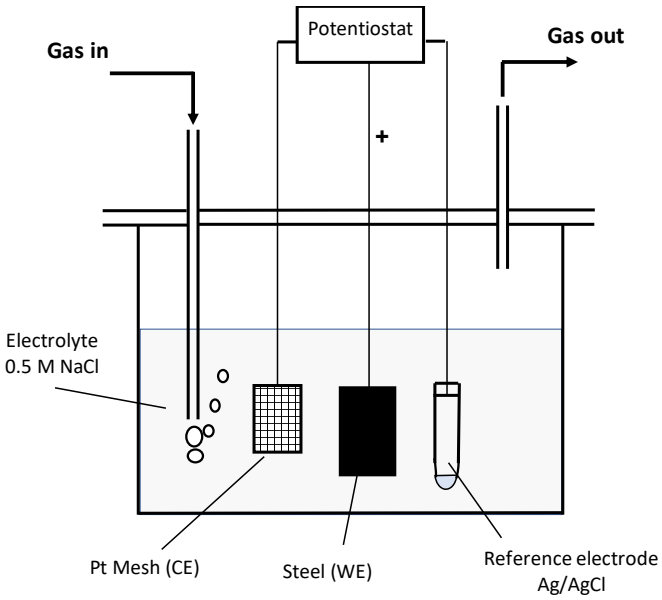

Figure 3-1. A schematic of the typical configuration of a 3-electrode electrochemical cell with a bare steel WE, Pt mesh CE, and Ag/AgCl RE. The electrolyte used was 0.5 M NaCl solution with pH 6.8.

REs should be chosen to have a stable potential, *i.e.,* non-polarizable, and be chemically and electrochemically reversible so that the potential can be calculated using Nernst equation. The RE is usually placed close to the WE surface to reduce potential losses from the electrolyte resistivity. Silver/silver chloride electrode (Ag/AgCl), calomel electrode (Hg/Hg_2Cl_2), and mercurous sulfate electrode MSE (Hg/Hg_2SO_4) are examples of the most frequently used REs. The choice of the RE depends on numerous factors such as the type of electrolyte and the experimental temperature. Unless stated otherwise, Ag/AgCl RE was used in our experiments for its stable potential, and to avoid using toxic mercury from mercury-based REs. The electrolyte is chloride rich, and therefore, there is no presented harm in using chloride-containing electrodes. When a Ag/AgCl RE was not used, all the potentials in our data were reported against the Ag/AgCl scale. The CE, on the other hand, is ideally polarisable and should not react with the electrolyte. Platinum (both wire and mesh) was used as CE in our experiments. Both VersaSTAT (Princeton Applied Research) and Autolab PGSTAT30 potentiostats were used in the electrochemical measurements.

3.2.1.1 Planar coupon electrodes

Planar X56 carbon steel coupons (composition: 0.12 wt. % C, 0.60 wt. % Mn, 0.045 wt. % P, 0.045 wt. % S, balance Fe) with an exposed surface area of ~0.3 cm^2, unless stated otherwise, were used as WEs. The coupons are mounted in epoxy and gradually wet-abraded to 4000-grit SiC paper finish, and then degreased by rinsing with acetone and deionized water prior to the reaction. A rectangular container was fixed to support the deposit, covering the whole

surface of the coupon, as shown in Figure 3.2a. A mesh-type cover was used to keep the deposit in place whilst avoiding the solution blockage. Both the support container and cover were 3-D printed out of Polylactic Acid (PLA) wires using a 3-D printer Ultimaker 2+ with a 100 µm layer resolution.

Once the deposit was applied to cover all the surface of the electrode, the electrode was immersed in a continuously N_2-purged 0.5 M NaCl electrolyte, as demonstrated in Figure 3.2b. The oxygen content, despite purging with N_2, is unknown and assumed to be a systematic error that repeats across the experiments. The deposit-covered coupon was connected to the working electrode terminal of the potentiostat.

The electrode was initially left to stabilise in the test solution for 1.5 h while the OCP was continuously being measured. After stabilising, the potential was swept from –250 mV vs. OCP in the anodic direction, at 500 $mV.s^{-1}$ scan rate. The sweep was stopped at –100 mV vs. Ag/AgCl RE. Potentiostatic tests at higher potentials, –450 mV (vs. Ag/AgCl RE) and +100 mV (vs. OCP), were used as accelerated corrosion tests to study the surface deformation. The effect of deposit size, thickness, and type were examined, and the data are presented in terms of the effect of each parameter on the OCP and the polarisation profile.

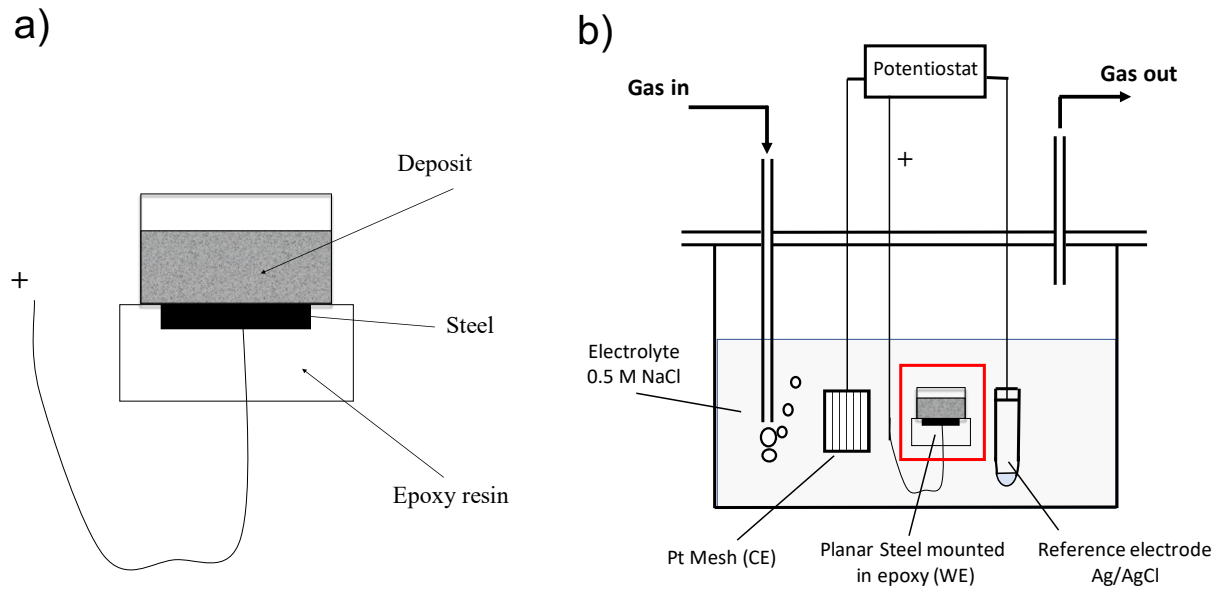

Figure 3-2. (a) A schematic showing a planar electrode, mounted in epoxy with a fixed cup to support the applied deposit. (b) The planar coupon is connected as a WE in the 3-electrode electrochemical cell configuration.

3.2.1.2 Wire artificial pits

One-dimensional artificial pit electrodes were prepared by mounting 250 μm-diameter, 99.5%-purity, low-carbon steel wires (C < 1000 ppm, Advent Research, Oxford, UK) in a transparent epoxy resin (Struers EpoFix). A custom-designed mould that allows mounting multiple wires was 3D printed (Figure 3.3). The mould enabled us to produce a multi-electrode array of artificial pits to be tested simultaneously. Individual electrodes could also be cut from the array to be tested separately, which was the protocol used throughout this study, unless stated otherwise.

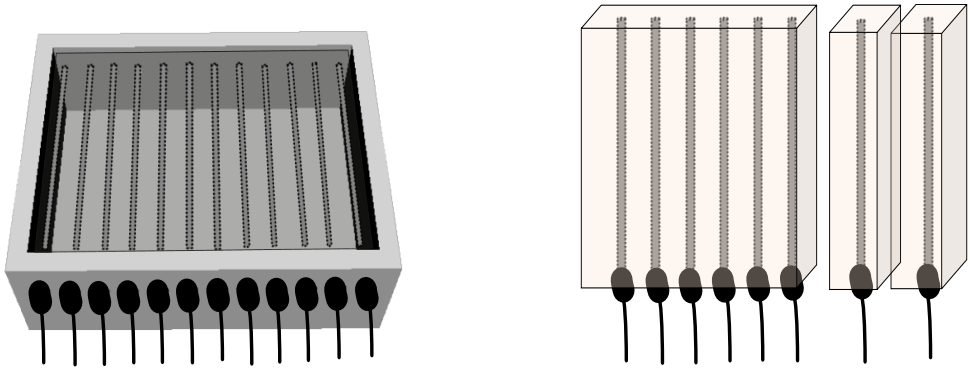

Figure 3-3. A 3D-printed mould, custom-designed to mount multiple artificial pit electrodes that could be used either collectively or individually.

Initially, the outer surface of the inert support was successively wet-abraded to a 4000-grit paper finish, which ensures that a constant cross-sectional area would be exposed to the electrolyte. Extra controls such as applying vacuum, to remove microbubbles during the resin curing, and careful cleaning of the wires were used to reduce crevices and minimise the errors during subsequent pit depth measurements.

Deposits were physically incorporated the same way as described with planar electrodes using plastic cups and mesh-type covers, to enclose all the wire cross-section prior to the start of the measurements, as demonstrated by the schematic in Figure 3.4a. Electrochemical tests were carried out with deposits present above the pit cavity. The electrodes were placed in a dilute NaCl electrolyte solution and connected as anodes, as shown in Figure 3.4b. The whole set of the artificial pit measurements were performed at room temperature while the cell was open to air, unless H_2S gas was used.

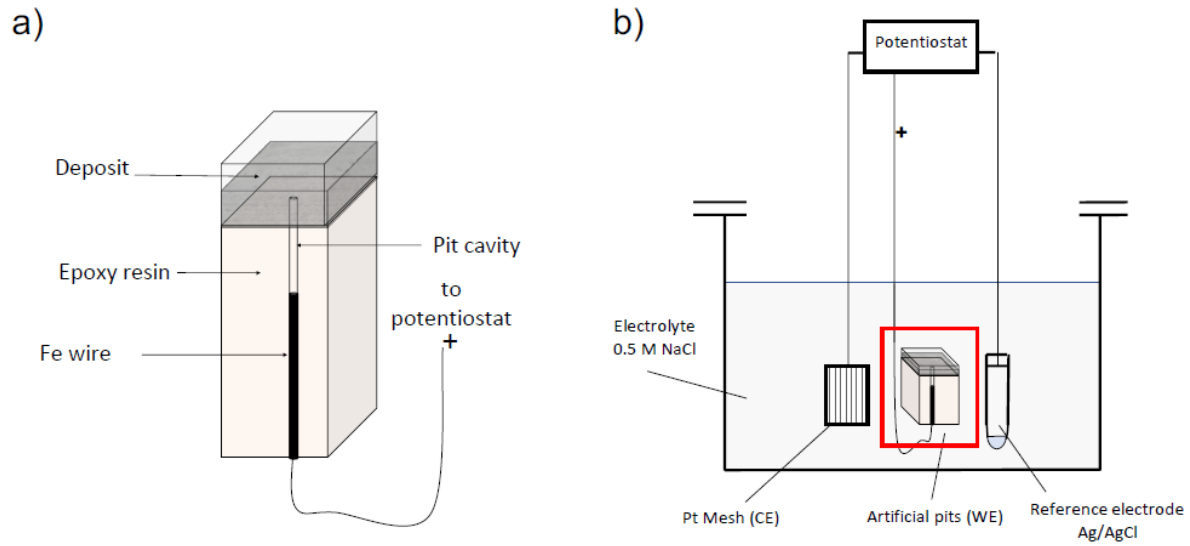

Figure 3-4. A schematic artificial pit electrode (a), showing a 250 µm diameter wire embedded in transparent epoxy with a plastic cup fixed at the pit mouth to support the deposits. The wire is recessed inside the epoxy by anodic polarisation using a 3-electrode electrochemical configuration (b), allowing for the formation of an artificial cavity.

To initiate pitting, the wire anode was subjected to an initial pulse of +900 mV for 20 seconds. The potential was then stepped down to +500 mV and held constant until the surface of the steel wire, in contact with the deposit and/or the electrolyte, recedes down to form a 1D pit cavity. Different pit depths were formed by varying the duration of the potential hold. The pit depth was calibrated by visually confirming the depth, using an optical microscope coupled to a CCD camera, and comparing it to a theoretical value calculated from Faraday's 2nd Law, assuming 100% current efficiency.

Once a cavity was formed to a known depth, cyclic voltammograms (CVs) were measured; potential is swept from a high positive potential (typically +500 mV, but a higher value was used in specific cases, as will be shown later) and downwards to -400 mV at 10 mV.s^{-1}. Each measurement was performed for three scans to achieve a relative steady state, but only the last cycle is reported.

Various pit depths, bulk solution pH, and chloride ion concentration were initially studied prior to introducing the deposit. Pit depths from ~200 to 800 µm were studied; the pit depth was maintained at 450-500 µm when the effects of other factors were studied, unless stated otherwise. NaCl solution with pH 6.6 and 0.5 M chloride concentration was used throughout this study, unless the bulk solution chemistry is under investigation. In which case, different chloride ion concentrations of 0.5 M, 1 M and 3M were studied at a fixed pH 6, while a 0.5 M NaCl electrolyte solution with pH values of 3, 6, 9 and 12 was used to study the effect of hydrogen ion concentrations in the bulk solution.

Finally, sand, with different particle size and layer thickness, and iron sulfide deposits were introduced above the pit cavity, and CVs were measured to directly obtain the dissolution kinetics as a function of pit depth and the deposit's particle size, thickness, and type.

3.2.2 Zero Resistance Ammetry (ZRA)

ZRA is a special ammeter designed to measure precisely the current flow between two points of different potential in low resistance, low current circuits. In electrochemical tests, the current drop by internal resistance is substantial, which causes significant errors in the current flow measurement. Using a feedback loop that feeds voltage to the current output terminal, ZRA can achieve zero internal resistance[28,101,132]; a battery provides current which flows through a variable resistor until the internal resistance drop matches the open circuit. When the potentials match, the potential drop between the two working electrodes is zero and the galvanometer will indicate zero current. Hence, the ammeter will register the actual current. Usually, modern potentiostats have a built-in ZRA mode, and the connections on how to establish a ZRA circuit might differ between the manufacturers.

Both geological pyrite minerals FeS_2 and powdered troilite-pyrrhotite mixture FeS were tested for galvanic corrosion by coupling to mild steel electrodes. To use ZRA for galvanic corrosion tests, the setup in Figure 3.5 was used, where both electrodes are connected as WE1 and WE2, along with an Ag/AgCl RE.

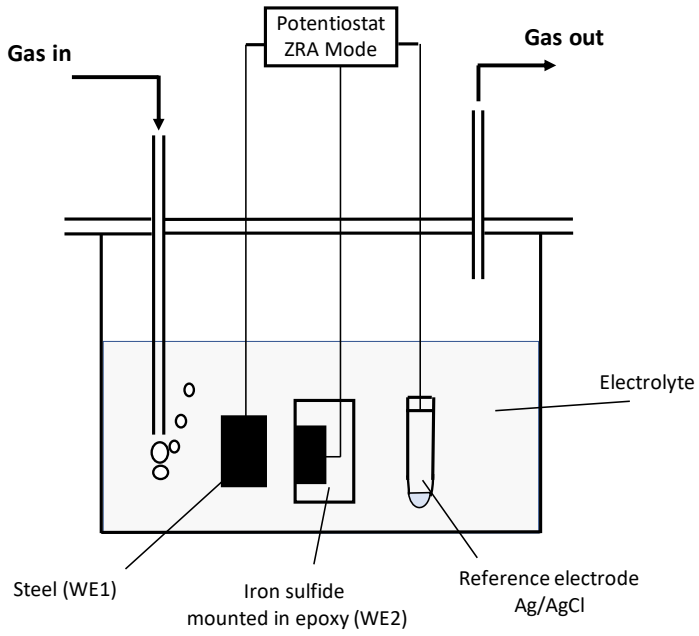

Figure 3-5 Zero Resistance Ammetry (ZRA) cell to measure the galvanic current between two working electrodes of different potentials. The couple potential is measured against Ag/AgCl RE and the electrolyte is a 0.5 M NaCl solution.

Both iron sulfides were machined according to the starting material of the polymorph: the natural geological FeS_2 was cut into small pieces, while the FeS powder was pressed into 1 cm-diameter pellets using a mechanical press at 10 kPa for 30 second. Electrical connections were then attached to the machined material using silver paste to form working electrodes. The electrodes were finally casted in a transparent epoxy. After setting, the electrode surface was ground with SiC paper to a 4000-grit finish exposing an area of ~1 cm^2.

The 0.5 *M* NaCl electrolyte was purged with N_2 before and throughout the course of the measurement. The area ratio between the steel and iron sulfides electrodes is close to 1:1. Upon immersion, OCP measurements were initially carried out for several minutes before measuring the galvanic coupling. The galvanic coupling current and potential were measured using Versastat, ivium and ACM potentiostats, interchangeably. The ohmic drop is not considered in the potential measurements since the electrolyte is concentrated with 0.5 M NaCl, which increases the solution conductivity. After the experiment, samples were washed using DI-water and acetone, and dried using de-oxygenated nitrogen gas. The oxygen content is unknown and is assumed to be a systematic error that repeats across the experiments. Samples were eventually stored under vacuum in a desiccator before further surface analysis.

3.2.3 H_2S testing

To study the sour environment's effect on iron dissolution, both the 3-electrode and ZRA electrochemical measurements were repeated in presence of an H_2S saturated solution. The same setup arrangements, described in the previous sections with the non-H_2S cases, were used here as well, with the introduction of H_2S-related measures. Figure 3.6 describes the typical experimental setup, in this case representing the 3-electrode cell with artificial pit multielectrode configuration, allowing for multiple measurements to be performed simultaneously.

The electrolyte solution, 0.5 *M* NaCl, was first purged with N_2 overnight in a separate glass vessel (left side in Figure 3.6). The N_2 pressure was used to transfer the solution to the test cell that has the electrodes. H_2S was then introduced at a constant purging (30 cc per min) to maintain the partial pressure close to 1 atm., and the solution was left to charge with H_2S for 2-3h prior to the electrochemical measurement. No adjustment of pH was carried out. The residual unreacted H_2S passes through to an H_2S absorber during the reaction, and the waste solution was eventually purged overnight with nitrogen through the H_2S absorber to render it safe for disposal. An H_2S sensor was placed close to the final outlet to ensure no gas leaks into the atmosphere.

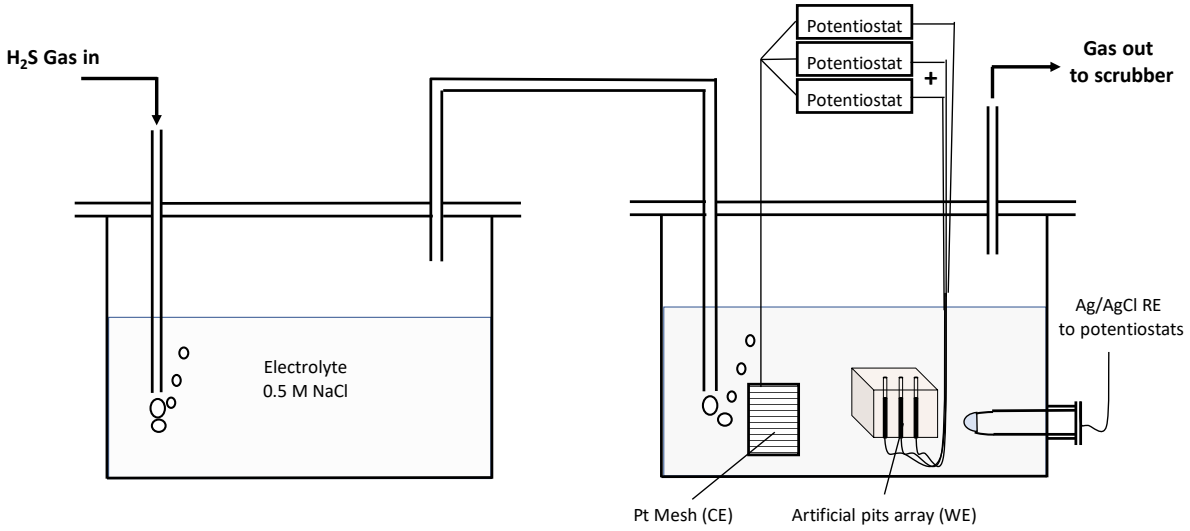

Figure 3-6 A schematic showing a two-vessel experimental setup used to measure the electrochemical behaviour of under-deposit systems in H_2S: artificial pits, planar coupons, and ZRA electrodes. The schematic describes the case of a 3-electrode electrochemical cell with 0.5 M NaCl electrolyte, Ag/AgCl RE and a Pt Mesh CE, and a multi-artificial pit array acting as anodes.

In the artificial pit experiments, measurements were carried out simultaneously on separate pits from the array. Sequential CV measurements on the same pit was avoided to minimise the errors associated with the corrosion history of the metal. Two protocols are contrasted: (1) the wire was pre-corroded in aerated conditions, followed by exposure to the H_2S-saturated solution at open circuit conditions, and eventually performing the CV measurement, and (2) the wire was corroded inside the H_2S-saturated solution, followed directly by CV. Although protocol (1) is more favourable to avoid oxidation of H_2S, which practically minimises the pre-corrosion rate, protocol (2) was used as the standard protocol since it showed reproducibility in the test results.

In the planar coupon and ZRA measurements the electrodes were conditioned in the H_2S purged solution for 2-3 h prior to the measurement. Conditioning is assumed to allow a steady state to be reached after corrosion films are formed on the metal surface. To study the effect of deposits on the iron sulfide film formation in H_2S, steel samples were immersed in the test solution and left under open circuit conditions for 4-6 h. After the reaction, samples were washed using deionised-water and acetone and dried using de-oxygenated nitrogen gas and eventually stored under vacuum in a desiccator before later surface examination.

The H_2S experiments were facilitated by Dr James Hesketh and Mr Phil Cooling from Professor Gareth Hinds' lab at the National Physical Laboratory (NPL). Due to limited resources and time for the H_2S experiments, multiple electrodes were measured

simultaneously using several potentiostats with common reference and counter electrodes. Therefore, a larger solution quantity was used to accommodate several samples.

3.3 *Ex-situ* surface analysis

SEM-EDS and Raman spectroscopy were performed to analyse the morphology and chemical composition of the reacted surfaces, both the metal and the deposit, before and after the corrosion reaction.

3.3.1 Scanning Electron Microscopy and Energy Dispersive X-ray Spectroscopy (SEM-EDX)

SEM-EDX is a surface analysis technique to characterise the surface morphology and chemical characteristics under vacuum conditions. In an SEM, the electron beam is focused into a fine probe that is then raster-scanned over a region in the sample. The SEM beam is accelerated up to moderate energies (~1 – 30 kV) generating many signals representing different interaction depths, hence making it versatile for several applications. SEMs can provide information on topographical features, surface morphology, phase distribution, crystal structure and orientation, as well as elemental composition (spectroscopic) information. This technique is extremely useful for studying and characterising the morphology of surface corrosion films or the film's cross-section.

All SEM images in this work were obtained using the secondary electrons (SEs) emitted as a result of the inelastic scattering of the incident beam. SEs originate from depths of approximately 5-50 nm. As the incident angle of the beam increases, the electrons' escape distance decreases, and a greater number of electrons are emitted and detected. Therefore, SE images provide surface topography contrast with edge features appearing brighter than uniform surfaces. A large depth of field, which is a measure of the nearest and furthest surfaces from the lens that appear in focus, is achieved by electromagnetic lenses. Image construction in SEM is accomplished by detecting and mapping the intensity of the signal in each point onto a viewing screen or film, and the magnification is adjusted by changing the size of the area scanned on the specimen.

The excitation of the surface atoms by the incident electron beam leads to the emission of characteristic X-rays that can be utilised to provide elemental analysis of the probed surface, *i.e.,* EDX. In EDX, the detected X-ray intensity at characteristic energies is translated into atomic or weight concentration of the constituent elements of a sample. The generated X-rays are absorbed on a semiconductor crystal detector (typically Si or Ge) leading to the generation of a photoelectron and an X-ray photon, which can be reabsorbed further in lower energy

shells to generate other photoelectrons. The photoelectrons released from a cascade of these events travel in the semiconductor crystal and scatter inelastically giving up their energy to other electrons. Due to this energy transfer between the photoelectrons, electrons in the valence band gain energy to rise to the conduction band. Under an applied voltage, the electron in the conduction band moves freely leaving a hole behind. The energy required to generate an electron-hole pair in the detector crystal is known, and hence the energy of the original X-ray photon can be identified from the number of electron-hole pairs generated.

The surface morphology and elemental composition of the steel surface and corrosion films in this work were examined using Quanta FESEM (Field Emission SEM) in SE mode with 20 kV acceleration voltage. It was also used to view the deposit particle size and morphology, and to analyse the surface chemical composition of the applied deposits before and after the electrochemical experiments.

3.3.2 Raman spectroscopy

The Raman effect has become an important spectroscopic tool for the characterisation of materials. It involves inelastic scattering of single wavelength light – from a laser – inside the sample due to the excitation of characteristic vibrations of molecules and crystals. When light is incident on a sample, it scatters either elastically with a similar frequency (Rayleigh scattering) or inelastically with a modification in the energy (Raman scattering). Raman scattering takes place when the vibrational energy of the molecule is lower or higher than the incident beam, respectively denoted Stokes and anti-Stokes.[133] If the molecule is polarisable, there is Raman scattering.

In our study, Raman spectroscopy was used to detect alterations in the chemical species of both the deposit and the reacted steel surface. The analysis was performed using Reinshaw inVia Raman microscope, a confocal Raman Imaging Microscope system combined with Renishaw's WIRE software. The sample was excited using visible green laser of 523 nm wavelength, and a microscope objective of 50x magnification was used for the measurement spectra.

Before each session, Si calibration and alignment of the laser were carried out using an internal standard. The spectra were recorded from 106 to 1365 cm^{-1} Raman shift at room temperature and ambient air atmosphere without any special protection. For each sample, a minimum of ten locations were analysed using powers from 1 % to 5%, with 10 s acquisition time and 3 accumulations. The spectra were finally analysed using Wire 4.1, a software provided by Reinshaw™. The low powers were chosen due to the iron sulfide sensitivity, and the power effect was checked by repetitively acquiring on the same location, with no variation

observed in the spectrum using the 532 nm wavelength. Peaks were fitted to different sources from the literature to identify the associated chemical species.

3.4 *In-situ* synchrotron analysis

3.4.1 Beamlines, photo-absorption, and X-ray absorption spectroscopy (XAS)

Unlike the microscopy-spectroscopy techniques described above, analysis using synchrotron X-rays provides the high spectral and spatial resolution necessary for accurate chemical speciation and structure analysis of small amounts of materials.[45,134] In synchrotron X-ray sources, electrons are produced at high energy by an electron gun, and accelerated in a linear accelerator before entering a large storage ring where they circulate at relativistic velocities. A schematic of the main structure of a synchrotron facility is shown in Figure 3.7.[135]

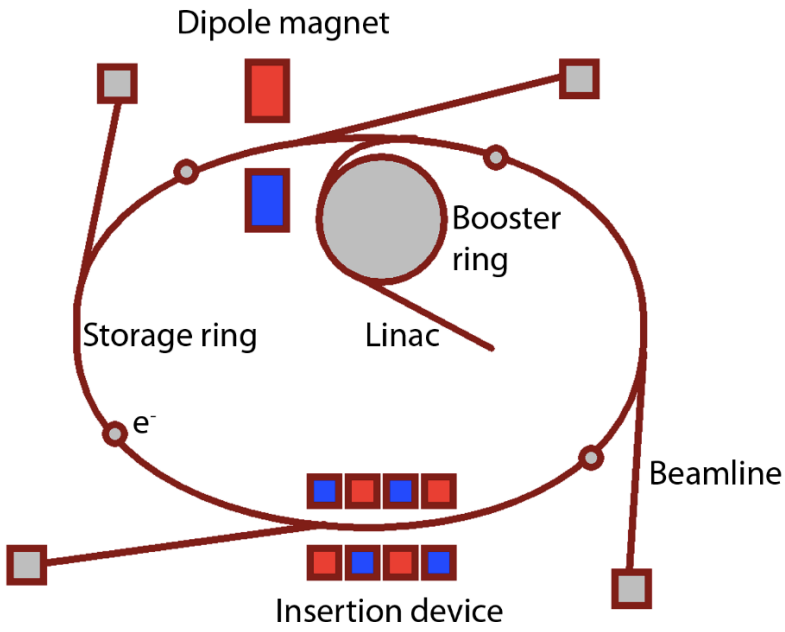

Figure 3-7 A schematic of the main structure of a synchrotron facility.[135]

The electrons are steered around the ring by magnetic fields applied by a single or array of magnets called insertion devices. As the electron's trajectory is bent by the magnets, the energy is lost due to deceleration and is emitted in the form of electromagnetic radiation. The spectral bandwidth can be tuned by adjusting the magnetic field through changing the gap between the top and bottom magnets.[136] The radiation is then emitted into many different beamlines which convey the photons to the experimental chambers, providing a wealth of characterisation techniques.

The X-ray techniques presented in this work are based on the photo-absorption interaction between incident photons and target atoms. Figure 3.8 shows the principle of photo-absorption.[135] An incident photon with an energy equal to or exceeding the binding energy of an inner shell electron is absorbed. The ejected electron due to the ionisation of an atom by a photon is called photoelectron. When the incident photon has a much larger energy than the binding energy of the inner shell electron of the target atom, the photons are scattered inelastically. Different signals such as the element's specific binding energies and the fluorescence arise from the photo-absorption process, which help in the chemical identification of the material under investigation.

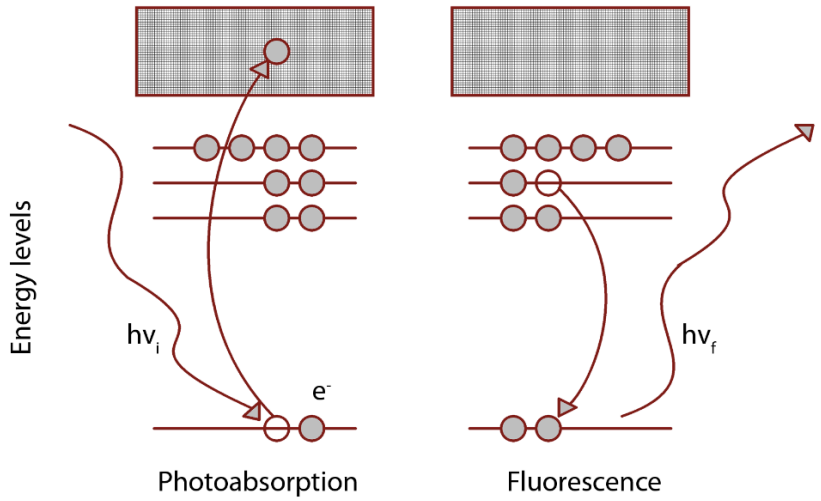

Figure 3-8 A schematic of the X-ray photo-absorption interaction followed by fluorescence. An incident photon of energy hv_i is absorbed by the atom, ejecting an electron from an inner shell. The atom relaxes to fill the vacancy by emitting an X-ray photon with a characteristic energy *hv_f.*[135]

In-situ synchrotron X-ray experiments were carried out at the microfocus spectroscopy Beamline I18 at Diamond Light Source, Didcot, UK. XAS beamlines typically contain slits to define the X-ray profile, a monochromator to select the beam energy, a harmonic rejection mirror to reduce the harmonic content of the beam, a sample stage, and ionisation or other detectors to measure the intensity of the X-ray beam.[137] Diamond's I18 beamline has a Si (111) monochromator to produce an X-ray beam working over a 2-20 keV energy range. The Si (111) single crystals are designed such that a particular atomic plane is parallel to the surface of the crystal. By rotating the crystal in the X-ray beam, only X-rays with energies that satisfy Bragg's Law are diffracted. Therefore, the energy of the diffracted X-rays can be controlled by varying the angle of the monochromator crystal relative to the incident X-ray beam. The energy resolution is affected by the beam divergence, which is determined by the source and/or the focusing objects that precede the monochromator in the beamline.[137]

The incident and transmitted/fluoresced X-ray intensities are measured using ionisation chambers or solid-state detectors placed upstream and downstream of the sample, respectively, as shown in Figure 3.10.[135] The detector, in fluorescence measurements, is positioned at a 90° relative to the incident beam direction, with the sample being positioned at a 45°, as illustrated in Figure 3.10(b). The 90° angle between the detector and the incident beam direction is used because the intensity of the scattered X-rays is minimum at 90°, while the fluorescence X-rays are emitted from a sample in an isotropic manner. Therefore, the greatest signal to background noise ratio is obtained at a 90° angle between the incident beam and the detector. Ionisation chambers do not distinguish X-ray photons based on their energies, and therefore in case of fluorescence, or where signals have large backgrounds, solid-state detectors present better detection limits. Solid-state detectors utilise a semiconducting material that generates a number of electron-hole pairs proportional to the energy of the incident radiation. Nowadays, multi-element detectors (MEDs) have multiple detector channels within the same detection unit, and the fluorescence signal from each detector channel are collected and summed.

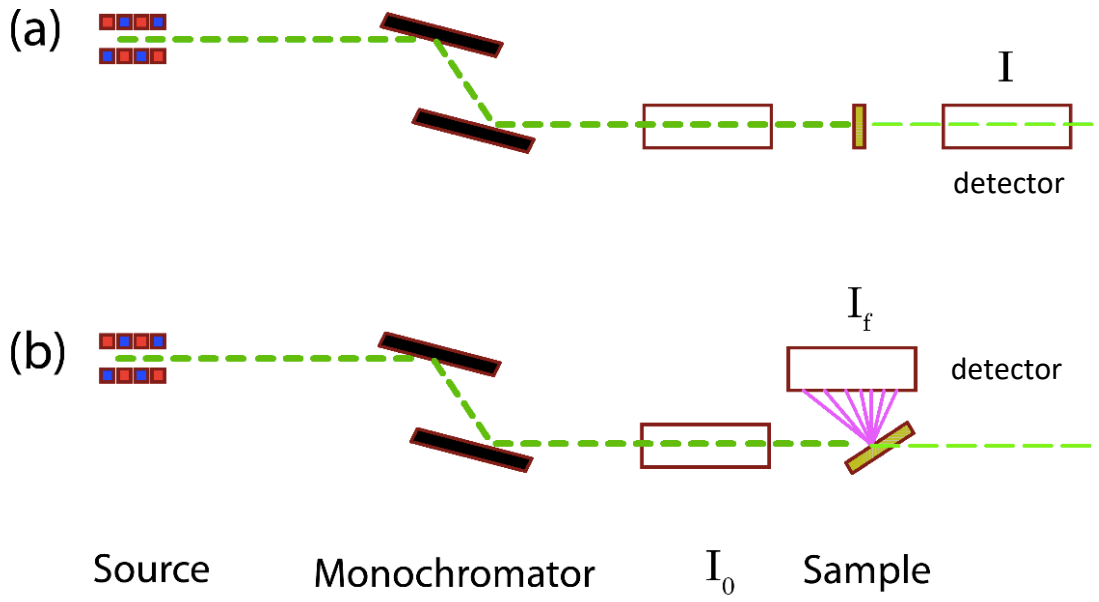

Figure 3-9 The beamline configuration showing the typical apparatus for XAS measurements in (a) transmission geometry, and (b) fluorescence geometry.[135]

Beer-Lambert's law (Equation 3.1) establishes the relationship between the intensity of the incident X-ray beam I_o and the transmitted beam I.

$$I = I_o e^{-\mu x} \qquad \text{Equation 3.1}$$

Where μ is the linear attenuation coefficient which describes the fraction of the beam that gets absorbed or scattered per unit thickness of a specific element, and μx is known as the

absorbance. XAS involves measuring the absorbance as a function of X-ray energy. It can be deduced from Equation 3.1 that the transmitted intensity decreases by 63% by increasing the thickness of the sample by one absorption length. The absorption coefficient can subsequently be derived from the number of fluorescence X-rays I_f since the atomic relaxation (fluorescence) processes are proportional to the preceding photo-absorption, as in Equation 3.2.

$$\mu x \ \alpha \ \ln \frac{I_f}{I_o} \qquad \text{Equation 3.2}$$

The probability for absorption of an X-ray by the target atom increases sharply when the incident X-ray energy equals the energy required to excite a target electron (photo-absorption). These steps in the absorption coefficient are termed absorption edges that are characteristic to each element, *i.e.,* the binding energy of its electrons. In XAS, when the X-ray energy is scanned across a particular edge in a specific sample, it gives rise to a distinctive X-ray absorption spectrum, as shown in Figure 3.10.[137]

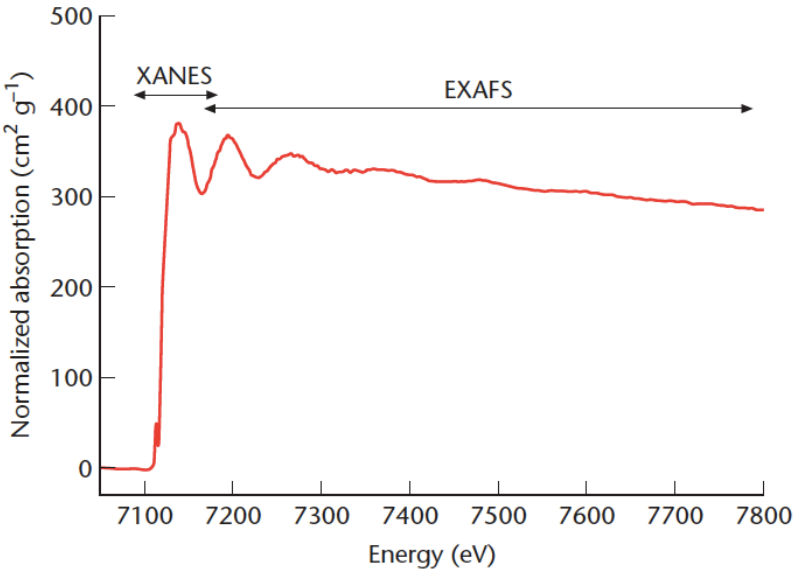

Figure 3-10 An example of an X-ray absorption spectrum indicating the main spectrum regions: XANES and EXAFS.[137]

The region of the spectrum which is near the absorption edge step is termed X-ray absorption near edge structure (XANES), while the region at 50-100 eV beyond is called the extended X-ray absorption fine structure (EXAFS). XANES provides information on the oxidation state of the atom as well as the binding geometry. EXAFS can provide additional information on local environments including the type, the number of neighbouring atoms, and interatomic distances (this work does not involve EXAFS analysis).

XAS can be collected both in transmission and fluorescence modes. The fluorescence mode is the preferred measurement where the element of interest is more dilute in the sample. This is because in the transmission mode, the signal to noise ratio (SNR) applies to the total absorption data, and for dilute elements the SNR will be degraded by a factor related to the dilutions, which may make it difficult to extract in practice. On the other hand, in highly concentrated samples the fluorescence X-rays may be reabsorbed by the element of interest (self-absorption), causing an attenuation in the fluorescence signal.

In addition to micro-XAS, Diamond I18 beamline is optimised to perform micro- XRF mapping studies and micro-XRD. All three synchrotron X-ray measurements were carried out on iron foil artificial pit electrodes.

3.4.2 Electrochemical cell for *in-situ* synchrotron studies of artificial pits

An electrochemical cell for the *in-situ* measurements was 3D-printed and assembled according to Figure 3.11. Thin iron foil, with 25 μm thickness, was used for design considerations, and to avoid excessive attenuation of the beam. A multielectrode array, composed of three electrodes in this case, was prepared by sandwiching 3 mm-wide foil strips between epoxy araldite and polyimide (Kapton, 8 μm thickness) film (Advent Research Materials, UK), leaving an exposed cross section to act as a fixed area electrode. This allows multiple experiments to be performed simultaneously using two ivium potentiostats such that X-ray measurements could be carried out on one electrode whilst another one is being pre-corroded. The third electrode was left as a spare. Transparent epoxy was used to allow for visual inspection of the pit propagation. Kapton tape was used to attach the electrodes to the cell body, and to act as a support for the deposit at the same time. This design keeps the electrical connections external to the cell, reducing the overall system complexity.

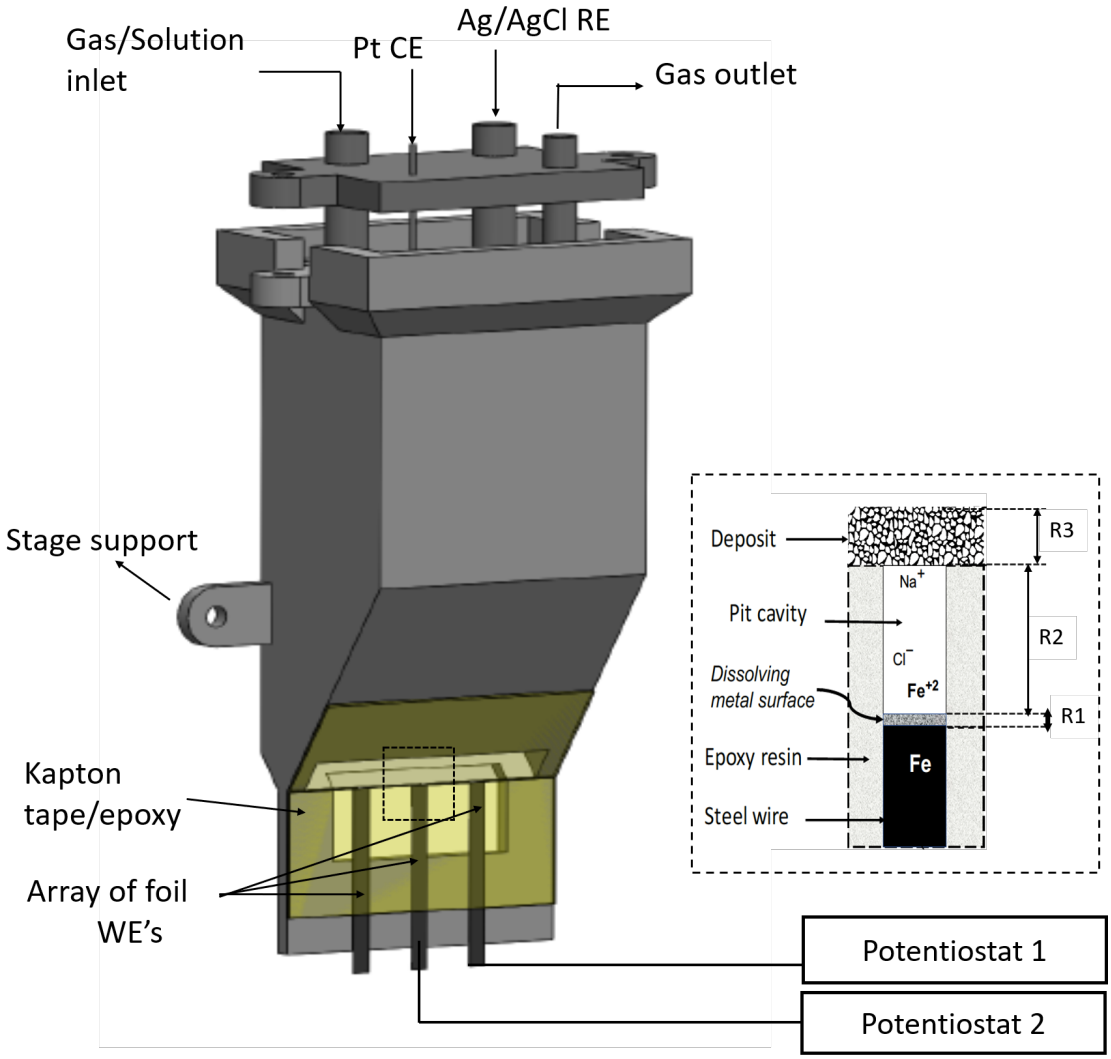

Figure 3-11. In-situ synchrotron X-ray cell with an array of 3 artificial pit electrodes. A pit is comprised of a 25 µm thin iron foil sandwiched between two layers of epoxy and Kapton. The inset image indicates the metal interface and the diffusion barriers R1 (for the salt film), R2 (for the pit depth) and R3 (for the applied deposit when present).

The *in-situ* cell was filled with 50 ml of *0.5 M* NaCl solution, and Pt CE and Ag/AgCl RE were used. The artificial pits were initially activated at +800 mV and grown to different depths before carrying out synchrotron X-ray measurements at the dissolving interface. Shallow pits are identified to be 500-750 µm, whereas the *'deep'* pits are approximately 2 mm deep. All solutions used in this experiment were prepared with deionised water and chemical reagents of analytical grade. When the H_2S conditions were tested, a previously saturated solution was transferred to the cell under controlled arrangements, and no further H_2S purging is used during the synchrotron experiment for health and safety reasons.

The synchrotron X-ray measurements were performed with the support of colleagues from Prof Ryan's lab: Dr's Miguel Gomez Gonzalez, Mohamed Koronfel and Milly Stitt helped with

the beam measurements, and Ms Noora Al-Qahtani prepared the H_2S saturated electrolyte for the *in-situ* artificial pit experiment presented in chapter 6.

3.4.3 The *in-situ* X-ray measurements at Diamond I18 beamline

The beam was set to a size of 1.5 μm (w) x 25 μm (h) to achieve high spatial vertical resolution while acquiring a large horizontal sample. The beam energy varies according to the type of X-ray measurement. To avoid beam damage and bubble formation in the solution, the X-ray beam was attenuated by aluminium foil absorbers. The ionisation detector is set to 1.5 V with varied sensitivities to avoid the saturation of the detector. The beam size and energy, filters and detector arrangements are mainly aimed to achieve a high resolution and reasonable signal-to-noise ratio.

The cell was positioned at a 45^o angle to the beam for fluorescence detection. The step motorized sample stage could be translated horizontally and vertically. Initially, the dissolving interface was visually inspected to ensure that a unidirectional dissolution had taken place. In our typical *in-situ* synchrotron experiment, XRF, XANES, and XRD measurements were carried out when the interface reached the required depth.

3.4.3.1 X-ray fluorescence (XRF)

Initially, an XRF line scan was performed to define the accurate position of the interface by measuring the transmitted X-ray intensity; the interface was positoned at halfway intensity between the electrolyte and the salt film. During measurements, the sample stage was used to move the electrochemical cell to a position where the X-ray beam is few micrometers below the metal interface.

To study the ionic diffusion inside the pit, the pit continued to corrode at diffusion-limited conditions, *i.e.,* +0.8 V (Ag/AgCl), while XRF measurements were being performed. A beam energy of 12 keV was used throughout all the XRF measurements with the insertion of a 1.5 mm Al filter. A fixed point XRF scan was used so that X-ray measurements could be recorded at a fixed position relative to the recessing interface, *i.e.,* the stage is static. The measurement started when the beam was at 5-10 μm below the interface, acquiring at a scan step of 1 second until the beam started to record the pit solution above the interface. Fixed point XRF scans give accurate estimations of the diffusion profiles close to the interface; the stage is static and only the interface is moving.

The line scan used to measure the interface position was used to provide information about the diffusion profile over longer distances above the interface, *i.e.,* from the pit bottom to the pit mouth. The typical line scan starts at an arbitrarily reference position below the sample

interface, typically 50 μm, sampling the metal and moving upward across the dissolving interface and the pit solution. In this case, the stage is moving with respect to the beam position. The measurement step size was variable according to the proximity to the interface; it was 1 μm for 100 μm above the interface and becomes larger at 40 μm upwards until it reaches the pit mouth. The acquisition time of each step was 1 second. Where a deposit was used above the pit mouth, the scan step size was lowered to 1 μm during scanning close to the deposit. All the XRF measurements were normalised to their respective metal-side intensity to account for the different beam attenuations due to the electrode's epoxy-Kapton wall thickness.

3.4.3.2 References materials for XANES

Standards were selected to encompass the different components that may be present (Table 1). An Fe foil of 5 mm thickness with 99.5% purity was used as a reference to calibrate the energy of all the measurements. Solid powder standards of Fe compounds ($FeCl_2.4H_2O$, FeS, FeS_2, Fe_2O_3, and $Fe_2(SO_4)_3$) were weighed and diluted with boron nitride (BN) powder, pressed into a pellet and sealed between two layers of Kapton tape briefly before the X-ray measurements. XANES spectra of the solid standards were carried out in the transmission mode, whereas spectra of solution standards were obtained in the fluorescence mode. Solution standards of $FeSO_4.7H_2O$ and $Fe_2(SO_4)_3$ were prepared by weighing the powder and transferring into volumetric flasks to prepare the solution. The solutions were then transferred into special cells or plastic cuvettes: a thin-walled Teflon solution container with a 3 mm path length and Kapton windows at both sides. This procedure was typically carried out 1 h before measuring the spectra.

Table 3-1. The different standard materials used in the XANES study showing their physical state and valency.

Compound	State	Oxidation state	Resource
Fe	Film – 5μm thick	0	Available at Diamond
$FeCl_2$.4H2O	Powder	2	Sigma Aldrich
FeS	Powder	2	Alfa Aesar
FeS_2	Powder	2	Alfa Aesar
Fe_2O_3	Powder	3	Alfa Aesar
$Fe_2(SO_4)_3$	Powder	3	Sigma Aldrich
$FeCl_2$	Solution	2	Alfa Aesar
$FeSO_4.7H_2O$	Solution	2	Sigma Aldrich
$Fe_2(SO_4)_3$	Solution	3	Sigma Aldrich

3.4.3.3 X-ray absorption near edge structure (XANES)

The interface was defined again using an XRF line scan so that supplementary XANES measurements at the Fe-K edge could be carried out at the salt layer. The measurement point was determined at the *full width at half maximum* of the fluorescence intensity derivative during the XRF line scan. XANES were acquired while using Diamond and 0.25-mm Al filters, and the Fe-k edge is 7112 eV. The scan resolution is mainly determined by parameters such as the energy step size and the exposure time at each energy step.

The scan was divided into 6 regimes across the pre-edge, edge, and post-edge regions of the XANES spectrum. To increase the efficiency of data collection, the spectrum had different scan parameters according to the energy resolution requirements for each region. The pre-edge energy is used to determine background and a large step size of 5 eV was used. Smaller step sizes of 0.5 eV are required to resolve the features in the edge region. It is recommended to collect and average data from multiple scans on a sample to obtain better signal to noise ratios.[137] For each experiment, XANES scans were acquired 3 times in the range of 7000-7300 eV, with a varying step size as shown in Table 2 below.

Table 3-2. XANES measurement steps typically acquired for 3 times at a single point.

Region	Start/eV	End/eV	Step/eV	Time/s
1	7000	7090	5	1
2	7090	7095	1	1
3	7095	7120	0.5	1
4	7120	7150	1	1
5	7150	7200	2	1
6	7200	7300	5	1

Since the interface was dissolving, and to ensure XANES data are acquired at the interfacial salt layer, the interface was continuously tracked by moving the cell downwards with a speed similar to that of the interface recession. Therefore, further sequential XRF line scans across the interface were carried out to determine the interface recession rate, *i.e.,* corrosion rate. The velocity of the interface was determined by a least squares fit to the position of the electrode surface measured for 5 consecutive times at 2 min intervals over a 10 min period.

XANES data analysis was carried out using Athena software[138], where the raw data undergoes background removal followed by normalisation. Normalisation involves removing the variations between samples due to effects of analyte concertation and sample thickness, and therefore, XANES spectra are standardised to allow qualitative comparison with spectra of standard species. Normalisation was carried out by selecting two points which have the best

fit in the pre-edge and post-edge regions, and the normalisation range was kept consistent for any single measurement. The normalisation process is explained in Figure 3.12.[70] Finally, linear combination fitting was carried out, which is a quantitative analysis used to determine the composition fraction of species in the sample by modelling the spectra with those of the standards.

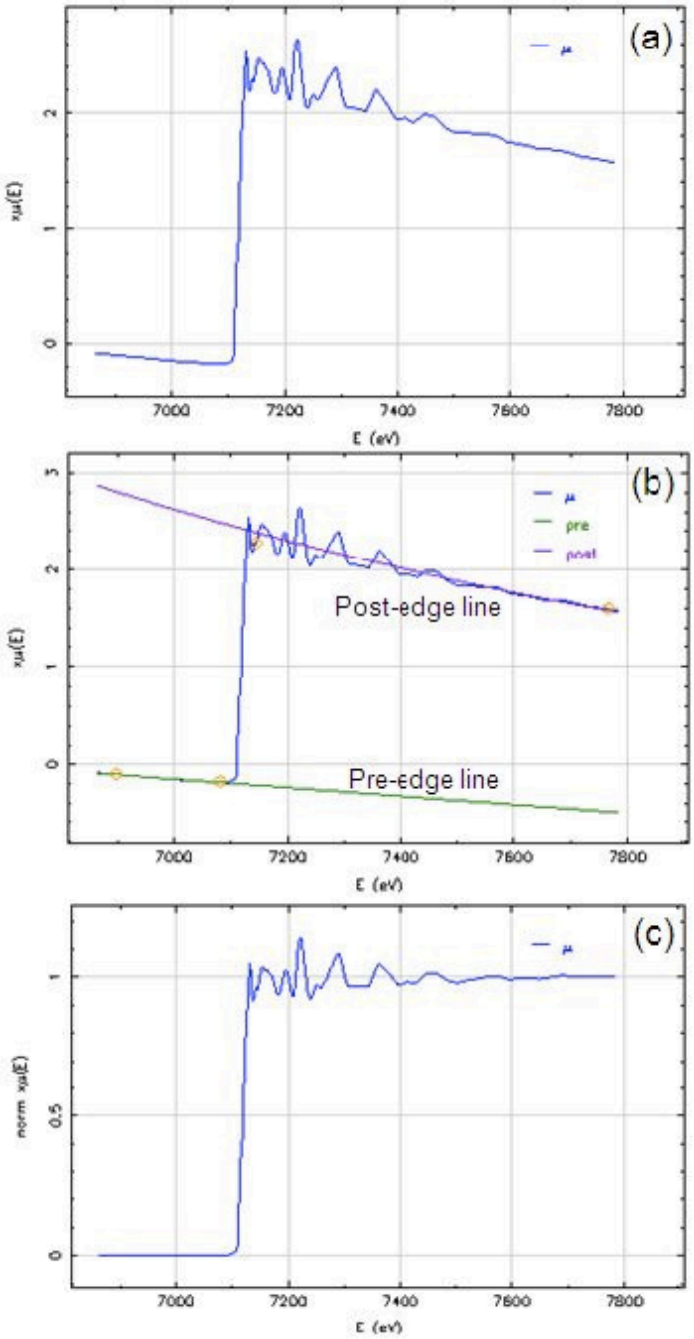

Figure 3-12 The normalisation procedure of XANES spectra using Athena software. Raw data (a) are processed by selecting the pre-edge and post-edge range for normalisation (b) to give a plot of normalised data (c).[70]

The absorption edge occurs when the energy of the incident X-ray is higher than the binding energy of the core electron. The shape of the absorption edge is related to the density of states available. The edge step region includes features such as a pre-edge peak, shoulder, and a strong peak at the edge step referred to as the *white* line (Figure 3.10). These features are caused by differences in the density of unoccupied electron orbitals that can be occupied by the excited photoelectron. The oxidation of an element (loss of electrons) shifts the absorption edge to a higher X-ray energy since a lower number of electrons (lower than neutral) exist which lowers the energy state of the remaining electrons.

In the post-edge region, when the incident photon has high energy, the electron is knocked out with a specific energy according to the incident X-ray energy. The electron wave is backscattered from neighbouring atoms, and the backscattered photoelectron wave interacts with its core state. The change in the incident energy causes phase oscillation between the photoelectron and the initial core state, and the absorption probability oscillates accordingly. The frequency of oscillation depends on the distance to the neighbouring scattering atoms. Therefore, for different atoms, individual elements' contributions can be identified because each element has characteristic variations in the amplitude and phase of the backscattered wave with energy. Our focus in this study, however, is limited to the edge region.

3.4.3.4 X-ray diffraction (XRD)

The sample stage was rotated to 0° to obtain a transmission mode for the XRD measurements; beamline configuration for XRD measurement is shown in Figure 3.13. XRD diffraction patterns were recorded at 14 keV (X-ray wavelength ~0.886 Å) in presence of a Diamond attenuation filter. Lanthanum hexaboride (LaB_6) was used as a standard to calibrate the instrumental broadening of diffraction peaks.

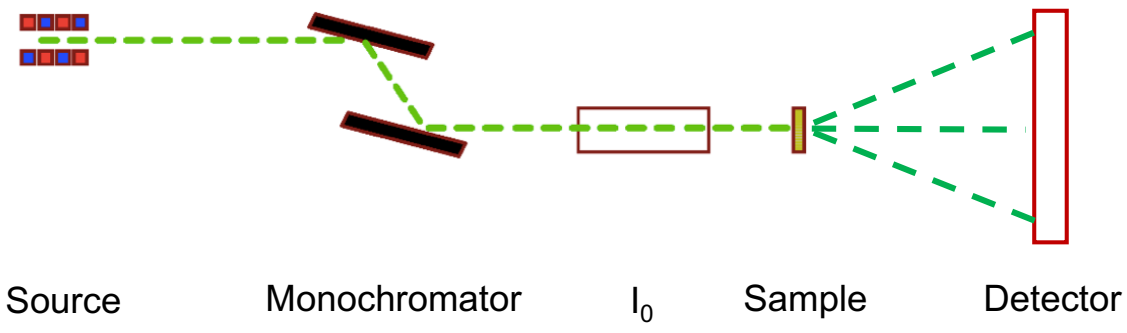

Figure 3-13 The beamline configuration and typical apparatus for XRD measurements.

Starting at 50 μm below the metal interface, the cell stage was stepped downwards in 2 μm increments whilst the beam was scanning through the metal salt interface. The data collection time was set to 30 s for each diffraction image. All XRD data were analysed using Dawn software[139,140] and patterns were fitted to standards from the National Chemical Database Service of the Royal Society of Chemistry (RSC), UK. The salt layer thickness was measured as a combination of the total size of the interface steps, as revealed by XRD, and the distance that the interface recessed during the course of the XRD scan.

4 Underdeposit Corrosion: the deposit-steel interdependent interaction from a *'general corrosion'* perspective

4.1 Introduction

Planar coupons are typically used to study the effect of various operating conditions on steel corrosion. In case of UDC in sour gas (H_2S-rich) environment, since H_2S is an efficient scale-forming agent, iron sulfide is formed in different phases and stoichiometries, alongside with conventionally present deposits, mainly sand from the formation.[4,5,14,20] In a typical electrochemical test to address UDC, deposits are conventionally applied to cover the corroding surface. The electrochemical behaviour, however, is expected to be dependent on the deposit chemical composition, particle size and layer thickness. The study of the chemical and physical characteristics of the solid deposits and their influence on the bare metal will, therefore, be helpful for the development of new corrosion inhibitors and mitigation strategies.[12,22]

The deposit characteristics and the corrosion measuring technique usually affect the choice of test design. In our study, both inert sand and reactive iron sulfides were used. Iron sulfides have inherent semi-conductive properties, and their solubility changes with the solution acidity, implying that a different corrosion behaviour than inert sand is expected.[141] Iron sulfides were chosen with different stoichiometry, pyrite FeS_2 and the more soluble troilite-pyrrhotite mix FeS, which are typically present in sour gas environments.[9,18,22,91,131]

The deposit-covered planar coupon was connected as an anode in a 3-electrode electrochemical cell and electrochemical measurements were performed. The OCP was monitored during the stabilisation period at the start of the experiment, after which potentiodynamic polarisation was carried out. The polarisation profile gives an insight into the overall electrochemical behaviour of the deposit-covered metal at different potentials.

Electrochemical accelerated corrosion tests cause rapid deterioration of the metal, which is expected to be accompanied by changes in the surface morphology and chemical composition of both the substrate iron and the externally applied iron sulfides. Potentiostatic control was, therefore, performed on the deposit covered coupons to correlate the morphological and chemical composition changes to the electrochemical response. Due to the reactive nature of iron sulfides, potentially affecting the response of the covered electrodes, steel coupons were coupled with iron sulfide electrodes to measure the galvanic currents. This provides an interesting insight into the galvanic corrosion mechanism and comprehends the study. The findings are presented in terms of the deposit-metal interdependent changes in the physical

and chemical characteristics as a function of the different properties of the applied deposit such as morphology, packing, and chemistry.

4.2 Results and discussion

4.2.1 Three-electrode electrochemical cell

4.2.1.1 Open Circuit Potentials (OCP) and Potentiodynamic Polarisation

OCP measurements are frequently used to indicate the thermodynamic tendency of the metal to corrode or participate in other electrochemical reactions with the surrounding environment. Higher OCP indicates a more thermodynamically stable (nobler) system that is less likely to participate in further corrosion reactions. When the system is perturbed by scanning the potential below and above the OCP, the system is said to be polarised. The polarisation profile gives an outline of how the material behaves across a specific potential range. Valuable information can be extracted including the anodic and cathodic Tafel slopes, corrosion current and pitting potentials. Both the OCP and polarisation profiles were measured as a function of the deposit type and physical properties, *i.e.*, thickness and particle size.

4.2.1.2 Different physical properties

Under open circuit conditions, the application of a 3 mm layer thickness of coarse sand (100-300 μm) seems to have no significant effect on the OCP, as shown in Figure 4.1a. However, the finer sand with particle size less than 44 μm showed a considerable decrease in OCP, which indicates the formation of a less stable system that is more prone to corrosion. Polarisation profiles are shown in Figure 4.1b: All deposits resulted in a rapid increase in anodic currents in the order of decreasing the deposit particle size. The gradient of Tafel slope is so steep at very negative end which can be due to H_2 bubbles formation or localised changes in pH due to deaerated local cells.

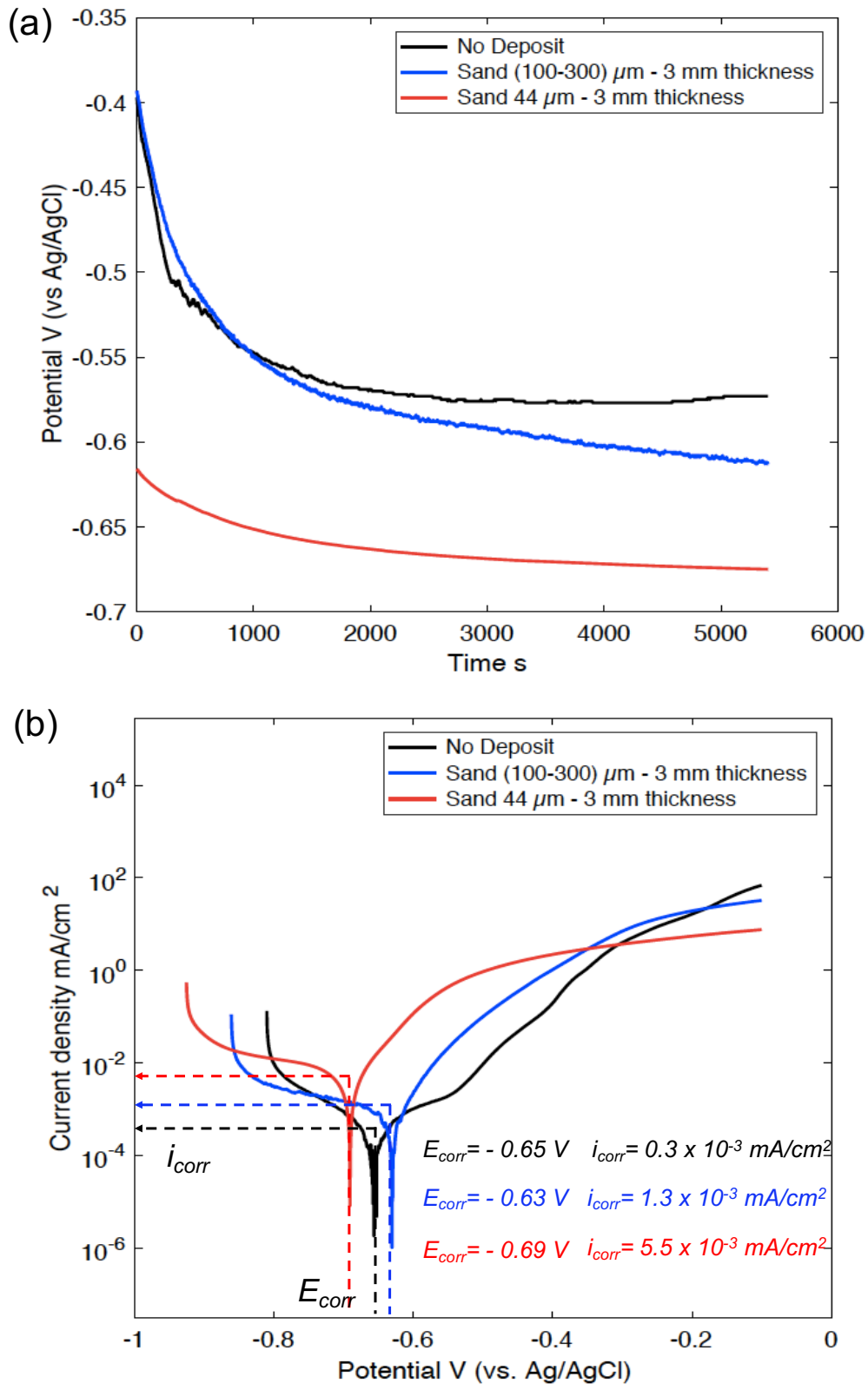

Figure 4-1 OCP vs. time (a) and Tafel polarisation (b) plots recorded for planar surfaces covered with sand (different particle size), compared to a control sample with no deposit. The potential was swept from –250 mV vs. OCP in the anodic direction until –100 mV vs. Ag/AgCl RE at 0.5 mV.s^{-1} scan rate. Solution was a 0.5 M NaCl, N_2-purged at room temperature.

The net pore volume and tortuosity of the deposit bed affect both mixing of the bulk solution with localised areas and the ionic diffusion process from the metal surface.[19,142] The net pore volume constitutes a measure of the quantity of solution that can interact with the steel: A high pore volume may be considered a closer case to the bare steel.[19]

As shown in Figure 4.2, the particles have various size distribution and do not have a well-defined shape such as perfect spheres. Hence, the theoretical porosity value cannot be representative, and therefore, it is measured experimentally by infiltrating water into the deposit bed that is contained in a fixed volume container. The net pore volume is the fraction of the volume of the infiltrated water to the total container volume. The pore volume was found to be ~35-40% of the total bed volume for the coarse sand and ~65-70% for the finer sand.

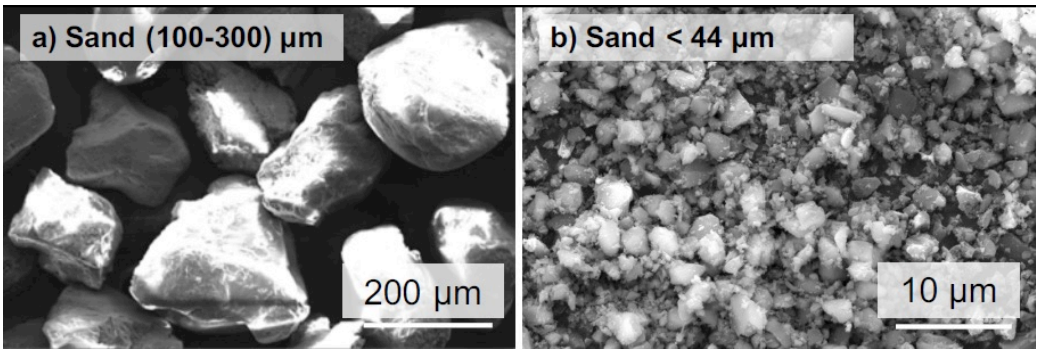

Figure 4-2 Sand deposits used in the experiments: (a) coarse sand with a 100-300 µm particle size, and (b) fine sand with a particle size of < 44 µm, identified commercially as -325 mesh.

The fine sand exhibited a clay-like behaviour, presenting high affinity to water: particles are so small (1-4 µm) that molecules of water adhere to the particles forming water-rich clusters of fine particles.[19,142] The tortuosity, which measures the actual path length that ions travel through voids in a porous deposit bed, strongly relies on the deposit wettability. Therefore, the transport through porous networks are affected in a way that decreases the path length in fine-sand beds, as shown in Figure 4.3.

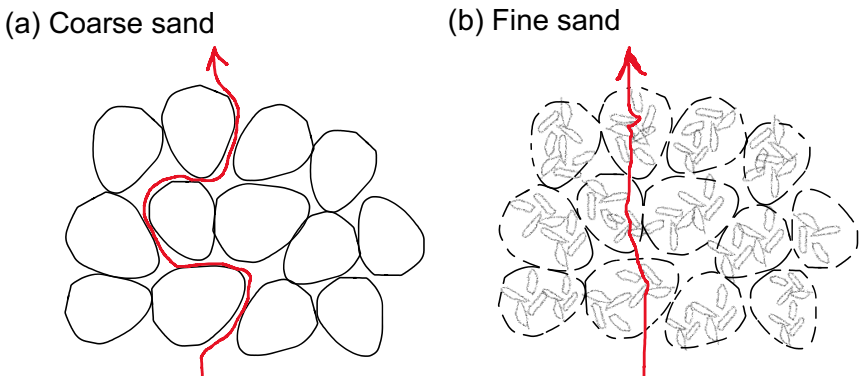

Figure 4-3 A schematic explaining the difference in tortuosity through a deposit bed: (a) coarse sand and (b) fine sand. The fine sand particles cluster to form larger size, water-rich aggregates.

The large void volume and lower tortuosity of the deposit bed are concluded to make mixing with bulk solution relatively easier, rendering the system more corrosive in the case of the fine sand. Besides, the small particle size most likely lowers the OCP by more effectively blocking the surface, creating deaerated local cells between the covered and uncovered parts underneath the sand. Therefore, it can be summarised that inert deposits cause an increase in the corrosion current as well as the steel susceptibility to pitting, which is in the order of increasing the deposit porosity.

In addition to the easier mixing with the bulk solution in the case of fine sand, the less tortuous transport path increases the concentration of reactants and decreases the boundary layer thickness at the surface. Therefore, the cathodic current and the hydrogen evolution rate exhibited higher values with the lower porosity sand.

4.2.1.3 Different deposit type

The porosity of reactive iron sulfides was tested in a similar way as above and found comparable to that of the coarse sand *i.e.,* ~40%. Therefore, coarse sand was used as a reference to define the role of reactive deposits. This measure, however, does not take into account the limiting pore size that might affect transport through porous networks.

Applying iron sulfides with a 3 mm layer thickness on the steel substrates showed a rather remarkably different behaviour from sand. Figures 4.4 (a and b) compares the OCP and potentiodynamic polarisation profiles of both FeS- and FeS_2-covered steel to the sand counterpart. As demonstrated in the figure, FeS application decreased both the open circuit and corrosion potentials, OCP and E_{corr}, to lower values than that of the sand samples. However, a high positive shift in OCP and E_{corr} was observed for the FeS_2-covered substrates. On the other hand, the corrosion current i_{corr} observed for the sulfides covered samples is significantly higher than the sand-covered and bare metal samples. The observation here suggests more aggressive deposits, despite the increase in OCP in the case of FeS_2, as shown in Figure 4.4b. The more negative E_{corr} with respect to the OCP could be attributed to localised changes in pH as a result of H_2 evolution or irreversible changes to the material structure and composition.

At relatively high applied potentials, the anodic current becomes almost the same as shown at the far end of the polarisation curve in Figure 4.1. This suggests that the reaction is limited by mass transfer through the porous media and salt films at the interface, with low influence of the deposit chemical properties. The cathodic kinetics were also affected by the type of deposit. The cathodic current and the rate of hydrogen evolution are much higher in the case of iron sulfides, with FeS being relatively higher than FeS_2. Therefore, iron sulfides, known to

be semiconductive, are assumed to offer extra cathodic sites that drive the corrosion reaction rate.

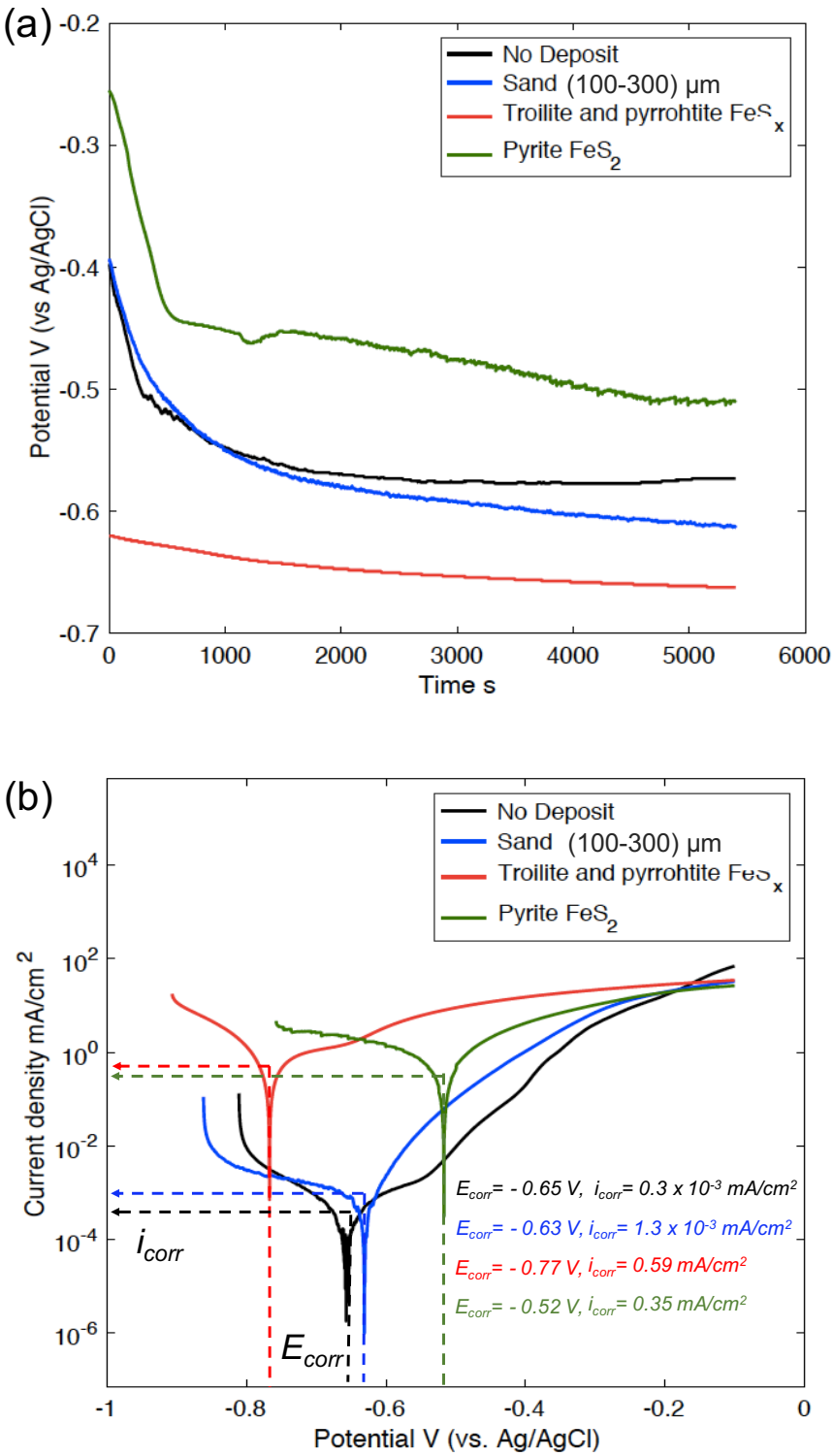

Figure 4-4 OCP vs. time (a), and Tafel polarisation (b) plots recorded for planar surfaces covered with sand, FeS, and FeS_2 (3 mm thickness layers with close porosities of ~40%), showing the effect of deposit type. The potential was swept from –250 mV vs. OCP in the anodic direction until –100 mV vs. Ag/AgCl RE at 0.5 mV.s^{-1} scan rate. Solution was 0.5 M NaCl, N_2-purged at room temperature.

4.2.2 Potentiostatic current profile under deposits

The potentiodynamic polarisation plots acquired for the deposit-covered steel samples provided us with insights into the overall behaviour of the metal at different potentials. At positive potentials relative to the corrosion potential, the steel corrodes at a higher rate according to the amount of the positive shift. Therefore, accelerated potentiostatic tests are often used to test the corrosion kinetics at shorter periods. It also provides information regarding the changes in the steel morphology and chemistry as a result of pre-set conditions of deposit and environment. Figure 4.5 sums the potentiodynamic polarisation profiles of planar coupons covered with FeS, FeS_2, and sand with different particle size.

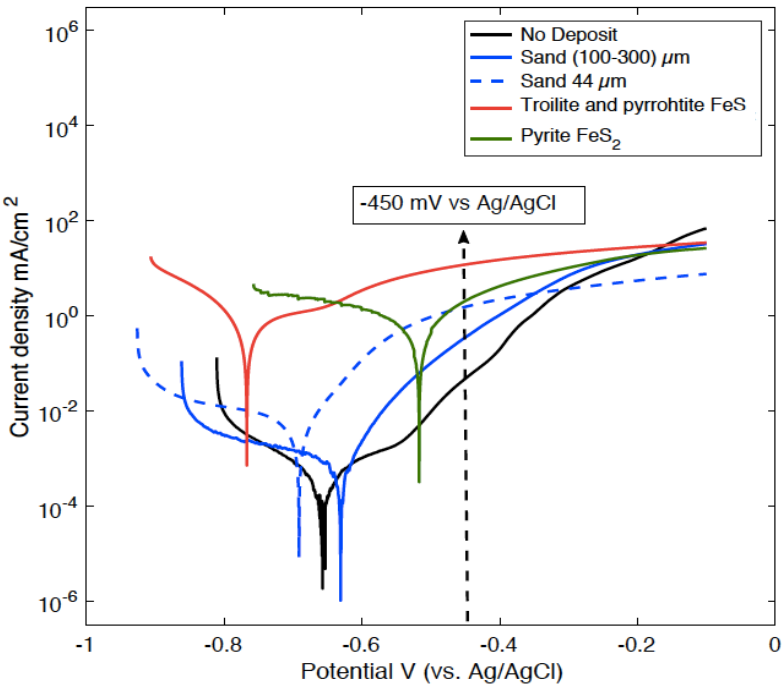

Figure 4-5 (a) Potentiodynamic polarisation profiles of iron coupons covered with sand of different particle size, FeS, and FeS_2 (3 mm thickness and close porosities of ~40%); the dashed arrow indicates a potential of -450 mV vs. Ag/AgCl RE, at which the current profiles in Figure 4.6(a) were acquired during a potentiostatic test.

Two potentiostatic regimes were applied: -450 mV vs. Ag/AgCl RE and +100 mV vs. the OCP. The applied potential of -450 mV (Ag/AgCl) is marked in Figure 4.3 by the dashed arrow. It indicates various degrees of positive shift relative to the corrosion potential of each sample.

The current-time profiles are shown in Figures 4.6. The addition of deposits led eventually to an increase in current during both potentiostatic controls, as compared to the bare steel current. Both FeS- and FeS_2-covered samples exhibited higher current profiles compared to the sand-covered samples. However, the current increase is more significant when the fixed

potential of -450 mV (Ag/AgCl) was applied to all samples, as demonstrated by the different y-axis scales in the figures. This can be explained by the higher applied potential on the samples, which exceeds the +100 mV potential difference during the +100 mV vs. OCP control. The observation of higher currents here, especially with FeS and FeS_2, agrees with the polarisation profiles, Figure 4.5 (a), which show higher currents over the whole scanned potential range.

When a -450 mV (Ag/AgCl) potential was applied in the case of FeS, the current was initially high, but a gradual decrease was then observed with time. The polarisation profile of FeS-covered steel shows a far negative corrosion potential of ~ –780 mV vs. Ag/AgCl. This makes the effective potential difference stands at ~ +330 mV vs. OCP when the -450mV vs. Ag/AgCl protocol is applied. The high potential difference, with respect to the corrosion potential, is thought to cause the initial high values of current. The gradual decay of current is assumed to be attributed to the deterioration of the FeS deposits by the effect of the applied potential, which is assumed to deactivate its cathodic activity. Characterising the surface morphology and chemical composition of the deposit can help validate this assumption.

Although deposits were thought to minimise the current due to the blocking effect and limiting the metal's exposed area, the result was rather the opposite. The observed increase in current with deposits can be attributed to creating deaerated local cells between the covered and uncovered parts underneath the deposit, as stated earlier. This effect becomes significant when iron sulfides are in direct contact with the polarised steel. The semi-conductive nature of iron sulfides implies that both the steel and iron sulfides are polarised, and since the deposit is in a powder form, the exposed surface area increases causing the produced current to increase. Additionally, metal sulfides can improve catalysis of H_2 evolution on its surface.[143] On the other hand, it can be argued that the inherent higher electrical resistance of iron sulfides, relative to the steel, leads to different real potentials after polarisation. Galvanic coupling can then be induced between the steel and the sulfide deposit, which accelerates the steel corrosion reaction.

Experiments to test the galvanic coupling between iron sulfide deposits and steel electrodes are explained later to investigate the effect of such reactive deposits in promoting localised corrosion.

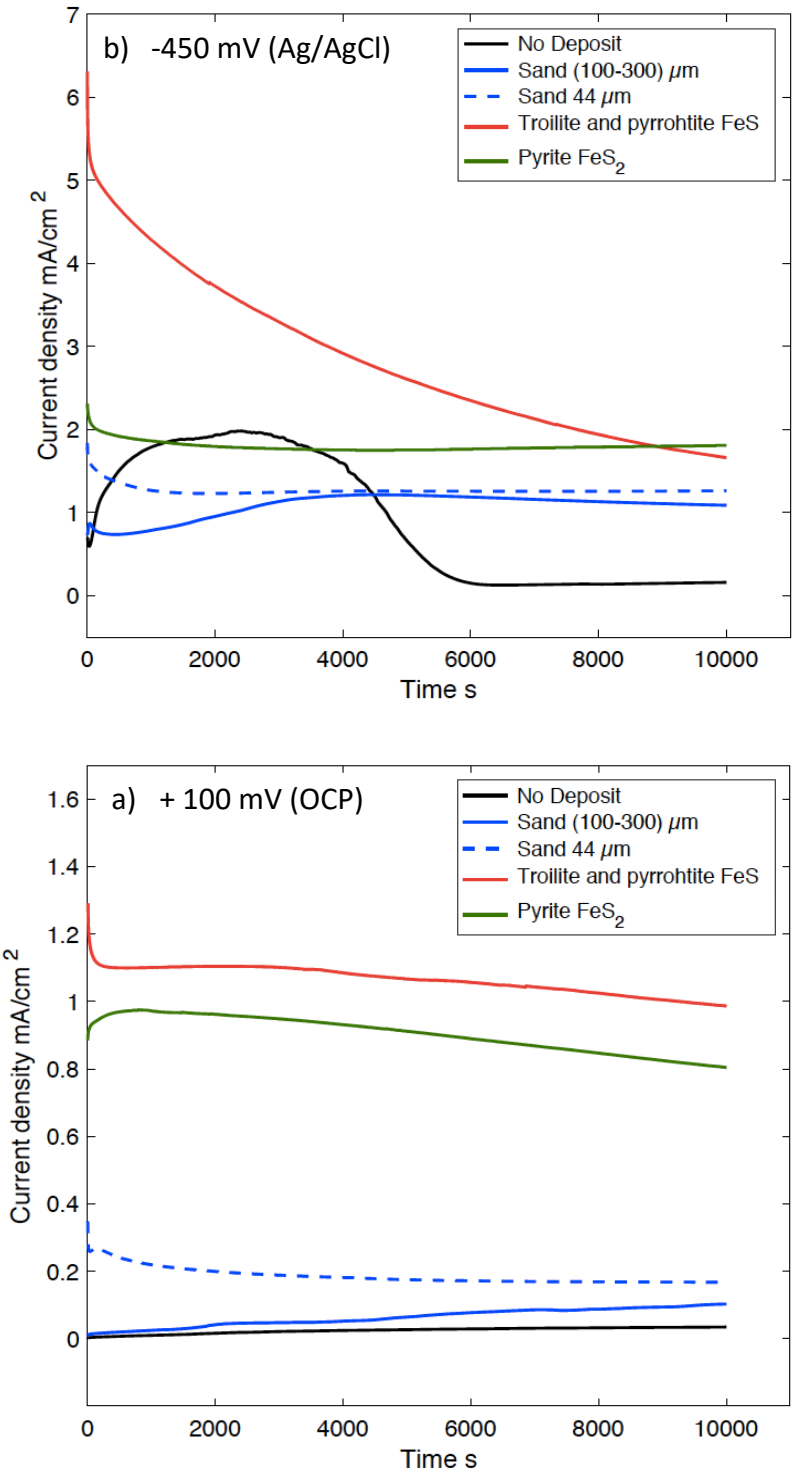

Figure 4-6 The effect of deposit application on the current profiles of iron during two different potentiostatic protocols: (a) -450 mV vs. Ag/AgCl, and (b) +100 mV vs. OCP. Deposits are 3 mm-thick and have close porosities of ~40%. Note the different scale of the current density y-axis.

4.2.3 Metal-deposit interdependent morphological and chemical changes

As explained in the previous section, during the accelerated corrosion tests, the steel responded differently when different deposits were applied. This result could strongly indicate a corresponding change in the coupon morphology and chemistry. Microscopy and spectroscopy analyses were performed on both the sample surface and the applied deposit to investigate the interdependent interactions. SEM was used to view the morphology while EDS and Raman spectroscopy were used to detect changes in the chemical composition. The potentiostatic control at -450 mV vs. Ag/AgCl was adopted since the OCP of each sample is different when deposits change, *i.e.,* changed potential difference. This is in order to account only for the deposit effect.

4.2.3.1 Metal surface alterations

Coupon morphology by SEM

Figure 4.7 shows the steel surface after the potentiostatic control whilst covered with inert sand of different particle sizes, as compared to uncorroded and corroded deposit-free controls. Although coarse sand (100-300 μm) would necessarily mean separation between covered and uncovered areas, which usually causes localised attack, deep general corrosion, was observed similar to the bare corroded sample, as shown in Figures 4.7 (b and c). Localised attack, on the other hand, was less frequent; it is observed in the form of dispersed pits at a size scale of few micrometres, as in Figure 4.7d. The less frequent localised attack could be attributed to the fact that galvanic coupling between covered and uncovered areas is rendered ineffective at high applied potentials. This leads to a general corrosion-like morphology even though the localised attack was expected.

On the other hand, when the fine-sized sand was used, a general corrosion morphology was observed alongside micron-sized pits dispersed all over the corroded surface, as shown in Figure 4.7 (e and f). In other instances, the fine sand has shown good wettability; it adheres to the metal surface, which induces galvanic coupling between closely spaced covered and uncovered areas underneath the deposit. This increased the localised corrosion susceptibility, leading to the development of a dispersed pitting structure, as shown in the figure.

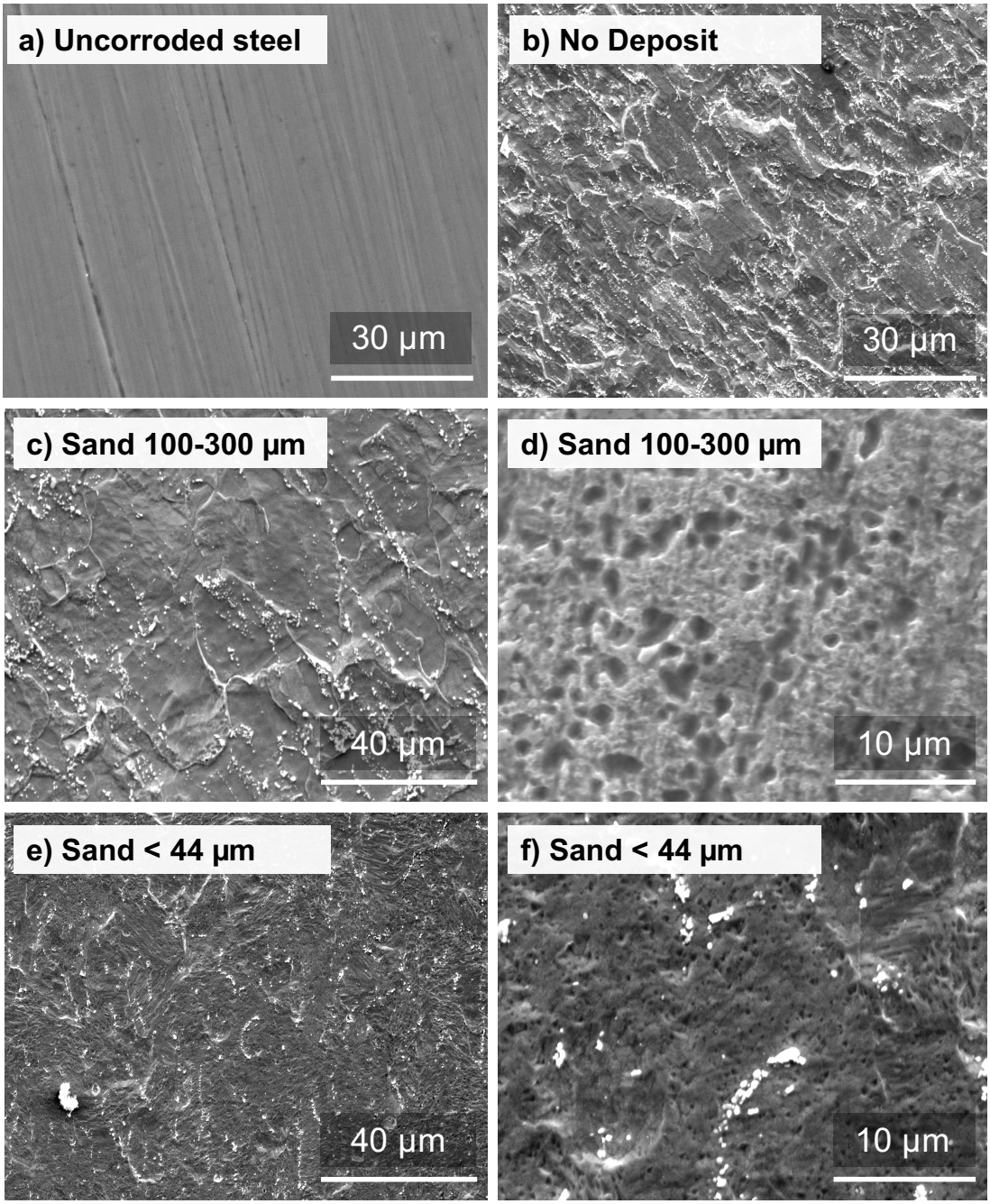

Figure 4-7 SEM images (a-f) of the steel surface after potentiostatic control at -450 mV (vs. Ag/AgCl RE) for 3h: uncorroded polished steel (a), corroded steel with no deposit (b), and corroded steel covered with coarse sand (c and d) and fine sand (e and f).

Figure 4.8 shows SEM images of the steel surface when FeS and FeS_2 were used. In the FeS-covered samples, images (a) and (b), a continuous interconnected porous structure was observed. As explained earlier, the low OCP of FeS-covered steel indicates a less stable corrosion reaction, which is assumed to be the reason for such aggressive deterioration. The FeS_2 application, on the other hand, led to the formation of a thick film that is easily observed on the steel surface in Figure 4.8 (c and d).

FeS_2 is considerably less soluble than troilite; it has a solubility product of 16.4 ± 1.2, compared to 5.1 ± 0.1 for pyrrhotite and 5.25 ± 0.2 for troilite.[144] It is also reported that the Fe^{2+} concentration did not vary with pH in the range of 1-4 in the case of FeS_2. Therefore, it can be concluded that the sulfur-rich FeS_2 participates in the reaction giving rise to the formation of thick films. The EDX measurements also showed higher amounts of sulfur at the surface. This observation, along with the high OCP values of FeS_2 -covered samples, suggest that the high currents during the potentiostatic and potentiodynamic tests were resulted originally from FeS_2 rather than the metal dissolution.

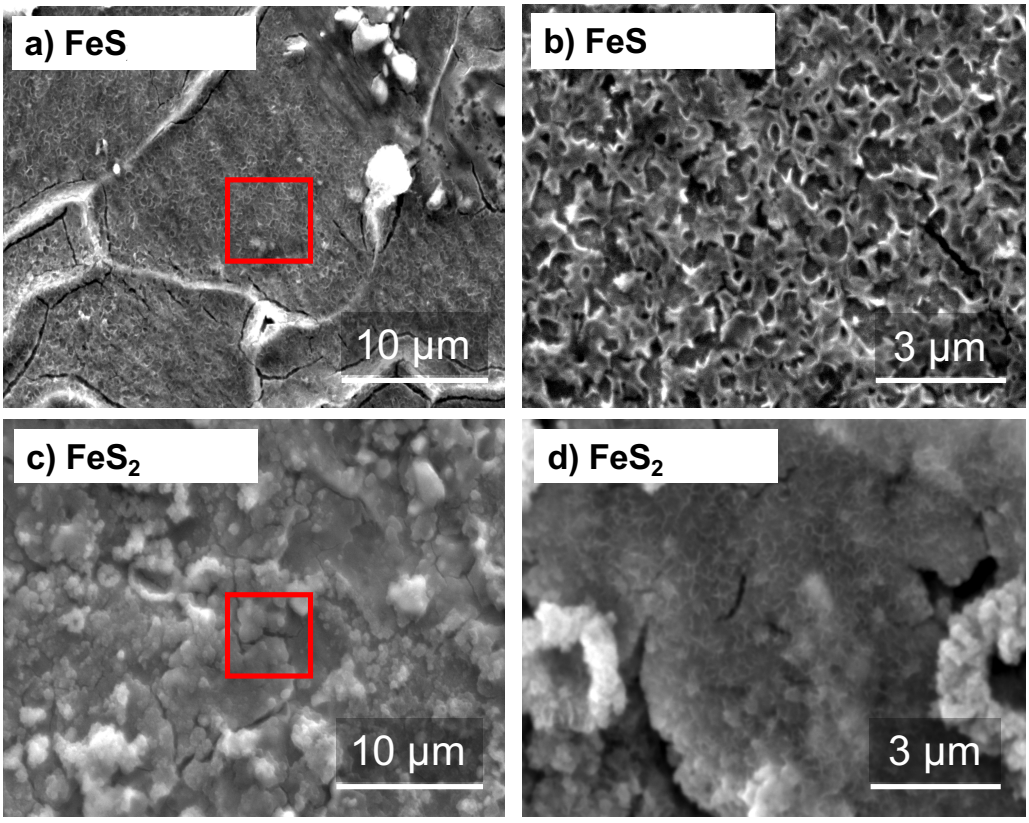

Figure 4-8 SEM images of the steel surface after potentiostatic control at -450 mV (Ag/AgCl) for 3h whilst fully covered with FeS (a and b) and FeS_2 (c and d).

Coupon chemistry using Raman spectroscopy

Figure 4.9 shows Raman spectra recorded on the steel surface after potentiostatic corrosion. A common Raman spectrum was observed on all the steel samples, as shown in Figure 4.9a, with peaks at 215, 281, 383, 487, 592, 665, and 1296 cm^{-1}. The two strong 215 and 281 cm^{-1} bands have been reported in studies involving iron sulfides to be corresponding to amorphous mackinawite, a precursor of more stable iron sulfide species.[145] This can be realistic in case of steel samples corroded under troilite or pyrite. However, since no sulfide species were present in the media in the cases of no-deposit control and inert sand, the peaks at 215 and

281 cm^{-1} are assumed to correspond to Hematite (α-Fe_2O_3), along with the peaks at 248, 592 and 1296 cm^{-1}.[86] The peaks at 383, 487, and 665 cm^{-1} indicate the presence of mixed oxides: Hematite and Goethite α-FeO(OH) (Goethite peaks are typically at 248, 383, 484, and 665 cm^{-1}).[40] This concludes that a mixture of iron oxides was always present on all samples.

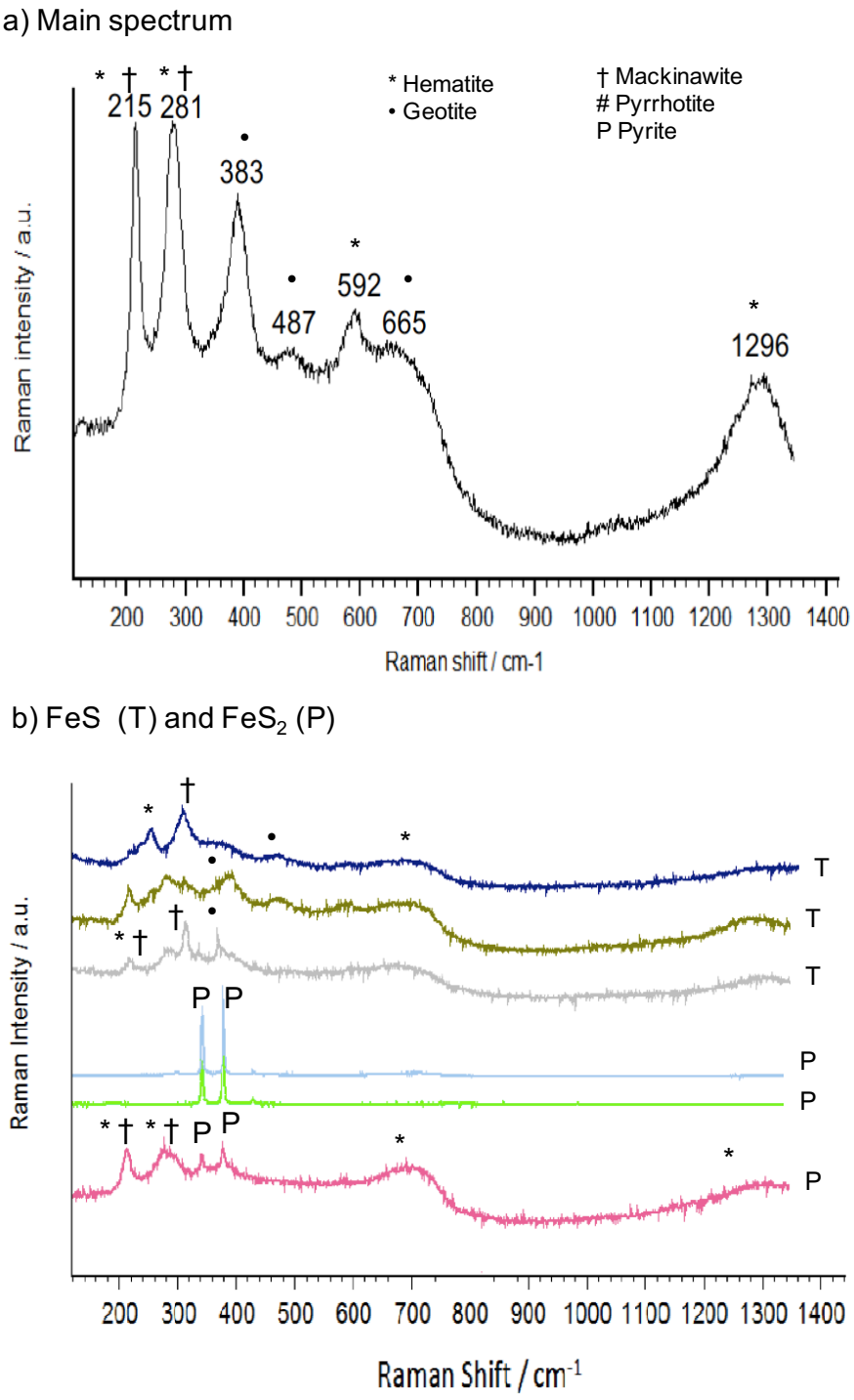

Figure 4-9 Raman spectra recorded on steel electrodes after potentiostatic corrosion: (a) a common spectrum observed on all samples, with and without deposit, and (b) the cases of troilite FeS (T) and pyrite FeS_2 (P).

Figure 4.9b shows additional spectra frequently observed on top of the iron surface in presence of FeS (T) and FeS_2 (P). The presence of iron sulfides on the steel surface is thought to form new iron sulfide species due to the reaction with the electrochemically polarised steel electrode. With troilite, the newly formed film was unstable, and the surface changed colour, from black to orange, upon exposure to air during the Raman spectra acquisition. Despite this, Raman spectroscopy gave rise to the observation of new peaks associated with FeS bands, along with the typically present mixed oxides. Raman shifts at 216, 255 and 279 cm^{-1}, previously thought as mixed oxides, can also be assigned to amorphous or poorly crystallised FeS Mackinawite since the characteristic 310 cm^{-1} shift is present, whereas the 387 and 476 cm^{-1} shifts are for pyrrhotite.[42,115]

On the other hand, pyrite particles remained adherent to the steel surface after the reaction, with no colour change, assuming a chemical reaction with the steel surface. Therefore, strong pyrite Raman shifts at 343 and 376 cm^{-1} were observed, which supports the argument that peaks at 215 and 280 cm^{-1} are best associated to asymmetric and symmetric stretching modes of FeS, respectively.[146,147]

4.2.4 Deposit stability after electrochemical tests

The accelerated corrosion experiments were carried out while the applied deposit was in direct contact with the polarised steel electrode. Therefore, the deposits will be subjected to the electrical fields of the applied voltage as well as chemical interaction with the dissolving ionic species from the steel electrode. These electro-chemical interactions are expected to cause morphological as well as chemical changes to the surface of the iron sulfide deposits. Changes in physical and chemical properties of the applied deposits were demonstrated by means of SEM/EDS and Raman spectroscopy. To study this, and prior to analysing the electrochemical changes, a control experiment was initially carried out where deposits were submerged in a 0.5 M NaCl solution to test for basic open circuit changes, which are not related to potential application.

4.2.4.1 Morphology using SEM

Control: deposit stability after submersion

SEM images in Figure 4.10 show the surface morphology of FeS and FeS_2 in both the as-received form and after submersion in electrolyte for 12 hours. The control experiment showed different degrees of morphological change in the particles' surfaces, which is more prominent in the case of FeS than in FeS_2. A flower-like morphology, images (b) and (c), which is a characteristic of iron oxide, is formed on top of the FeS particles. The change in the surface

morphology indicates a chemical reaction or phase transformation, and the formation of iron oxide may decrease the surface reactivity of the deposit.

The morphological change was accompanied by a slight decrease in the sulfur content compared to the as-received reagents, as concluded from the EDX analysis, while the oxygen content slightly increased. In the case of FeS_2, despite the high solubility product, only minor changes in the surface roughness were observed as clear from Images (d – f). This observation suggests that the less chemically stable troilites and pyrrhotites are more likely to affect the corrosion process. The troilite reactivity also explains the large noise in electrical signal recorded as the deposit was freshly introduced.

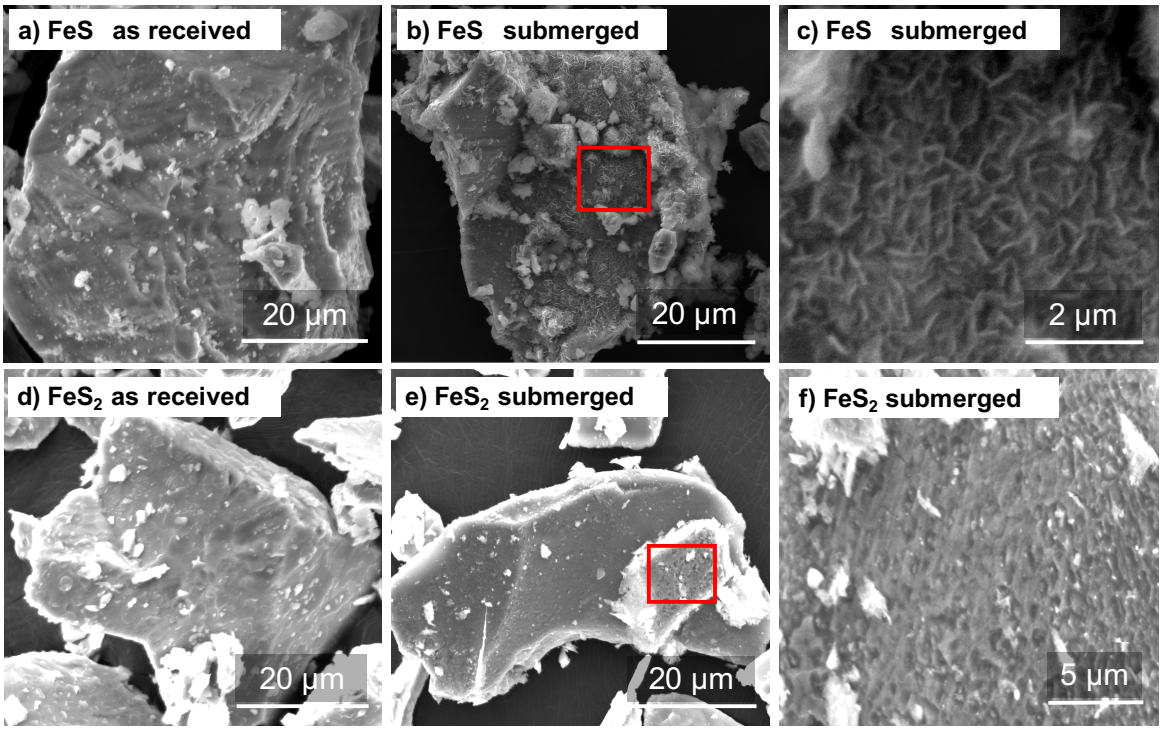

Figure 4-10 SEM micrographs showing the surface morphology of FeS (a-c) and FeS_2 (d-f) deposits before and after submersion in 0.5 M NaCl electrolyte for 12h. (c) and (f) are magnified views of the inset squares in (d) and (e), respectively.

Stability after Potentiostatic tests

On the other hand, a larger degree of morphological and chemical change was exhibited by the deposit after the potentiostatic tests, compared to those resulted from the submersion control test. SEM images in Figures 4.11, 4.12, and 4.13 explain the morphology changes in both types of iron sulfide in different ways.

Figure 4.11 explains the two main scenarios of interaction between a deposit particle and the substrate metal. The SEM images in the figure, at relatively low magnification, represent the case of FeS on top of the steel surface. While a film was found to cover the surrounding steel

surface as in image (a), image (b) shows that the steel surface is subjected to localised corrosion in the form of pits. Image (b) explains the galvanic effects that usually arise between areas of different local environments such as uncovered and covered areas, or under a deposit that is tightly and loosely packed in different areas.

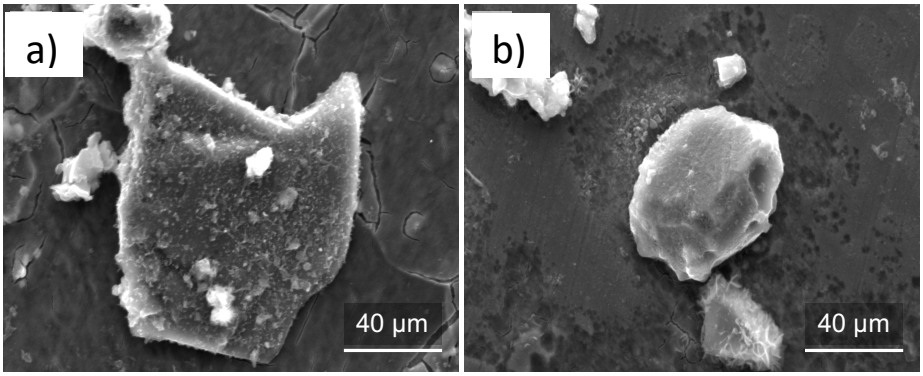

Figure 4-11 SEM images showing FeS particles remnant at the steels surface after positive potentiostatic polarisation test at -450 mV vs Ag/AgCl on FeS-covered steel highlighting the underneath metal morphology: (a) the steel is covered with a film, and (b) the steel has pitting characteristic to galvanic coupling. Electrolyte was a 0.5 M NaCl Solution.

Figure 4.12 represents FeS particles after the potentiostatic test; a remarkable deformation occurred to the particles' surfaces. Some particles have completely transformed to a flower-like structure, as shown in image (a), while some others were subjected to pitting deformation or superficial morphology changes, as shown in images (b) and (c), respectively.

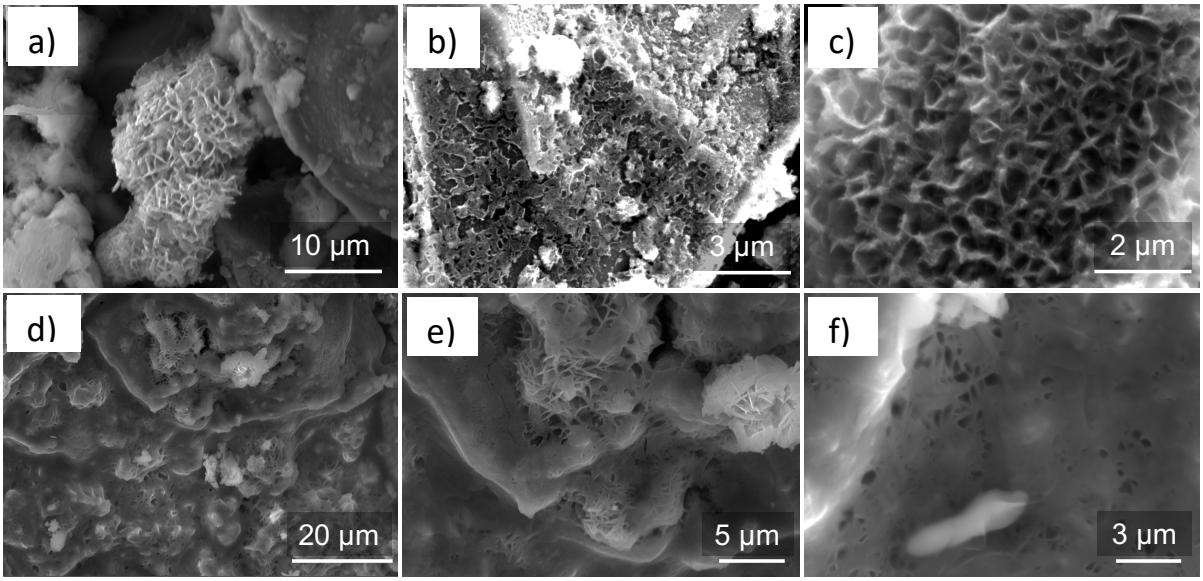

Figure 4-12 SEM images of FeS particles after positive potentiostatic polarisation of FeS-covered steel at -450 mV vs. Ag/AgCl, showing different morphological changes: (a) a high degree of surface transformation, (b) pitting or cavity deformation, (c) superficial morphology change, and (d-f) electrochemically sintered surfaces at various magnifications. Electrolyte was a deaerated 0.5 M NaCl Solution.

In other instances, FeS particles are thought to have undergone electrochemical sintering as shown in the SEM images (d –f) of the same particle, at different magnifications. This has led to progressive pore closure of the particles, which might have resulted in a reduced surface area of the deposit. Therefore, the reactivity of the iron sulfide surface decreases with time, which justifies the previously observed decay in current with longer potentiostatic tests. As the particles get sintered, they adhere to the steel surface allegedly protecting the metal substrate.

EDX measurements concluded a loss of sulfur content at a larger degree after the potentiostatic tests compared to the free submersion test. Similar to the submersion experiment, the sulfur loss was also accompanied by an increase in the oxygen content, which could be due to exposure to air post the experiment.

Figure 4.13 shows a particle of FeS_2 in image (a), with higher magnification in (b) and (c), where a thick film is found surrounding the particle, and the particle itself having a deteriorated porous surface and adhering to the steel by the effect of electrochemical sintering. Since pyrite adheres to the substrate metal, it can be argued that its contribution in the corrosion currents of both potentiostatic and potentiodynamic polarisation tests is higher than that that of the troilite. Images (d – f) show sulfur and iron EDS maps of the particle and the underlying steel. In agreement with observations from the control test, the degree of surface deformation as well as the loss in sulfur content was lower in pyrite than in the troilite case.

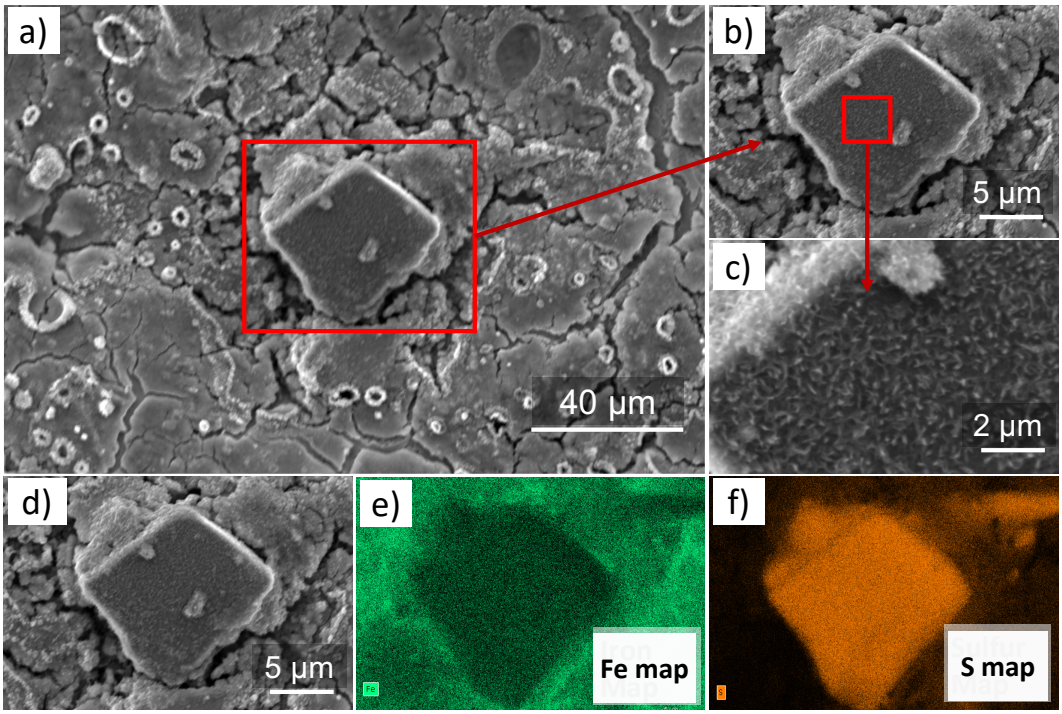

Figure 4-13 SEM images of an FeS_2 particle remnant at the steel surface after positive potentiostatic polarisation at -450 mV vs. Ag/AgCl, (a-c) at different magnification showing a slightly deteriorated particle surface and a surrounding thick film. (d-f) show iron/sulfur EDS maps. Electrolyte is a deaerated 0.5 M NaCl Solution.

The semiconductive nature of iron sulfides is assumed to be the reason behind such prominent transformation in the particles' morphology and chemistry as they get in direct contact with the positively polarised steel surface.

4.2.4.2 Deposit chemistry using Raman spectroscopy

Figure 4.14 (a and b) shows Raman spectra recorded on the surface of powdered troilite and pyrite, respectively, after the immersion control experiment in the 0.5 M NaCl electrolyte solution. As demonstrated in Figure 4.14a for FeS, some peaks representative to oxide and sulfide species disappeared in the reacted form. It is assumed that these species were impurities that are washed away during the immersion. These impurities are characterised as different stoichiometric and non-stoichiometric iron sulfides (223, 405 and 497 cm^{-1})[86], and iron oxide (242 and 291 cm^{-1}).[148]

On the other hand, with pyrite in Figure 4.14b, the reaction resulted in the formation of new Raman bands that can be assignable to elemental sulfur (153, 218 and 472 cm^{-1}) and Mackinawite (211 and 273-282 cm^{-1}).[86] Due to limitation in the *ex-situ* techniques that have been used, the morphological changes that took place at the surface of iron sulfides cannot be correlated to the Raman observations. This suggests that further analyses with *in-situ* characterisation capabilities should be carried out.

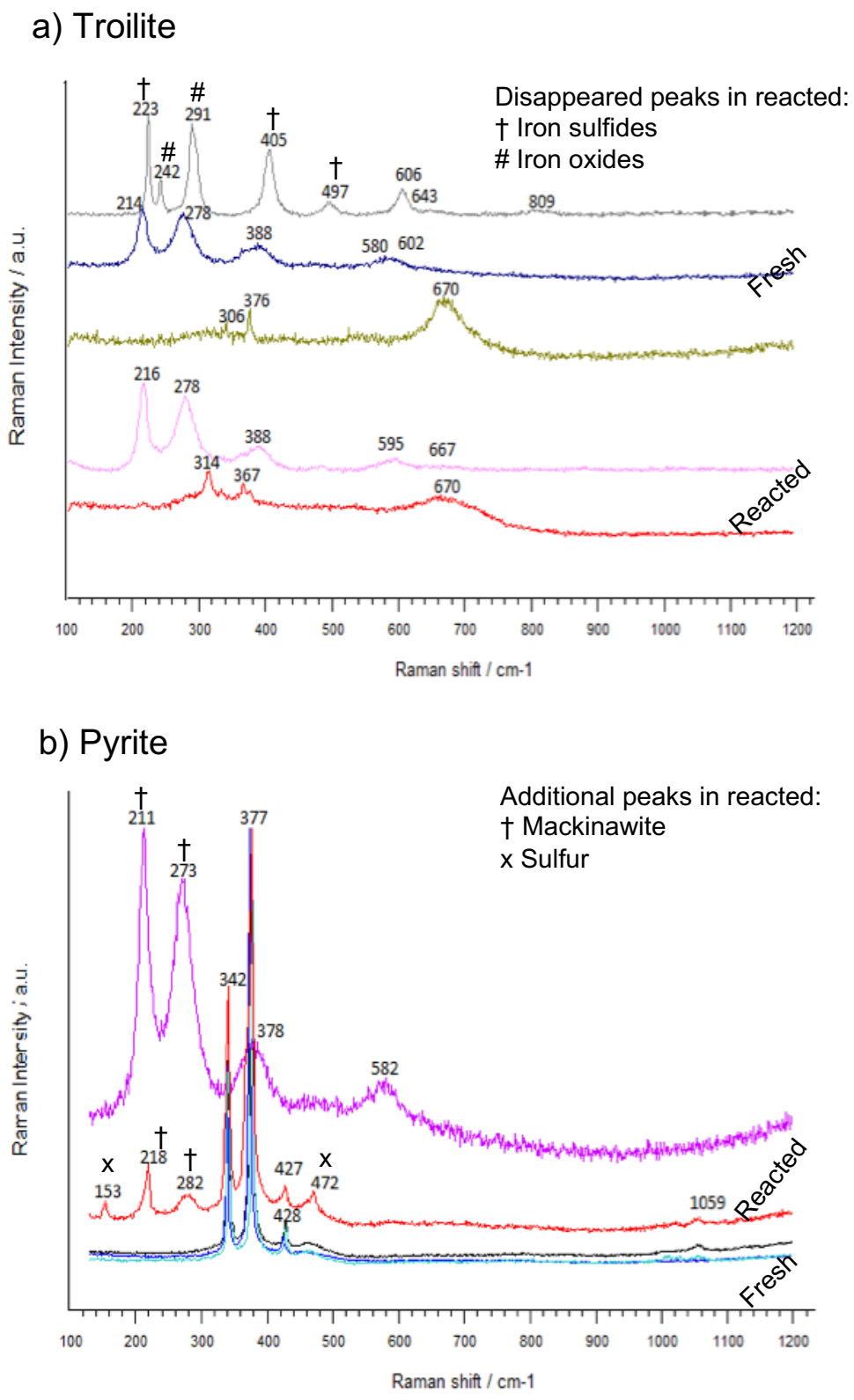

Figure 4-14 Raman spectra recorded on the surface of powdered troilite (a) and pyrite (b) before and after the potentiostatic reaction of the polymorph-covered steel at -450 mV vs. Ag/AgCl. Only peaks that were added or disappeared after the reaction are annotated. Electrolyte is a deaerated 0.5 M NaCl Solution.

4.2.5 Zero Resistance Ammetry (ZRA) electrochemical arrangement

According to the electrochemical responses of the involved under-deposit systems, and the following microstructural characterisation of the substrate metal and the applied deposits, it is concluded that the presence of iron sulfides on top of the steel coupon increases its rate of dissolution. This acceleration in the dissolution rate was suggested to be due to electrochemical coupling between the steel substrate and the iron sulfide deposits.

The galvanic interaction between the deposit and the substrate metal will hopefully provide new insights into the development of localised corrosion prevention protocols. In this study, the electrochemistry of mild steel coupled to FeS and FeS_2 was explored using ZRA, where the galvanic current and potential are measured with time in a N_2-purged environment. To further understand the interplay of the steel-corrosion products, the corresponding changes in the steel surface morphology and chemistry were examined by SEM and Raman spectroscopy.

In practice, the corrosion film properties are dependent on the operation conditions, and some films may have the tendency for breakdown more than others. The approach taken here represents a situation of a partly non-protective film.

4.2.5.1 Galvanic potential

OCP of individual electrodes was measured briefly at the start and end of the coupling reaction. The steel electrodes were left to stabilise to similar values of OCP before coupling with the troilite and pyrite electrodes. The potential against time diagram of each involved electrode in addition to the coupling potential are plotted in Figure 4.15. The couple potentials, as in image (a), initially decreased with time before stabilising at prolonged time. The galvanic potential of the troilite couple was higher than that of the pyrite couple.

The initial potential drop was thought by Tjelta *et al*.[93] to originate from the slow equilibration of iron sulfides rather than the formation of an iron sulfide layer on the steel surface. Local conditions and precipitation may have contributed to mixed potentials; therefore, the galvanic potential values are considered approximate.

The troilite couple

Typically, the steel electrode is expected to be polarised anodically when coupled to iron sulfides. However unexpectedly, the steel's OCP prior to the coupling measurement was, higher than that of troilite, as shown in Figure 4.15b. The high OCP values indicate a more noble material that has less tendency to participate in reaction. The steel is, therefore, expected to act cathodically when coupled to troilite. After the coupling was finished, the steel

and troilite electrodes switched polarities, where the steel became anodically polarised, *i.e.,* lower OCP

At the start of the coupling measurement, the galvanic potential was close to the OCP of the troilite. Eventually after prolonged coupling, the galvanic couple potential stabilised between the final OCPs of the steel and troilite electrodes. Since the OCP of steel shifted significantly compared to the troilite's OCP, the galvanic reaction was assumed to be limited by the reactions at the steel electrode. The unusual high OCP of the steel prior to coupling with troilite can be related to the fact that the system has not reached a steady state.

The pyrite couple

On the other hand, with the pyrite-steel couple as shown in Figure 4.15c, the steel electrode was polarised anodically before and after coupling, without switching polarity as in the troilite case. During the ZRA coupling, the galvanic potential of the pyrite couple remained close to the OCP of the mild steel anode. The OCP of the pyrite cathode shifted significantly compared to the steel's OCP, and therefore, the galvanic reaction was limited by the cathodic reaction.

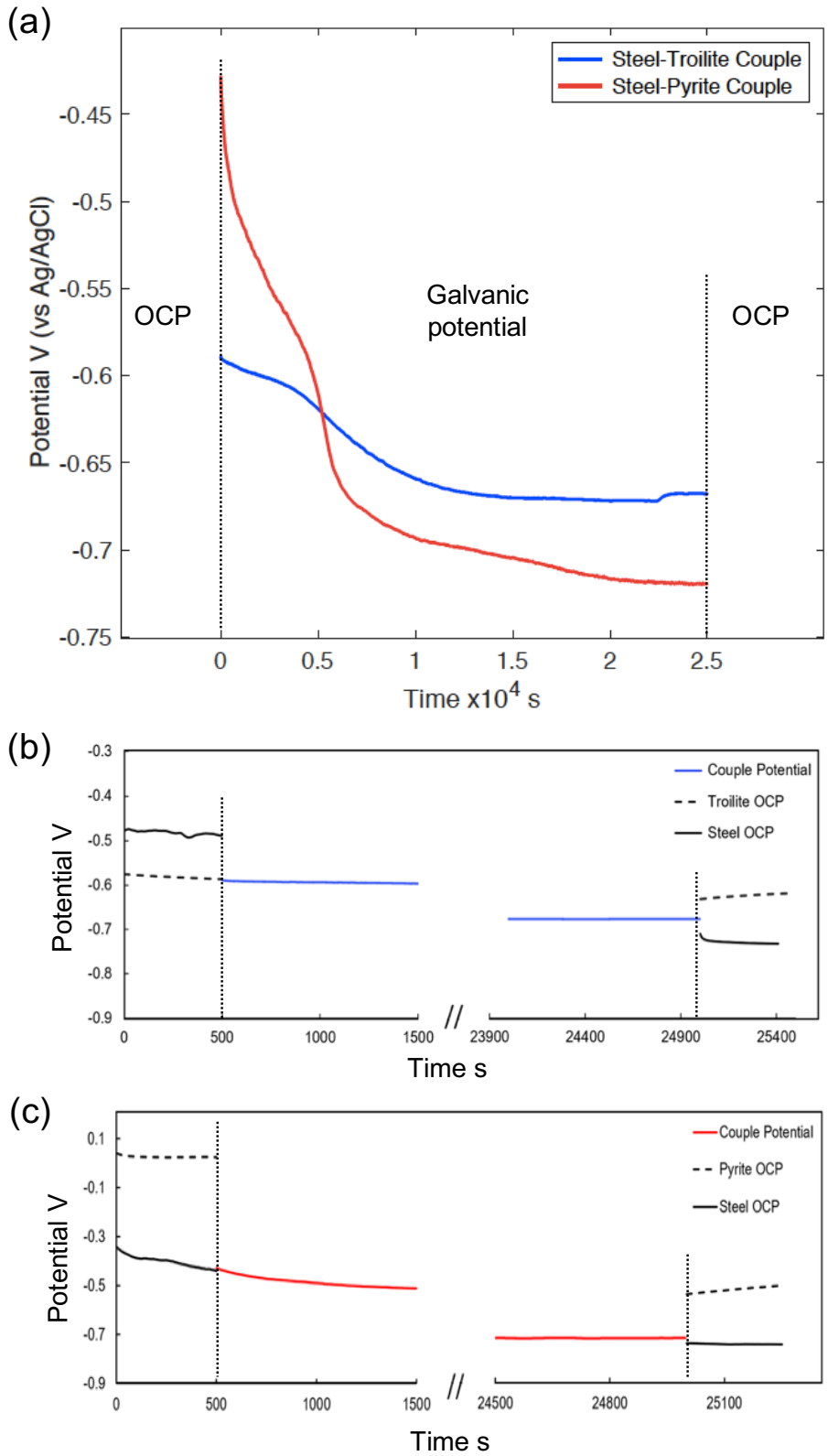

Figure 4-15 (a) The galvanic couple potential measured by ZRA for both pyrite and troilite electrodes coupled to mild steel electrodes, in a deaerated 0.5 M NaCl solution. (B) and (C) show the galvanic potential of the steel-troilite and steel-pyrite couples, respectively, compared to the OCP of individual electrodes measured prior to and after the coupling reaction.

4.2.5.2 Galvanic current

As shown in Figure 4.16, at the beginning of the coupling measurements, a significant change in the galvanic current was exhibited before stabilising at prolonged periods. The iron-troilite couple eventually exhibited a galvanic current higher than the iron-pyrite couple. This indicates that troilite is a more corrosive iron sulfide polymorph than pyrite.

The change in current with time can also be directly related to the potential difference between the coupled electrodes. The higher the difference in potential between the working electrodes, the higher the galvanic current. This means that, according to the OCP readings of individual electrodes shown in Figure 4.15, the pyrite coupling current is expected to be slightly higher than that of the troilite couple. The galvanic observations, however, showed a considerably higher galvanic current with the troilite pair. In the steel-troilite couple, as troilite initially polarised anodically, current showed negative values until the polarity is switched during the reaction and the steel became the anode, causing the current to increase.

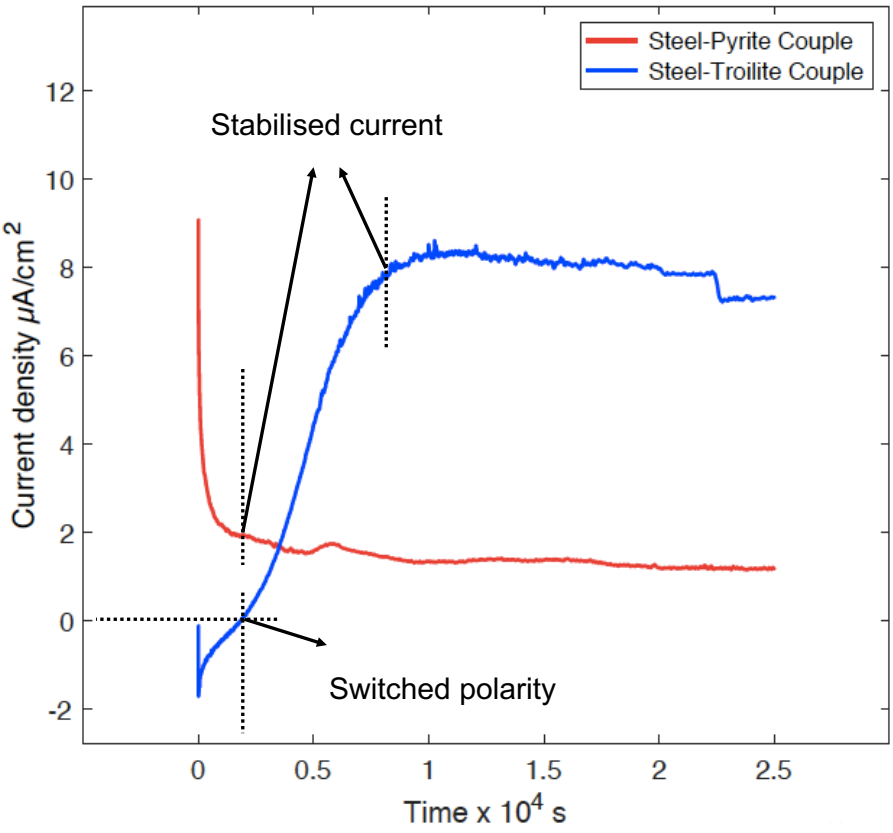

Figure 4-16 The galvanic current density measured by ZRA for both pyrite and troilite electrodes coupled to mild steel electrodes in a deaerated 0.5 M NaCl solution. Note y-axis of the current density is in μA/cm^2.

The steel area was used to normalise the galvanic current density despite Tjelta *et al*.'s assumption that the reduction rate of the nobler material determines the coupling current. The pressed pellets of troilite were not heat-treated, thus, the Fe-S bonding is not extensive as in the case of the raw pyrite mineral. The solution can then penetrate into the porous structure of troilite and the reaction takes place at the surface as well as the internal pores. Therefore, the initial change in current can be partially due to the wetting process, and accordingly, troilite took longer time to stabilise as the solution was gradually penetrating its surface. The change in the reactive surface area relative to the steel working electrode (assuming constant reactive anodic area) changes the cathode to anode area ration accordingly, which is speculated to change the potential and current with time.

Accordingly, the effective surface area of the troilite electrode is thought to be larger than the geometric area used to calculate the area-normalised current density. This subsequently could increase the total active area for reaction resulting in an increase in the galvanic current estimates relative to what is measured with the smoother surface pyrite. Additionally, troilite is more thermodynamically active and can improve the catalysis of H_2 evolution on its surface, which increases the overall current.[143] The surface area effects can be distinguished from catalytic effects by roughness estimations through measuring the double layer capacitance.[149] However, since the potential decreased only slightly with time, assuming that the effective surface area has not changed significantly, the troilite is considered to be more corrosive than pyrite. The photo effects on current were neglected based on Tjelta *et al.*'s previous finding that no indication of current change was observed upon covering the glass cell.[93]

4.2.5.3 Coupons morphology using SEM

After the coupling reaction, the steel, which was closely positioned (2-3 cm apart) to the iron sulfides electrodes during reaction, showed a thin black film formed on its surface. The steel surface was examined by SEM to identify the surface morphology. Figure 4.17 shows SEM micrographs of the steel electrodes after coupling with troilite and pyrite electrodes, as in images (a-c) and (d-f), respectively.

With the troilite couple, an extensive layer of a flower-like structure was uniformly formed on some parts of the steel surface, which has a pore size of less than 500 nm. The morphology is characteristic to chemically grown iron sulfide films, consistent with the one observed when mild steel is exposed directly to H_2S but with a smaller pore size, as will be shown later in chapter 6.

The pyrite couple, on the other hand, showed a less degree of surface deterioration, as can be justified by observing the polishing lines. In some parts, a slightly similar structure, with less packed flakes, was observed. The surface in this case was less stable; the black film transformed into an orange colour quickly upon air exposure.

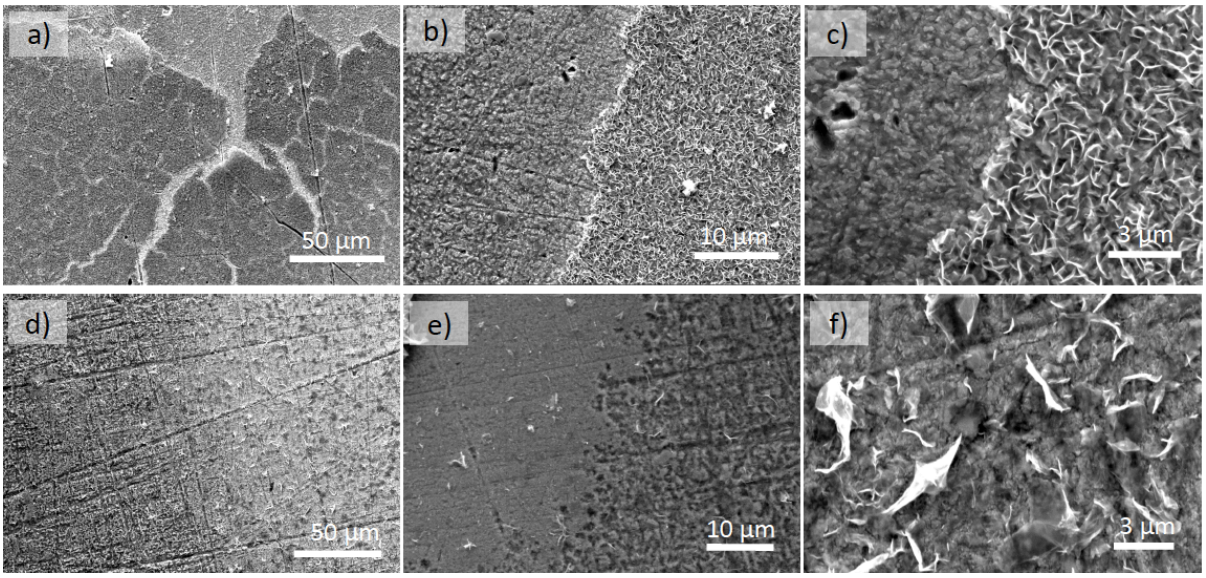

Figure 4-17 SEM micrographs of steel electrodes after ZRA coupling with troilite (a-c) and pyrite (d-f) electrodes in a deaerated 0.5 M NaCl solution

The newly formed iron sulfide film forms a protective solid-state diffusion barrier, but when it cracks or flakes off, it provides a condition for crevice and UDC. The galvanic coupling interaction in the near stagnant solution increases with excess amounts of iron sulfide in contact with the steel, enhancing its corrosion.

4.2.5.4 Coupons chemistry using Raman spectroscopy

The spectrum shown in Figure 4.18 was commonly observed on steel after coupling with both troilite and pyrite. The two sharp peaks at 215 and 280 cm^{-1} are in good agreement with observations by Boughriet *et al.*,[145] indicating amorphous or disordered mackinawite phases. However, the formation of a strong band at 668 cm^{-1} indicates the formation of magnetite, Fe_3O_4 or Goethite, α-FeO(OH). This could be assumed to be a result of transformation reactions of the initial corrosion product, mackinawite, to mixed oxides upon exposure to air during the *ex-situ* Raman spectroscopy measurements. On the other hand, the four bands at 215, 279, 393 and 1295 cm^{-1} indicate that hematite is the final transformation product, which was assumed by Genchev *et al.*[86] to be due to the interaction with the laser irradiation. Using a low laser power for short exposure times in our study, however, undermines the validity of

Genchev *et al,*'s assumption; the laser beam was validated experimentally to be non-destructive to the iron sulfides used, as stated earlier in the experimental section.

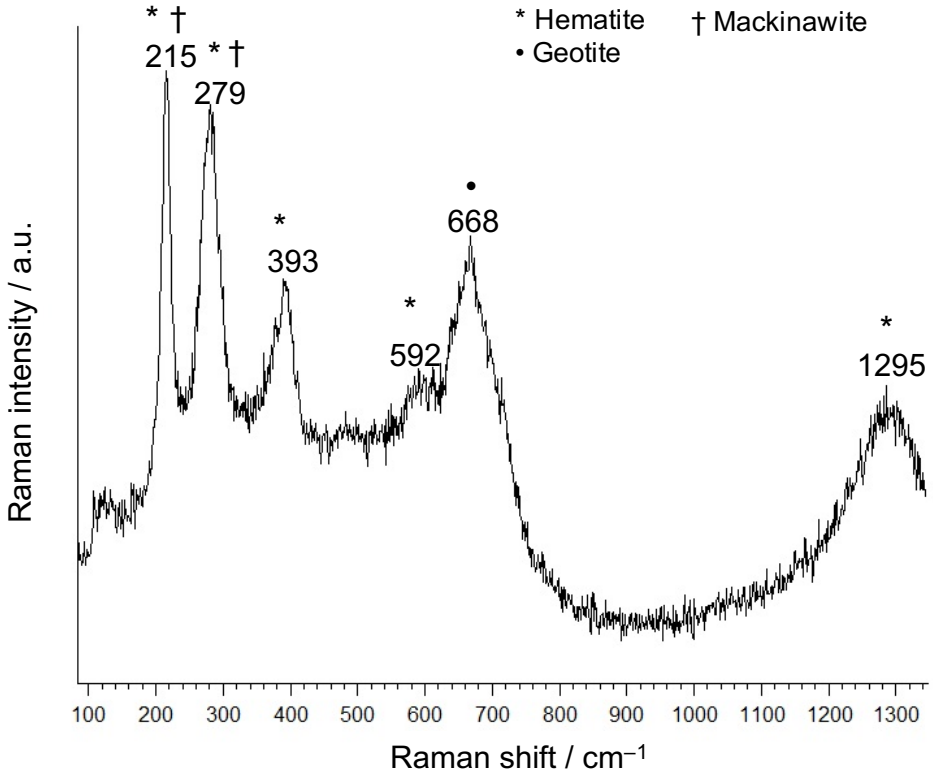

Figure 4-18 The common Raman spectrum recorded on the steel surface after coupling with troilite and pyrite using ZRA in a deaerated 0.5 M NaCl solution.

According to the potential of the electrodes, the following reactions are expected to take place during the galvanic reaction:

a) Anodic reaction of iron dissolution:

$$Fe = Fe^{2+} + 2e^{-} \ (E^{o} = +0.44\ V)$$

b) Cathodic reactions that could involve oxygen reduction, hydrogen evolution, in addition to iron sulfide reduction to release H_2S:

$$O_2 + 4H^{+} + 4e^{-} \rightarrow 2H_2O \ (E^{o} = +1.229\ V)$$

$$2H^{+} + 2e^{-} \rightarrow H_2 \ (E^{o} = 0.0\ V)$$

$$FeS + 2H^{+} \rightarrow Fe^{2+} + H_2S \ (\text{Log } K^{o}_{sp} = 3.5 \pm 0.25^{150})$$

$$FeS_2 + 4H^{+} + 2e^{-} \rightarrow Fe^{2+} + 2H_2S \ (E^{o} = +0.14\ V^{151})$$

The evolution of H_2S in the cell is considered to be the reason of iron sulfide film formation at the steel surface. The high galvanic current in the case of the troilite couple explains the formation of the more uniform corrosion film.

4.3 Summary and conclusions

Deposits are known to affect pitting corrosion differently at both the initiation and propagation stages according to their physical and chemical nature.[4,6,16] Electrochemical approaches to study UDC in steel conventionally involved measuring planar coupons whilst covered with deposits. A similar approach was initially followed in our work to test the effect of changing the deposit characteristics on the general behaviour of steel corrosion. Both inert sand and reactive iron sulfides were used as representatives to the most common case of UDC in sour gas pipelines. With the intention to isolate the different parameters, H_2S was absent from the system to avoid chemically formed iron sulfide deposits that add to the system complexity.

UDC experiments using planar steel coupons showed that inert deposits destabilise the steel by increasing the corrosion current and the susceptibility to pitting. The magnitude of destabilisation depends on the electrolyte transport through the applied deposit's porous networks, according to the limiting pore size. The steel was more stable when the inert deposit had lower porosity or larger tortuosity: this was clear from the OCP measurements that exhibited minor changes with coarse sand. In contrary, steel electrodes covered with fine sand showed a considerable decrease in OCP, which can be attributed to a more effective blocking of the surface, creating deaerated local cells between the covered and uncovered parts in a more prominent degree than bigger particles. The greater thermodynamic tendency of the metal to corrode under fine particles was accompanied by significant surface deterioration in the form of micro-sized pits during accelerated corrosion tests.

Iron sulfides, troilite and pyrite, on the other hand, were even more aggressive to the steel substrate than sand, causing a severe degree of surface corrosion as well as a modification to the surface chemistry. The steel electrodes covered with troilite and pyrite showed opposite shifts in the OCP with respect to the bare steel, with pyrite-covered steel being in the positive direction. Despite this, in both cases, the anodic and cathodic currents increased to significantly higher values than the sand-covered counterparts. The OCP of stand-alone pyrite is far more positive than that of troilite. Subsequently, when a fixed positive potential was applied, troilite was affected at a higher degree than pyrite due to the larger potential difference. This was supported by the observation of some preferential pitting at the steel surface with troilite*, i.e.,* more deformation. In the case of pyrite, however, a new film was formed on the steel surface, which was identified using Raman spectroscopy to be mixed oxides and sulfides.

The remarkably different influence of iron sulfides was attributed to the semiconductive nature that is thought to increase the galvanic coupling by adding more cathodic sites, and by effectively participating in the polarisation reactions. In addition, the iron sulfide deposits

themselves changed morphology and chemistry due to reaction: Raman spectra indicated a potential, yet non-conclusive, change in the chemical nature. Therefore, the severity of the deposit is assumed to be time dependent. This nature of iron sulfides in turn compromises the accuracy of the electrochemical measurements by over-estimating the corrosion current.

Previous studies identified the galvanic effects by coupling two electrodes of steel under different conditions of deposit or environment.[108] Despite this, they could not explain the origin of galvanic corrosion couples due to the multiscale of complexity: the conductive deposit provides an additional channel for a portion of electrons to be transferred through the deposit. The number of these electrons is unknown and does not take part in the corrosion reaction at the metal-solution interface, which in turn affects the accuracy of the electrochemical measurments.[21]

In our study, the deposit-metal current exchange was monitored by galvanically coupling stand-alone troilite and pyrite electrodes to bare steel electrodes using ZRA. The troilite couple was found to exhibit higher galvanic currents than the pyrite couple, but this current was negligible in magnitude compared to the corrosion current measured during potentiodynamic polarisation. As a result, it was hypothesised that the deposit-metal galvanic cells have a minimal contribution in the overall corrosion process under the studied conditions of this chapter.

Both couples tended to form another form of chemically grown iron sulfide at the steel surface -with different degrees proportional to the galvanic current, despite being physically separated in the solution. These films were attributed to the production of H_2S gas in the cell due to cathodic reactions taking place at the iron sulfide electrodes, which can provide new conditions for UDC. Therefore, the effect of chemically grown iron sulfide films is studied separately in chapter 6.

Through the experiments explored in this chapter, valuable insights were revealed, and it is concluded that UDC is a multidimensional corrosion phenomenon. As a result, many questions about the transport process, the pitting stability, and the role of newly formed corrosion films will be researched further in the following chapters, beyond the general corrosion paradigm, in order to understand the underpinning causes and mechanisms of UDC.

5 Artificial pits: understanding Underdeposit Corrosion in localised geometries

5.1 Introduction

Artificial pits have been used as a powerful technique in investigating the mechanism of localised corrosion. The technique is used to study mass transport, pit solution chemistry, and the corrosion film formation within pits.[34–37] As proposed in Galvele's model,[38] a quick hydrolysis equilibrium occurs at the pit bottom after the dissolution of the metal, which breaks down the passive layer and gives the minimum degree of localised acidification required for stable pitting. *In-situ* spectroscopic analysis revealed that the phases present in the salt film vary through their thickness, and that the metal ions have different chemical coordination environments depending on their proximity to the dissolving surface.[34–36] None of the reported studies, however, were carried out in the presence of surface deposits which may affect transport significantly.

Typically, the salt film as well as the depth of the pit comprise the main barriers to the transport of ionic species and/or inhibitors to and from the inside of the pit. The presence of deposits above the pit cavity forms an additional barrier, hence it is thought to affect the transport mechanism and the pitting stability. Figure 5.1 presents a schematic of the cross-sectional geometry of an artificial pit with deposits incorporated at the mouth. The salt film diffusion barrier is denoted R1, while the pit depth and the externally applied solid deposit are denoted R2 and R3, respectively.

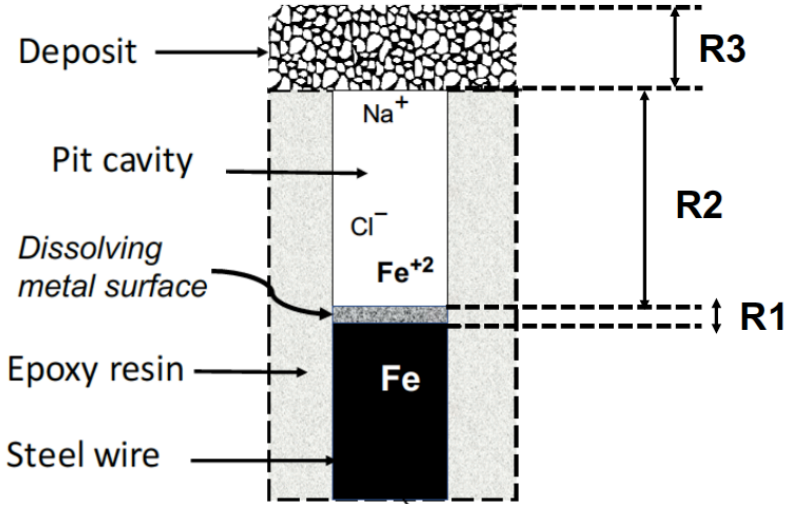

Figure 5-1 A schematic cross-sectional view of the artificial pit geometry under a deposit, showing the three main diffusion barriers namely R1 for the salt film, R2 for the pit depth and R3 for the externally applied deposit (scales arbitrary).

In this work, artificial pit electrodes are modified to allow incorporating controlled deposit geometries: to elucidate the role of the deposit's morphology and chemistry in the pit propagation process. The artificial pit acts as an anode in a three-electrode electrochemical cell, simulating an actively dissolving pit, whilst deposits cover the pit cavity. Electrochemical CV measurements[34,106] were used to obtain directly the dissolution kinetics. Sand deposits were used to study the effect of particle size and layer thickness. Troilite- and pyrite- covered pits were tested and contrasted to the sand pit kinetics to study the effect of reactive deposits.

Data are presented in terms of a transport-controlled model for pit propagation, showing the role of different types of deposits as well as other system variables such as the chloride ion concentration and pH on the pit kinetics. Complementary morphological and compositional characterisation of the artificial pit wire surface were carried out by means of SEM-EDS and Raman spectroscopy to study the physicochemical changes of the pit dissolving interface, and to correlate to the findings of the electrochemical measurements.

Recently, *in-situ* probing was enabled using highly advanced synchrotron-light sources. Due to their ability to penetrate electrodes and electrolytes at reasonable depths,[37,43] they demonstrated a potential in studying the pit chemistry transformations in addition to the transient structures of the newly formed films within pits. Synchrotron analyses namely XRF, XANES and XRD were performed on actively dissolving artificial pits under physically applied deposits. The obtained information can be used to validate ionic transport models that predict the long-term growth of corroding pits under deposits.

The experiments and results presented in this chapter are used to establish a fundamental understanding of the effect of deposits on artificial pits kinetics under aerated conditions, prior to introducing the sour (H_2S) gas variable in the following chapter.

5.2 Results and discussion

5.2.1 Electrochemistry

5.2.1.1 One dimensional pit growth and pit depth calibration

The dissolution kinetics of pits are simulated by dissolving the metal, at relatively high potentials, inside epoxy in one direction while avoiding the possibility of forming multiple pits. As the surface recedes down, a 1D cavity is formed; its epoxy wall has a cylindrical shape and its bottom is the iron surface. The top of the cavity is either open to the bulk solution or covered with a controlled deposit.

Pits were grown to various depths by varying the duration of the potential hold, according to the protocol specified in section 3.2. A typical potentiostatic pit growth, *i.e.*, current vs time behaviour, is shown in Figure 5.2, where the pit was grown for one hour at a potential of +500 mV (Ag/AgCl). The figure demonstrates a high current density at the early stages of pit growth until it reaches a plateau as the pit depth goes deeper inside the epoxy.

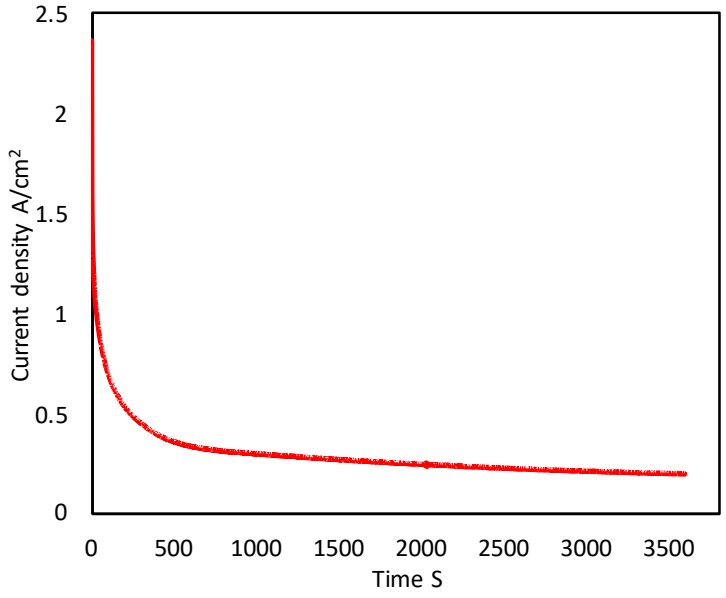

Figure 5-2 A typical pit growth current vs. time diagram. Pit is grown from zero pit depth for 1hr at +500mV vs. Ag/AgCl RE in a 0.5 M NaCl solution with pH 6.6, and with the cell open to air.

Pit depths were calculated from Faraday's 2nd law by integrating the current passed during pit growth, according to Equations (5.1) and (5.2) below. The calculated pit depths were then compared to the measured values obtained from an optical microscope coupled to a CCD camera.

$$Q = \int I\, dt = \frac{Ax\rho nF}{M_w} \tag{5.1}$$

$$Pit\ depth\ (x) = \frac{QM_w}{A.\rho.n.F} \quad (5.2)$$

Where Q is the charge calculated by integrating the current-time curve, A is the cross-sectional area of the wire, x is the pit depth, ρ is the density (8.05 g/cm^3 for iron), n is the average charge of ions during dissolution and assumed to be 2, F is Faraday's constant (96485 C/mole), and Mw is the atomic weight (55.845 g/mole), assuming pure iron.

Pit depths estimated by both methods are compared in Figure 5.3, which show a close agreement between the calculated pit depths from Faraday's law and the visually measured depths using the optical microscope (R^2=0.926).[152] An average general error of 8% was obtained with a few points exceeding this value, which can be attributed to measurement errors, such as bubbles or local crevices, or due to side reactions that limit the Faradaic efficiency. Errors were minimised by applying further controls, for instance, implementing a finer surface finish and applying a vacuum to remove microbubbles. The depth calculated from the passed charge is used throughout this study.

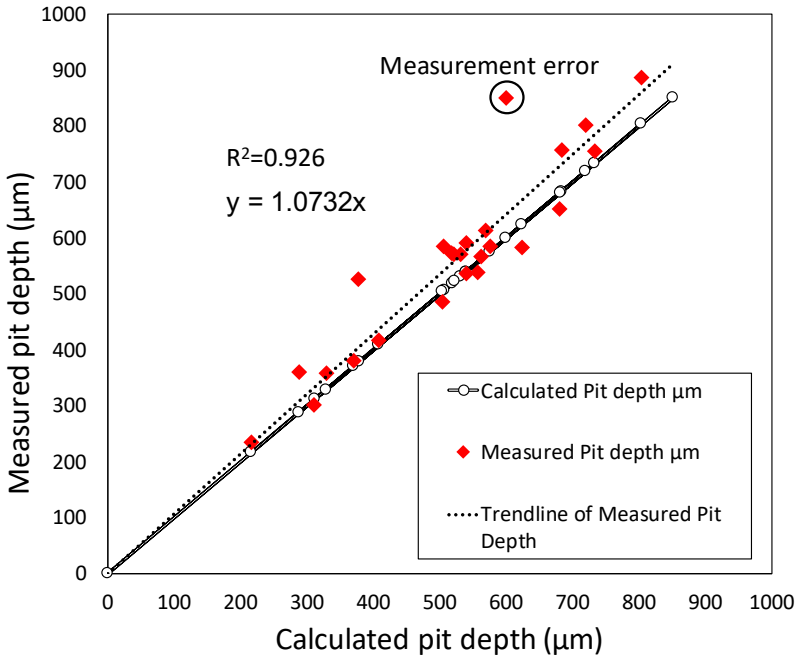

Figure 5-3 Measured pit depth (points) via optical microscopy compared to the theoretical values calculated from the cumulative charge (solid line). The dotted outliner represents the trendline fit of the measured pit depth data points.

5.2.1.2 Cyclic Voltammetry profile of artificial pits

During the pre-corrosion stage at +500 mV (Ag/AgCl), the pit grows unidirectionally under diffusion control since there is a salt film of iron chloride $FeCl_2$ formed on the dissolving interface inside the pit.[34,46] A typical CV measurement is shown in Figure 5.4 summarising

various pitting kinetics: the active (film-free) and diffusion-limited dissolution regimes are explained. Starting at the pit growth voltage, typically +500 mV (Ag/AgCl), and sweeping in the negative direction (a)-(b), the current remained potential-independent across this region indicating that a diffusion-limited dissolution was established. The current in this case, where a salt film is present, is called the diffusion-limited current i_{lim}, which is often used as an indication of the pit propagation rate and stability.[34]

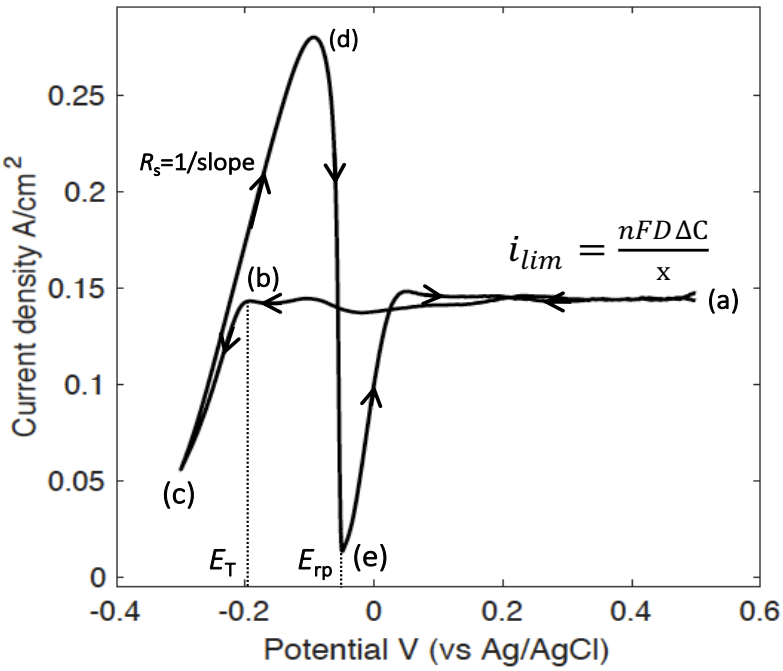

Figure 5-4 Typical anodic dissolution kinetics of a pure iron artificial pit in a 0.5 M NaCl solution (cell is open to air), showing the diffusion-controlled region (a – b), and the effect of supersaturation on extending the active dissolution region (b – c – d). The equation is Fick's law, where X is the pit depth representing the diffusion length from the metal interface till the pit mouth.

During the potential scan in the negative direction, the salt layer is thinned down gradually until it completely dissolves. As a result, the current shows a slight increase, due to salt film breakage, before it decreases linearly indicating that the growth is no longer diffusion-controlled; the dissolution is now activation or IR-controlled, in the region (b)-(c). The potential at which this transition happens is referred to as the transition potential E_T, after which the pit propagation is no longer controlled by the salt film.[34]

In the reverse scan as the potential is increased in absence of salt films, the current density increases, *i.e.,* the metal dissolution rate increases, at region (c)-(d). The reciprocal of the slope of this region of the scan represents the pit solution resistance, R_S. Supersaturation is achieved when the rate of ions production exceeds the ionic diffusion rate inside the pit. The salt layer precipitates eventually leading to a sudden drop in the current density (d)-(e). The potential at the inflection point where the current suddenly drops to its lowest point on the

reverse scan is referred to as the salt film reprecipitation potential E_{rp}. As the potential is increased further, the salt film self-regulates its thickness (it increases in this case), and the pit propagation returns to the diffusion-controlled state at current density i_{lim}, which can be considered a measure of how stable the pit propagation is, and is the main factor to investigate in this study.

5.2.1.3 Nitrogen control

In electrochemistry, deaeration of the electrolyte solution is a general procedure used to avoid errors in measurements due to oxygen reduction reactions. In artificial pits, however, the dissolving interface and the pit solution are very small, and the accessibility of oxygen is limited, especially under the continuous recession of the pit surface. Cathodic reactions may, however, affect the initial stages of pit growth. To ensure better control of the experiments, cyclic voltammograms were measured on the same pit prior to and after deaerating the solution using N_2 purging. As shown in the CV scans in Figure 5.5, no significant changes in the AP kinetics were recorded, and therefore, the electrochemical cell was left open to air throughout the measurements, except when H_2S was used.

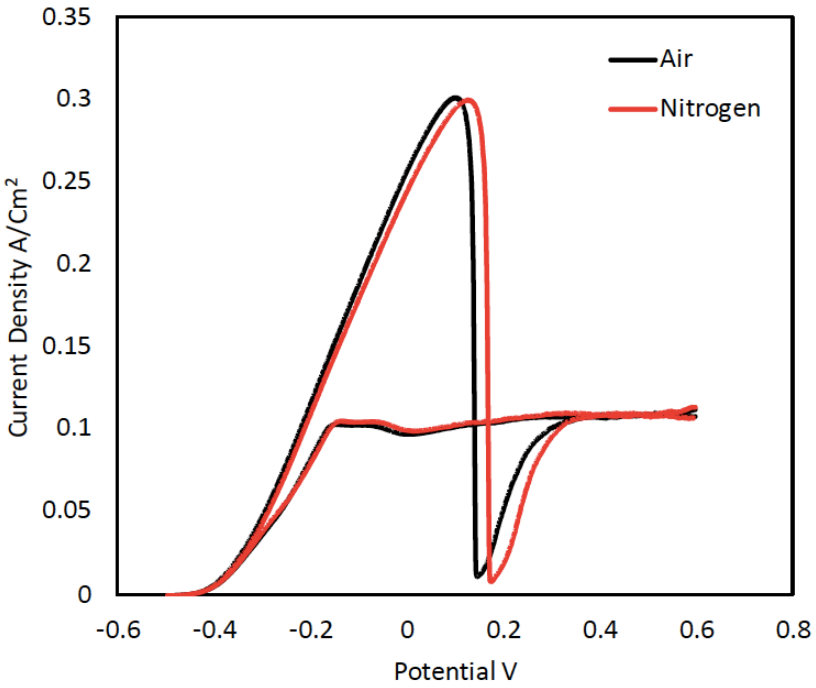

Figure 5-5 CV measurements on a 500 µm-deep artificial pit during N_2 purging compared to when the cell was open to air; no significant change was observed and the cell was left open to air throughout the artificial pit experiments.

5.2.1.4 Pit stability at various pit depths

CV measurements were obtained for pits pre-corroded to various depths (~200 to 800 µm) in absence of deposits, as shown in Figure 5.6, and the extracted parameters are demonstrated in Figures 5.6 (b-d). The diffusion limiting current density i_{lim} is found to decrease linearly with increasing pit depth (Figure 5.6b). The decrease in i_{lim} can be attributed to the increase in the diffusion length with deeper pits according to Fick's law in Equation (5.3) below, in agreement with the diffusion-controlled model of pit growth.[34,35,106]

$$\mathrm{i}_{lim} = \frac{nFD\Delta \mathrm{C}}{\mathrm{x}} \qquad (5.3)$$

Where i_{lim} is the diffusion-limited current density in the pit, x is the pit depth, D is the diffusion coefficient, ΔC is the concentration gradient, n is the average charge of ions during dissolution and assumed to be 2, and F is Faraday's constant 96485 C.mol^{-1}.

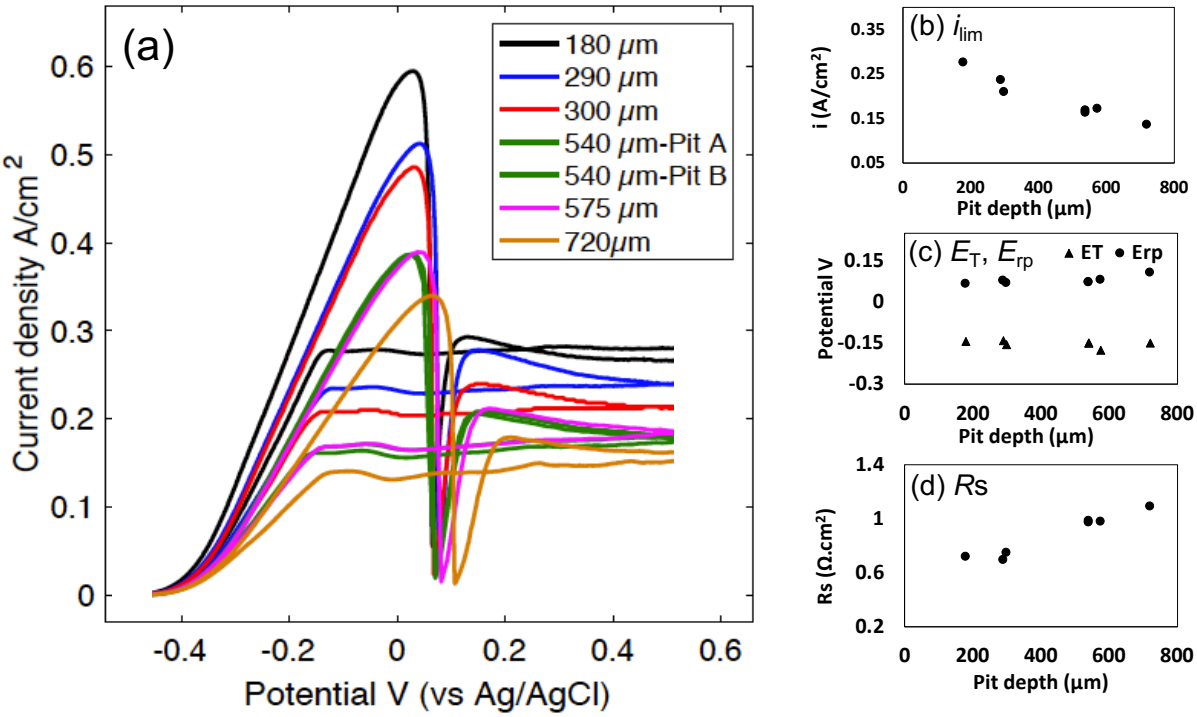

Figure 5-6 Pit stability at different pit depths in absence of deposits: (a) CV diagram of various pits at different depths. i_{lim}, E_T and E_{rp}, and R_s are extracted in (b), (c) and (d), respectively. Two different pits with 540 µm depth are demonstrated for reproducibility purposes, and a 575 µm-deep pit exhibited a similar behaviour to the 540 µm-deep pits.

The values of *E*rp and E_T remained independent of the pit depth as shown in Figure 5.6c. Although it can be argued that a higher *IR* potential drop (marked by the higher resistance R_S at deeper depths, as in Figure 5.6d) may have also aided in decreasing i_{lim}, Isaacs stated that almost all the *IR* potential drop is contained in the thin adjacent resistive layer on the anode,

which renders the potential gradient to be relatively unimportant.[102] This observation indicates that the solution chemistry at the bottom of the cavity maintained the pit stability; for deep pits, smaller amounts of current are needed to maintain a stable propagation. The results here are consistent with previous observations reported for stainless steel artificial pits.[38,153,154]

Shallow pits are expected to be largely affected by minimal changes in the environment, whereas excessively deep pits can be completely isolated from such changes in the environment or the deposit. Therefore, medium-depth pits (~450-500 μm) are chosen to provide reasonable and reliable indications of the effect of external parameters, unless stated otherwise.

5.2.1.5 Pit stability at different bulk solution chemistry

The bulk chloride ion concentration

The effect of the bulk chloride ion concertation is addressed using three concentrations of NaCl solution, 0.5, 1 and 3 *M*, on pits grown to a depth of 450-500 *μm*. The CV measurement scans are shown in Figure 5.7: the extracted parameters, i_{lim} and R_S are found to be minimally affected by the chloride concentration of the bulk electrolyte, as explained in Figure 5.7(c and e). On the other hand, a decrease in both E_T and E_{rp} was exhibited when the chloride concentration increased to 3 *M*, as shown in Figures 5.7d.

Lower transition potential E_T values are usually associated with thicker salt films such that sweeping to a further negative potential is required to thin down the salt film until it eventually breaks. Therefore, the decrease in E_T values at high chloride ion concentrations may indicate the formation of a relatively thicker $FeCl_2$ salt film at the dissolving interface, *i.e.,* a larger potential drop.

A similar finding was observed on pure iron by Soltis *et al.,*[106] where a logarithmic relationship was obtained between E_T and the chloride concentration: the transition potential E_T decreases with increasing chloride concentration. Their study found that E_T dependency on chloride concentration is entirely due to the variation of the potential drop within the pit caused by the changing resistivity of the bulk solution.

On the other hand, in the back scan, a lower reprecipitation potential E_{rp} indicates an ease to reactivate the pit, *i.e.,* to form the active chemistry needed for diffusion-controlled propagation. Low E_{rp} values also mean that the ionic production rate is high compared to the escape rate outside the pit, hence the salt film reprecipitates relatively quicker. This could also be attributed to a decrease in the diffusion coefficient $D\Delta C$ of Fick's law, Equation (5.3), when the bulk chloride ion concentration is high. Eventually, a high retention rate of ions is achieved, and a

small potential was thus needed to restore the salt film-controlled growth regime. The solution in the pit, however, is too highly saturated to make this change significant.

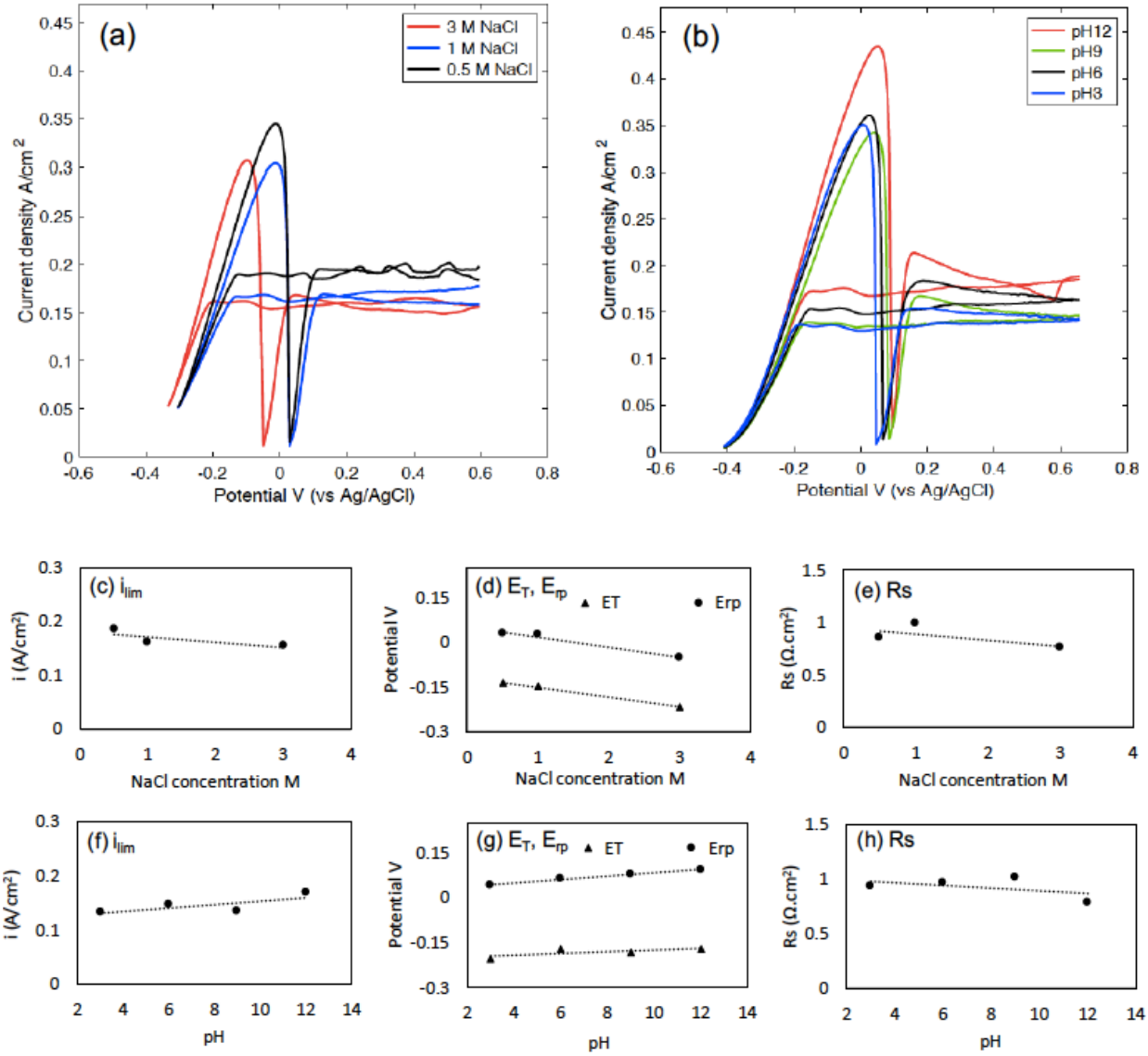

Figure 5-7 The bulk solution chemistry control: CV measurements on pits of 450-500 µm depth, in absence of deposits at the pit cavity. (a) CV diagram of various pits at different chloride concentration. i_{lim}, E_T and Erp, and Rs are extracted in (c), (d) and (e), respectively. The pH effect on the CV measurements is shown in (b), and the i_{lim}, E_T and Erp, and Rs are extracted in (f), (g) and (h), respectively.

pH of the bulk solution

NaCl solutions of 0.5 *M* concentration and different pH values of 12, 9, 6 and 3 were used to study the kinetics of artificial pits in different solution acidity; pits pre-corroded to a 450-500 µm depth. The extracted parameters from the CV measurements of Figure 5.7b, i_{lim},E_T, E_{rp} and R_S, remained independent of the bulk solution pH, as explained in Figures 5.7 (f - h). The

effective pH inside the pit is mainly influenced by hydrolysis reactions of iron ions, with a limited effect of the hydroxyl or hydrogen ions of the bulk electrolyte. This relationship may, however, change if the pit is shallow, *i.e.,* the diffusion length is short for close interaction between the bulk and localised solutions.

In conclusion, the higher chloride concentrations inside active pit render the equivalent effect due to the bulk hydroxyl negligible. Additionally, the transition potential E_T is measured when the pit is saturated with ferrous ions, and thus becomes unaffected by the bulk solution pH. The same observation was recorded by Soltis *et al.*, where E_T remained unaffected by the bulk solution pH or the presence of buffer species within the pit.[106] This resulted in a minimal- or no-effect of both the bulk pH and chloride ion concentration on the diffusion-limited current density i_{lim}.

Whereas this was the general observation, and unlike the case of changing the chloride concentration, a very slight increase in E_{rp} was observed at higher pH values. The ions escape rate outside the pit in this case can be high compared to the production rate at the pit bottom, hence a higher potential is needed to re-precipitate the salt film. Generally, high pH values render the iron dissolution low, thus requiring higher potentials to increase the flux of ions production.

5.2.1.6 Influence of the deposit's physical properties

In this study, sand of the same base material, *i.e.,* silicon dioxide SiO_2 was used to simulate the inert deposit case. Different porosity of deposit layers was achieved using different particle size, and therefore, two types of sand, different in grain size and shape, were used as explained in the experimental chapter, section 3.1.

5.2.1.6.1 Experimental controls for deposit experiments

Deposit support method

The procedure to support the deposit was the same throughout; a plastic cup is fixed on top of the artificial pit where the deposit is placed. A plastic mesh is then pushed against the deposit layer surface to hold it in place. Packing the deposit with the mesh was feared to affect the electrochemistry diffusion results. Therefore, the experiment was repeated without a mesh, and it was found that no significant difference is observed when the deposit is covered with the plastic mesh, as explained in Figure 5.8, thus ensuring reproducibility.

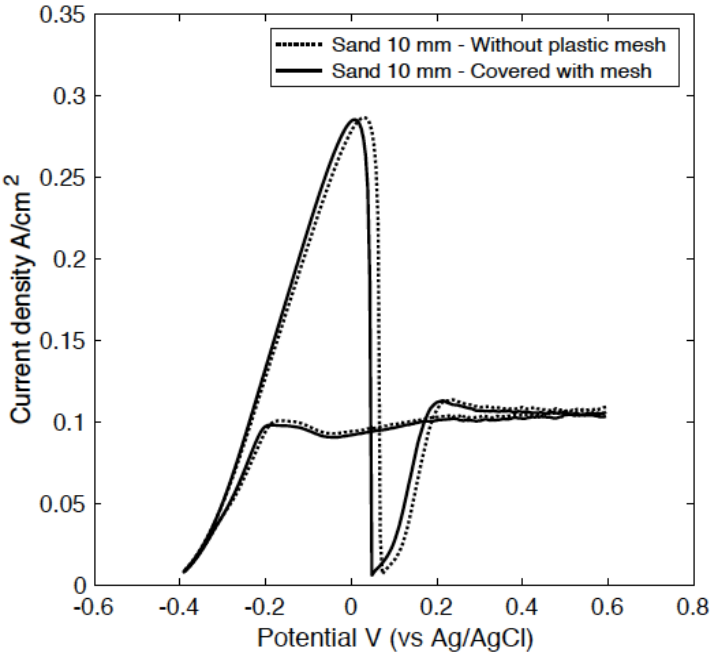

Figure 5-8 A negligible change in the CV measurements is observed when a plastic mesh was used to hold the deposit in a cup above the artificial pit.

Deposit application before vs. after the pit growth

In the practical world of pipelines, pits can start to initiate and propagate whilst under pipeline deposits. In other cases, pits that have been previously initiated without deposits present at their pit cavity can also continue to grow as newly formed deposits start to form and settle above their openings. In the context of our artificial pit experiments, deposits were placed above the pit cavity both before and after pit growth, as explained in Figure 5.9. Both scenarios can be different with regard to the pit corrosion kinetics: initiation, propagation, and (or) termination.

This difference in propagation kinetics was examined by carrying out CV measurements on two pits of the same depth: one whilst the deposit was initially present before the pit growth, and the other with the deposit applied after the pit had already grown to the required depth. In this case, the pit was 500 µm deep, and the deposit used was fine-grained sand with a 3 mm layer thickness. The CV results are shown in Figure 5.10. The result from this control experiment has usually been a consistent shift of both E_T and E_{rp} to more positive values when the deposit was applied after pit growth, *i.e.,* the deposit was not initially present at the pit cavity.

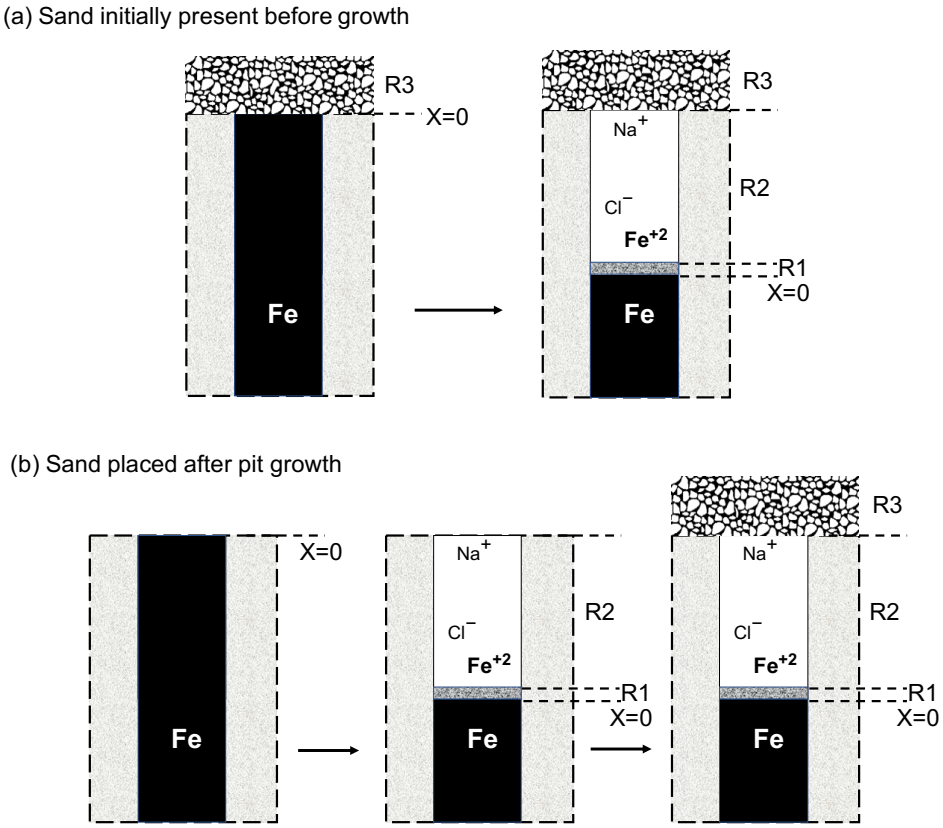

Figure 5-9 A schematic of artificial pits explaining the difference in the order of applying the deposit: (a) the deposit is applied before corroding the pit, and (b) the pit is corroded first to the required depth followed by applying the deposit. X represents the interface position.

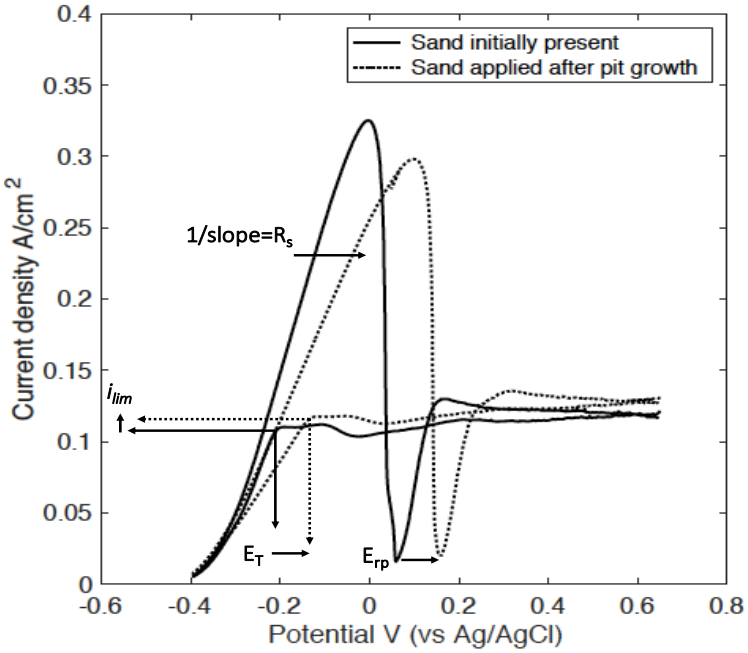

Figure 5-10. CV measurements showing the difference in propagation kinetics according to the order of applying the deposit. A negligible change in i_{lim} is observed when the deposit is applied after growing the pit. The pit is 500 µm deep covered with a 3 mm layer of fine sand.

When deposits were initially present at the pit cavity, the large flow of ions at the beginning aided to create steady diffusion passages through the deposit porous network. On the other hand, after the pit had already grown, the addition of deposits was hypothesised to cause a sudden change in the ionic diffusion so that a relatively higher retention rate of ionic species was exhibited, *i.e.,* a higher pit solution resistivity. For easy transport through the porous network, the newly added deposit must wet completely. When the deposit is not completely wet, ions take a more tortuous path to transport, thus increasing R3, the deposit component of the resistance. This also explains the slight change in diffusion-limited current i_{lim}, despite having not considerably changed as a result of the change in deposit application order.

Only 3 CV scans were carried out. Therefore, it can be hypothesised that the CV parameters would turn closer to the case of 'initially present deposit' at extended periods of dissolution time, and as the particles take their respective stable position in the deposit bed, *i.e.,* steady state ionic trajectories. In this study, the deposit was applied before the pit was grown, unless stated otherwise.

5.2.1.6.2 Inert (silica) deposits modify the ionic transport

The results of the CV measurements are shown in Figure 5.11 for artificial pits pre-corroded to the same pit depth of 450 μm under inert silica deposits. The deposit presence resulted in a decrease in the i_{lim} value. The decrease in i_{lim} is proportional to the deposit layer thickness; with the decrease rate declining as subsequent deposit layers were added, *i.e.,* with increasing the thickness. This suggests that there is a threshold point beyond which further thickness increase seems to have a minimal effect on the pit kinetics.

The decrease in i_{lim} can be explained by the fact that the deposit impedes the passage of ions outside the pit and creates tortuous paths for ion diffusion, which increases the diffusion length and resistance. As detailed earlier in chapter 4, section 4.2.1.2., the fine sand (<44 μm) behaves like clay, providing easier mixing with the bulk solution and a less tortuous transport path for reactants.[19,142] The shorter ionic transport path with a reduced resistance against ions diffusion provides higher diffusion-limited currents accordingly.

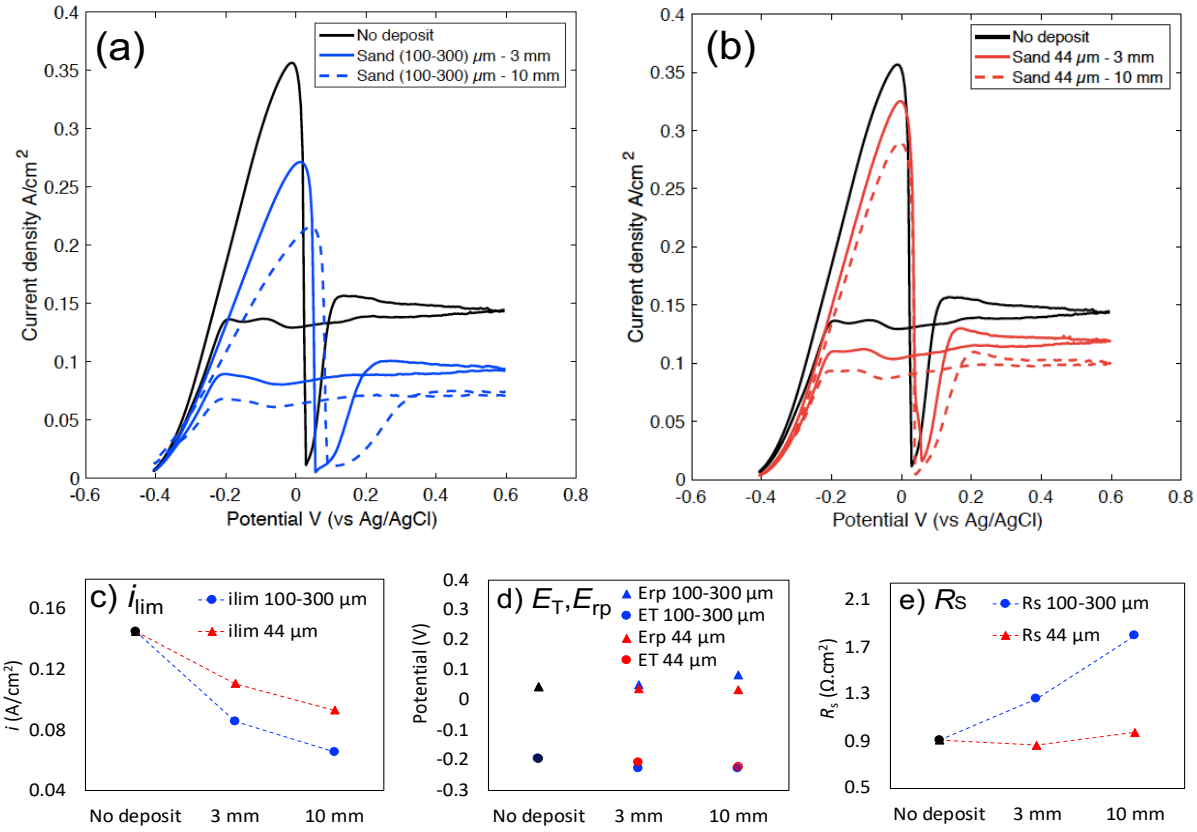

Figure 5-11 CV measurements of Fe artificial pits showing the effect of the deposit's physical properties. (a) coarse sand and (b) fine sand; each size is applied with 3- and 10-mm layer thickness. i_{lim}, E_T and Erp, and R_s are extracted in (c), (d) and (e), respectively. The pit has a cavity depth of 450 μm grown in 0.5 M NaCl solution at a scan rate of 10 mV s^{-1}.

By comparing the CVs of pits covered with coarse sand (Figure 5.11.a) with ones covered with fine sand (Figure 5.11.b), it can be observed that a smaller i_{lim} was obtained with larger particle size, as explained in Figure 5.11c. This observation is consistent with the planar coupon results in chapter 4, which conclude that the more accessible the solution through the deposit, the lower the effective resistance to the ions flow. This measurement, however, does not take into account the *limiting* pore size which might affect transport through porous networks.

Small changes in the extracted E_T, E_{rp} and R_s, as shown in Figure 5.11 (d and e), can be attributed to the minimal effects that inert deposits could impose to the pit solution chemistry, as they do not participate in chemical or electrochemical reactions. However, when the coarse sand was used, *i.e.,* lower porosity, R_s increased remarkably as demonstrated in Figure 5.11e. The observed increase in R_s dictates that the presence of a relatively thicker and/or denser deposit slows the diffusion of ions outside the pit, which may lead to the formation of a thicker and/or denser salt film.

5.2.1.6.3 Minimised effect of inert deposits on deep pits

In the real environment, pits with high aspect ratios (depth:mouth diameter) exhibit more propagation stability than those with low aspect ratios.[38,155] This is in accordance to Galvele's model of pit propagation where a critical *ix* value called the pit stability product is required for stable pit growth (*i* is current density and *x* is pit depth).[38] As a result, applying deposits on cavities with different aspect ratios is expected to change their propagation kinetics with various degrees.

The effect of the deposit's particle size, representing deposit beds with different porosities, was investigated with two different pit depths to study the relative influences of the deposit's physical arrangements and the pit depth. Two pits at depths of 450 µm and 900 µm were tested under 3 mm thick deposit layers of both the <44 µm and 100-300 µm sands. As shown in Figure 5.12, the influence of the deposit on i_{lim} decreases as the pit gets deeper.

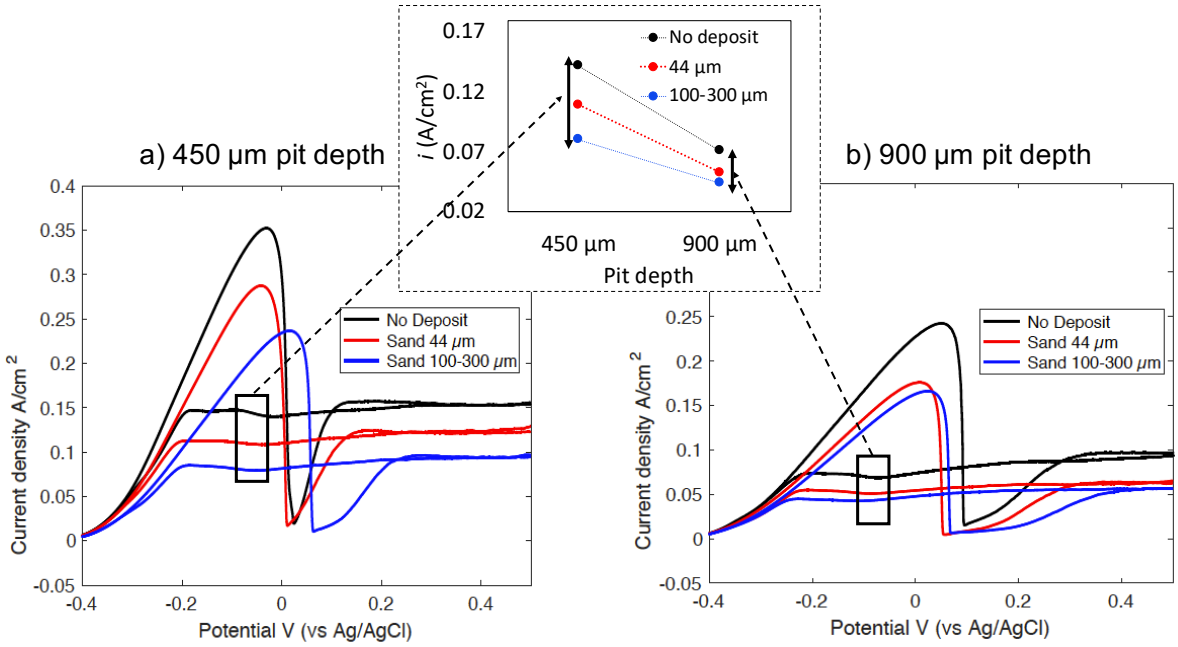

Figure 5-12 CV measurements of Fe artificial pit electrode showing the effect of deposit on pits with various cavity depth: (a) 450 µm and (b) 900 µm. The deposit is coarse- and fine- grained sand, and the pit corroded in a 0.5 M NaCl solution at a scan rate of 10 mV s^{-1}. The inset shows the i_{lim}, values in both cases.

As the diffusion length becomes larger with deeper pits, the resistance component R2, as shown in the schematic in Figure 5.13 below, becomes large so that changes in R3, due to changing the deposit physical properties, cannot affect the kinetics significantly. It can also be hypothesised that changing R2 by changing the pit depth would have a small effect if R3 is large, due to a relatively tighter or thicker deposit, and vice versa. This result suggests that

the pit depth dominates the pit behaviour at deeper depths, and that the effective diffusion length and diffusion resistance components, *i.e.,* pit depth and deposit layer, are different, and competing.

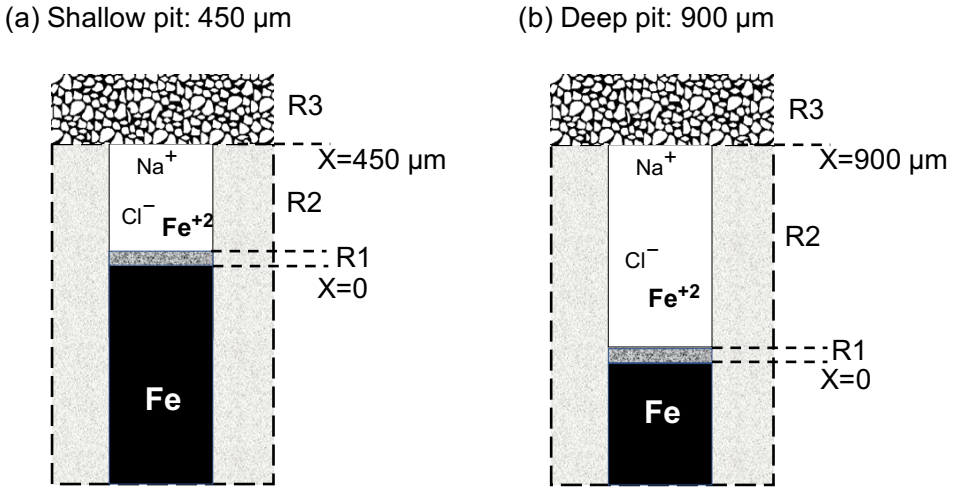

Figure 5-13 A schematic of artificial pits corroded to two different depths: (a) 450 µm, and (b) 900 µm, with the deposit present above the pit cavity.

5.2.1.6.4 Role of 'reactive' deposits

The chemistry of the used deposit is expected to influence the corrosion process. A reactive deposit may alter the water chemistry inside the pit, change the chemical composition and morphology of the corrosion products, and react with the steel to form films on the surface. The deposit itself can also undergo changes in its morphology and composition and transform to other phases and/or compounds. Here, the artificial pit kinetics were examined under sand, FeS, and FeS_2. The net pore volume of FeS_2 and FeS is similar to the 100-300 µm sand (~40%). Therefore, both types of iron sulfide were compared to the coarse sand, and all the deposits were applied with a layer thickness of 3 mm.

As discussed earlier, changing the deposits physical characteristics exhibits minimal effects on deeper pits' kinetics. Therefore, deeper pits of 900 µm depth were chosen for the reactive deposit experiment to minimise the effects of porosity and thickness, and hence the deposit chemistry becomes the main variable. As illustrated in Figure 5.14, applying iron sulfides resulted in a significant decrease in the value of i_{lim}: much lower values than their sand counterparts. Both FeS and FeS_2 also exhibit higher E_T, E_{rp}, and R_s values. The two CV behaviours represented in the figure for iron sulfides were observed with both phases, but the curve with highest E_{rp} was more frequently observed with FeS; the figure is annotated accordingly.

The low values of i_{lim} as well as the high values of E_{rp} and R_s, especially the exceptionally high E_{rp} value of +1 V in the case of FeS, indicates a much more aggressive local chemistry inside the pit. The supersaturation charge is indicated in the figure for each deposit's CV, which is the area under the curve from the most negative potential till the sudden drop of current at E_{rp}. The charge represents the amount of current or dissolution needed to supersaturate the pit and precipitate the salt film: it is lowest for FeS, which indicates a small amount of current (i_{lim}) is needed for salt film precipitation and stable pit propagation (at a lower rate).

Iron sulfides are reactive compounds, which may react with the local electrolyte that is already highly acidic, releasing sulfur species into the pit cavity. As a result, other forms of iron sulfides may form on top of the Fe surface at the bottom of the cavity, in competition with the conventional chloride salt films normally present during the diffusion-controlled pit growth. Depending on the nature of the newly formed film, the pit can be stabilised, or passivated.

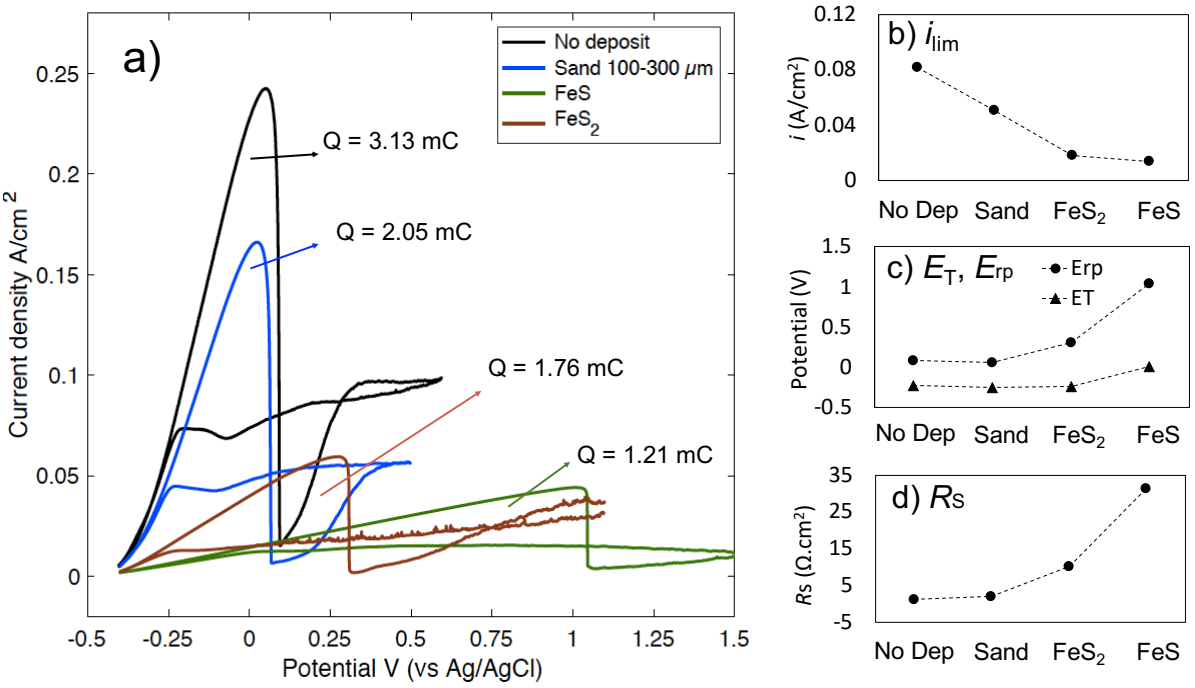

Figure 5-14 The effect of deposit type on the kinetics of Fe artificial pits. (a) CVs of the artificial pit electrode with a cavity depth of 900 μm without and with a deposit bed of coarse sand, FeS, and FeS_2. i_{lim}, E_T and E_{rp}, and R_s are extracted in (b), (c) and (d), respectively. Note the supersaturation charge (in Millicoulomb mC) is assigned to each CV scan. Pits were grown in a 0.5 M NaCl solution, at a scan rate of 10 mV s^{-1}.

5.2.2 Surface morphology and chemical identification

5.2.2.1 The pit surface

The existence of deposits on top of the pit has affected the electrochemical dissolution behaviour of iron, and it was assumed that a change in the solution chemistry had caused such changes, especially when iron sulfides were used. It is therefore hypothesised that these changes in solution chemistry had affected the salt film formation and precipitation, and hence its morphology and chemical composition. In order to examine the pit surface, artificial pits were disassembled, and the wires' cross-sections were examined in terms of surface morphology and chemical composition using SEM/EDS.

SEM images in Figure 5.15 show the surface of Fe wires following the various conditions described above: in absence of deposits, and in presence of coarse sand (100-300 μm), fine sand (<44 μm), FeS_2, and FeS. The morphology in the cases of iron sulfides is significantly different from the sand and no-deposit cases. In the latter, pits of few micrometres in size were observed dispersed on the surface, and the number of pits is highest in the absence of deposit and decreases in case of the fine- and coarse-grained sands, respectively. This is the same order of the i_{lim} decrease observed in Figure 5.14. A thin dense film, on the other hand, was typically observed with iron sulfide-covered samples as shown in Figure 5.15 (d and e). Where delamination of the film took place, as in Figure 5.15d, an interconnected pitting structure could be viewed, indicating that a more aggressive dissolution had already taken place.

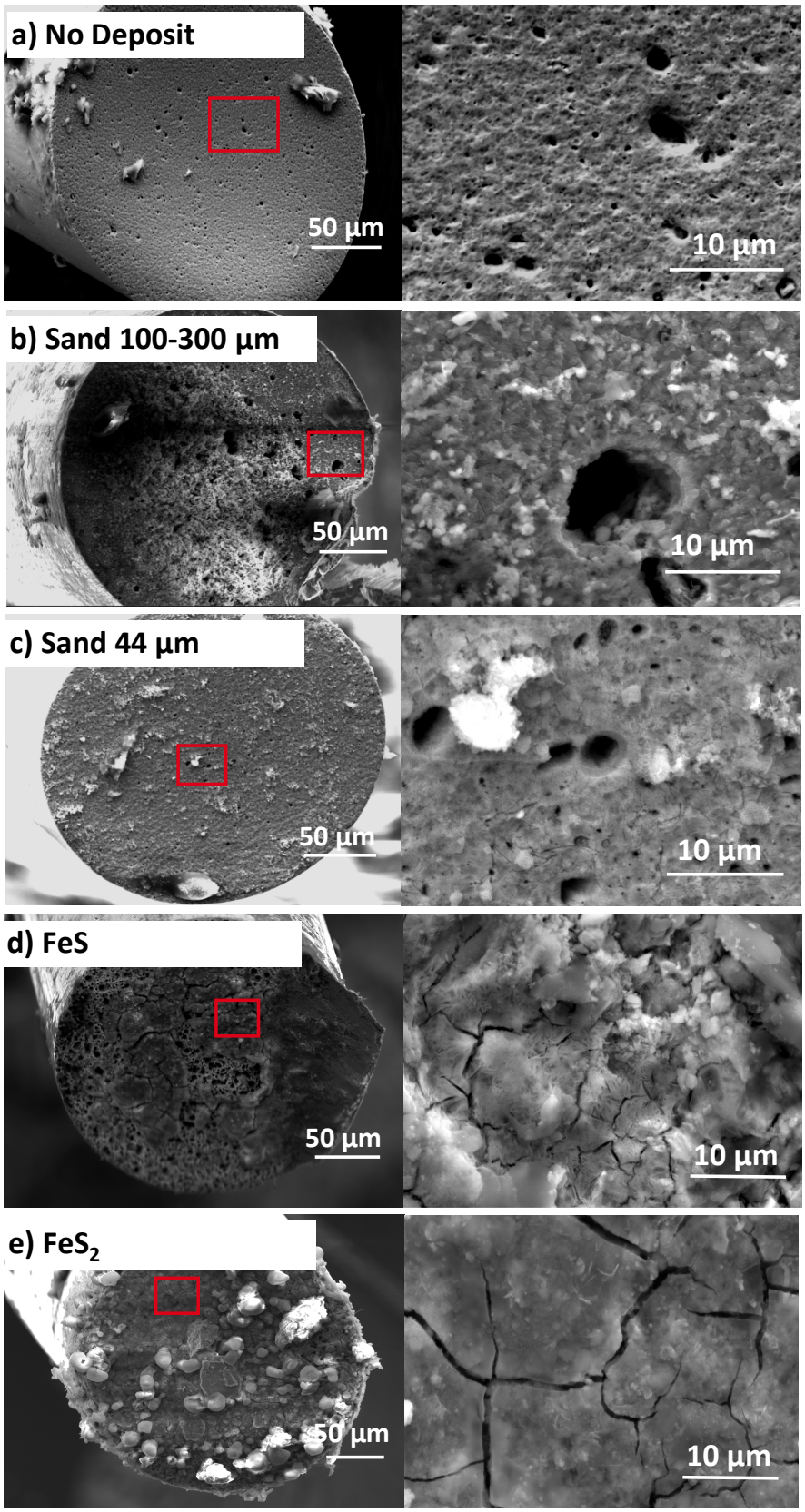

Figure 5-15 SEM micrographs of the Fe wire surface after the formation of artificial pits in absence of deposits (a), and in the presence of sand 100-300 µm (b), sand <44 µm (c), FeS (d), and FeS_2 (e); the images on the right hand side are magnified views of the marked regions in the respective images on the left.

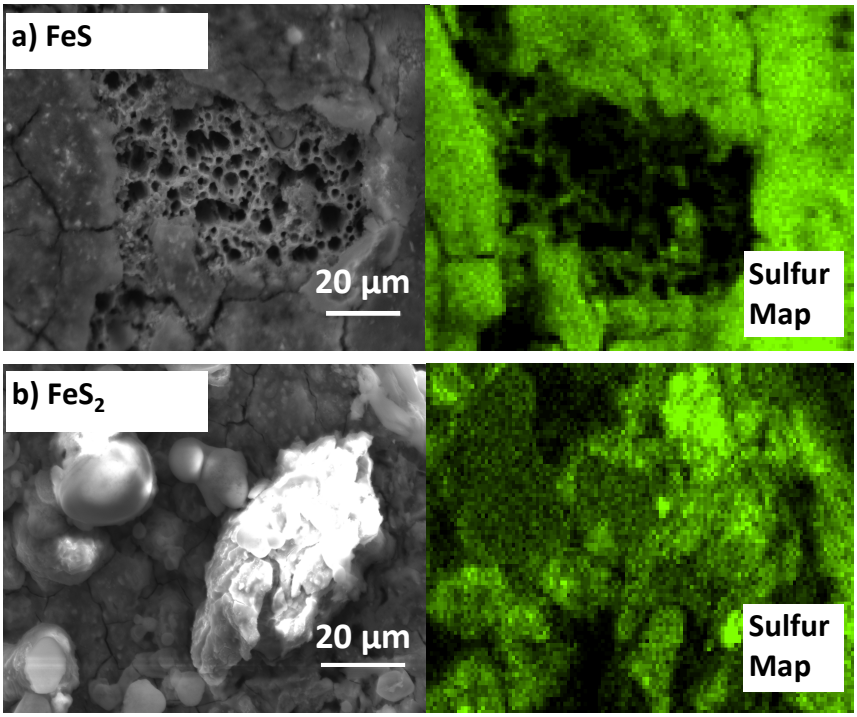

Figure 5-16 SEM micrographs and the corresponding EDS sulfur maps of the artificial pit wire surface when dissolved under (a) FeS and (b) FeS_2.

The EDS sulfur maps and SEM images shown in Figure 5.16 indicate that a sulfur-containing film was formed on the surface of the dissolving interface. The EDX elemental composition measurements on the sulfur containing films (Table 5.1) revealed a higher amount of sulfur content in the case of pyrite-covered pits. An Fe:S ratio of 3:1 was observed with FeS_2 as opposed to 15:1 with FeS. It can be assumed that the sulfur-rich pyrite provides more sulfur quantities that participate in the reaction inside the pit. On the other hand, the corroded wires from both the no-deposit and sand experiments showed higher percentages of chloride compared to the iron sulfides-covered pits. In the case of iron sulfides covered pits, the newly formed sulfur-containing films are expected to inhibit the formation of chloride salt films, *i.e.,* $FeCl_2$, which provides a reasonable correlation to the electrochemical findings.

Table 5-1. EDX analysis of the pit wire surface after the pre-corrosion and CV measurements, in the absence of deposits, and under sand, FeS, and FeS_2.

Elemental ratio	Atomic %				
	No deposit	Sand 100-300 µm	Sand <44 µm	FeS	FeS_2
Fe:S	—	—	—	14.89	3.21
Fe:Cl	6.07	7.34	15.38	28.14	21.57

In some pyrite covered pits, EDS mapping of the corroded surface, as in Figure 5.17, showed a presence of sulfur and sodium rich areas, in which iron was absent. This indicates the formation of elemental sulfur at the metal surface in its final form of sodium sulfide (Na_2S) or sulfate (Na_2SO_4).

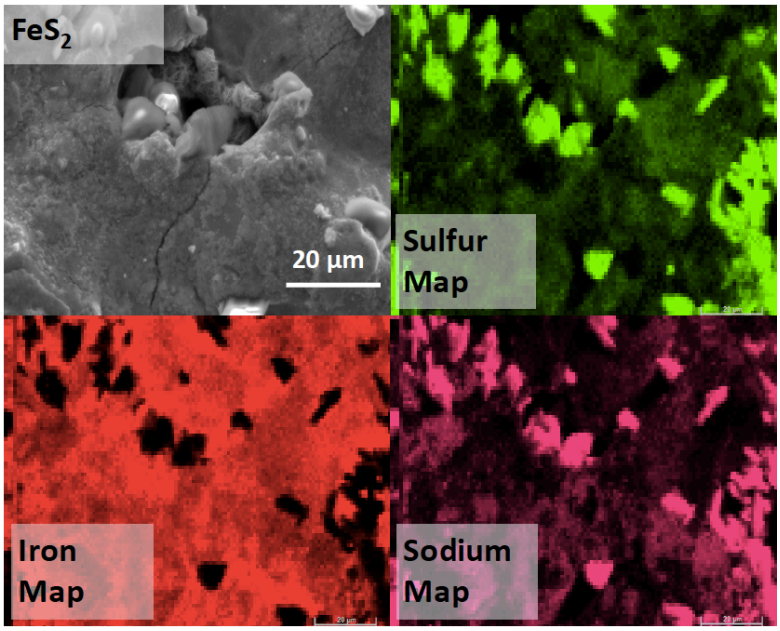

Figure 5-17 An SEM micrograph of an artificial pit wire surface corroded under FeS_2, along with the corresponding sulfur, iron, and sodium EDS maps.

Hydrogen sulfide gas can be released from the iron sulfide reduction reactions by the influence of the high H^+ concentration inside the pit. As a result, elemental sulfur can be formed by the oxidation of hydrogen sulfide due to the ingress of oxygen or the presence of reducible ferric ion in the form of iron (III) oxide, according to the reactions in Equations 5.4 to 5.6. The equations describe the typical reactions of elemental sulfur formation by the oxidation of hydrogen sulfide as explained in the literature,[112,156,157] which is assumed to hold in our case as well.

$$8H_2S + 4O_2 \rightarrow 8H_2O + S_8 \quad (5.4)$$

$$8Fe_2O_3 + 24\ H_2S \rightarrow 16FeS + 24H_2O + S_8 \quad (5.5)$$

$$2SO_4^{2-} + 6H_2S \rightarrow S_8 + 4H_2O + 2OH^- \quad (5.6)$$

5.2.2.2 On the chemical identification: Raman spectroscopy

The chemical composition of the films formed in the pit was further investigated using Raman spectroscopy. Figure 5.18 summarises the Raman spectra of the surface films formed inside the pit. A mixture of iron oxides was typically present at the metal surface in all the studied cases. Peaks associated with sulfur-containing species appeared when iron sulfides were applied. In the absence of deposits, the spectra in Figure 5.18 (a) indicated a mixture of maghemite Fe_2O_3 (387, 673 and 713 cm^{-1}) and magnetite Fe_3O_4 (304 and 521 cm^{-1}). When sand was introduced with different sizes, as in (b) and (c), both hematite Fe_2O_3 and goethite α-FeO(OH) were formed, respectively corresponding to Raman peaks at (215-219 and 276-286 cm^{-1}) and (386 and 468 cm^{-1}).

In the cases of iron sulfides, Figure 5.18 (d and e), the shifts at 211-216 and 273-279 cm^{-1} are strong, suggesting the presence of amorphous mackinawite. The peaks at 380-389 and 473-479 cm^{-1} can also be associated with pyrrhotite. These observations agree with the Pourbaix E–pH diagram developed by Anderko and coworkers[158] for a multi-component and non-ideal aqueous iron sulfide solution, where iron monosulfide was formed and followed by a sequence of $Fe(HS)^+$, amorphous ferrous sulfide, mackinawite, and pyrrhotite. This observation also supports the EDS results that indicated sulfur species at the pit surface (Figure 5.16). However, this did not prevent the formation of iron oxides, and a mixture of iron oxides and sulfides was typically formed in iron sulfides- covered pits.

On the other hand, in conjunction with the observations from the EDS maps in Figure 5.17, the application of pyrite resulted in the evolution of elemental sulfur in the form of sodium sulfate, as can be seen from the peaks at 458, 618, 636, 989-994 and 1134 cm^{-1} in Figure 5.18 (e). Iron sulfides are active in terms of their semi-conductive nature and also the solubility that changes with the solution acidity.[141] Troilite is more soluble (especially at low pH) than pyrite, whose solubility is reported not to vary with pH in the range of 1-4.[144] Accordingly, various sulfur-containing species can be present to different degrees inside the pit cavity. Due to the lower solubility of pyrite, a solid-state chemical reaction is assumed to occur between some pyrite residuals and the polarised interface, causing such sulfur-rich films to precipitate or form at the surface.

The observations from the SEM, EDS and Raman spectroscopy analyses dictate that the different morphologies and chemical compositions of the pit surface films is a direct result of the change in the deposit type. This can be correlated to both the increase in Rs and the decrease in i_{lim} during the CV tests when iron sulfides were applied. However, it cannot alone provide a solid conclusive remark on the specific reason for their different electrochemical responses.

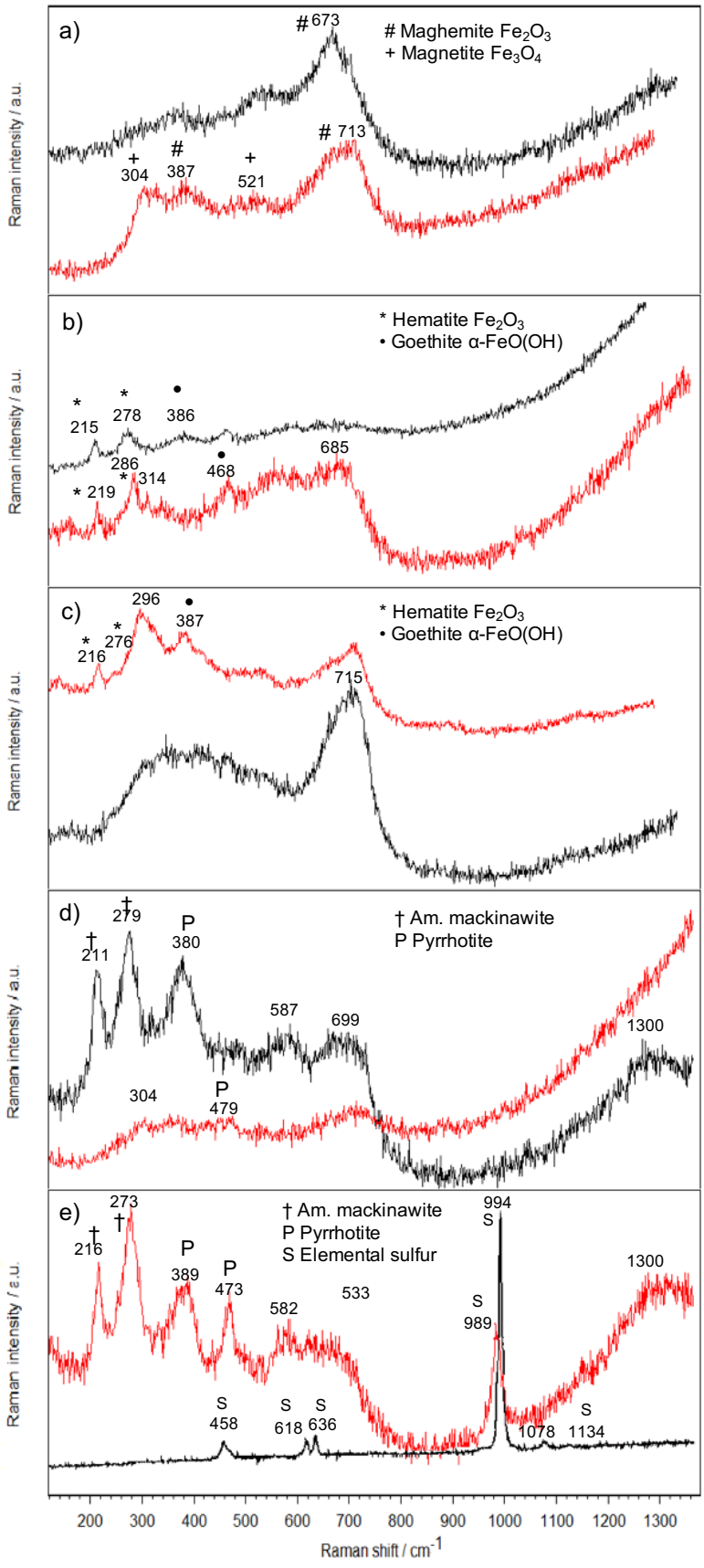

Figure 5-18 Raman spectra at the surface of artificial pit wires corroded in absence of deposits (a), and under sand (100-300 µm) (b), sand (<44 µm) (c), FeS (d), and FeS_2 (e).

5.2.3 *In-situ* synchrotron X-ray characterisation

The electrochemical findings, and the subsequent *ex-situ* pit surface characterisation, demonstrate potential significant changes in the pit solution chemistry as a result of applying different deposits above the pit cavity. Techniques, such as SEM, EDS and Raman spectroscopy, cannot provide much details about the real time chemical alterations and the reason behind such changes eventually, despite being helpful in driving the above-mentioned hypothesis.

In corrosion, where fast microstructural changes take place, *in-situ* synchrotron radiation can be more suitable, for their short acquisition time. This previously enabled reliable *in-situ* X-ray induced fluorescence and diffraction measurements to be performed on operating electrochemical cells, without a significant loss of the intensity of the probing light.[43,45,46] Therefore, understanding the pit chemistry transformations and the transient structures of the newly formed films under deposits was allowed. Additionally, since the pit is micron-sized and the solution quantity is very small, the capacity of focusing the beam to a micron-sized spot is necessary to detect local variations in the concentrations of iron complexes.

Iron artificial pits, this time in the form of epoxy-embedded foils, 25 μm in thickness and 3 mm in width, were activated at +800 mV (Ag/AgCl) and *in-situ* synchrotron measurements were carried out on the actively dissolving interface. Figure 5.19 shows optical images taken at the beamline for the cross-section view of the iron foil artificial pit electrodes: (a) the pit was already formed, (b) before dissolution whilst sand was placed above the wire. The electrodes were uniformly dissolved to the required depth prior to the X-ray measurements. Typically, large depths are chosen to do the X-ray measurements to take advantage of the minimal movement of the interface.[43] However, since deposits reportedly exhibited larger contribution to changing the dissolution kinetics when the pit depth is small, and vice versa, and also to maximise the effect of the external deposit variable, shallow pits were used in this study, unless stated otherwise.

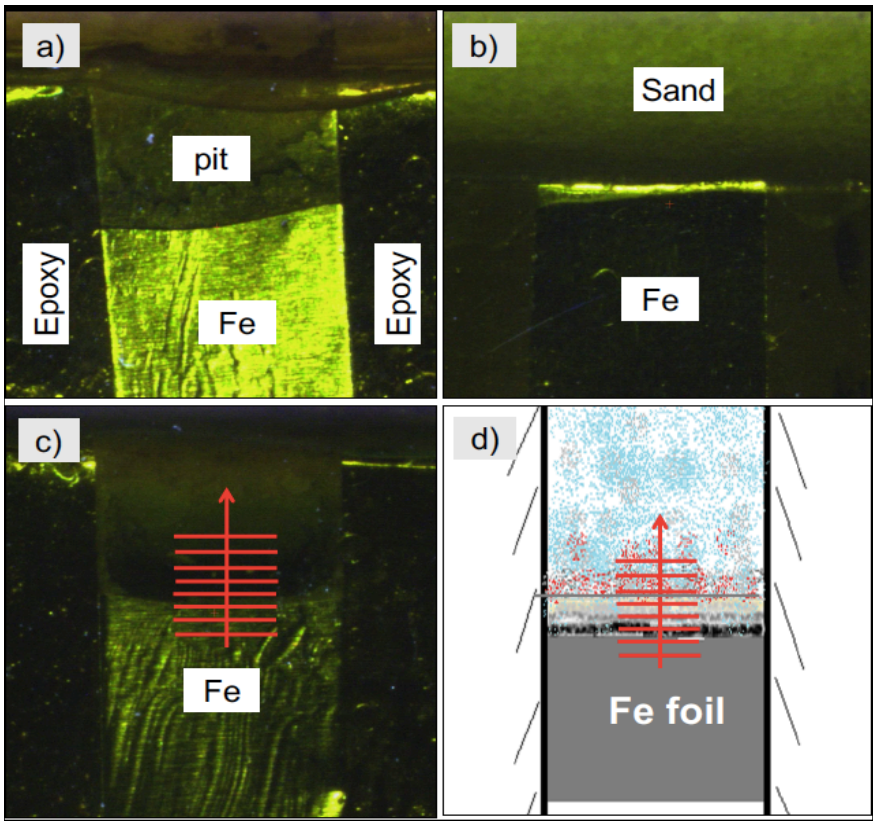

Figure 5-19 Optical images of the cross section of iron artificial pit foil electrodes (3 mm in width) used in the in-situ measurements: (a) a grown pit, (b) an uncorroded pit with sand at the top. (c) and (d) represent the XRF measurement steps.

In our typical *in-situ* synchrotron experiment, XANES, XRF mapping, and XRD techniques were used. XRF point measurements were also acquired at different levels above the dissolving interface, as shown in Figure 5.19c and the schematic representation in Figure 5.19d. XANES data at the Fe-K edge, alongside with XRD, at the salt film as well as the pit mouth, were used to elucidate the intermediate species during the salt film precipitation. Essential information about Fe dissolution under deposits, and the intermediate species generated by the interdependent interaction with the applied deposits, can be extracted from the findings of our synchrotron experiments, as detailed in the following sections.

5.2.3.1 Diffusion profiles inside corroding pits

Whilst the pit was corroding under diffusion-limited conditions at high potential (+0.80 V vs. Ag/AgCl), XRF measurements were initially performed at the metal interface. XRF scans can provide information about the interface position, the speed of corrosion, and the ionic diffusion profile. A typical XRF scan using the non-normalised raw data is shown in Figure 5.20, where the interface position corresponds to the distinct drop in intensity. XRF scans were carried out using two different protocols, namely line scan and fixed-point scan.

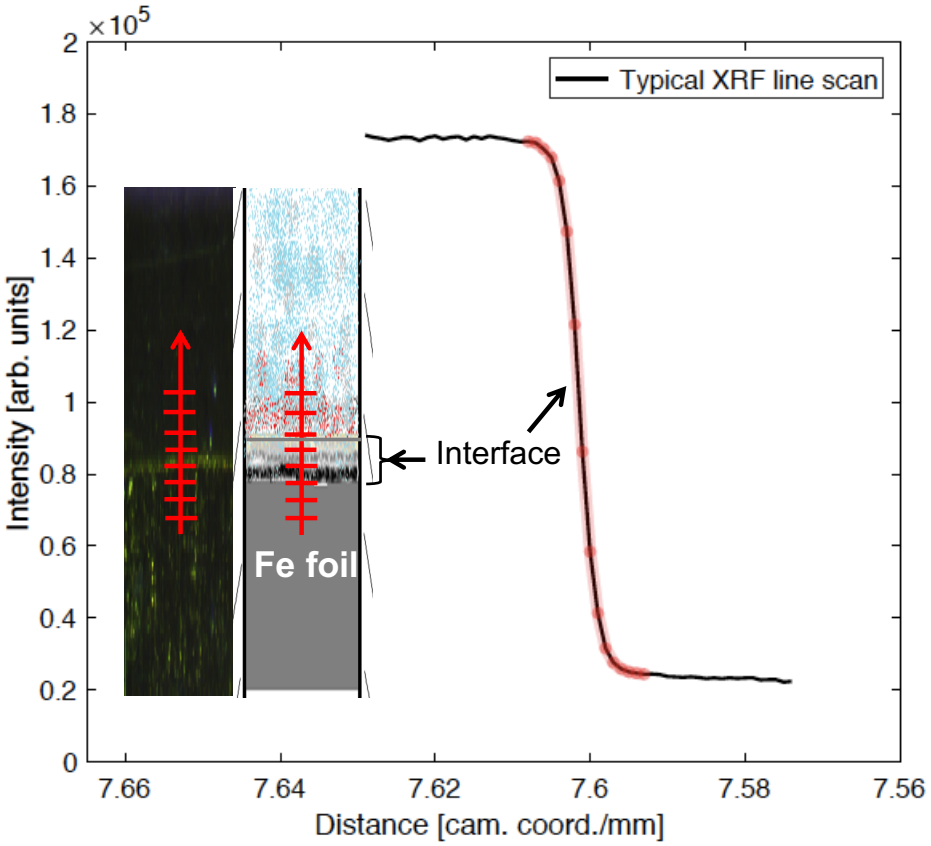

Figure 5-20 A typical XRF line scan across the metal-solution interface. The scan starts from the metal side below the interface and ends in the pit solution above the salt layer. The insets are actual and schematic representations of the metal-salt-solution X-ray stepped scan.

In the fixed-point XRF scan, XRF measurements were recorded at a fixed position relative to the recessing interface, *i.e.,* the stage was static, and the beam was at a fixed position slightly below the interface. XRF point measurements were acquired at a scan step of 1 second as the interface recesses, and the acquisition continued until the metal was dissolved so that the beam records the pit solution above the interface. The fixed-point XRF scans were aimed to give more accurate estimations of the diffusion profiles close to the interface; the stage is static and only the interface is moving, hence more accurate measurements.

On the other hand, in the XRF line scan, an arbitrarily reference position, typically 50 μm below the sample interface, was chosen as a starting point to scan upward across the dissolving interface and the pit solution. The XRF line scan, where the stage moves with respect to the beam position, was used to define the interface position as well as the speed of the metal surface recession, which will be used later to measure the salt film thickness more accurately. Unlike the fixed-point scans, XRF line scan can also provide information about the diffusion profile over longer distances, *i.e.,* from the pit bottom to the pit mouth.

From the different parameters reported in this study, three cases were studied *in-situ* when H_2S was not present: (1) in absence of deposits (Pit 1, 625 µm deep), (2) in presence of the 100-300 µm sand (Pit 2, 585 µm deep), and (3) in presence of FeS_2 at the pit mouth (Pit 3 and Pit 4). Two pits at different depths were used for the FeS_2 measurements to investigate the deposit-pit depth dominating behaviours; Pit 3 is 1 mm deep and pit 4 is 410 µm. These conditions were assumed representatives of the *ex-situ* experiments and were selected for the *in-situ* measurements for time efficiency reasons.

Initially, all the XRF scans were normalised to the highest intensity, *i.e.,* the metal-side fluorescence, to account for the differences in the epoxy thickness in different samples, as shown in Figure 5.21 for the fixed-point XRF measurements.[43] It can be seen from the figure that the slope of the metal-solution transition curve is different. This was initially assumed to be due to a change in the salt film thickness and could be used for estimating the salt film thickness. However, since the surface roughness and the speed of corroding the pit can lead to similar changes, XRF scans were not used to measure the salt film thickness. Stepwise XRD measurements were rather used following the XRF scans to measure the salt film thickness, as detailed in the later sections.

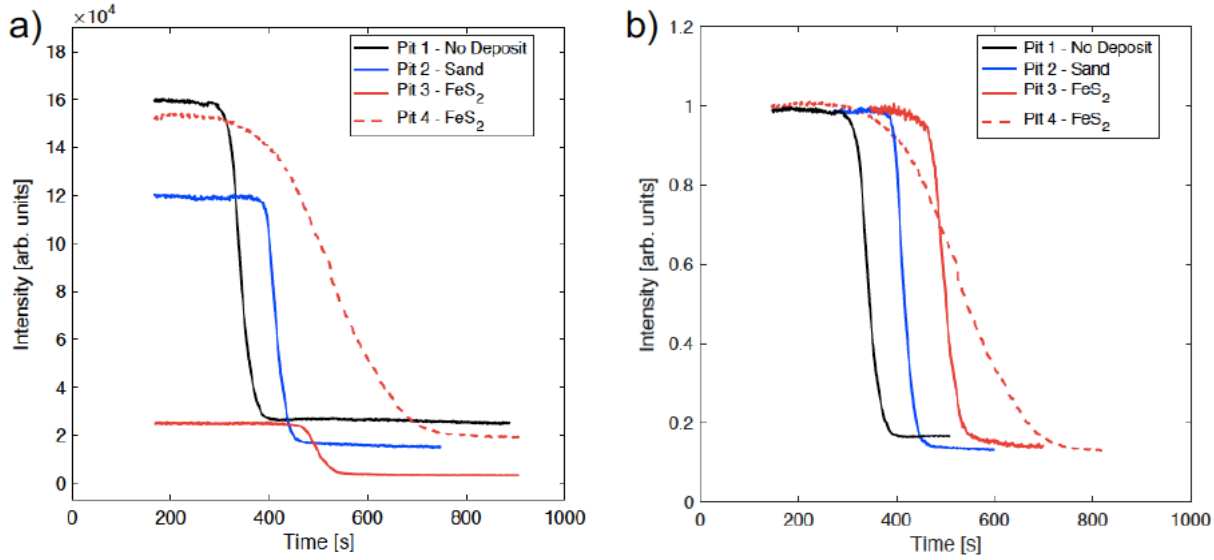

Figure 5-21 Fixed-point XRF scans recording the iron ion intensity at the interface of artificial pits as they recess at +800 mV (Ag/AgCl). (a) the raw data and (b) the data normalised against the highest intensity. Pit 3 (1 mm) and Pit 4 (410 µm) represent two cases of FeS_2 covered pits. Pit 3 exhibited a significant low intensity in the raw form as the detector was un-intentionally set at a larger distance from the samples than normal.

XRF: Diffusion- vs activation-controlled dissolution

Two different potentials, +800 mV and -200 mV (Ag/AgCl), were applied to the foil artificial pit, representing the diffusion- and activation-controlled dissolution regimes, respectively. Figure 5.22 shows the electrode-to-solution XRF intensity transition during corroding at +800 mV and -200 mV for the cases involved in this study: no-deposit, under sand, and under FeS_2. When the dissolution was diffusion-limited at +800 mV, there was a smooth interfacial transition, as shown in Figure 5.22 (a, c and e). On the other hand, when the growth regime was transitioned to be activation-controlled at -200 mV, a roughened profile during fluorescence transition is observed as shown in Figure 5.22 (b, d and f). The roughened transition indicates a lack of a properly defined interface, which could be due to a roughness in the surface or a disruption in the diffusion process.

On the other hand, a thicker salt film was argued to form, but previous XRD studies indicated the formation of iron carbide Fe_3C clusters that were not etched away by the slow outward diffusion at low potentials.[37,127] Therefore, an XRD study is helpful to explain these observations, however, only the diffusion-limited dissolution regime was considered due to the limited beamtime. The diffusion-limited dissolution represents the stable dissolution phase under the conditions relevant to the scope of this study. An XRD study is fairly explained in chapter 6 for both diffusion-limited and activation-controlled dissolution phases in presence of H_2S.

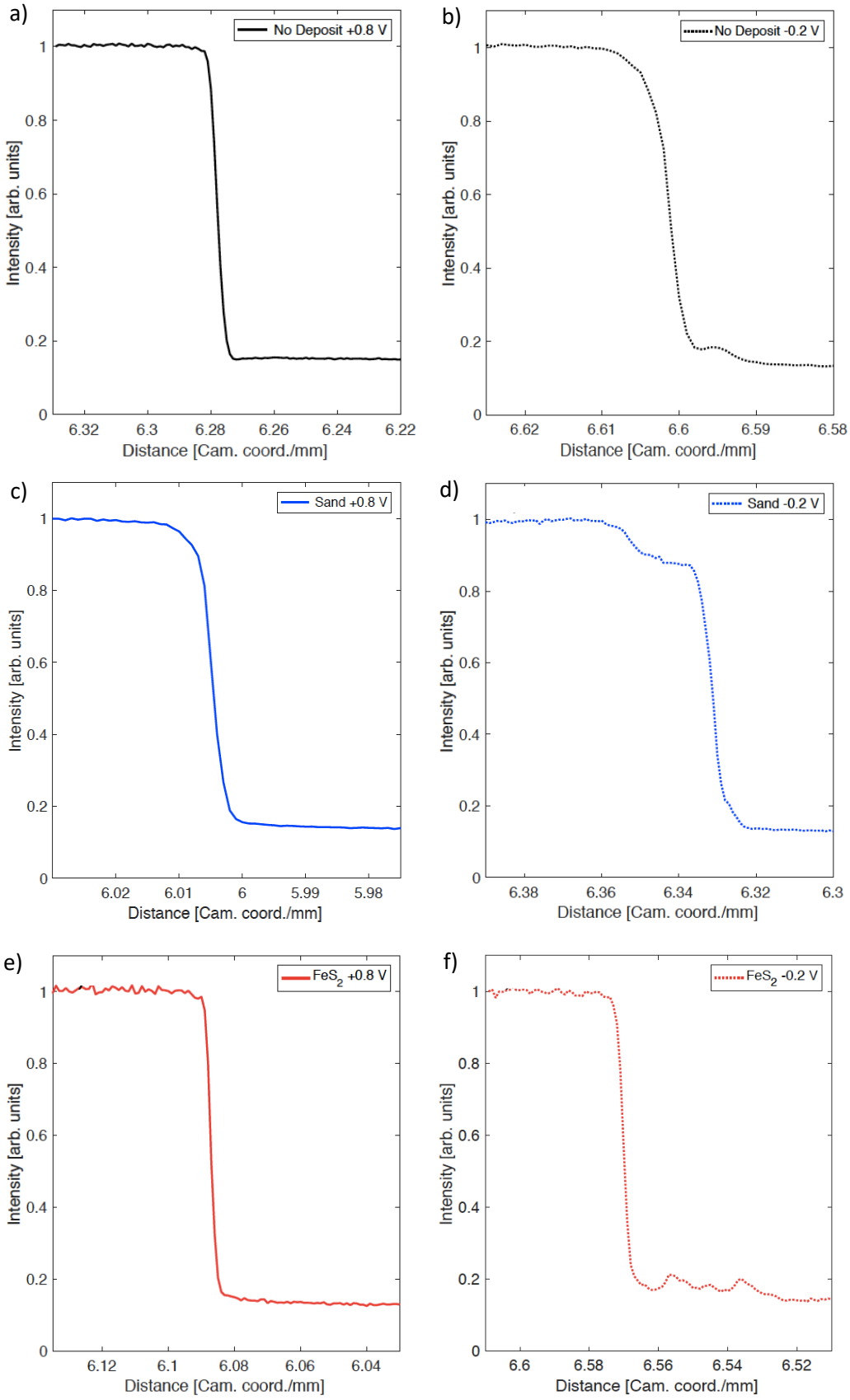

Figure 5-22 XRF line scans across the interface of foil artificial pits corroding in absence of deposits (a and b), under sand (c and d), and under FeS_2 (e and f) at two different potentials; +800 mV (a, c and e) and -200 mV (b, d and f) vs. Ag/AgCl RE.

Diffusion blockage by deposits

During the electrochemical CV measurements, it was hypothesised that a change in the solution resistance Rs (R1, R2 and R3) inside the pit was the reason behind obtaining different i_{lim} values under different deposits. This hypothesis was tested by observing the diffusion profiles and the ionic concentration, in terms of fluorescence intensity using XRF scans, at the dissolving interface and the pit solution.

Figure 5.23 shows the diffusion profiles divided into two components: (a) the interface component recorded from the fixed-point XRF scans after the interface transition, and (b) the pit solution component recorded from the XRF line scans 30 μm above the interface outwards. In both cases, the x-axis was corrected to indicate the distance with reference to the interface position. Since the data from the fixed-point XRF measurements was originally plotted as intensity vs. time, the speed of interface recession was used to correct the x-axis by multiplying the interface speed by the time of fluorescence transition. The speed of corroding the pit was measured at the synchrotron using consecutive XRF line scans across the interface, where the interface position was monitored with respect to time. Table 5.2 details the speed of the interface recession and the depths of the pits involved in this study.

Table 5-2. The pits involved in the non-H_2S synchrotron study showing the pit depth and the rate of surface recession

	Pit 1 No Deposit	**Pit 2 Sand**	**Pit 3 FeS_2**	**Pit 4 FeS_2**
Pit depth (μm)	625	585	1000	410
Surface recession rate (μm/s)	0.032	0.043	0.030	0.020

Figure 5.23a shows the XRF scan for few micrometres above the dissolving interface, *i.e.,* after the metal-solution intensity transition. When deposits were present, the intensity of iron fluorescence, representing iron ion concentration, was less than the no-deposit control. The concentration gradient, as observed from the slopes, indicates a decrease in concentration with deposits. A similar observation was recorded in Figure 5.23b at extended distances above the interface, except with the shallow Pit 4 under FeS_2. As shown in the figure, for shallow pits (Pit 1, Pit 2 and Pit 4), the addition of deposits seems to hinder the diffusion of iron ions by the blockage effect of the deposit conformations at the pit mouth. The XRF results presented here are in agreement with the electrochemical findings, where lower i_{lim} values were obtained when deposits were used.

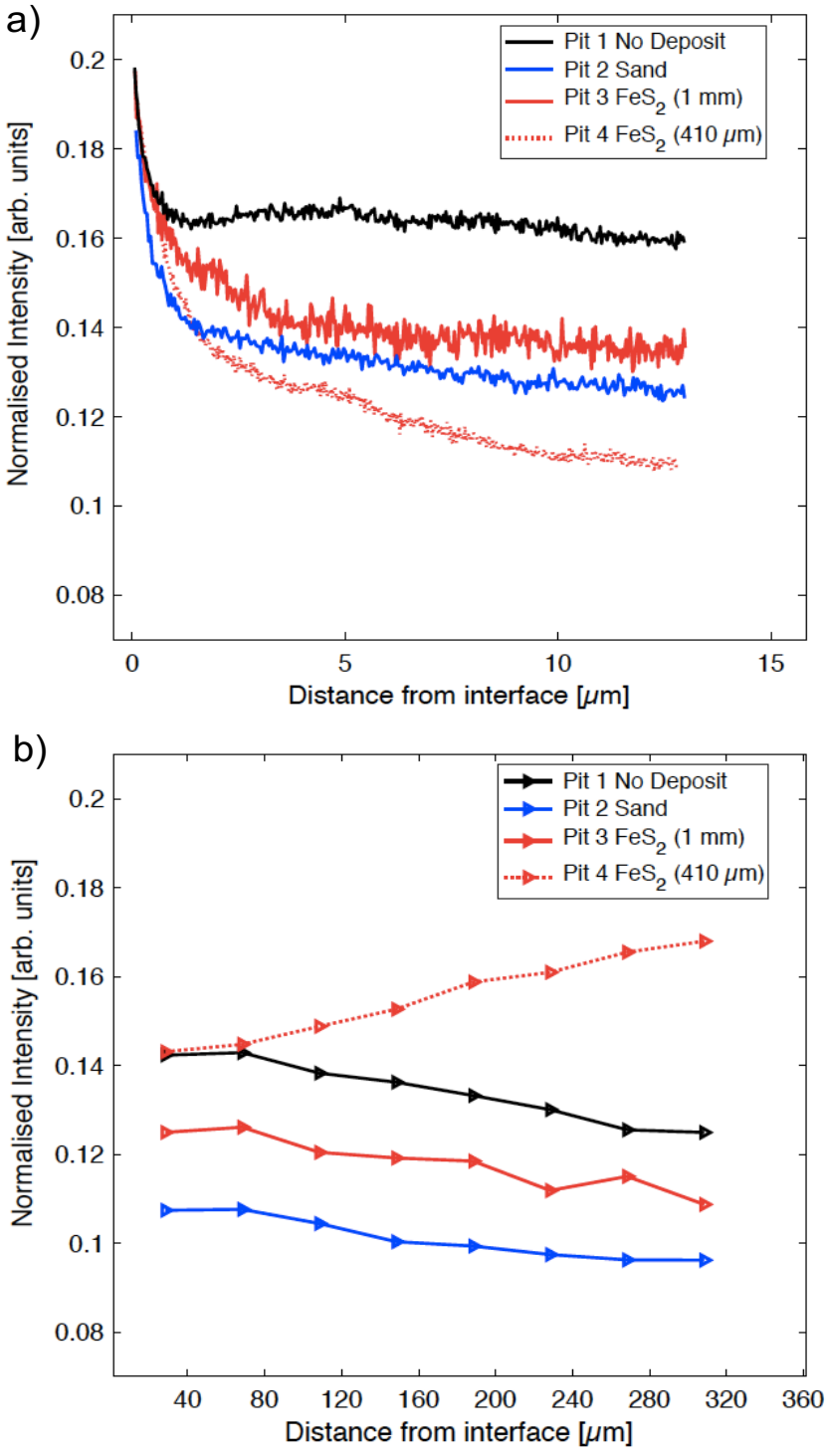

Figure 5-23 XRF intensity profiles inside corroding pits in absence of deposits and in presence of sand and FeS_2 at the pit mouth; (a) Fixed-point XRF scans recording few microns above the interface, and (b) XRF line scans across the pit solution, starting from 50 μm above the salt film at a 40 μm step size. The raw data (camera coordination) are corrected to show the distance.

Figure 5.24 shows point XRF intensity measurements at 30 μm below the pit mouth. Unlike the intensity profiles in Figure 5.23, this figure shows a rather increased concentration of iron ions, indicating a retention of ionic species inside the pit when deposits were applied. The ionic retention increases the solution resistance, and in accordance the precipitation of salt films with a larger density. This is assumed to be the reason for such a change in the XRF intensity lines above the interface, *i.e.,* the denser the salt film, the lower the concentration of iron ions in the pit solution.

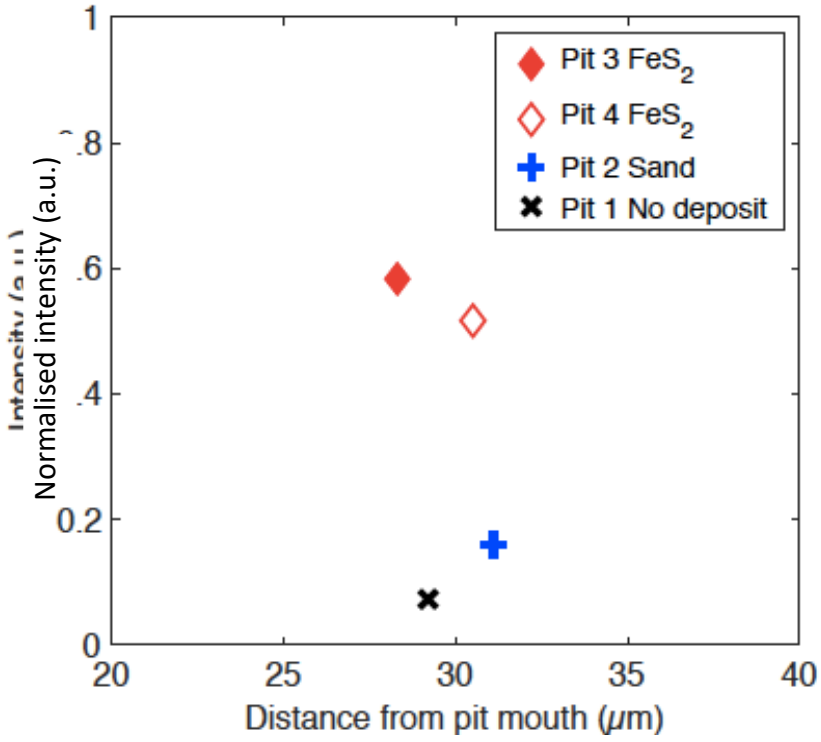

Figure 5-24 Point XRF measurements at 30 μm below the pit mouth, in absence of deposits and in presence of sand and FeS_2 at the pit mouth.

In shallow pits, the short diffusion length facilitates interaction between the pit and bulk solutions, *i.e.,* the diffusion of ionic components to and from the pit. This interaction is obvious when the XRF scans of Pit 3 (1 mm) and Pit 4 (410 μm) are contrasted in Figure 5.23a. It is demonstrated that the shallow pit has lower concentration of iron ions above the interface, which indicates the presence of a denser and/or thicker film, with respect to the deeper pit.

At extended lengths above the interface, the XRF intensity is higher in the shallow pit under FeS_2 (Pit 4), see Figure 5.23b. This is because the inward diffusion of iron species from the FeS_2 deposit at the pit cavity was relatively easier, which increased the concentration of iron ions in the pit solution. The effect of the FeS_2 deposit decreases gradually from the pit mouth and inward. The deeper pit (Pit 3), on the other hand, was not affected by the deposit above

the cavity. This observation could be related to the domination competition between the pit depth (R2) and the applied deposit (R3), as previously explained in Section 5.2.1.6.3. This entails that when the pit is deep, deposits have a minimised effect on the pit kinetics. In this case, the addition of FeS_2 did not affect the localised kinetics at the pit bottom; it has rather impacted the general behaviour of ionic diffusion patterns as a whole. To conclude, the effect of applied deposits is dominant when the pit depth is small.

Figure 5.25 shows a schematic representation of the iron ions diffusion patterns inside the pit cavity, according to the findings of Figures 5.23 and 5.24. In the uncovered pit, represented with the black line in Figure 5.25, the iron ion concentration decreases gradually from the interface until it reaches the bulk solution concentration at the pit mouth. Where sand is applied (blue line), it imparts resistance to the ionic flow, and therefore, the iron concentration at the pit mouth is higher than in the case of the uncovered pit. The behaviour of Pit 3 (deep pit) and Pit 4 (shallow pit) under pyrite are combined in one pattern (red line), demonstrating a high iron concentration at both the pit bottom and mouth, with the lowest iron concentration is at an equilibrium point inside the cavity. The represented diffusion patterns outside the cavity, through the deposit and the bulk solution, are just speculative and have not been studied in this work.

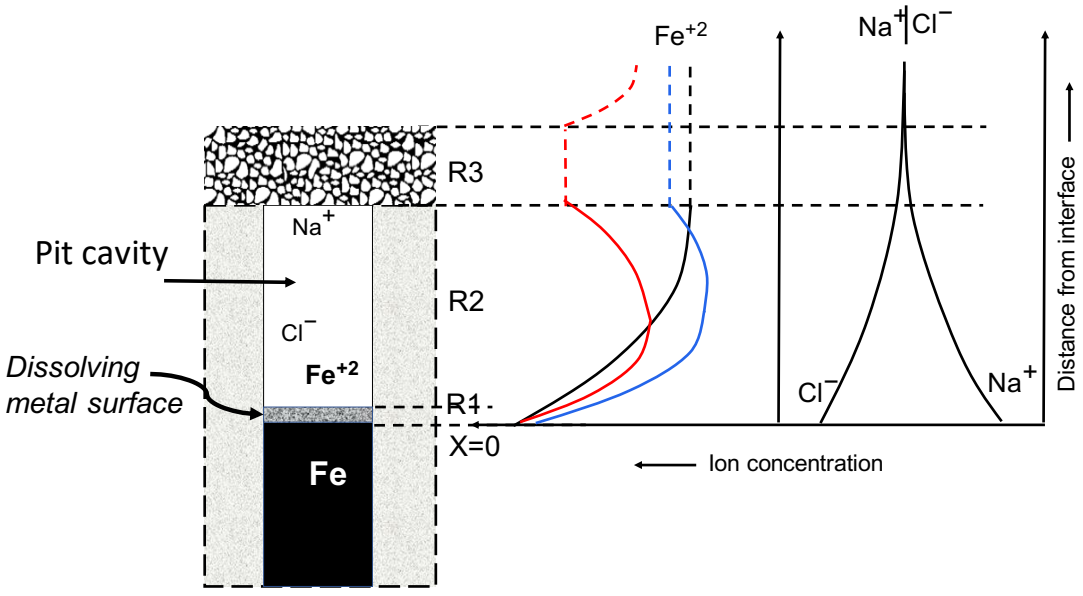

Figure 5-25 A schematic representation of the diffusion profiles inside artificial pits corroding in absence of deposits (black), and under sand (blue) and FeS_2 (red). The dashed profiles of diffusion outside the pit are just speculative. The pit depth is assumed constant.

5.2.3.2 Salt film structure and thickness during diffusion-limited dissolution

A typical XRD across the metal interface in the pit

In a similar way as the XRF line scan, the structural phases of the salt layer at the metal-solution interface were recorded by performing XRD line scan with a vertical interval of 2 μm and 20s acquisition time. Figure 5.26 shows the typical stack plot of diffraction patterns recorded at the metal-solution interface of artificial pits; this case is for a shallow pit (pit depth ~650 μm) with no deposit above the pit cavity. It also demonstrates a crystalline metal salt ($FeCl_2.4H_2O$) structure.[37] A metallic peak was present at 2theta=25.1°, and a few very week peaks were visible in the solution above the salt layer.

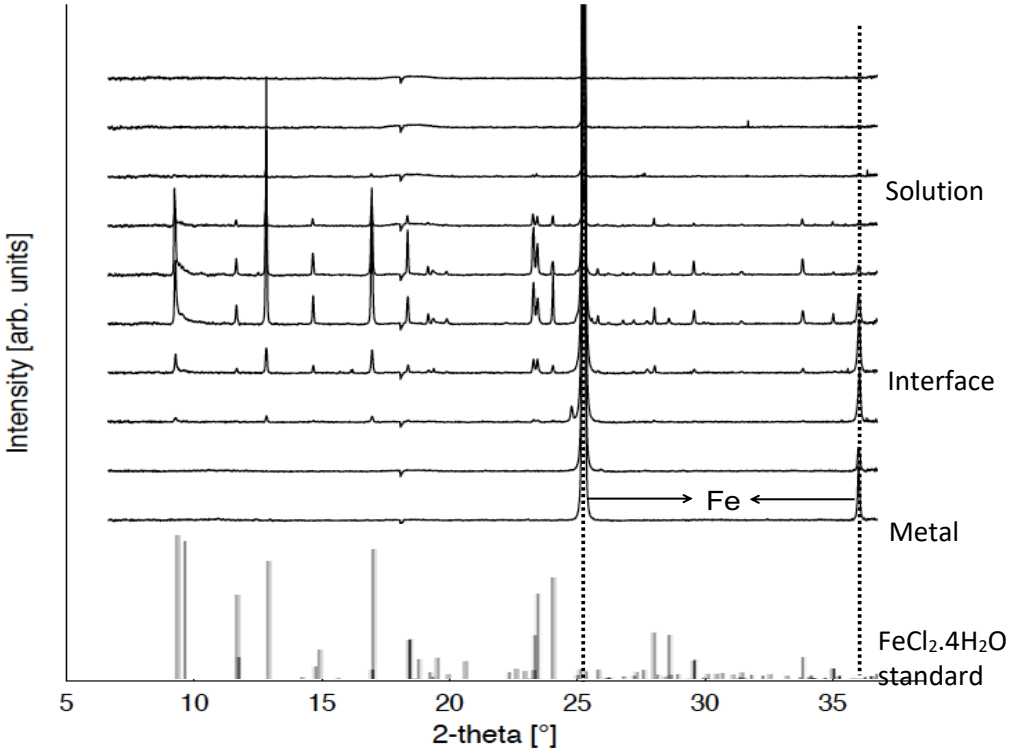

Figure 5-26 A stack plot of XRD patterns for a dissolving interface in an Fe aritificial pit collected using an XRD scan at 2 μm intervals, and overlayed with an $FeCl_2.4H_2O$ standard pattern. This pit is ~650 μm deep with no deposit present above the pit cavity.

Effect of applied deposits

An $FeCl_2.4H_2O$ pattern has been consistently identified in all the interface slices when sand and FeS_2 were physically incorporated at the pit cavity opening, as shown in Figure 5.27. The no-deposit case's XRD absolute intensity was higher than the sand and the FeS_2 cases, in agreement with the XRF result. Despite observing a sulfur-containing film during the *ex-situ*

SEM-EDS analysis of the pits in both the FeS_2 and H_2S cases (Figures 5.16 and 5.17), no signs of sulfur species were detected in the *in-situ* XRD measurements. The sulfur species inside the pit are thought to have depleted during the initial stages of pit propagation, and the inward diffusion of more species from the bulk solution is limited by the continuous outward flow of dissolved Fe ions. This effect has possibly inhibited the reaction between the sulfur and iron species at the metal interface.

Cycling the pit in earlier *ex-situ* electrochemical measurements involved multiple processes of metal dissolution, supersaturation and precipitation of salt films. Therefore, sulfur rich residuals could have formed at the metal after the reaction had finished. However, in the *in-situ* experiment, where the pit was continuously under a high applied potential, a salt film existed at the continuously dissolving interface, preventing precipitation of other films at the metal surface. Hence, it could be argued that the observed sulfur-containing films in the SEM/EDS were formed during the handling process after the dissolution had stopped. On the other hand, since the pit was previously cycled, any formed films might have dissolved at the start of the reaction, and hence could not be detected in the X-ray measurements.

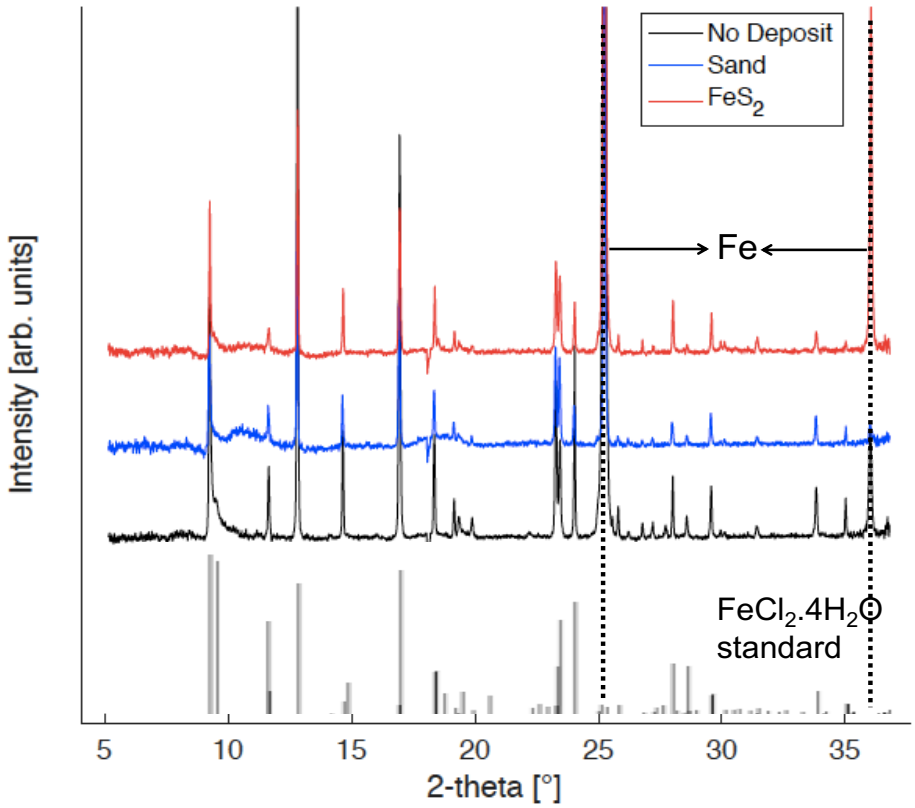

Figure 5-27 XRD patterns of the salt film of dissolving Fe artificial pit in absence of deposit and in presence of sand and FeS_2, as compared to the $FeCl_2.4H_2O$ standard pattern. The applied potential is +0.8 V (Ag/AgCl) and the bulk solution is 0.5 M NaCl. The same pattern was observed with shallow and deep pits.

5.2.3.2.1 Salt film thickness using XRD

The number of interfacial steps in the XRD stack plots, e.g. Figure 5.26, can provide estimates of the salt film thickness by multiplying it by the step size. This provides underestimated values because of the continuous recession of the metal surface in an opposite direction to the scan. Therefore, the thickness was corrected with the distance that the pit recessed during the interface XRD measurement. The recession distance was calculated from both the rate of surface corrosion and the time of salt film acquisition. Table 5.3 details the variables used to measure the salt film thickness; the number of salt film XRD steps, time of salt film XRD acquisition, and the corrosion rate in each of the studied cases.

The diffraction patterns in Figure 5.26, for the no deposit aerated control pit, presented five steps that indicated a crystalline metal salt phase. As illustrated in the table, this is equivalent to 10 μm in thickness. Since the pit was continuously growing, the time of the interface measurement was recorded (100s) and multiplied by the experimentally measured corrosion rate, *i.e.,* the speed of pit recession (0.032 μm/s) to estimate the distance recessed during the XRD interface acquisition. The final thickness after combining both components of the distance, was concluded to be ~13.0 μm for the no deposit aerated pit.

Table 5.3 The salt film thickness measurements from the XRD scan plots, corrected with the distance recessed during the interface measurement. The step size is fixed to 2 μm.

	Depth (μm)	Interface steps	Thickness from steps (μm)	Interface measurement time (s)	Recession speed (μm/s)	Distance recessed (μm)	Total thickness (μm)
No Deposit (Shallow)	625	5	10	100	0.032	3.25	13.24 ± 1.00
Sand (Pit 2)	845	3	6	60	0.043	2.57	8.57 ± 1.00
FeS_2 (Pit 3)	1000	3	6	60	0.030	1.81	7.81 ± 1.00
No Deposit (Deep)	2350	5	10	100	0.015	1.55	11.55 ± 1.00

From the table, the addition of deposits seems to reduce the salt film thickness, where it previously showed lower XRF intensities, *i.e.,* iron concentrations. A deep pit with no deposit was also tested to measure the salt film thickness. Despite the large increase in pit depth, the salt film thickness has only decreased slightly. Therefore, it is suggested that, in the cases of sand and FeS_2, with medium pit depth, the significant decrease in the salt film thickness is attributed to the deposit effect, rather than the increase in pit depth.

Figure 5.28 represents schematically the diffusion profiles of iron ions inside the pit cavity, assuming linearity. In the same way explained above with the XRF results, the addition of deposits increases the iron ion concentrations near the pit mouth. This decreases the overall concentration gradient, and the diffusion of newly dissolved iron ions to the pit solution is thought to be hindered. This is hypothesised to limit the process of building up thicker salt films. The same effect holds, although in a smaller way, with long diffusion distances of deep pits. The high resistance during CV in the case of longer depths, sand, and FeS_2 (highest with FeS_2), indicates a lower amount of dissolution was required to achieve supersaturation. It is, therefore, assumed that a denser salt film with lower thickness is formed in these cases.

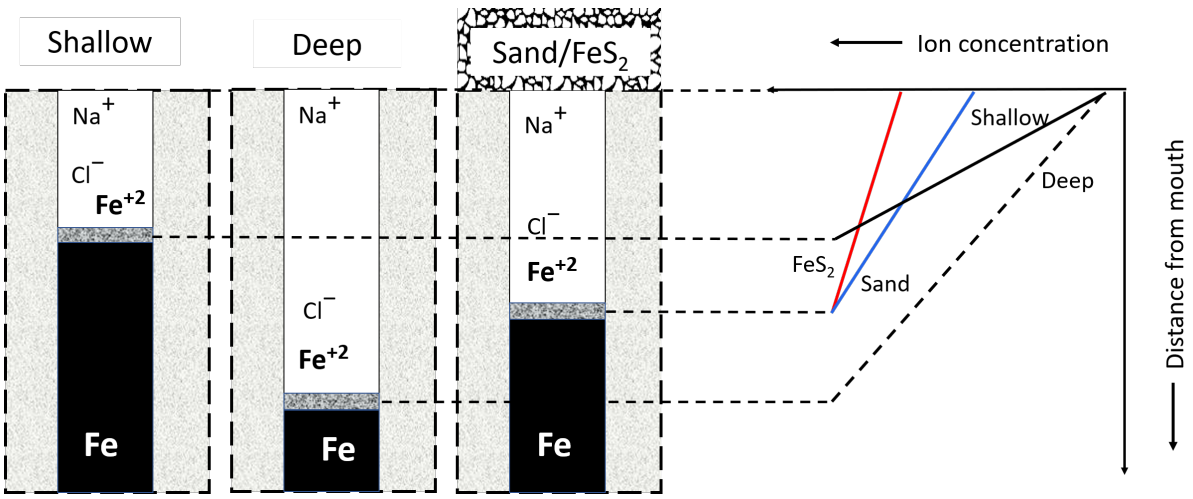

Figure 5-28 A schematic representation of the concentration gradient of iron ions inside iron artificial pits. The represented cases are: a shallow pit with no deposit (solid black), mid-deep pits with sand (blue) and FeS_2 (red), and a deep pit with no deposit (dashed black) at the pit mouth. Diffusion is assumed to be linear.

5.2.3.3 Fe spectroscopy at salt films under diffusion-limited conditions

XANES spectra were acquired at the dissolving interfaces and mouths of pits growing under diffusion-controlled conditions in absence of deposit and in presence of sand and FeS_2. The absorption edge positions were compared to that of the reference materials to examine the oxidation state.

5.2.3.3.1 XANES spectra of reference materials

A series of reference materials was selected to encompass the species likely to be found inside the pit. XANES spectra collected for the reference materials are shown in Figure 5.29. All the spectra were calibrated according to the inflection point of iron at 7112 eV. While the metal foil was measured in transmission, all the other reference standards were measured in fluorescence.

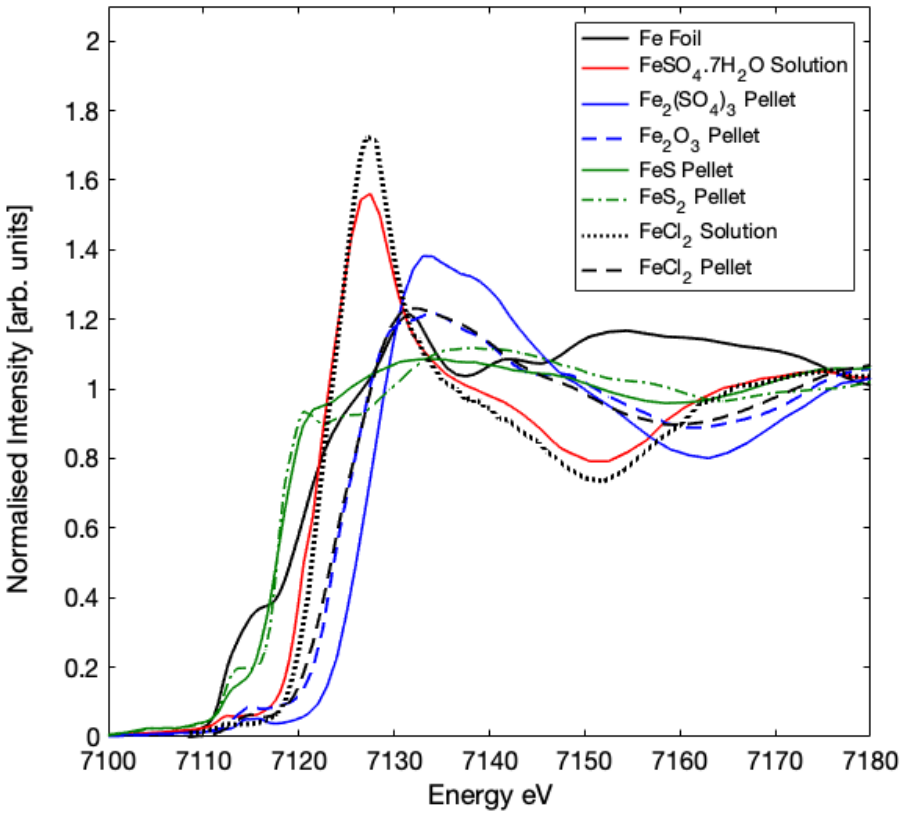

Figure 5-29 Normalised Fe K edge absorption spectra for reference materials: iron foil (Fe°), $FeSO_4.7H_2O$ (solution, Fe^{+2}), $Fe_2(SO_4)_3$ (solution, Fe^{+3}), Fe_2O_3 (powder, Fe^{+3}), $FeCl_2$ (solution and powder, Fe^{+2}), FeS and FeS_2 (powders, Fe^{+2}). All the spectra were measured in fluorescence except the iron foil, measured in transmission.

5.2.3.3.2 Fe XANES under different deposits

A. Pit interfaces

XANES spectra were fitted using a linear combination of the standard spectra to determine the oxidation state of the iron species in the pit. The fit results and weights are illustrated graphically, as shown in the absorption spectra presented in Figure 5.30, indicating various percentages of Fe (II) species. While only $FeCl_2$ and $FeSO_4$ standards were fitted in all the measured cases, the FeS standard was also present in the pyrite measurement fit. The observation of FeS species during the XANES measurement in Figure 5.30c indicates an *in-situ* formation of iron sulfides inside the pit, though with small quantities. The previously explained XRD did not show characterising peaks of iron sulfides, which could be partly due to their amorphous nature and their small amounts with respect to the crystallised iron chloride. Therefore, it was helpful to use different X-ray measurement techniques to complement the results.

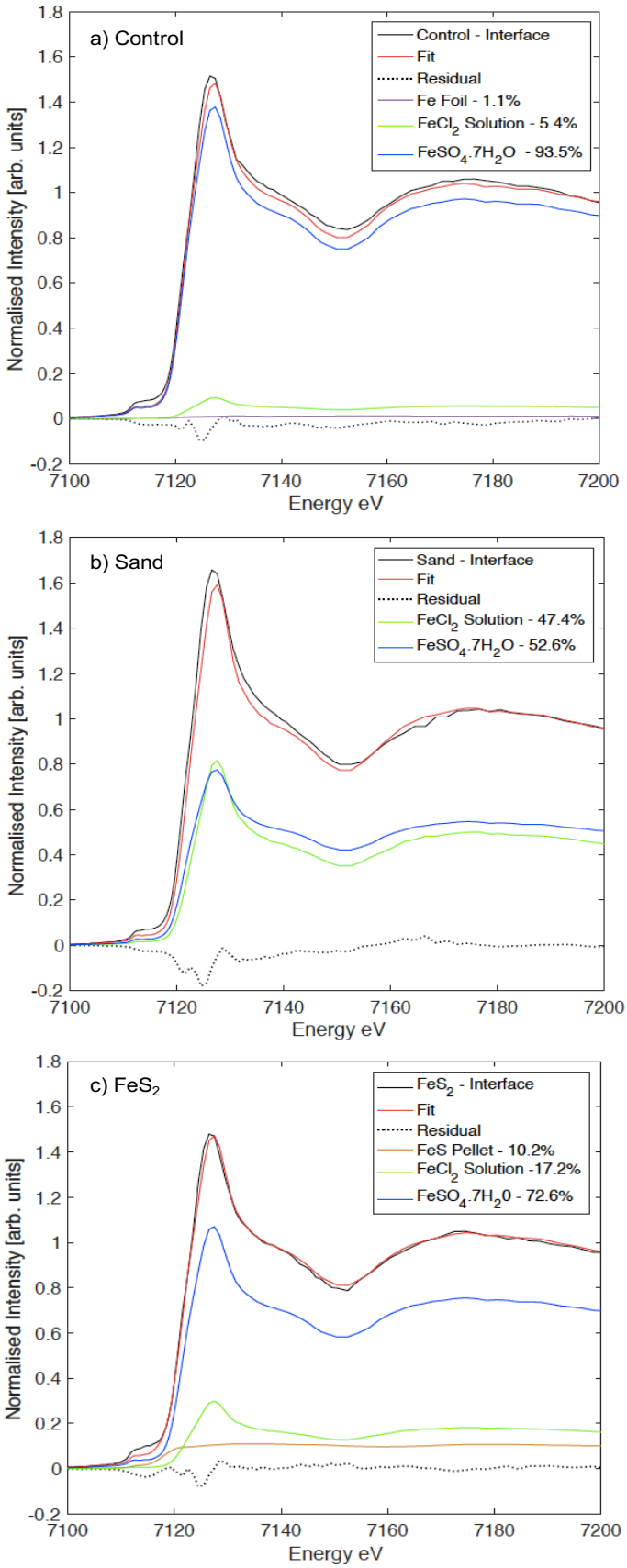

Figure 5-30 XAS spectra of the dissolving interface of artificial pits under different deposits: (a) in absence of deposit, (b) in presence of sand, and (c) in presence of FeS_2. Spectra are overlaid with best-fit results obtained by a linear combination of relevant reference materials. The data shows Fe (II) species to be solely present with some FeS standard inside the FeS_2 covered pit.

B. Pit mouths

XANES measurements were also obtained at the pit mouth. The fit results and weights are illustrated graphically in Figure 5.31, indicating $FeCl_2$ (II) as the major speciation. In the absence of deposits, represented in Figure 5.31a, $Fe_2(SO_4)_3$ (III) reference was present with a considerable weight. This could be attributed to the oxidation of Fe (II) to Fe (III) at the pit mouth due to oxygen ingression. When the deposit was present, oxygen diffusion was limited, and therefore, Fe (III) content was hardly observed under sand. In the case of pyrite deposits, the Fe (III) contribution was relatively high (~7.4%). Due to diffusion limitation, Fe (III) presence can be attributed to the oxidation of Fe (II) from the pyrite itself rather than the steel pit, due to closeness to the bulk oxygen. FeS_2 (II) standard was present in the XANES fit of the under-pyrite pit mouth.

In Figure 5.32, the edge energy and white line intensity at both the pit mouth and interface are contrasted. A positive shift in the edge energy is exhibited with all the cases of pit mouth measurements, with a higher degree when deposits were absent. This is indicative of a more oxidised iron Fe (III) content since the oxygen content is higher at the pit mouth than at the bottom. The maximum absorbance is also higher at the interface because of the high concentration of iron at the pit bottom except in the case of FeS_2, which is due to the presence of iron-rich deposit above the pit mouth.

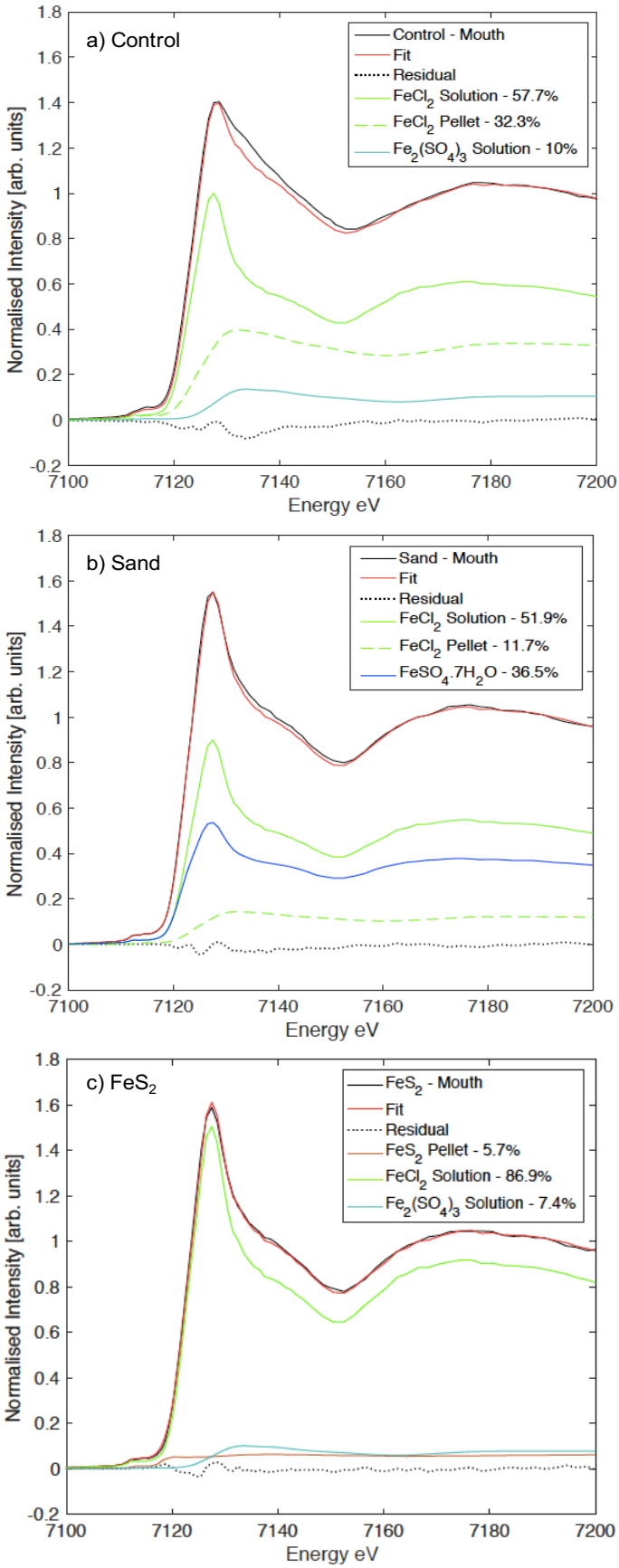

Figure 5-31 XAS spectra at the mouth solution of artificial pits under different deposits(a) in absence of deposit, (b) in presence of sand, and (c) in presence of FeS_2. Spectra are overlaid with best-fit results obtained by a linear combination of relevant reference materials.

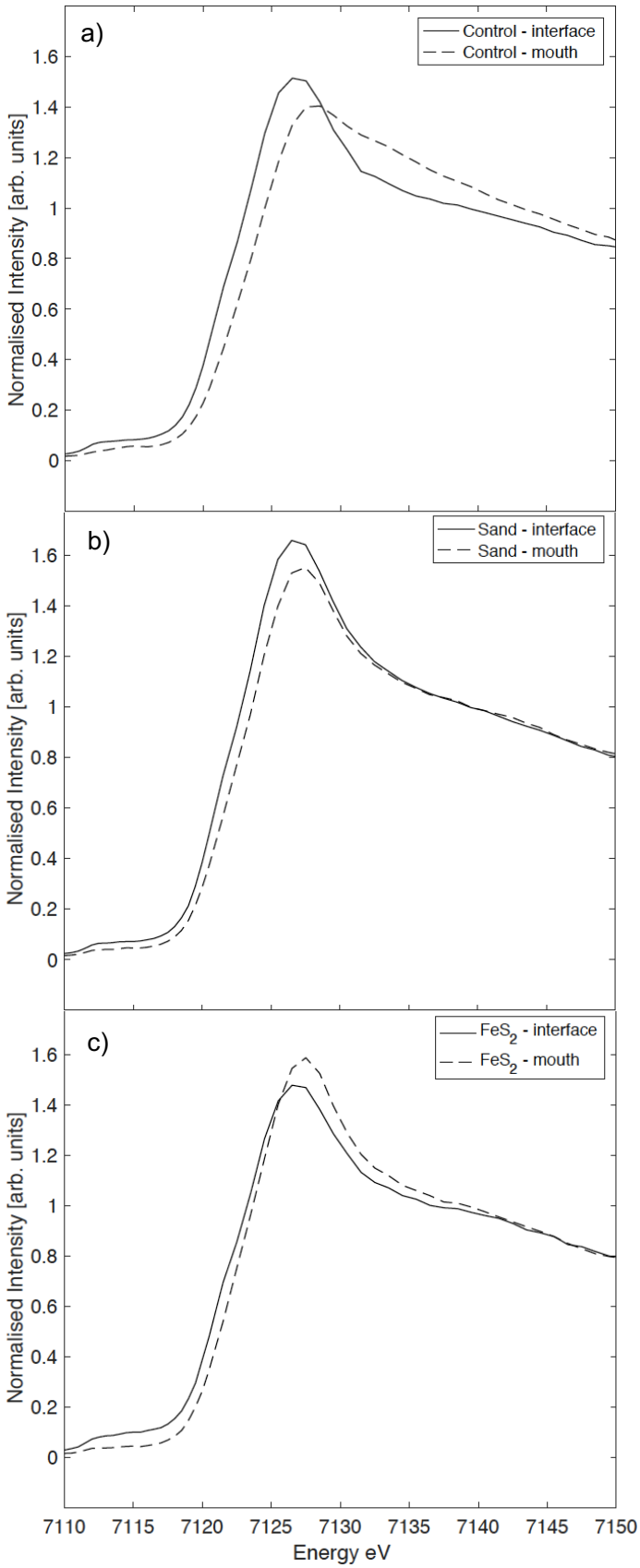

Figure 5-32 Normalised Fe K edge spectra (measured in fluorescence) comparing between the interfacial salt film (solid line) and the solution at the pit mouth (dashed line) of artificial pits corroding at +0.8 V (Ag/AgCl) in a 0.5 M NaCl solution in absence of deposit (a), and in presence of sand (b) and FeS_2 (c).

5.3 Summary and conclusions

Artificial pits have been reported in the literature to be an effective tool in studying the localised corrosion kinetics such as the mass transport and the solution chemistry within pits.[34–37] Galvele's model[38] of mass transport calculated the conditions required for stable pitting. Further experiments by Isaacs and co-workers revealed that the phases present in the salt film vary through their thickness, and that the metal ions have different chemical coordination environments depending on their proximity to the dissolving surface.[34–36,59,60,102–105] None of the reported studies, however, were carried out in the presence of external deposits that may affect transport significantly.

In our study, artificial pits were successfully constructed, and electrochemical measurements were used alongside a multitude of *ex-situ* and *in-situ* measurements to study the dissolution kinetics of iron pits under deposits. When subjected to high applied potentials, artificial pits grow unidirectionally under diffusion-limited conditions, with a salt film precipitating above the dissolving interface. Changing the physical and chemical properties of deposits applied above the pit cavity as well as the pit depth were found to be directly affecting the kinetics of dissolution and the process of salt film formation. Sand and iron sulfides (troilite and pyrite) were used in this study to represent typical sour pipeline environments.

Control experiments, in the absence of deposits, showed that increasing the ionic diffusion length, *i.e.,* the pit depth, stabilises the pit growth at a slower rate. Deep pits, despite showing slower corrosion kinetics identified by lower i_{lim} values, needed only smaller amount of dissolution to form the aggressive chemistry of salt films. Hence, deeper pits propagate more stably. This is consistent with the diffusion-controlled model of pit growth and Fick's law, where the current is inversely proportional to the diffusion length.[34,35,106]

When deposits were applied, an extra barrier against ions diffusion was introduced. The deposit impedes the passage of ions outside the pit and creates tortuous paths for ions transport, which increases the diffusion length and R_s that causes a decrease in i_{lim}. The magnitude of decrease in i_{lim} is dependent on the deposit physical properties and type. Lower porosity and/or thicker deposit layers have a higher effect on stabilising the propagation kinetics, but there is a threshold point beyond which further thickness increase seems to have a negligible effect. This process is dependent on the deposit chemistry.

Deposits composed of reactive iron sulfides were found to result in remarkably lower limiting currents required for continued pit growth. Despite the sluggish kinetics indicated by low i_{lim}, the pit propagation is more stable. The high reprecipitation and transition potentials as well as the high pit solution resistance in the case of iron sulfides implies that, in addition to their typical physical barrier, a more corrosive local chemistry was formed due to the deposit

chemistry. Post-reaction characterisation of the interface surface using SEM-EDS and Raman spectroscopy revealed a mixture of iron oxides and sulfides. Elemental sulfur was also occasionally present when pyrite was used. The different morphology can be correlated to the decrease in i_{lim} as well as the increase in Rs, and the newly formed films are expected to provide an extra ionic diffusion barrier at the bottom of the pit. Deep pits were not affected to a large degree by changing the deposit characteristics, hypothesising a domination competition between the different variables involved: pit depth and deposit.

The electrochemistry measurements and the *ex-situ* surface analysis could not provide details on the chemical alterations that drove such electrochemical and morphological changes. *In-situ* synchrotron XANES, XRF and XRD techniques were, therefore, used to characterise the salt film and pit solution inside actively dissolving pits. The ionic diffusion profiles, revealed by XRF scans at the interface, indicated a decrease in the iron concentration in the pit solution above the salt film. This confirms the electrochemical findings of lower i_{lim} and higher Rs values when deposits are incorporated at the pit cavity.

Supporting our previously mentioned hypothesis of depth–deposit domination competition, the effect of applied deposits was proven by XRF to be dominant when the pit depth is small. The retention of ionic species inside the pit due to the deposit's blockage effect was evidenced using point XRF measurements at the pit mouth, which indicated higher concentrations of iron ions. Accordingly, the concentration gradient inside the pit decreases with deposits, reducing the driving force to build thicker salt films, which eventually leads to thinner films that are assumed to be denser. The salt film was identified using *in-situ* XRD as $FeCl_2.4H_2O$, with no sign of sulfide presence. The thickness was determined by performing XRD line scans, with an identified vertical interval, across the metal interface: the addition of deposits was found to reduce the salt film thickness significantly, and it only slightly decreased in deep pits.

Complementary XANES spectra at the dissolving interface showed that the positions of the absorption edge fit well with the iron oxidation state +2, with a small contribution of the FeS standard found when pyrite was present. This supports the SEM observations of the surface that showed sulfur-rich films. The use of a series of diverse analytical tools helped providing valuable insights into the UDC phenomenon. A future direction to extend the work presented in this chapter, is to run additional synchrotron experiments to further support the findings from our proposed study.

6 Localised and general corrosion in sour environments

6.1 Introduction

The corrosion behaviour of under-deposit planar coupons and artificial pits were explored in the previous two chapters to establish a basic understanding of UDC in aerated and N_2 environments. The effect of deposits was thoroughly investigated using electrochemistry and both *ex-situ* and *in-situ* characterisation techniques. In this chapter, H_2S, as an active gas, was introduced to the same systems, where both general and localised corrosion kinetics were investigated using the same methods and characterisation tools.

The presence of H_2S adds a relative complexity to the chemical and electrochemical reactions of steel corrosion due to additional cathodic reactions, adsorption on the steel surface, and the formation of different iron sulfides.[159] In an aqueous environment, the following H_2S dissociation reactions can take place:

$$H_2S_{(g)} \rightleftharpoons H_2S_{(aq)} \quad (6.1)$$

$$H_2S_{(aq)} \rightleftharpoons HS^-_{(aq)} + H^+_{(aq)} \quad (6.2)$$

$$HS^-_{(aq)} \rightleftharpoons S^{2-}_{(aq)} + H^+_{(aq)} \quad (6.3)$$

A saturated aqueous solution of H_2S was reported to have a pH of ~4.0 at room temperature owing to the acidic nature of H_2S (pK_{a1} = 6.98).[160] At the cathode under such acidic conditions, hydrogen evolution is the dominant reaction, which is often limited by mass transport of H^+ to the steel surface. A direct reduction of H_2S can also contribute an additional wave of current according to the following reactions:

$$2H_2S_{(aq)} + 2e^- \rightleftharpoons 2HS^-_{(aq)} + H_{2\,(g)} \quad (6.4)$$

$$HS^-_{(aq)} + e^- \rightleftharpoons S^{2-}_{(aq)} + \tfrac{1}{2} H_{2\,(g)} \quad (6.5)$$

At the anode, it was reported that aqueous H_2S has a catalytic effect on the anodic dissolution of the steel upon its adsorption on the surface.[161] A direct chemical reaction between dissolved ferrous ions and sulfide ions can take place to precipitate a new iron sulfide film.[159]

$$Fe + HS^- \rightleftharpoons FeHS^-_{(ad)} \quad (6.6)$$

$$FeHS^-_{(ad)} \rightleftharpoons FeHS_{(ad)} + e^- \quad (6.7)$$

$$FeHS_{(ad)} \rightarrow FeHS^+_{(ad)} + e^- \quad (6.8)$$

$$Fe^{2+}_{(aq)} + HS^-_{(aq)} \rightleftharpoons FeS_{(s)} + H^+_{(aq)} \quad (6.9)$$

In general corrosion systems using planar steel coupons, the newly formed iron sulfide layers can be protective to some extent against corrosion.[14,162] It is thought, however, that the presence of other pipeline deposits influences the successive formation of protective FeS and its integrity, which establishes a state where localised pits are formed at longer exposure time. The presence of deposits also affects the solution chemistry at the metal surface to various degrees due to the physical blockage effect or the chemical interaction with the applied deposit. This may cause the formation of different iron sulfide phases, different in their stoichiometry and morphology. The electrochemical behaviour of deposit-covered steel substrates and the newly formed FeS film properties were studied, in presence of different deposits in an H_2S-saturated 0.5 M NaCl solution. Moreover, the galvanic current between the steel and iron sulfide electrodes was monitored under the same conditions of H_2S gas saturation.

In the localised corrosion context, the presence of H_2S was studied for its effect on the transport kinetics of artificial pit electrodes. The salt film that forms at the metal surface and regulates the diffusion of ionic species can change its properties due to the incoming sulfide ions from the bulk solution. Accordingly, the corrosion kinetics and the pit solution chemistry are expected to change. The electrochemistry of artificial pits was studied using the protocol described in chapter 5, but with the introduction of H_2S in absence of external deposits to represent the case of chemically formed deposits inside the pit. With the artificial pits actively dissolving, *in-situ* X-ray microprobe analyses, XRF, XRD and XANES, were carried out to study the salt layer and the pit solution during anodic dissolution of Fe.

6.2 Results and discussion

6.2.1 Planar coupons under deposits

6.2.1.1 Open circuit potential (OCP) and potentiodynamic polarisation

OCP and potentiodynamic polarisation measurements can provide a comprehensive insight into the electrochemical behaviour of the metal as a function of the nature of the applied deposit. Both measurements were performed on steel coupons covered with sand and iron sulfides, as shown in Figure 6.1, to measure the corrosion kinetics in presence of an H_2S-saturated solution.

In both the bare and sand-covered steel electrodes, OCP readings reached close values after exposure to the H_2S saturated solution for 30 min, as in Figure 6.1a. Close OCP values indicate that at this short exposure time, the reaction kinetics were mainly controlled by the H_2S presence rather than the presence of inert deposits. The chemical reaction between H_2S and the iron ions leads to the formation of iron sulfide films on the surface, which is expected to be the reason behind the slight change in OCP.

Samples covered with reactive iron sulfide deposits exhibited lower OCP than the bare and sand-covered samples, with the troilite FeS case showing the lowest values of OCP. Accordingly, the FeS-covered samples comprise a less thermodynamically stable system that is more likely to corrode and participate in other reactions compared to the other cases.

According to the potentiodynamic polarisation plots in Figure 6.1b, all samples were subjected to pitting, directly upon the application of anodic potentials. The sand-covered samples exhibited, however, a slight positive shift in the corrosion potential, and the anodic current density was slightly decreased. Similarly, the corrosion potential of the pyrite case was slightly higher than the no-deposit control case. On the other hand, the steel electrodes covered with troilite presented a more negative corrosion potential with the anodic current being notably higher, suggesting a case that is more susceptible to pitting.

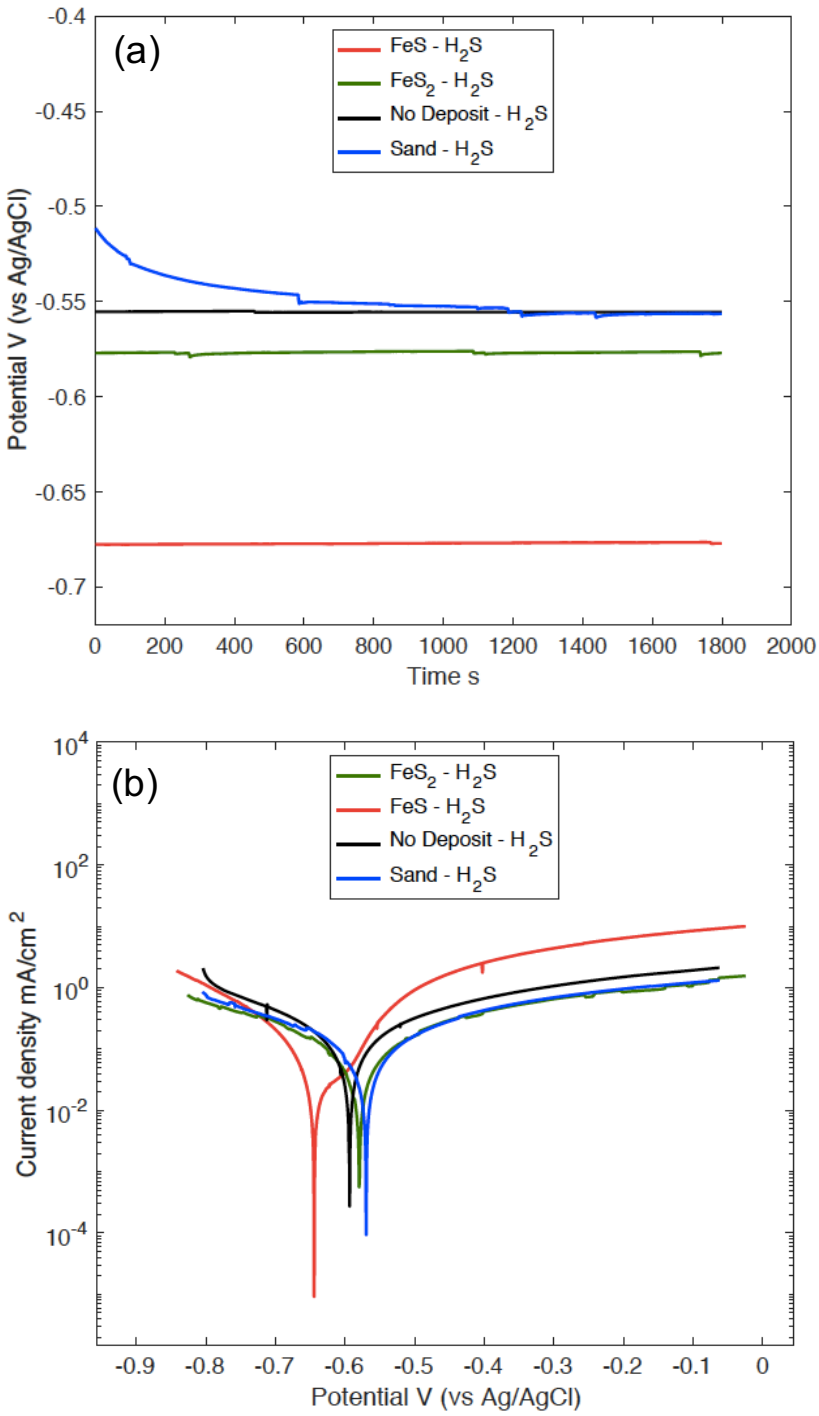

Figure 6-1 OCP vs. time (a), and Tafel polarisation (b) plots showing the effect of the deposit type in H_2S environment on planar surfaces covered with sand, FeS, and FeS_2. The electrolyte is a 0.5 M NaCl, at room temperature and atmospheric pressure.

The findings from the H_2S study were compared to those in the N_2-purged environment previously presented in chapter 4; Figures 6.2 and 6.3 compare the OCP and potentiodynamic sweeps, respectively. As shown in Figure 6.2a for the no-deposit and sand cases, the presence of H_2S formed a less active system indicated by a higher OCP, whereas it comprised a more active system when iron sulfides were present, as in Figure 6.2b.

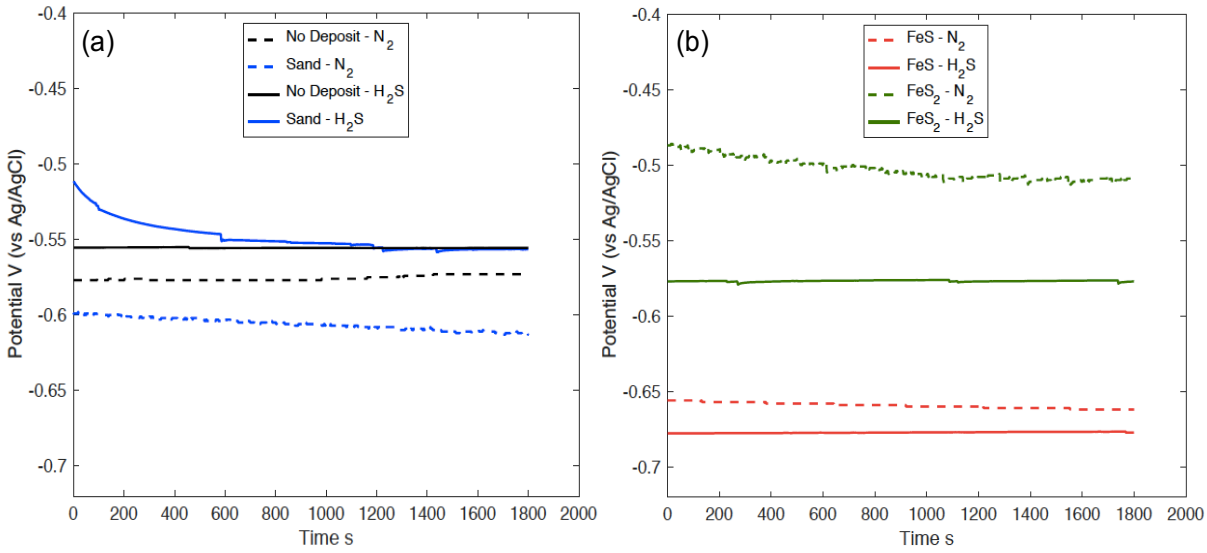

Figure 6-2 OCP vs. time plots recorded for planar coupons in H_2S environment (solid line) compared to the N_2-purged samples (dashed line) reported in chapter 4; (a) the bare and sand-covered samples and (b) with FeS and FeS_2 covered samples.

In Figure 6.3a, the positive shift in corrosion potential observed with H_2S as a result of inert deposit conditions is comparable to the observation from the N_2 environments. The pH of the bulk solution is lower in H_2S than it is in N_2, which demonstrates the higher corrosion currents in both cases of inert deposit presence and absence. However, the application of sand deposits when H_2S is present has lowered the corrosion currents, in contrary to the N_2 case where corrosion currents are higher in presence of sand.

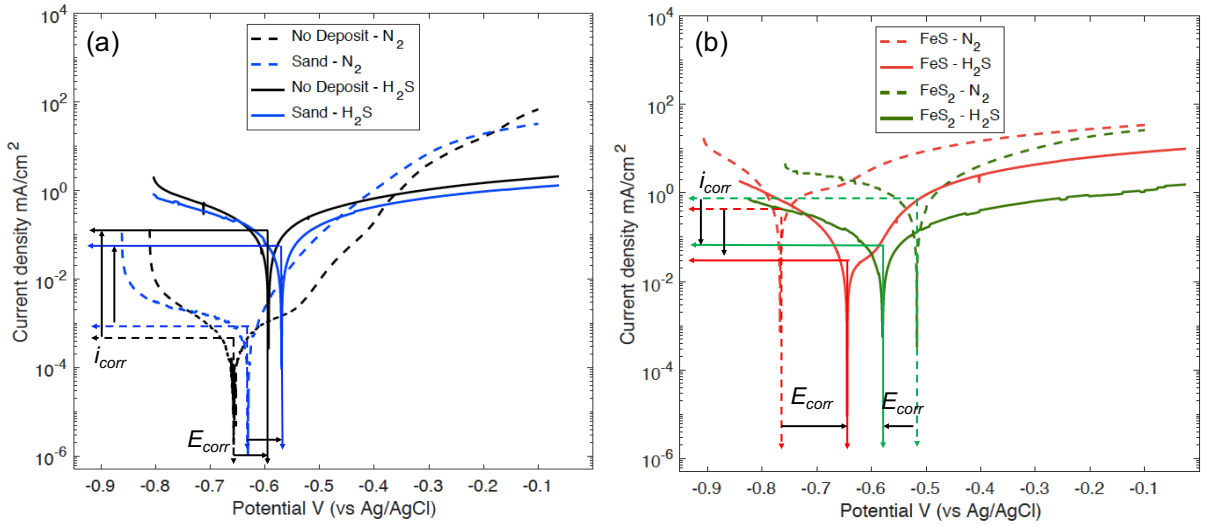

Figure 6-3 *Tafel polarisation plots recorded for planar coupons in H_2S environment (solid line) compared to the N_2-purged samples (dashed line) reported in chapter 4; (a) is the bare and sand-covered samples and (b) is for samples covered with FeS and FeS_2 deposits.*

The result agrees with previous investigations from the literature, where it was observed that the bulk solution pH has no effect in UDC in presence of sand due to the limited mixing between the local and bulk chemistry.[6] The literature study has also demonstrated higher pH values at the interface under sand deposits due to the reaction with H_2S to form iron sulfide films, and hence lower corrosion currents.

Newly formed iron sulfide films are typically thought to form on the steel surface as a result of reaction with H_2S, which adds another transport barrier, in addition to the physically applied sand deposits. Moreover, the chemically formed iron sulfide films are assumed to minimise the formation of aerated corrosion microcells under the deposit. This is considered to be the reason for the lower anodic currents, relative to the N_2 environment at higher applied potentials, where the reaction is limited by mass transfer. On the other hand, the chemically formed iron sulfide films are assumed to offer extra cathodic sites due to their semi-conductive nature. This is thought to drive the corrosion reaction rate, in a similar case to physically applying iron sulfides in N_2 environments, as described in chapter 4, section 4.2.1.3.

In the case of steel samples covered with iron sulfides, the corrosion potentials are indicated in Figure 6.3b, where the H_2S presence demonstrated a comparable observation to that of the N_2 purged. Pyrite showed a positive shift while troilite showed a negative shift with respect to the corrosion potential of the control no-deposit experiment. However, with respect to the N_2 counterparts, a negative shift in E_{corr} was observed with pyrite, and a positive shift with troilite. This contradicts the OCP measurements where a negative shift was observed when H_2S is introduced in both the cases of troilite and pyrite. This observation implies that the equilibrium was likely changed due to applying external potentials.

As explained earlier in chapter 4, the troilite changed its surface morphology (oxidised) upon applying external potentials, which was thought to relatively reduce its activity. Therefore, it can be assumed that during potentiodynamic polarisation, the troilite conductivity decreased, and therefore acted as a cathode at a lower degree, which shifted the overall E_{corr} anodically, *i.e.,* more positive. This observation implies that the cathodic reaction is not only controlled by O_2 reduction when active deposits are present.

The magnitude of the shifts, however, was less in the presence of H_2S. This assumes that the corrosion reaction of H_2S and steel brought the system kinetics closer to the control case by the formation of newly formed iron sulfides at the steel surface. In contrary to the inert deposit case, the cathodic and anodic currents were lower in the case of H_2S than with N_2, and hence iron sulfide-covered samples showed lower degrees of pitting susceptibility.

At high positive potentials in presence of H_2S, the reaction was no longer limited by mass transfer as in the N_2 case, since the anodic current was observed to significantly differ with

different deposits. This could imply that the newly formed iron sulfide films had different physical properties that varied their blockage effect: a denser film under pyrite. Validating this hypothesis can be facilitated by using SEM imaging of the surface morphology, as will be explained in following section.

6.2.1.2 Film formation under deposits

6.2.1.2.1 Morphology using SEM

The change in the electrochemical behaviour as a result of applying deposits indicates a change in the surface morphology. The steel surface was examined by SEM after open circuit exposure conditions for 4-6 h in H_2S-saturated solution. Figure 6.4 presents a control case in the absence of deposits contrasted against the under-sand cases, both coarse- and fine-sized. In the bare steel case, as in images (a) and (b), films with a flower-like structure were barely observed at higher magnifications, with the presence of a micron-sized pitting structure at the steel surface. The surface films in this case could not be easily viewed except at higher magnifications, indicating that the film might have been dissolved in the solution so that only remnants of it were left behind.

The continuous injection of 100% H_2S gas into the solution essentially led to higher H_2S concentrations, decreasing the bulk solution pH. Under open circuit conditions, H_2S purging is reported to form loose mackinawite or amorphous ferrous sulfide films at the surface.[22,163] Since there were no deposits limiting the mixing with the low-pH bulk solution, the formed iron sulfide films are expected to dissolve or delaminate, which is not contributory to the inhibiting effect. Therefore, pitting corrosion was easily observed, which also justifies the high anodic currents observed with the no-deposit case compared to the sand samples.

In Figure 6.4 (c and d), where a coarse sand layer was applied with 5 mm thickness, a flower-like structure was observed similar to, yet denser than, the no-deposit case. This structure is typically reported in the literature to be for mackinawite. Different morphologies (framboid and etched structures) were observed when the fine-sized sand was present, as shown in Figure 6.4 (e-h). The electrochemistry of steel covered with fine sand is not included in this study, and therefore, a correlation to the surface morphology cannot be established.

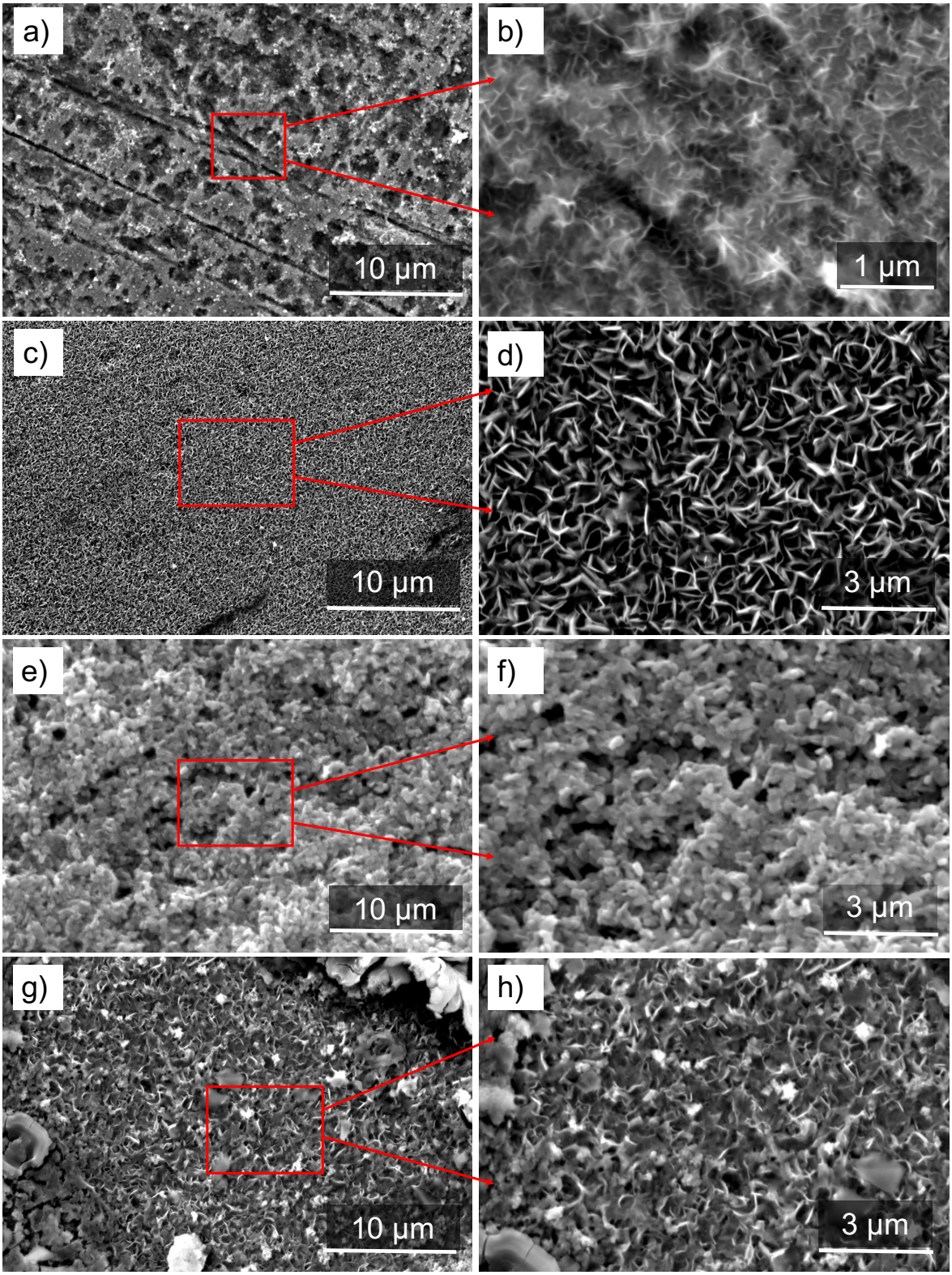

Figure 6-4 SEM micrographs of steel surfaces corroded under open circuit exposure conditions in a 0.5 M NaCl solution saturated with H_2S for 4h, representing the control sample in absence of deposits (a and b), and covered with coarse sand (c and d), and fine sand (e-h).

Other morphologies were also occasionally observed when coarse sand was present at the steel surface, as shown in the SEM images of the surface films in Figure 6.5. A mixture of the typical flower-like morphology and a sulfur-rich framboid structure is presented in images (a) and (b) at two different magnifications. Images (c) and (d) show the two different morphologies uniformly formed at two separate locations on the steel surface. It is possible that the deposit packing was not homogeneous, especially with the large size of particles. The different packing is expected to result in different local chemistries by changing the diffusion of both sulfide and ferrous species to and from the steel surface. Eventually, the steel had various reactivities, and hence obtaining corrosion products that are different in stoichiometry, and accordingly in morphology.

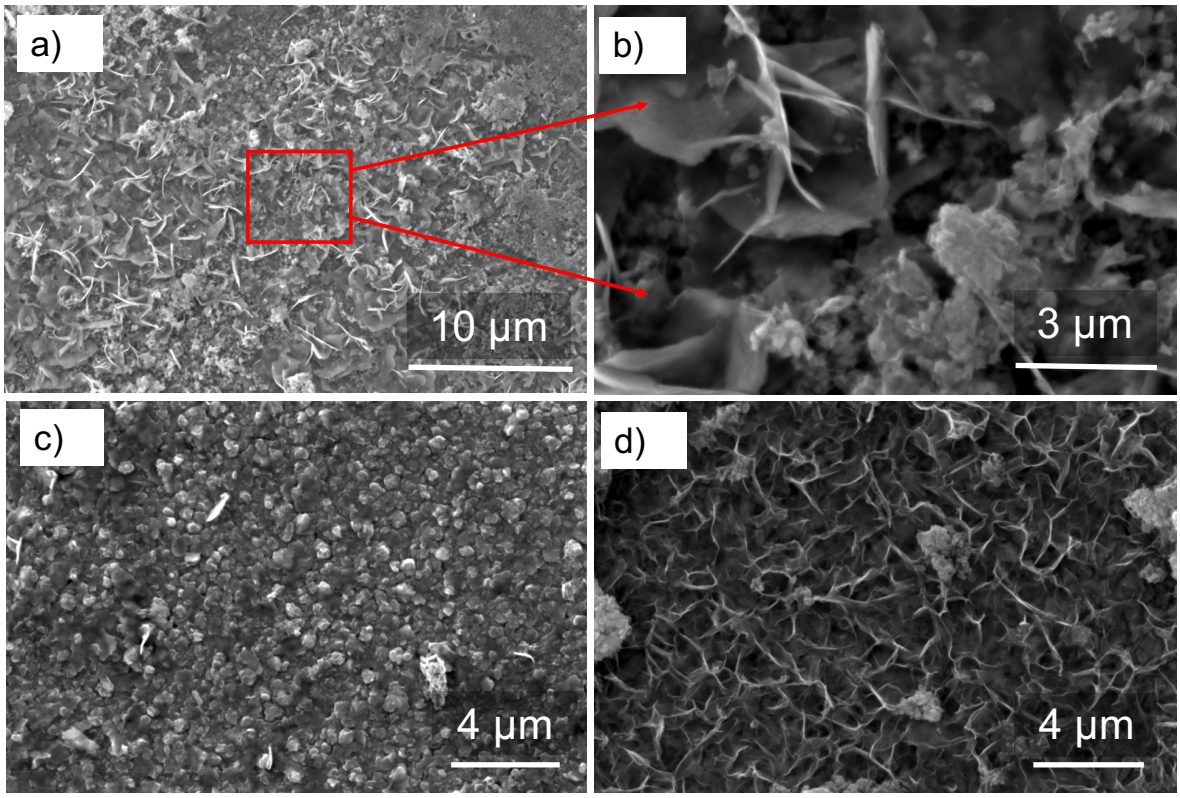

Figure 6-5 SEM micrographs of occasionally observed surface morphologies of steel corroded whilst covered with coarse sand under open circuit exposure conditions in a 0.5 M NaCl solution saturated with H_2S for 4h. (a) an area of mixed morphology with a magnified view in (b). (c) and (d) represent separately the two observed morphologies.

The presence of iron sulfides on the steel surface resulted in two different morphologies, as shown in Figure 6.6. In the case of troilite, the typical morphology of newly formed iron sulfide films was absent, as in Figure 6.6 (a and b). EDX measurements also showed smaller traces of sulfur with troilite, compared to all the other studied cases that exhibited a tangible sulfur content in the film. However, EDX is not a reliable measurement of stoichiometry and cannot provide conclusive remarks on the phases produced. The low OCP of troilite-covered steel,

accompanied with the high anodic current (Figure 6.1), explain the observation of large degrees of surface deterioration. On the other hand, a flake-like structured film with relatively large features was consistently observed in the case of pyrite, as shown in Figure 6.6 (c and d). The film produced under pyrite is, therefore, expected to be protective, decreasing the surface corrosion rate, as explained by the low anodic current in Figure 6.1. The observation here is consistent with the findings of the N_2-purged environment where troilite is more corrosive whilst pyrite is more protective.

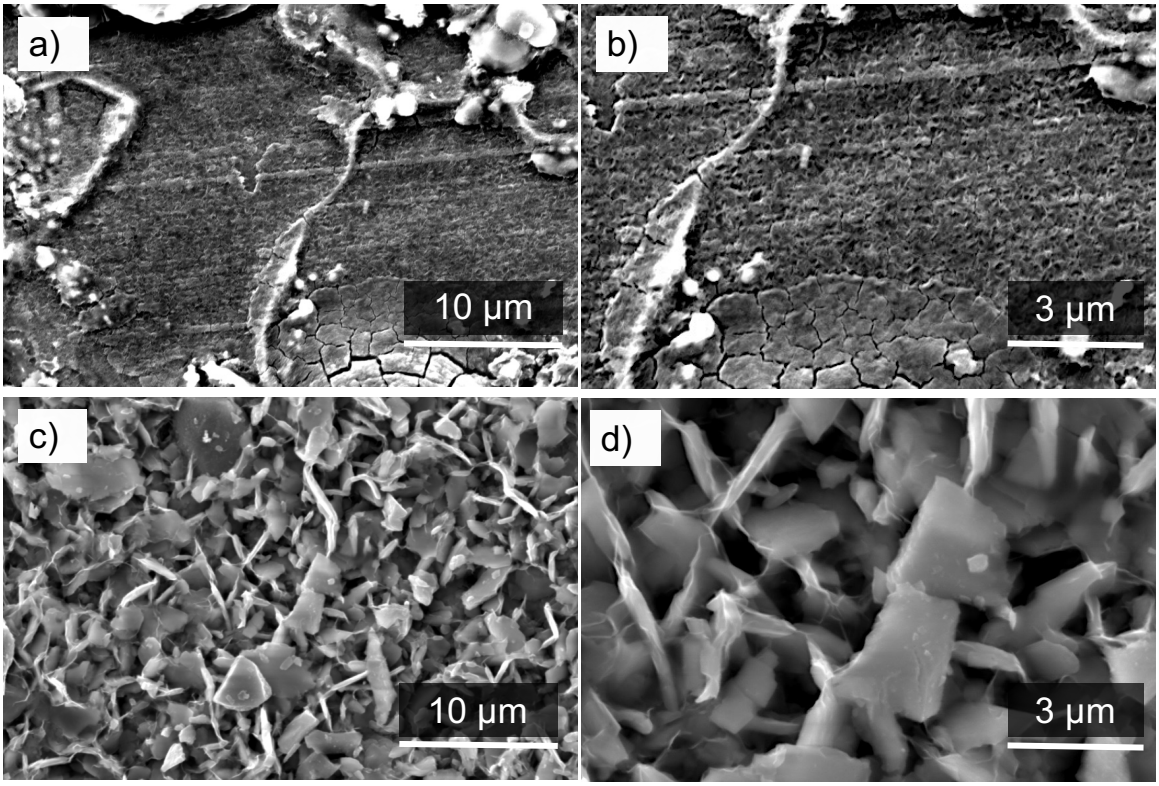

Figure 6-6 SEM micrographs of steel surfaces fully covered with FeS (a and b) and FeS_2 (c and d), corroded under open circuit exposure conditions in a 0.5 M NaCl solution saturated with H_2S for 4h. Images (b) and (d) are magnified views of (a) and (c), respectively.

The different diffusion capabilities of reactive species to and from the surface, as well as the stoichiometry of the applied deposit, can result in different solutions' chemistry at the steel surface. Accordingly, this leads to the formation of iron sulfide films with different stoichiometry and morphology. The sulfur-rich pyrite is assumed to increase the sulfur component at the interface, which led to a thick film of relatively big features. On the other hand, the troilite has less sulfur content and may have reacted preferentially with the intermediate sulfide ions (HS^- and S^{2-}) from the H_2S dissociation reactions in the solution, preventing them from reacting with the ferrous ion at the steel surface. The observation here is consistent with the higher

anodic currents exhibited by a troilite-covered metal and the smaller current with pyrite, which also implies that troilite inhibits the protective effect of H_2S.

Iron sulfide film formation is directly dependent on pH, H_2S concentration, and the Fe^{2+} concentration at the interface, *i.e.,* the dissolution rate. It has been commonly understood that the pH is higher under deposits, which stimulates the process of film formation. In the case of sand, the corrosion current is relatively smaller than the bare case, which makes the interface less acidic, stabilising the conditions for film formation. In the case of troilite, Fe^{+2} concentration is expected to be higher because of the higher corrosion current of the troilite-covered steel. A more acidic environment can then form at the interface, preventing the formation of newly formed iron sulfide films. Nonetheless, the high solubility of troilite is thought to provide a platform for smaller scale interactions with the substrate metal and the newly formed film, eventually dissolving them, which is not yet evidenced. On the other hand, pyrite is thought to cause a higher pH due to lower dissolution and hydrolysis, as well as its sulfur rich nature, which catalyses the film formation process to produce a thick film rich in sulfur.

To conclude, where films are formed at the surface, this is indicative of a local environment with high pH values. Therefore, in case of sand and pyrite deposits, the pH at the interface is expected to be higher than in the cases of troilite and no-deposit.

6.2.1.2.2 ZRA galvanic coupling

Electrochemical coupling was also investigated using ZRA to measure the galvanic current and potential of steel electrodes coupled to iron sulfide electrodes; troilite and pyrite. Prior to the ZRA measurements, the electrodes were initially conditioned in the test solution whilst continuously purged with H_2S, in order to allow for the stabilisation of the system by forming a homogeneous sulfide film on the steel surface. The OCP of each electrode, prior to the ZRA measurement, is shown in Figure 6.7 compared to the initial coupling potentials at the start of the measurement. It can be shown that the steel electrode was polarised anodically with respect to its self-corrosion potential. Both iron sulfide polymorphs acted as cathodes, with pyrite exhibiting a higher positive potential. The galvanic potentials of both couples stabilised between the OCP of the steel electrode and that of the iron sulfide electrodes, and remained close to the OCP of the steel anode.

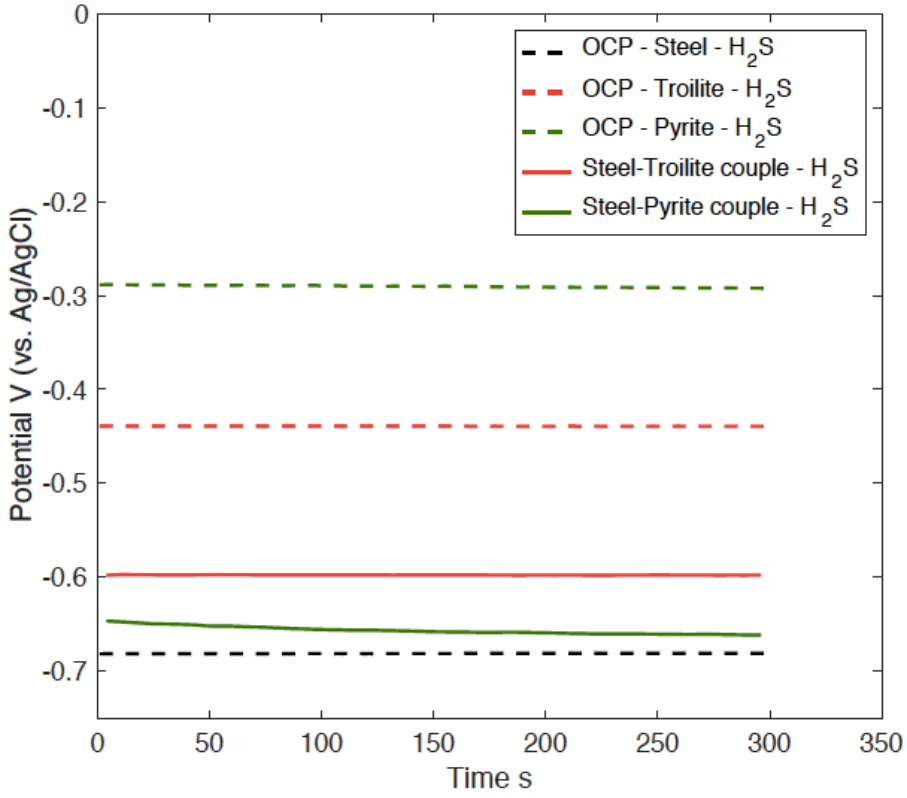

Figure 6-7 The galvanic potential (solid line) of steel-troilite and steel-pyrite couples at the initial stages of coupling contrasted to the OCP (dashed line) of the individual steel and iron sulfide electrodes prior to the coupling reaction. Electrolyte is an H_2S-saturated 0.5 M NaCl solution.

Film formation and precipitation and the local conditions are expected to contribute to the mixed potentials. Therefore, the galvanic potential values are considered approximate. Figure 6.8 shows the coupling potentials and currents of the steel-troilite and steel-pyrite couples for the full duration of the measurement. The galvanic potential of troilite couple was relatively stable at a higher value, with respect to that of the pyrite couple that initially dropped before increasing again to a stable value closer to the troilite potential, as shown in Figure 6.8a. Such transience in the pyrite couple potential could be attributed to the formation of iron sulfide films from the reaction of H_2S with the dissolved Fe. Since Fe dissolution in the pyrite case is much less than troilite, as shown in Figure 6.8b, the film formation might have taken a longer time to form uniformly at the surface. Potentiodynamic polarisation after longer times of coupling is strongly recommended in future research to help deconvolute the effect of film formation.

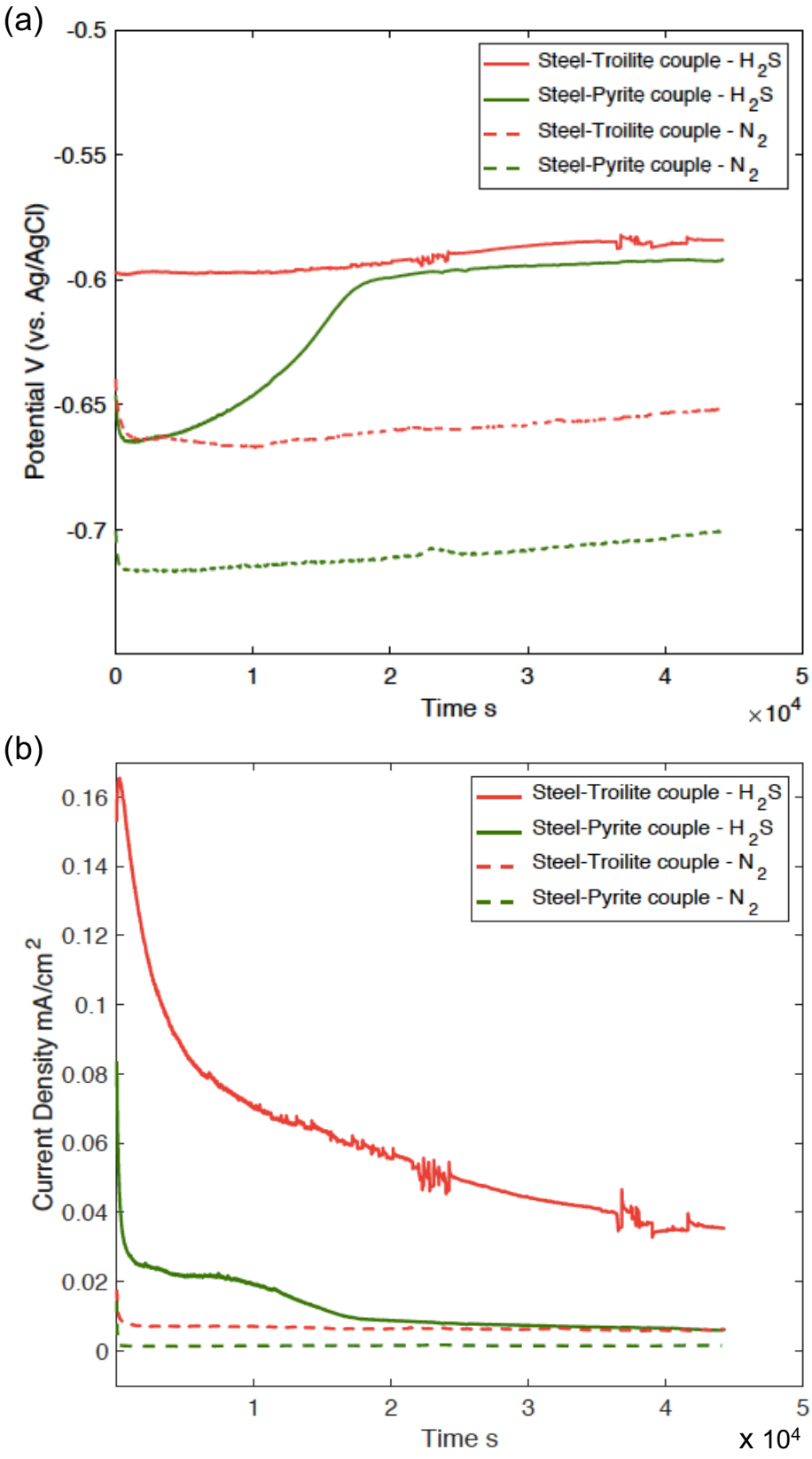

Figure 6-8 Galvanic coupling potential (a) and current density (b), measured by ZRA, for both pyrite and troilite electrodes coupled to mild steel, in both H_2S-saturated (solid line) and N_2-Purged (dashed line) 0.5 M NaCl solution.

In Figure 6.8b, a higher galvanic current can be seen with troilite than with pyrite, indicating a more corrosive nature troilite. This is correlated to the higher difference in OCP between the troilite and the steel electrodes. An initial transient in the galvanic current density was observed which is believed to be associated with the film formation process at the steel surface. However , according to Tjelta *et al.,*[93] it was attributed to properties adherent to the slow equilibration of iron sulfides, and not a direct consequence of a protective film build-up on the steel surface. The slow equilibration is due to adsorption/desorption or limited solution transport through pores and cracks. Tjelta *et al.'s* study[93] justified this by comparing the shape of the galvanic current curves with potential steps performed on steel and iron sulfides: the time required to reach a steady value following a potential step was almost instantaneous for steel compared to several minutes for iron sulfides.

The previous results in N_2-purged environments, detailed in chapter 4, are replotted in Figure 6.8 to correlate the effect of H_2S gas presence to the previous observations. It can be demonstrated that the galvanic potentials and current densities were consistently higher in H_2S than in N_2. The troilite couple potential and current density were, however, higher than that of the pyrite couple, consistent with the N_2 environment measurements. These observations also resonate with the previously reported OCP values of deposit-covered steel in Figure 6.1, where a less stable system was reported with troilite.

When H_2S was present, the difference in OCP between steel and pyrite decreased, as compared to the N_2 environment. On the other hand, the OCP difference between steel and troilite increased. The inhibition effect of the iron sulfide films, from the reaction of H_2S with the steel, was neglected as it was thought to dissolve because of the low pH, resulting from the continuous pumping of H_2S. This indicates a less stable coupling when H_2S is present. On the other hand, the OCP difference between the pyrite and steel electrodes is higher than that between the troilite and steel. Despite these observations, the galvanic current did not necessarily follow the potential difference-current relationship for reasons that remain unclear. Therefore, further research should be carried out to study the electroactivity of both troilite and pyrite electrodes in H_2S.

6.2.2 Artificial pits

In this section, the transport kinetics of artificial pit electrodes are explained in the presence of H_2S. The protocol, previously used in chapter 5, was assumed here using wire artificial pits in a 0.5 M NaCl electrolyte saturated with H_2S. A similar setting, but using foil electrodes, was used for the *in-situ* XRF, XRD and XANES analyses to correlate the salt film chemistry and structure to the electrochemical findings.

6.2.2.1 Pit depth calibration in H_2S

The current-time diagram shown in Figure 6.9a is for an artificial pit wire electrode grown under diffusion-controlled dissolution at +500 mV for 1 h with no deposits present at the pit mouth, under both the aerated and H_2S-saturation conditions. The presence of H_2S was found to decrease the current during pit growth, and therefore, the pit required more time to grow to the same depth obtained in aerated conditions.

Figure 6.9b compares the visually measured pit depth, using an optical microscope, to the theoretical values calculated from the passed charge using Faraday's law.[106] Unlike the good agreement when pits were corroded in air as previously explained in chapter 5, a larger deviation from the theoretical values was observed at larger depths when H_2S was present, whilst the good agreement was always held for shallow pits. As a result, Fick's law that relates the pit depth to the diffusion limited current i_{lim} may not hold at larger depths, and therefore, this part of the study was focused on, but not limited to, shallow pits.

Side reactions such as the reduction of S^- to HS^- ions are thought to consume anodic dissolution currents: this effect becomes larger with longer dissolution times, *i.e.,* deeper pits. The current efficiency is thus decreased, eventually leading to underestimations in the depths calculated from the charge passage, which corresponds to the net current measured from both anodic and cathodic reactions at the interface. Noise in the electrical signal was also observed as the pre-corrosion started in H_2S, which could be attributed to the formation of iron sulfide film on the wire surface due to exposure to H_2S prior to applying potential. The formed iron sulfide film is conductive, and therefore, transients in the current signal were detected.

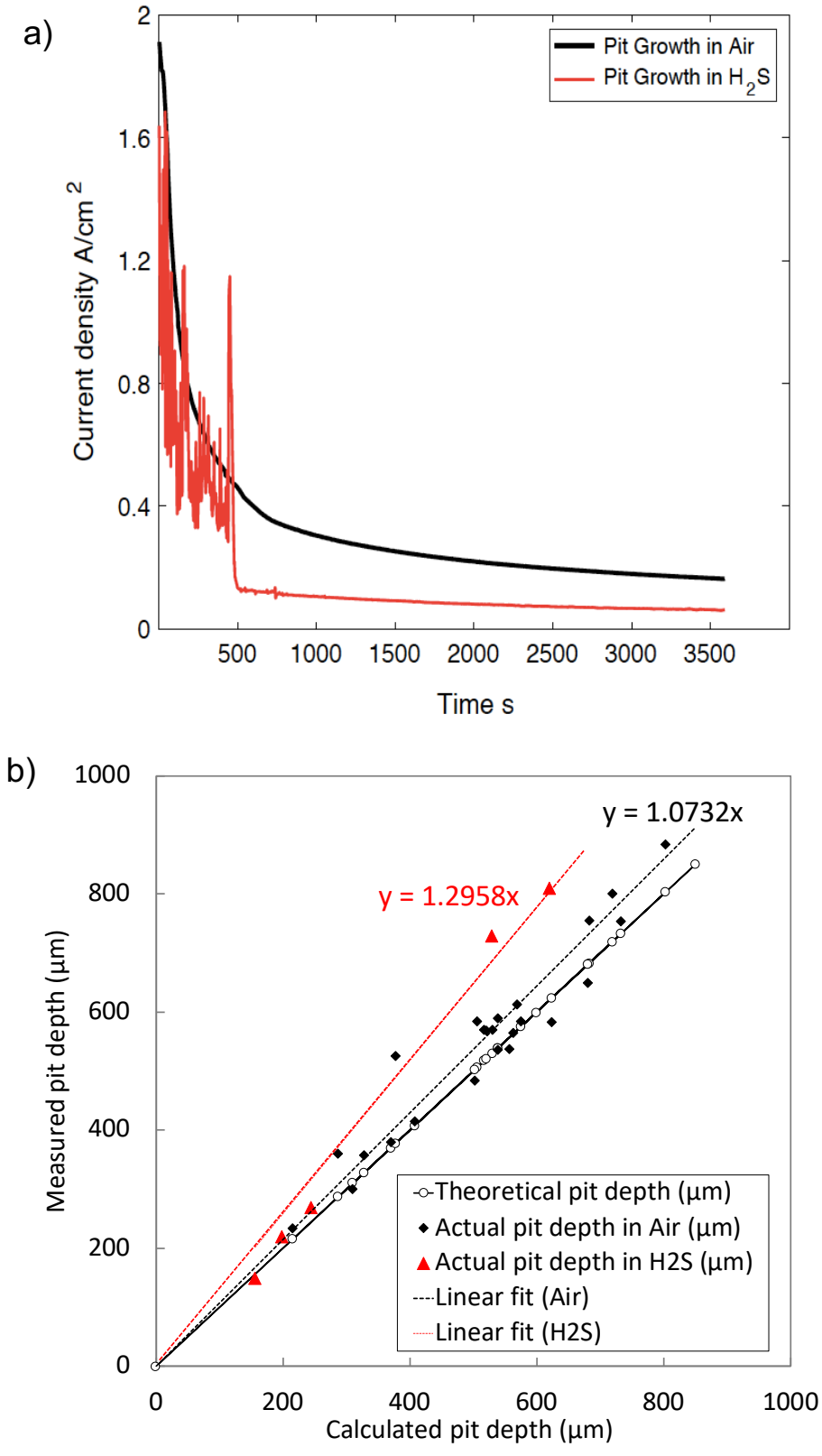

Figure 6-9 The pit growth kinetics in an H_2S-saturated solution compared to the previously acquired N_2-purged measurements. (a) The current-time behaviour of artificial pits corroding at +500 mV. (b) The pit depth calibration curve represented as a comparison between the visually measured and theoretically calculated depths.

6.2.2.2 Propagation stability at different pit depths

The stability of pit growth in H_2S, as contrasted to an aerated non-H_2S control experiment, is demonstrated by the cyclic voltammograms in Figure 6.10a for pits pre-corroded to different depths. The current during the diffusion-limited dissolution regime, i_{lim}, is a measure of the pit propagation rate and stability: it remained potential-independent by the effect of salt film precipitation.[34] When the pit transitioned from diffusion-controlled to activation-controlled dissolution, the salt film broke down and completely dissolved. In the reverse scan, the metal dissolution rate increased rapidly, and the reciprocal of the slope at this stage is the pit solution resistance (R_S), which informs about the chemistry of the pit solution.

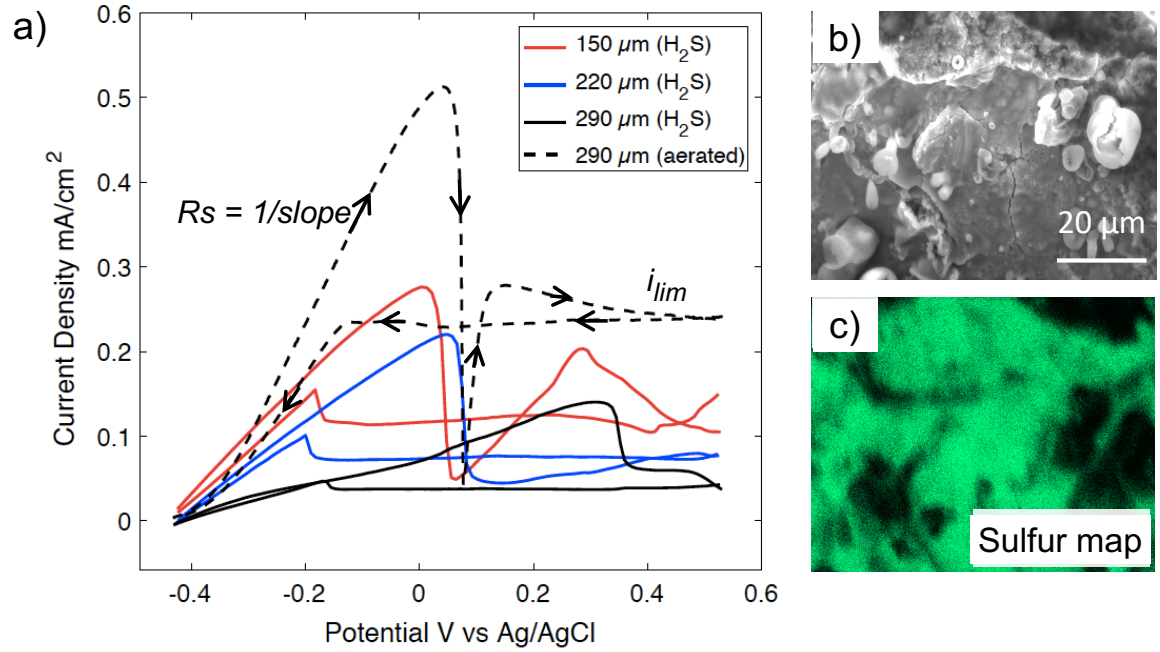

Figure 6-10 (a) CVs representing the effect of pit depth of artificial pits corroded in H_2S -saturated 0.5 M NaCl solution, compared to an aerated control. (b) An SEM image of the wire surface after the potentiostatc pit growth. (c) A sulfur EDS map corresponding to image (b). The experiment was carried out at room temprature and atmospheric gas pressure.

In close agreement with the diffusion-controlled model of pit growth and Fick's law,[34,35,106] i_{lim} decreased with larger pit depths, *i.e.,* longer diffusion lengths. Despite the similar outcome observed under aerated conditions[38,153,154],as explained in chapter 5, the value of i_{lim} is much lower in H_2S, as clear from the 290 μm deep pits in Figure 6.10b. The pit solution resistance R_S was also modified by the H_2S presence, resulting in a response similar to that reported when iron sulfides were applied above the pit cavity. The observed low i_{lim} implies a less rapid, yet stable pit propagation. The high R_S values indicate that the transport barrier components

(R1 of the salt film and R2 of the diffusion length) are altered in a way that maintained an active chemistry at the pit bottom, which is required for stable pit propagation.

In both cases of H_2S and the previously reported iron sulfides, a sulfur-containing film was observed on the wire surface, as revealed by the post-test SEM-EDS analysis shown in Figure 6.10 (b and c). Ferrous ions reacted with sulfide ions from the solution presumably forming insoluble iron sulfide (at pH > 1.9[141,164]) on top of the Fe surface at the bottom of the cavity, in competition with the conventional chloride salt films. Since $FeCl_2$ salt films are freely soluble in typical acidic environments,[165,166] the sulfur-rich iron sulfide film was thought to add an extra diffusion barrier and/or change the physical structure of the salt film in a way that caused i_{lim} to decrease. It could be argued, however, that the sulfide film was formed after the reaction was already finished, during the handling process.

Despite the importance of these initial observations to drive a kinematic theory, experimental evidence is still lacking to justify such changes in pit kinetics. Therefore, *in-situ* X-ray characterisation of the electrochemically active Fe interface was carried out. This is aimed to reduce the effects of uncontrollable structural changes that may occur during analysis and handling in *ex-situ* conditions.

6.2.2.3 *In-situ* synchrotron X-Ray analysis

6.2.2.3.1 Diffusion profile using XRF

The XRF line scan across the active interface provides qualitative insights into the diffusion profile at the pit bottom. As shown in Figure 6.11, the normalised XRF intensity in the solution side, *i.e.,* after the metal-solution intensity transition, is lower when H_2S was present in the solution. This result is comparable to the case of physically applied deposits, where the diffusion of iron ions is hindered, in agreement with the electrochemical findings, which is also assumed to be due to the formation of a thicker and/or denser salt film.

Figure 6.12 demonstrates the XRF line scan across the metal-solution interface in presence of H_2S in both the diffusion-limited and activation-controlled growth regimes. When the dissolution is diffusion-limited, there is a smooth interfacial transition in the interface region, whereas a roughened transition is observed when the dissolution is activation-controlled. This indicates a lack of a defined interface due to surface roughness, the formation of a thicker salt film, or ,as noted in the literature, dispersed iron carbide crystallites nonuniformly etched away from the surface.[37,127] An XRD study explains this in more details in the following section.

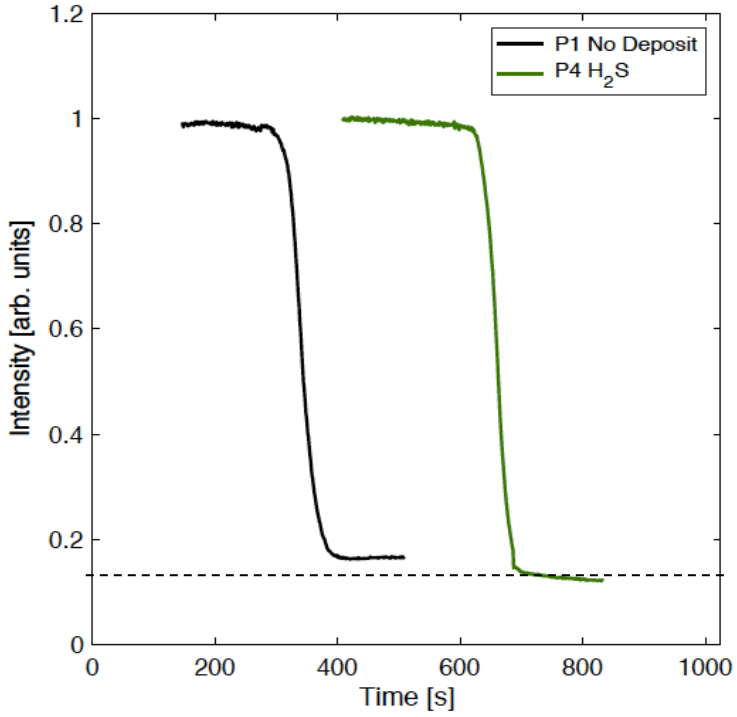

Figure 6-11 XRF line scans recording iron ion intensity at the interface of foil artificial pits dissolving in H_2S saturated solution (P4), compared to the air control (P1), in absence of deposits (P1). P4 (H_2S) exhibited a lower intensity in the region after the interface intensity transition. Shallow pits were used, and the growth potential was at +800 mV (Ag/AgCl).

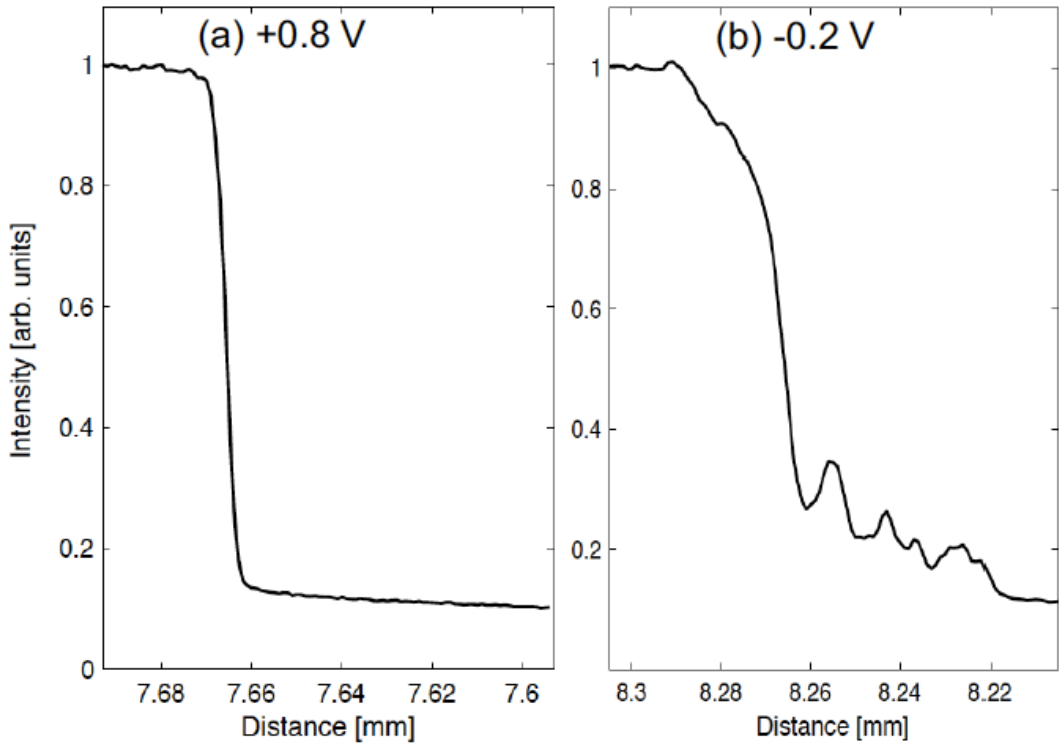

Figure 6-12 XRF line scans across the interface of foil artificial pits corroding in absence of deposits under two different dissolution regimes: (a) diffusion-limited growth at +800 mV, and (b) activation-controlled growth at -200 mV. Distances were taken relative to arbitrarily reference positions below the steel surface and the scan range is 100 μm. Potentials are measured against Ag/AgCl RE.

6.2.2.3.2 Interfacial salt film structure and thickness using XRD

Diffusion-limited dissolution

The structural phases of the salt layer were recorded by performing XRD line scans with a vertical interval of 2 μm and 20 s acquisition time. The crystalline metal salt ($FeCl_2.4H_2O$) pattern[37] has been consistently identified in the interface slices, similar to the cases of pits grown in aerated conditions, as shown in Figure 6.13.

Despite observing a sulfur containing film in the SEM-EDS analysis of the pits (Figure 6.10), no signs of sulfur species were detected in the *in-situ* XRD measurements. Sulfur species are thought to deplete inside the pit during the initial stages of propagation, and the inward diffusion of species from the bulk solution was limited by the continuous outward flow of dissolved Fe ions. This effect has possibly inhibited the reaction between the sulfur and iron species at the metal interface. The pH at the interface is also very low which dissolves the newly formed iron sulfides. It could also be argued that the observed sulfur-containing films in the SEM/EDS were formed during the handling process after the dissolution has stopped. However, the pit was previously cycled which could involve dissolution of the films that have formed at the start of the reaction, and hence cannot be detected in the X-ray measurements.

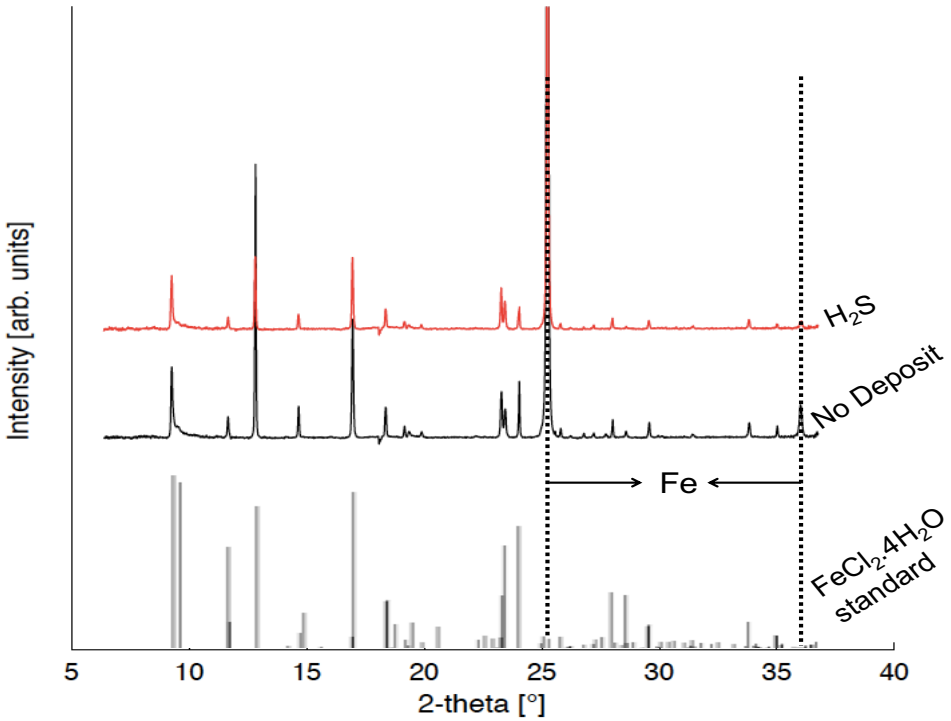

Figure 6-13 XRD diffraction patterns of salt films formed on the dissolving interface of Fe artificial pits with sand and FeS_2 at the pit mouth in H_2S saturated solution, compared to the deposit-free aerated control. Pits are corroded under diffusion-limited conditions at +0.80 V.

As previously detailed in chapter 5, the number of interfacial XRD steps provide estimates of the salt film thickness. In the no-deposit aerated control pit, a total thickness of ~13.0 μm was concluded after measuring the interfacial crystalline XRD steps and correcting with the distance that the pit recessed during the interface measurement. When H_2S was present in the media, a slightly higher number of crystallised slices was observed in the XRD stack, accounting for a thicker salt film (~17.0 μm).

Due to the high resistance observed in the electrochemical CV measurements, the diffusivity of iron ions decreased (according to: $1/R \propto D\ dC/dX$), which lowers the concentration at the pit mouth. The amount of dissolution until supersaturation and precipitation of the salt film is smaller with H_2S, as indicated by the low i_{lim}. A lower XRF intensity after the interface transition was also observed in Figure 6.12. This could indicate salt build-up at the interface as a result of the easier supersaturation. Figure 6.14 represents schematically the diffusion profiles of iron ions inside the pit cavity in both H_2S and aerated conditions, assuming linearity.

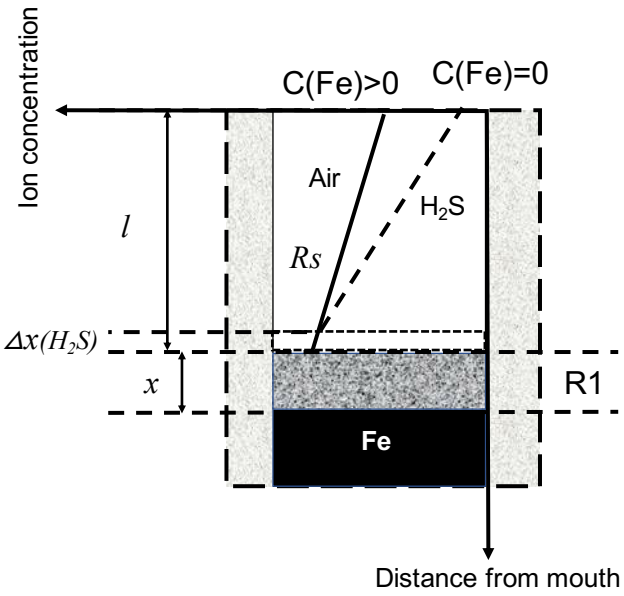

Figure 6-14 A schematic representation of the diffusion profiles of iron ions inside artificial pits corroded in aerated and H_2S conditions in absence of deposits. Diffusion is assumed linear and pit depths are equal. Concentration of iron at the interface is relatively smaller in H_2S as demonstrated by the XRF scans. X is the salt film thickness and Δx is the thickness increase due to H_2S presence.

The change in the salt film thickness can also be attributed to other reasons. For instance, the interface may be rough enough so that the 25 μm-wide X-ray beam continues to record the metal salt at prolonged distances. In addition, it can be related to a change in the salt film stoichiometry, which in turn affects the film conductivity. As a result, the diffusing reactants will have different diffusion coefficients, forming salt film structures at prolonged distances above the interface.

Activation-controlled dissolution

Following the pit growth under salt film conditions in H_2S, the growth was transitioned to the activation-controlled (salt free) regime by applying a potential as low as -200 mV (Ag/AgCl). In contrary to the $FeCl_2.4H_2O$ patterns normally observed at high potentials, new patterns were formed as demonstrated in Figure 6.15a. Patterns were added to make the diffraction pattern more visible and easier to interpret, as shown in Figure 6.15b.

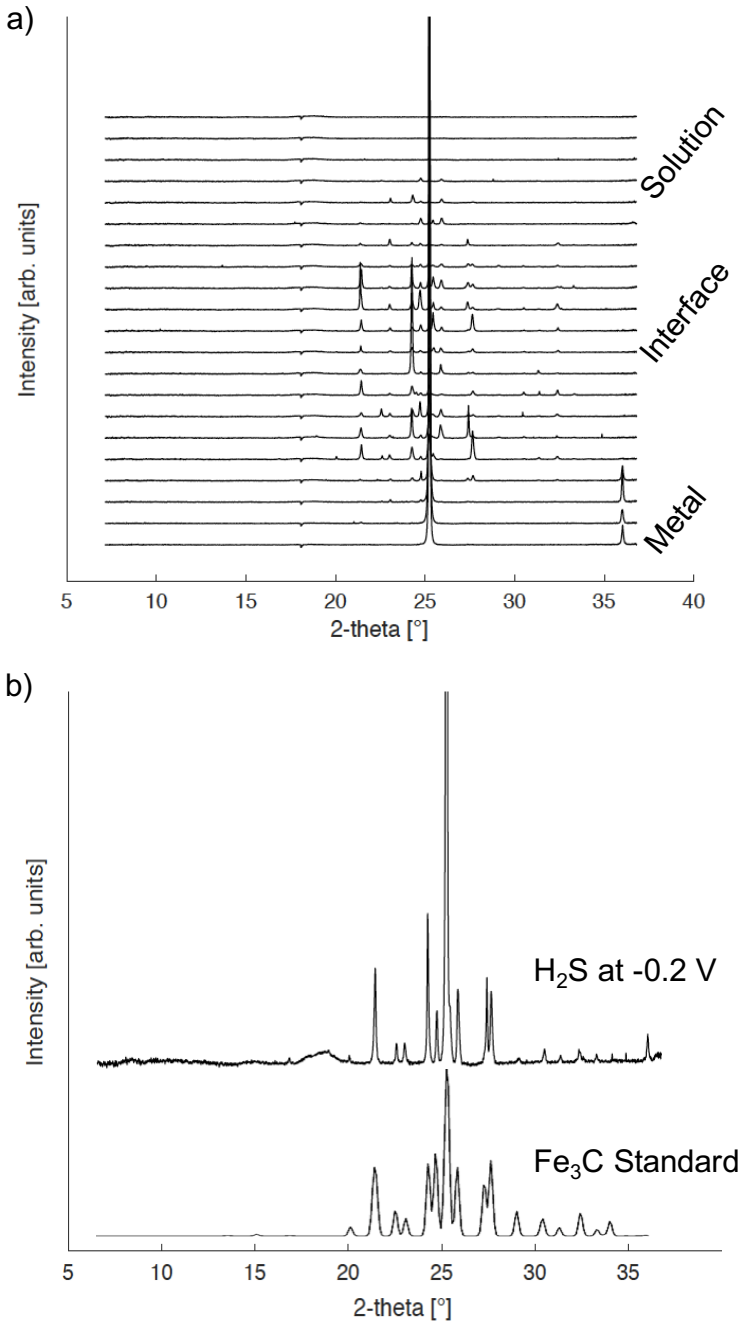

Figure 6-15 XRD patterns of the solution adjacent to the dissolving interface of an Fe artificial pit. The stack plot of one X-ray scan (a) is averaged and fitted (peak positions) to the Fe_3C standard pattern (b). The pit depth was 1.2 mm, corroding under activation control at -0.20 V (Ag/AgCl) in H_2S-saturated 0.5 M NaCl solution. Deposits were not present at the pit mouth.

Iron sulfide phases were initially expected to form by a direct reaction between inflowing sulfide species and the dissolving iron. Also, since the local pH is relatively higher due to low hydrolysis, pyrite is the most thermodynamically favoured product.[9,167] However, when the patterns were averaged, an iron carbide (Fe_3C) pattern was determined, with no evidence of $FeCl_2.4H_2O$ or iron sulfides presence. Due to the ohmic electrochemical response, the film is likely to be in the form of a porous network, which is also clear from the different intensities of the XRD patterns above the interface. The discontinuity of the intensity of the XRD patterns of the slices indicates that the Fe_3C layer was not uniformly dense. The newly formed Fe_3C structure was observed over a larger number of XRD scan steps, indicating that it extended to a large distance above the electrode surface compared to $FeCl_2.4H_2O$, as explained in Figure 6.16.

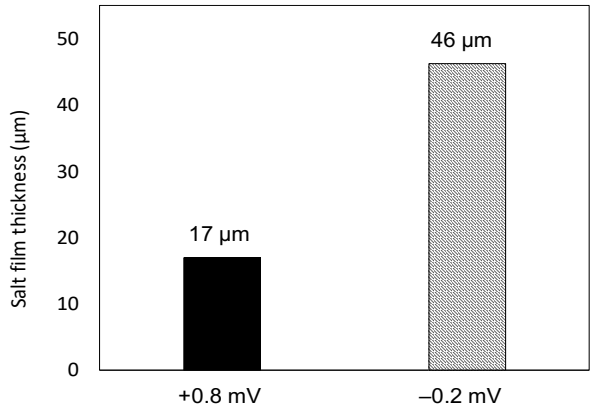

Figure 6-16 Thickness of salt films at the interface of dissolving pits in H_2S saturated 0.5 M NaCl solution at diffusion-limited dissolution conditions (+0.80 V) compared to the conditions of activation-controlled dissolution (-0.20 V). The thickness wes calculated from the number of the crystalline X-ray slices at the interface after correction with the speed of recession of the metal surface. Deposits were absent at the pit mouth.

The wires used in this study are high-purity iron with carbon content <1000 ppm existing in the form of interstitial carbon atoms and/or carbides Fe_3C. As the wire was slowly dissolved, Fe_3C precipitates were possibly accumulated above the interface inside the pit cavity. Fe_3C reportedly dissolved electrochemically at higher voltages, near that of iron dissolution. Therefore, according to a Pourbaix diagram constructed by Xu *et al*.,[37,127] Fe_3C is stable at the low applied potential of -0.20 V. Since the thermodynamic potential of carbon oxidation is consistently higher than that of Fe_3C, a thin layer of carbon is thought to form on the Fe_3C crystallites, which passivates the surface and prevents its dissolution.[168] In addition, at this low applied potential in our study, the current was low enough to prevent the precipitation of $FeCl_2.4H_2O$ crystals; only Fe_3C remained present above the metal interface. On the other

hand, at higher potentials, the carbon layer became no longer passivating, and Fe_3C oxidises or dissolves in solution.

The newly formed low-resistivity[169] Fe_3C crystallites compose an extra diffusion barrier. This barrier, in addition to the pit's narrow cavity and length, is thought to hinder the diffusion of sulfide species from the bulk solution, which could explain the absence of iron sulfides at the pit bottom. Figure 6.17 presents a schematic of the Fe_3C formation inside the pit, representing the effect of the applied potential: Fe_3C is partly etched at low potentials and dissolves completely at high potentials. Therefore, the electrochemical behaviour of artificial pits in H_2S, *i.e.,* low limiting currents and high reprecipitation potential and pit solution resistance, is consistent with the formation of a non-protective porous, low resistivity layer. Despite the assumed effect of Fe_3C, it is not clear if they persist at high potentials during the further cycles of the CV measurement.

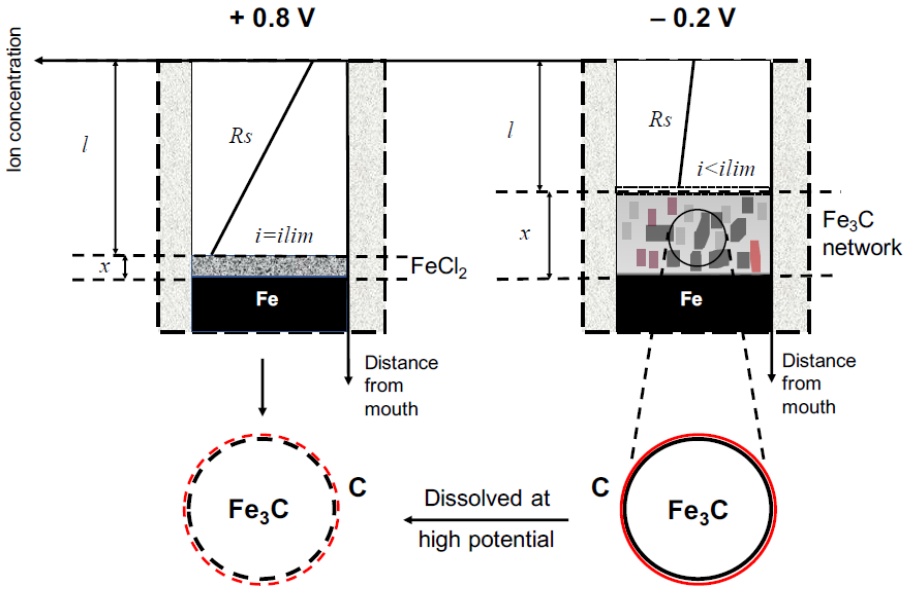

Figure 6-17 A schematic representation of artificial pits corroded at high (+0.8V, left) vs. low (–0.2V, right) potentials in H_2S, showing a thicker etched Fe_3C network at low potentials and a thin iron chloride salt film at high potentials. At low potentials, Fe_3C is protected by a passive thin layer of carbon, but it dissolves at high potentials.

6.2.2.3.3 XANES at pit interface and mouth

Figure 6.18 shows XANES spectra acquired at the interface and mouth of a pit dissolving in H_2S-saturated solution. The spectra were fitted using a linear combination of the standard spectra to determine the oxidation state of the iron species in the pit. The fit results and weights of the interface measurements are illustrated graphically in Figure 6.18a, indicating a majority of $FeCl_2$ with only a small amount of the FeS standard. As explained in chapter 4, the absence of sulfide species during the XRD measurements could assume an amorphous nature of the

formed iron sulfides. For the pit mouths, a similar observation was held, except with the detection of a large percentage of Fe (III), as $Fe_2(SO_4)_3$. The linear combination using the current set of standards did not provide a satisfactory fit, as shown in Figure 6.18b, and more standard materials should be included.

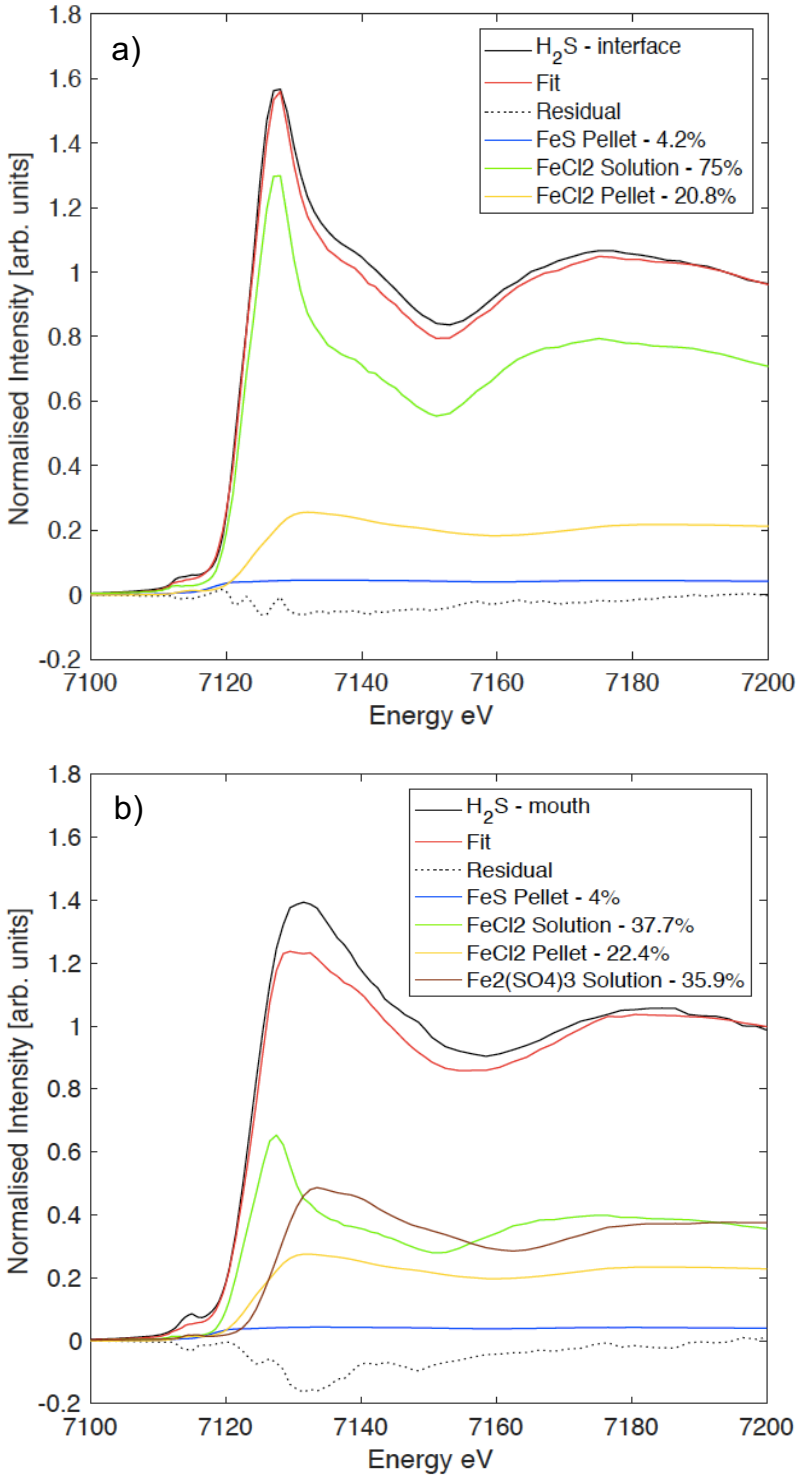

Figure 6-18 XAS spectra at the interfaces (a) and mouths (b) of artificial pits dissolving in H_2S saturated solution, overlaid with best-fit results obtained by a linear combination of the different reference materials potetnially existing in the sample.

The XANES spectra of the H_2S environment were contrasted to that of the control aerated experiments. As shown in Figure 6.19, the positive shift in the edge energy, typically observed with mouths' spectra, was observed, which is assumed to be a result of the oxidation of Fe (II) close to the interface to Fe (III) due to oxygen ingression. The H_2S presence exhibited even a larger positive shift in the edge energy with both the interface and mouth spectra, indicating a higher tendency to oxidise Fe (II) in H_2S media. The white line intensity (maximum absorbance) at the interface is higher in H_2S than in aerated environments due to the higher concentration of iron at the pit bottom. This could be attributed to the newly formed films, specific to the H_2S environment, that slow down the outward diffusion of iron species. Systematic changes in the overall shape of XANES spectra could also indicate that the coordination of iron varies within the pit.

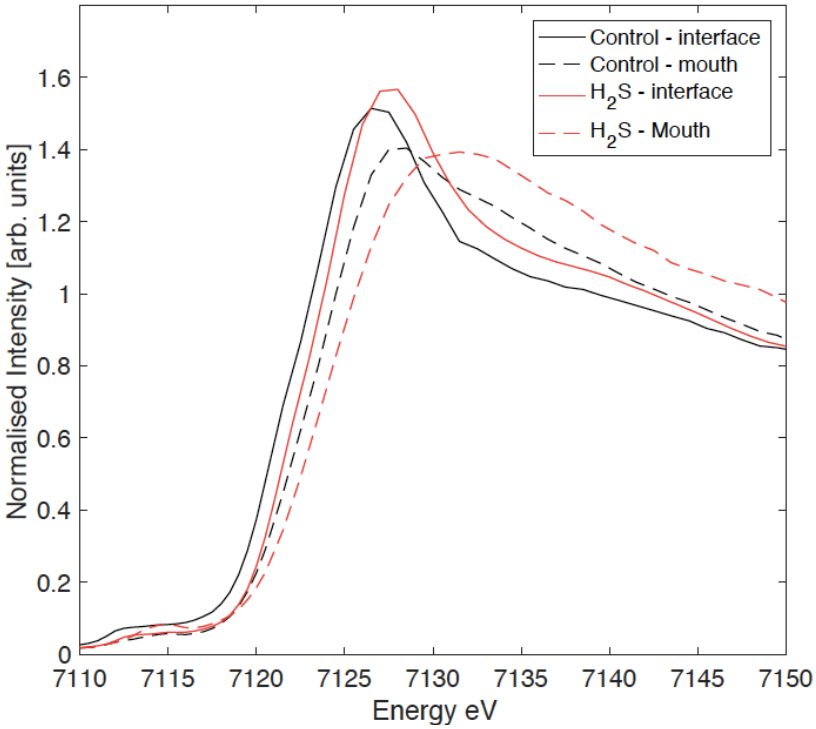

Figure 6-19 Normalised Fe K edge XAS spectra (measured in fluorescence), of both the mouth solution and the interfacial salt film of an artificial pit dissolving under diffusion-controlled conditions in both the aerated conditions (black) and H_2S-saturated solution (red) cases.

6.3 Summary and conclusions

In the case of sour environments, the corrosion process is reported to be mainly decided by the presence of iron sulfide layers and its different phases, which decide the galvanic coupling and the mass transport process of corrosion species. These studies, however, investigated the uniform corrosion, but have not provided conclusive remarks about the localised corrosion kinetics under sour gas conditions. In our study, the general and localised kinetics of UDC in sour environments were investigated. Under-deposit systems in H_2S are found to corrode differently from the N_2-purged systems.

Initially, the steel's general corrosion kinetics were investigated using electrochemical measurements on planar coupons in an H_2S saturated solution, whilst under physically applied deposits. Typically, sand deposits increase the corrosion susceptibility of steel by forming aerated corrosion microcells underneath. However, in H_2S environments, iron sulfide films form at the surface due to the chemical reaction of steel and H_2S. These formed films are thought to block the formation of the aerated corrosion microcells, leading to a reduction in the general steel corrosion rate. This demonstrates the higher OCP values and the lower anodic currents observed in the cases of uncovered or under-sand steel. Therefore, it is concluded that the introduction of H_2S resulted in a more electrochemically stable system when under inert deposit conditions.

Systems covered with reactive iron sulfides were destabilised. Menendez and co-workers,[91] had previously deduced that the *in-situ* precipitated mackinawite exhibited significant localised attacks, more representative to the sour environment. Mackinawite, however, is a metastable form of iron sulfide that transforms to more stable phases such as pyrrhotite and pyrite. In our study, however, troilite and pyrite were tested as stable forms of iron sulfide. Troilite rendered the system more susceptible to pitting corrosion, being the most corrosive among the studied cases (sand and pyrite). Pyrite, on the other hand, had a less significant effect in destabilising the system: it demonstrated OCP and anodic current density values close to that of the sand-covered steel.

Due to the semiconductive nature of iron sulfides, deposit-metal current exchange is unknown and does not take part in the corrosion reaction, which in turn affects the accuracy of the corrosion current measurments.[21] Therefore, the galvanic current exchange was monitored by coupling troilite and pyrite electrodes to steel electrodes using ZRA. The steel dissolved anodically when galvanically coupled to troilite and pyrite electrodes, and the troilite couple exhibited higher galvanic currents. This can be correlated to the higher difference in OCP between the troilite and the steel electrodes. Although the electrochemical observations were consistent with the findings of the N_2-purged environment, the general corrosion kinetics were

highly determined by H_2S: the galvanic current was significant with respect to the overall corrosion current. The influence of the deposit alone was minimised by introducing H_2S, which is assumed to be a direct result of the formation of interfacial iron sulfide films.

Different phases of iron sulfides, with various degrees of protectiveness, are commonly produced during the corrosion process in H_2S environment.[9,18,22,84,85] The effect of external deposits physical and chemical properties on the film formation has not been previously investigated. A brief H_2S exposure test was therefore used to support the electrochemical findings by observing the changes in the steel surface. SEM images of the surface showed that films were formed under sand and pyrite, which were presumed protective. Whereas in the case of troilite, the films were completely absent. The difference in solution access through the applied deposit as well as the changes in the deposit reactivity, *i.e.,* solubility and conductivity, have resulted in changes in the local chemistry. Therefore, the surface films were observed with different morphologies and stoichiometries when different deposits were used or when the deposit packing was not homogeneous. On the other hand, the films were absent from the bare steel surface because of the low solution pH resulting from the continuous injection of H_2S.

Localised corrosion insights were obtained using artificial pit experiments for the first time in an H_2S environment. Artificial pit experiments in H_2S could be used to represent the under-deposit conditions of chemically formed iron sulfides in absence of physically incorporated deposits. The presence of H_2S reduced the current efficiency, and therefore, shallow pits were used to avoid large deviation from the linear pit depth - diffusion limited current proportionality in Fick's law. The electrochemical results indicated lowered diffusion limited current i_{lim} and increased pit solution resistance R_s, which is assumed to be a result of hindering the ionic transport.

In H_2S, the produced Fe^{2+} ions at the pit bottom reacted with the incoming flux of HS^-, forming a more resistive solution and/or an additional diffusion barrier of iron sulfide films at the dissolving interface. As a result, the Fe^{2+} depletion led to different concentration gradients. This is thought to affect the ionic production at the pit bottom as well as the physical structure of the salt film, *i.e.,* thickness and density. The cumulative result for these processes was an aggressive pit solution chemistry that stabilised the propagation process at a slower rate. A follow-up SEM-EDS analysis detected sulfur-containing films at the metal surface, but it was not conclusive enough to understand the transport phenomenon in sour environments. Therefore, supporting *in-situ* X-ray characterisation of the electrochemically active interface was performed. Numerous studies by Issacs and co-workers[35,102,104,105] investigated the artificial pit chemistry and dissolution and passivation kinetics, but no similar study was reported on sour environment conditions.

Under diffusion-limited conditions, the interfacial XRF scans confirmed the electrochemical findings of lower i_{lim}: the iron dissolution and the diffusion of iron ions was hindered by the presence of H_2S. XRD and XANES measurements were further used to characterise the structure and chemistry of the interfacial films. An *in-situ* XRD analysis indicated a salt film of $FeCl_2.4H_2O$, similar to the aerated conditions but with a larger thickness. Complementary XANES demonstrated a +2-oxidation state. Because of the high solution resistance and the transport limitations inside the pit, ions tend to build-up at the interface. This was assumed to be the reason of the eventual increase in the salt film thickness. No iron sulfide species were detected *in-situ* at the pit bottom, which could be reasoned by: (1) the depletion of sulfide ions at the initial stages of pit propagation, (2) the continuous outward flow of Fe ions, which possibly inhibited solvated sulfide species from diffusing to and precipitating at the interface, and finally (3) the low pH at the interface that dissolved the newly formed iron sulfides.

When pits were dissolved under activation control at low potentials, the XRF metal-solution transition lacked a defined interface, indicating a non-uniform, partly etched film. An Fe_3C pattern was determined by XRD, with no evidence of a $FeCl_2.4H_2O$ or iron sulfide presence. As the pit slowly dissolved, Fe_3C, from the interstitial spaces, precipitated inside the pit cavity, extending to large distances above the metal interface. Fe_3C crystallites are naturally passivated with a thin layer of carbon that prevents its dissolution. At high potentials, the protective carbon layer dissolves, and the Fe_3C oxidises or dissolves accordingly. This demonstrates the absence of Fe_3C during the diffusion-limited pit propagation. On the other hand, the Fe_3C formed a non-uniformly porous network during the activation-controlled dissolution, as demonstrated by the discontinuity of the XRD patterns' intensity. The *in-situ* outcomes support the electrochemical findings of low i_{lim} and high Rs values, consistent with the formation of a non-protective porous and low resistivity layer inside the pit cavity.

This blended approach to study both the general and localised attributes of the UDC phenomenon have proven efficient in providing a comprehensive overview of the sour corrosion of steel. As a result, the metal behaviour at large scale can be directly linked to the salt film properties inherently responsible for the pitting corrosion stability. Therefore, new protection protocols can be adopted.

7 Conclusion

The high failure rate of oil and gas pipelines due to UDC steered extensive research to understand its mechanism and inhibition protocols. Despite this, no systematic study from the available literature was reported to analyse the inherent properties of the deposits in correlation to the pitting process. The aim of the present work was to elucidate the dissolution mechanism of steel under different deposit arrangements, and to use such a protocol to provide kinetic and mechanistic information on different scenarios of the UDC phenomena.

According to the *general* corrosion experiments on planar coupons, inert deposits were found to destabilise the metal by increasing the corrosion current and pitting susceptibility. Under fine-grained sand, the steel surface is effectively blocked, creating deaerated local corrosion cells. A common observation in the literature is that smaller particles form a tight packed deposit bed, which decreases the corrosion rate accordingly. However, the extra fine particles involved in our study undergo wetting to behave like clay, providing shorter tortuous paths for the diffusing iron ions, thus increasing the corrosion rate. Therefore, the fine sand showed a stronger deviation from the no-deposit control in the case of non-H_2S media than the coarse particles. In an H_2S environment, however, the corrosive effect of deposits was minimised. H_2S was found to decrease the likelihood of pitting by protecting the steel surface with a homogeneous corrosion film. This film blocks the formation of deaerated cells responsible for the pitting corrosion that typically occurs under inert deposits.

Reactive deposits, in the form of physically incorporated iron sulfides, rendered the metal more prone to corrosion. Previous studies concluded that mackinawite exhibited significant localised attacks, more representative to the sour environment, but mackinawite is metastable and transforms to other stable forms of iron sulfide short time after its formation.[4,6,16,91] Therefore, our study involved stable forms of iron sulfide, troilite and pyrite, representing a more relevant case to longer term pit propagation. The troilite-covered steel has shown to be most susceptible to pitting corrosion. On the other hand, the low solubility pyrite was relatively more protective by forming of a dense film on the surface. Introducing H_2S brought the kinetics of such reactive under-deposit systems closer, lowering the susceptibility to pitting with respect to the N_2 controls. Other reactions such as H_2S reduction and deposit polarisation could also take place at the polarised steel surface. As a result, the current efficiency decreases and only an unidentified part of the measured current is associated to the steel dissolution.

In an attempt to account for the currents associated with the semiconductive nature of iron sulfides, complementary ZRA electrochemical measurements were carried out. Typical galvanic investigations involve coupling two electrodes of steel under different conditions of deposit or environment.[108] However, this cannot explain the origin of galvanic corrosion

couples due to the conductive deposit that provides an additional channel for a portion of electrons to be transferred through the deposit. Therefore, our study measured the galvanic currents between separated, externally coupled iron sulfide and steel electrodes. Troilite produced a higher galvanic current exchange than pyrite, but this current was insignificant in magnitude compared to the corrosion current measured during potentiodynamic polarisation. This concludes a minor contribution of the deposit-metal galvanic cells in the overall corrosion process.

The introduction of H_2S to the ZRA setup was found to increase the galvanic current further, with the highest values obtained with the troilite couple as well. In contrary to the non-H_2S couple, the galvanic current in this case was significant with respect to the overall corrosion current. The high current in this case could be attributed to the low solution pH at the steel surface, *i.e.,* more corrosive solution chemistry. Consequently, it is assumed that both the local deaerated galvanic cells, from local chemistry changes, and the deposit-metal 'chemical' interaction are the underlying causes behind the corrosive nature of iron sulfides.

According to the planar experiments and the post-reaction surface characterisation, troilite showed the most corrosive nature. At the same time, our study observed that the troilite's chemical and physical nature changed with reaction, undergoing electrochemical sintering and phase transformations, which could affect the subsequent deposit-metal interactions. Further investigation is, therefore, needed to study the effect of the real-time deposit's transformations on the different corrosion reaction processes.

Once pits are formed, the propagation process was also found to be determined by the deposits accumulated at the pit mouth. The pitting stability was measured using artificial pits to simulate actively dissolving pits, following Galvele's model[38] of mass transport and previous artificial pit studies by Issacs[35,102,104,105], Newman[59,60], and Rayment[37,130] co-workers. Our study contributes to the existing knowledge of pitting kinetics by introducing the effects of external deposits and sour environments on the artificial pit propagation. The deposit was found to stabilise the pit propagation by making the chemistry inside the pit more suitable for salt film precipitation, which maintains an aggressive environment for metal dissolution at the pit bottom. The propagation process was, however, dependent on the deposit nature and characteristics.

An important finding to emerge from this study is that reactive iron sulfide deposits showed pit propagation kinetics that are remarkably different from the inert deposit counterparts. The pit solution resistance was much higher, and the diffusion-limited current was rather lower, indicating a solution chemistry that favours the formation of salt films, necessary for a stable pit propagation. Iron sulfide deposits not only acted as an effective transport barrier, but also

perturbed the chemistry inside the pit, presumably by effect of the dissolved sulfur species that diffuse inwards. This gave rise to the formation of sulfide films at the interface despite the absence of H_2S gas, as was revealed by *ex-situ* SEM-EDS and Raman spectroscopy analyses. The same effect on pit propagation stabilisation was observed when H_2S gas was introduced to represent a chemically formed deposit inside the pit, rather than a physically incorporated deposit at the pit mouth.

Furthermore, *in-situ* synchrotron X-ray absorption spectroscopy and diffraction measurements were carried out on dissolving artificial pits (diffusion-controlled) to obtain valuable information about the pit solution and salt film. The diffusion profile of iron ions was shown by XRF scans to be affected by the blocking effect of the deposit above the pit cavity. When deposits were placed at the pit mouth, the diffusing iron ions were retained, increasing the ion concentration at the pit mouth. Moreover, when iron sulfides were used, they partly dissolved inside the pit, which increased the iron ions concentration further. According to these data, we can infer that the concentration gradient became lowest when reactive iron sulfide deposits were present, followed by inert sand, and finally the bare pit. The interfacial salt films, characterised in all cases using *in-situ* XRD as iron chloride tetra-hydrate ($FeCl_2.4H_2O$), was found to have its thickness directly proportional to the concentration gradient, *i.e.,* thinnest under iron sulfides. On the other hand, in the presence of H_2S, the pit mouth was relatively depleted of iron ions, which led to a higher concentration gradient and salt film thickness.

Salt films define the corrosiveness of pitting corrosion by providing the aggressive chemistry necessary for a stable pit propagation. When the salt film dissolves, pits grow under activation control at a low potential, well below the oxidation potential of the interstitial iron carbides. As a result, it was found that carbide residuals from the steel were not etched away during the activation-controlled dissolution, forming a porous network that extends to tens of microns above the interface. The carbide network acted as a transport barrier in the activation dissolution mode, but it was not enough to induce a diffusion-controlled dissolution. It rather contributed to the effective solution resistance. Further work should include careful characterisation of this network and its role in inhibitor transport into the pit cavity.

Complementary XANES indicated Fe (II) oxidation state of the salt film at the interface, confirming the findings of previous work by Rayment *et al.*[46]. However, a small contribution of FeS in the XANES linear combination fit was obtained where iron sulfides or H_2S were present, which supports the *ex-situ* measurements and the hypothesis of forming new iron sulfide films at the pit base. Therefore, the absence of sulfide species at the interface in the XRD results could indicate an amorphous FeS nature, and possibly with small amounts below the detection limit of the XRD detector (with respect to the $FeCl_2.4H_2O$ signal intensity). Due to the oxygen ingression at the pit mouth, especially when deposits were not present, iron ions were oxidised

at the pit mouth. Further synchrotron experiments could be carried out to investigate the salt film density and crystallite arrangements, which affect the transport phenomenon accordingly.

From this piece of work, UDC was demonstrated as a multiscale phenomenon that traditional electrochemical methods are not sufficient to investigate the underpinning causes and mechanism. The blended paradigm adopted here, to study both the general and localised attributes, can directly link the metal behaviour at large scale to the salt film properties inherently responsible for the pitting corrosion stability. Our multiscale investigation that included both *ex-situ* and *in-situ* measurements has provided valuable temporal and spatial insights, which confirmed the electrochemical theory and observations of pits under deposits.

In conclusion, this study has led to a mechanistic understanding of the pitting kinetics of steel under the deposits of the sour environment. It helped understanding the underlying mechanism of pits propagation under deposits, in addition to the different dissolution regimes that pits follow to propagate and stabilise. The findings suggest potential electrochemical fingerprints for the various UDC scenarios in real pipelines. This work has also provided a protocol suitable for inhibitor testing, paving the way for developing in-line monitoring techniques for large scale industrial applications.

7.1 Future directions

In response to the findings described in this study, potential electrochemical fingerprints for various UDC scenarios in real pipelines can be obtained and predictive models can be established. Troilite has shown a corrosive nature representative to a *pitted* pipeline corrosion scenario, but a combination of wide range of deposits simulating the pipeline environment should be used. Since the collected deposit during pigging does not represent the local composition, an array of different deposit compositions should also be included in future work.

Future research should evaluate the deposit and film compositions and the time-dependent transformations. Since reactive deposits, iron sulfides in our case, were proven to change nature with time, it is suggested to consider studying the overall changes in the system in correlation to the deposit transformations with time. *In-situ* characterisation techniques such as Raman spectroscopy and Environmental SEM could provide information about the early stage film formation and the deposit transformations as a function of time.[40,170]

Furthermore, the local chemistry under deposits and inside pits is another important factor for realising the localised corrosion of steel and its inhibition. Microelectrode arrays of pH sensors such as iridium/iridium oxide (Ir/IrO_x) can be designed and adapted to map the pH distribution inside the pit.[171,172] Ag/AgCl reference electrodes can be used, for its stability, to measure the Cl ion concentration inside the pit,[173,174] however, a difficulty arises since it may affect the

chloride concentration. Therefore, design considerations should be in place to support the pH and Cl ion concentration sensors in confined micro-scale spaces, in such a way that does not interrupt the system integrity. For instance, the electrodes shall not touch the steel wire to avoid short circuits and the reference electrode should compose of materials that do not intervene with the local chemistry.

Ir/IrO_x working electrodes have proven to be most sensitive and were widely used in the medical research.[175] Preliminary calibration experiments were carried out using a 50 µm diameter Ir wire, after growing IrOx, which provided a sensitivity of 70 mV/pH compared to 59 mV/pH for a commercial glass electrode. However, the material is very expensive, and therefore, a gold substrate with an electrodeposited layer of iridium from iridium salts can be economically feasible. The proposed thin film-deposited electrodes can be composed of alternating microscale gold and silver electrodes, where selective deposition and growing of Ir/IrO_x on gold electrodes and selective growing of AgCl on silver electrodes can take place. In order to prevent the short circuits between the wires and to increase the stability of the electrodes, Nafion can be a good ion transport material that covers the whole array. Identifying the local chemistry will help correlate to the different stoichiometric iron sulfide films formed at the steel surface under different deposits in H_2S. Models can then be built to assess these films' protectiveness and stability.

Preliminary trials using inhibitors were performed (not covered in this thesis) and have shown different *general* electrochemical response. Therefore, possible inhibition protocols, under the similar conditions covered in this study, should be considered using both the blended electrochemistry and the *in-situ* synchrotron experimental approaches. Longer tests under real pipeline conditions of temperature, pressure and flow should also be adopted with an aim to develop in-line monitoring probes for industrial use.

8 References

1. Gerhardus, K. *et al.* International Measures of Prevention, Application, and Economics of Corrosion Technologies (IMPACT) Study. *NACE Int.* 1–216 (2016).
2. Abass, H. H., Nasr-El-Din, H. A. & BaTaweel, M. H. Sand Control: Sand Characterization, Failure Mechanisms, and Completion Methods. in *SPE Annual Technical Conference and Exhibition* (Society of Petroleum Engineers, 2002). doi:10.2118/77686-MS
3. Moghissi, O., Sun, W., Mendez, C., Vera, J. & Place, T. Internal Corrosion Direct Assessment Methodology For Liquid Petroleum Pipelines. in *CORROSION 2007.* Paper No. 07169 (Houston, TX: NACE International, 2007).
4. Vera, J. R., Daniels, D. & Achour, M. H. Under Deposit Corrosion (UDC) in the Oil and Gas Industry: A Review of mechanisms, Testing and Mitigation. in *CORROSION 2012.* Paper no. 0001379 (Houston, TX: NACE International, 2012).
5. Been, J. *et al.* Development of a Test Protocol for the Evaluation of Underdeposit Corrosion Inhibitors in Large Diameter Crude Oil Pipelines. in *CORROSION 2011.* Paper no. 11263 (Houston, TX: NACE International, 2011).
6. Huang, J. Mechanistic Study of Under Deposit Corrosion of Mild Steel in Aqueous Carbon Dioxide Solution. (PhD Thesis, Ohio University, 2013).
7. Brownlee, J. K., Dougherty, J. A. J. A. J. A., Saima, T. & Hausler, R. H. Solving Iron Sulfide Problems in an Offshore Gas Gathering System. in *CORROSION 2000.* Paper no. 00104 (Houston, TX: NACE International, 2000).
8. Sun, W. Kinetics of Iron Carbonate and Iron Sulfide Scale Formation In CO2/H2S Corrosion. (PhD Thesis, Ohio University, 2006).
9. Kvarekval, J., Nyborg, R. & Choi, H. Formation of multilayer iron sulfide films during high temperature CO2/H2S corrosion of carbon steel. in *CORROSION 2003.* Paper no. 03339 (Houston, TX: NACE International, 2003).
10. Rippon, I. J. Corrosion Management for an Offshore Sour Gas Pipeline System. in *CORROSION 2005.* Paper no. 05638 (Houston, TX: NACE International, 2005).
11. Pandarinathan, V., Lepková, K., Bailey, S. I. & Gubner, R. Inhibition of Under-Deposit Corrosion of Carbon Steel by Thiobenzamide. *J. Electrochem. Soc.* **160,** 432–440 (2013).
12. Herbert, F. W. Mechanisms Governing the Growth, Reactivity and Stability of Iron Sulfides. (PhD Thesis, MIT, 2015).
13. Menendez, C., Jovancicevic, V., Ramachandran, S., Morton, M. & Stegmann, D. New Method For Assessing Corrosion Under Iron Sulfide Deposits And CO2/H2S Conditions. in *CORROSION 2011.* Paper no. 11265 (Houston, TX: NACE International, 2011).
14. Sun, W., Nešić, S. & Papavinasam, S. Kinetics of iron sulfide and mixed iron sulfide/carbonate scale precipitation in CO2/H2S corrosion. in *CORROSION 2006.* Paper no. 06644 (Houston, TX: NACE International, 2006).
15. Zhang, Y., Moloney, J. & Mancuso, S. Understanding Factors Affecting Corrosion Inhibitor Performance in Under-Deposit Testing with Sand. in *CORROSION 2013.* Paper no. 2575 (Houston, TX: NACE International, 2013).
16. Kvarekval, J. Morphology of localised corrosion attacks in sour environments. in *CORROSION 2007.* Paper no. 07659 (Houston, TX: NACE International, 2007).

17. Runstedtler, A., Boisvert, P. G. & Place, T. D. Parametric Modeling Studies for Sediment Deposition as Sites for Under-Deposit Corrosion in Oil Transmission Pipelines. *CORROSION* **71,** 726–736 (2015).

18. Bai, P. *et al.* Investigations of the diverse corrosion products on steel in a hydrogen sulfide environment. *Corros. Sci.* **87,** 397–406 (2014).

19. Huang, J. *et al.* Internal CO2 Corrosion of Mild Steel Pipelines under Inert Solid Deposits. in *CORROSION 2010.* Paper no. 10379 (Houston, TX: NACE International, 2010).

20. Alanazi, N. M. *et al.* Corrosion of pipeline steel x-60 under field-collected sludge deposit in a simulated sour environment. *CORROSION* **71,** 305–315 (2015).

21. Sridhar, N., Yang, L. & Song, F. Application of Multielectrode Array Sensor to Study Dewpoint Corrosion in High Pressure Natural Gas Pipeline Environments. in *CORROSION 2006.* Paper no. 06673 (Houston, TX: NACE International, 2006).

22. Shoesmith, D. W., Taylor, P., Bailey, M. G. & Owen, D. G. The Formation of Ferrous Monosulfide Polymorphs during the Corrosion of Iron by Aqueous Hydrogen Sulfide at 21°C. *J. Electrochem. Soc.* **127,** 1007–1015 (1980).

23. Pedersen, A., Bilkova, K., Gulbrandsen, E. & Kvarekvål, J. CO2 Corrosion Inhibitor Performance In The Presence Of Solids: Test Method Development. in *CORROSION 2008.* Paper no. 08634 (Houston, TX: NACE International, 2008).

24. Yang, L. & Sridhar, N. Coupled multielectrode array systems and sensors for real-time corrosion monitoring- A review. in *CORROSION 2006.* Paper no. 06681 (Houston, TX: NACE International, 2006).

25. Turnbull, A., Hinds, G., Cooling, P. & Zhou, S. A multi-electrode approach to evaluating inhibition of underdeposit corrosion in CO2 environments. in *CORROSION 2009.* Paper no. 09445 (Houston, TX: NACE International, 2009).

26. Tan, Y. Experimental methods designed for measuring corrosion in highly resistive and inhomogeneous media. *Corros. Sci.* **53,** 1145–1155 (2011).

27. NACE International Task Group (TG) 380 “Underdeposit Corrosion— Testing and Mitigation”. *Underdeposit Corrosion (UDC) Testing and Mitigation Methods in the Oil and Gas Industry*. *NACE International* (2014).

28. Salas, B. V. & Wiener, M. S. Techniques for corrosion monitoring, edited by Lietai Yang. *Corros. Eng. Sci. Technol.* **44,** 88 (2009).

29. Hinds, G. & Turnbull, A. Novel Multi-Electrode Test Method for Evaluating Inhibition of Underdeposit Corrosion—Part 2: Sour Conditions. *CORROSION* **66,** 056002-056002-6 (2010).

30. Han, J. Galvanic Mechanism of Localized Corrosion for Mild Steel in Carbon Dioxide Environments. (PhD Thesis, Ohio University, 2009).

31. Han, J., Brown, B. N. & Nešić, S. Investigation of the galvanic mechanism for localized carbon dioxide corrosion propagation using the artificial pit technique. *CORROSION* **66,** 0950031–09500312 (2010).

32. Han, J., Yang, Y., Brown, B. & Nesic, S. Roles of Passivation and Galvanic Effects in Localized CO2 Corrosion of Mild Steel. in *NACE International* 1–19 (2008).

33. Marsh, J. W., Palmer, J. W. & Newman, R. C. Evaluation of inhibitor performance for protection against localized corrosion. in *CORROSION 2002.* Paper no. 02288 (Houston, TX: NACE International, 2002).

34. Laycock, N. J. & Newman, R. C. Localised dissolution kinetics, salt films and pitting potentials. *Corros. Sci.* **39,** 1771–1790 (1997).

35. Tester, J. W. & Isaacs, H. S. Diffusional Effects in Simulated Localized Corrosion. *J. Electrochem. Soc.* **122,** 1438–1445 (1975).

36. Isaacs, H. S. The localized breakdown and repair of passive surfaces during pitting. *Corros. Sci.* **29,** 313–323 (1989).

37. Xu, W. *et al.* In-situ Synchrotron Studies of the Effect of Nitrate on Iron Artificial Pits in Chloride Solutions: I. On the Structures of Salt Layers. *J. Electrochem. Soc.* **162,** C238–C242 (2015).

38. Galvele, J. R. Transport Processes and the Mechanism of Pitting of Metals. *J. Electrochem. Soc.* **123,** 464 (1976).

39. Singer, M., Al-Khamis, J. & Nešic, S. Experimental study of sour top of the line corrosion using a novel experimental setup. *Corrosion* **69,** 624–638 (2013).

40. Hansson, E. B., Odziemkowski, M. S. & Gillham, R. W. Formation of poorly crystalline iron monosulfides: Surface redox reactions on high purity iron, spectroelectrochemical studies. *Corros. Sci.* **48,** 3767–3783 (2006).

41. Pandarinathan, V., Lepková, K. & van Bronswijk, W. Chukanovite (Fe2(OH)2CO3) identified as a corrosion product at sand-deposited carbon steel in CO2-saturated brine. *Corros. Sci.* **85,** 26–32 (2014).

42. El Mendili, Y., Abdelouas, A., El Hajj, H. & Bardeau, J. F. Phase transitions of iron sulphides formed by steel microbial corrosion. *RSC Adv.* **3,** 26343–26351 (2013).

43. Isaacs, H. S. In Situ X-Ray Microprobe Study of Salt Layers during Anodic Dissolution of Stainless Steel in Chloride Solution. *J. Electrochem. Soc.* **142,** 1111 (1995).

44. Virtanen, S., Schmuki, P., Büchler, M. & Isaacs, H. S. Electrochemical Behavior of Fe in Phosphate Solutions Studied by In Situ X-Ray Absorption Near Edge Structure. *J. Electrochem. Soc.* **146,** 4087 (1999).

45. Bilderback, D. H., Elleaume, P. & Weckert, E. Review of third and next generation synchrotron light sources. *J. Phys. B At. Mol. Opt. Phys.* **38,** S773–S797 (2005).

46. Rayment, T. *et al.* Characterisation of salt films on dissolving metal surfaces in artificial corrosion pits via in situ synchrotron X-ray diffraction. *Electrochem. commun.* **10,** 855–858 (2008).

47. Capcis Limited. *Review of corrosion management for offshore oil and gas processing*. *Health and Safety Executive -Offshore Technology Report* (2001).

48. Koch, G. H.; Brongers, M. P. H.; Thompson, N. G.; Virmani, Y. P.; Payer, J. H. *Corrosion costs and preventive strategies in the United States*. *FHWA-RD-01-156* (2002).

49. Marsh, J., Teh, T., Ounnas, S. & Richardson, M. Corrosion Management for Aging Pipelines--Experience From the Forties Field. *SPE Proj. Facil. Constr.* **4,** 1–7 (2009).

50. Dicken, G., Bruce, K., Johnson, B. & Al-ghafri, M. J. The Use Of Carbon Steel Tubulars In Highly Sour Oil And Gas Production Systems. in *SPE International Oilfield Corrosion Conference* 135–143 (Society of Petroleum Engineers, 2008). doi:10.2118/114140-MS

51. Kane, R. D. & Cayard, M. S. Roles of H2S in the behavior of engineering alloys: a review of literature and experience. in *CORROSION 98.* Paper no. 274 (Houston, TX: NACE International, 1998).

52. Nesic, S. Effects of Multiphase Flow on Internal CO 2 Corrosion of Mild Steel Pipelines. *Energy & Fuels* **26,** 4098–4111 (2012).

53. Hernandez, S., Hassani, S. & Nassef, A. S. Erosion–corrosion. in *Trends in Oil and Gas Corrosion Research and Technologies* 341–362 (Elsevier, 2017). doi:10.1016/B978-0-08-101105-8.00014-0

54. Telegdi, J., Shaban, A. & Trif, L. Microbiologically influenced corrosion (MIC). in *Trends in Oil and Gas Corrosion Research and Technologies* 191–214 (Elsevier, 2017). doi:10.1016/B978-0-08-101105-8.00008-5

55. Videla, H. A. & Herrera, L. K. Microbiologically influenced corrosion: Looking to the future. *Int. Microbiol.* **8,** 169–180 (2005).

56. Eslami, A. *et al.* Stress corrosion cracking initiation under the disbonded coating of pipeline steel in near-neutral pH environment. *Corros. Sci.* **52,** 3750–3756 (2010).

57. Albarran, J. L., Martinez, L. & López, H. F. The Sour Gas Susceptibility of an X-80 Steel for Oil and Gas Transport. *Scr. Mater.* **38,** 749–755 (1998).

58. *Uhlig's Corrosion Handbook*. (John Wiley & Sons, Inc., 2011). doi:10.1002/9780470872864

59. Ernst, P. & Newman, R. C. Pit growth studies in stainless steel foils. II. Effect of temperature, chloride concentration and sulphate addition. *Corros. Sci.* **44,** 943–954 (2002).

60. Ernst, P. & Newman, R. C. Pit growth studies in stainless steel foils. I. Introduction and pit growth kinetics. *Corros. Sci.* **44,** 927–941 (2002).

61. Hinds, G. THE ELECTROCHEMISTRY OF CORROSION Edited by Gareth Hinds from the original work of J G N Thomas. 15 (2008).

62. Kelly, R., Scully, J., Shoesmith, D. & Buchheit, R. *Electrochemical Techniques in Corrosion Science and Engineering*. (CRC Press, 2002). doi:10.1201/9780203909133

63. Frankel, G. *et al.* Localised corrosion: general discussion. *Faraday Discuss.* **180,** 381–414 (2015).

64. Suter, T. & Böhni, H. A new microelectrochemical method to study pit initiation on stainless steels. *Electrochim. Acta* **42,** 3275–3280 (1997).

65. Suter, T. & Böhni, H. Microelectrodes for corrosion studies in microsystems. *Electrochim. Acta* **47,** 191–199 (2001).

66. SUZUKI, T., YAMABE, M. & KITAMURA, Y. Composition of Anolyte Within Pit Anode of Austenitic Stainless Steels in Chloride Solution. *CORROSION* **29,** 18–22 (1973).

67. Wilde, B. E. & Williams, E. The use of current/voltage curves for the study of localized corrosion and passivity breakdown on stainless steels in chloride media. *Electrochim. Acta* **16,** 1971–1985 (1971).

68. Mankowski, J. & Szklarska-Smialowska, Z. Studies on accumulation of chloride ions in pits growing during anodic polarization. *Corros. Sci.* (1975). doi:10.1016/0010-938X(75)90015-3

69. Mi, N. Synchrotron X-ray studies of atmospheric pitting corrosion of stainless steel. (PhD Thesis, University of Birmingham, 2013).

70. Monir, M. XANES STUDY OF CHEMISTRY OF LOCALISED CORROSION IN ARTIFICIAL PITS OF 316L STAINLESS STEEL AND TITANIUM. (PhD Thesis, University of Birmingham, 2011).

71. West, A. C., Grimm, R.-D., Landolt, D., Deslouis, C. & Tribollet, B. Electrohydrodynamic impedance study of anodically formed salt films on iron in chloride solutions. *J. Electroanal. Chem.* **330,** 693–706 (1992).

72. Grimm, R.-D. & Landolt, D. Salt films formed during mass transport controlled dissolution of iron-chromium alloys in concentrated chloride media. *Corros. Sci.* **36,** 1847–1868 (1994).

73. Hunkeler, F., Krolikowski, A. & Böhni, H. A study of the solid salt film on nickel and

stainless steel. *Electrochim. Acta* **32,** 615–620 (1987).

74. Chernov, V. Y., Makarenko, V. D., Kryzhanivs'kyi, E. I. & Shlapak, L. S. On the causes of corrosion fracture of industrial pipelines. *Mater. Sci.* **38,** 880–883 (2002).

75. Wu, S. L. *et al.* Characterization of the surface film formed from carbon dioxide corrosion on N80 steel. *Mater. Lett.* **58,** 1076–1081 (2004).

76. Sun, W., Nešić, S. & Papavinasam, S. Kinetics of Corrosion Layer Formation. Part 2—Iron Sulfide and Mixed Iron Sulfide/Carbonate Layers in Carbon Dioxide/Hydrogen Sulfide Corrosion. *CORROSION* **64,** 586–599 (2008).

77. Kermani, M. B. & Morshed, A. Carbon Dioxide Corrosion in Oil and Gas Production—A Compendium. *CORROSION* **59,** 659–683 (2009).

78. Smith, S. N. & Joosten, M. W. Corrosion of Carbon Steel by H2S in CO2 Containing Oilfield Environments -10 Year Update. in *CORROSION 2015.* Paper no. 5484 (Houston, TX: NACE International, 2015).

79. Soltis, J. Passivity breakdown, pit initiation and propagation of pits in metallic materials - Review. *Corrosion Science* **90,** 5–22 (2015).

80. Stewart, S., Jovancicevic, V., Menendez, C., Moloney, J. & Wamburi, W. Evaluation Of A New Sour Gas Corrosion Inhibitor For Field Applications Via Localized Corrosion Monitoring Techniques. in *CORROSION 2010.* Paper no. 10274 (Houston, TX: NACE International, 2010).

81. Velázquez, J. C., Caleyo, F., Valor, A. & Hallen, J. M. Technical Note: Field Study—Pitting Corrosion of Underground Pipelines Related to Local Soil and Pipe Characteristics. *CORROSION* **66,** 016001-016001-5 (2010).

82. Oddo Houston, TX (United States)], J. E. [Champion T. I. & Tomson Houston, TX (United States)], M. B. [Rice U. Method predicts well bore scale, corrosion. (1998).

83. Herbert, F. W., Krishnamoorthy, A., Yildiz, B. & Van Vliet, K. J. Diffusion-limited kinetics of the antiferromagnetic to ferrimagnetic λ -transition in Fe 1−x S. *Appl. Phys. Lett.* **106,** 092402 (2015).

84. Bai, P., Zheng, S., Chen, C. & Zhao, H. Investigation of the iron-sulfide phase transformation in nanoscale. *Cryst. Growth Des.* **14,** 4295–4302 (2014).

85. Smith, S. N., Brown, B. & Sun, W. Corrosion at higher H 2 S concentrations and moderate temperatures. in *CORROSION 2011.* Paper no. 11081 (Houston, TX: NACE International, 2011).

86. Genchev, G. & Erbe, A. Raman Spectroscopy of Mackinawite FeS in Anodic Iron Sulfide Corrosion Products. *J. Electrochem. Soc.* **163,** C333–C338 (2016).

87. Sun, W. & Nešić, S. A Mechanistic Model of H2S Corrosion of Mild Steel. in *CORROSION 2007.* Paper no.07655 (Houston, TX: NACE International, 2007).

88. Ramanarayanan, T. A. & Smith, S. N. Corrosion of Iron in Gaseous Environments and in Gas-Saturated Aqueous Environments. *CORROSION* **46,** 66–74 (1990).

89. Sun, W. & Nešić, S. A Mechanistic Model of Uniform Hydrogen Sulfide/Carbon Dioxide Corrosion of Mild Steel. *CORROSION* **65,** 291–307 (2009).

90. Achour, M., Kolts, J., Humble, P. & Hudgins, R. Experimental Evaluation Of Corrosion Inhibitor Performance In Presence Of Iron Sulfide In CO2/H2S Environment. in *NACE International* 1–11 (2008).

91. Menendez, C. M., Jovancicevic, V., Ramachandran, S., Morton, M. & Stegmann, D. Assessment of Corrosion Under Iron Sulfide Deposits and CO2/H2S Conditions. *CORROSION* **69,** 145–156 (2013).

92. Butler, E. C. & Hayes, K. F. Effects of Solution Composition and pH on the Reductive Dechlorination of Hexachloroethane by Iron Sulfide. *Environ. Sci. Technol.* **32,** 1276–1284 (1998).

93. Tjelta, M. & Kvarekvål, J. Electrochemistry of Iron Sulfide and its Galvanic Coupling to Carbon Steel in Sour Aqueous Solutions. in *CORROSION 2016.* Paper no. 7478 (Houston, TX: NACE International, 2016).

94. Tan, Y., Fwu, Y. & Bhardwaj, K. Electrochemical evaluation of under-deposit corrosion and its inhibition using the wire beam electrode method. *Corros. Sci.* **53,** 1254–1261 (2011).

95. Zhang, G. A., Yu, N., Yang, L. Y. & Guo, X. P. Galvanic corrosion behavior of deposit-covered and uncovered carbon steel. *Corros. Sci.* **86,** 202–212 (2014).

96. Reus, J. A. M. de *et al.* Test methodologies and field verification of corrosion inhibitors to address under deposit corrosion in oil and gas production systems. in *CORROSION 2005.* Paper no. 05288 (Houston, TX: NACE International, 2005).

97. Mok, W. Y., Jenkins, A. E., Keenan, S. R. & Gamble, C. G. Control of localized corrosion using green corrosion inhibitors. in *CORROSION 2005.* Paper no. 05289 (Houston, TX: NACE International, 2005).

98. Crolet, J. L., Thevenot, N. & Nesic, S. Role of Conductive Corrosion Products in the Protectiveness of Corrosion Layers. *CORROSION* **54,** 194–203 (1998).

99. Qi, Y. *et al.* Effect of temperature on the corrosion behavior of Carbon steel in Hydrogen sulphide environments. *Int. J. Electrochem. Sci.* **9,** 2101–2112 (2014).

100. Budiansky, N. D., Bocher, F., Cong, H., Hurley, M. F. & Scully, J. R. Use of Coupled Multi-Electrode Arrays to Advance the Understanding of Selected Corrosion Phenomena. in *CORROSION* **63,** 537–554 (2007).

101. Yang, L., Chiang, K., Shukla, P. & Shiratori, N. Internal Current Effects on Localized Corrosion Rate Measurements Using Coupled Multielectrode Array Sensors. *CORROSION* **66,** 1150051–12 (2010).

102. Isaacs, H. S. The Behavior of Resistive Layers in the Localized Corrosion of Stainless Steel. *J. Electrochem. Soc.* **120,** 1456 (1973).

103. A. Turnbull. Corrosion chemistry within pits, crevices, and cracks: proceedings of a conference held at the National Physical Laboratory, Teddington, Middlesex, on October 1-3, 1984. in *H.M.S.O. London, 1987* p.27 (H.M.S.O, 1987).

104. NEWMAN, R. C. & ISAACS, H. S. DISSOLUTION AND PASSIVATION KINETICS OF Fe-Cr-Ni ALLOYS DURING LOCALIZED CORROSION. in *Passivity of Metals and Semiconductors* 269–274 (Elsevier, 1983). doi:10.1016/B978-0-444-42252-1.50044-8

105. Steinsmo, U. & Isaacs, H. S. The dissolution and repassivation kinetics of Fe-Cr alloys in pit solutions. *Corros. Sci.* **35,** 83–88 (1993).

106. Soltis, J., Krouse, D. & Laycock, N. Localised dissolution of iron in buffered and non-buffered chloride containing solutions. *Corros. Sci.* **53,** 2152–2160 (2011).

107. Standlee, S., Efird, K. D. & Spiller, D. Under Deposit Corrosion From Iron Sulfide. in *NACE International* 1–10 (2011).

108. Esmaeely, S. N. Galvanic Localized Corrosion of Mild Steel under Iron Sulfide Corrosion Product Layers. (PhD Thesis, Ohio University, 2018).

109. Olorunniwo, O. E., Imasogie, B. I. & Afonja, A. a. Evaluation of pipeline corrosion in sour-gas environment. *Anti-Corrosion Methods Mater.* **54,** 346–353 (2007).

110. Liu, M., Wang, J., Ke, W. & Han, E.-H. Corrosion Behavior of X52 Anti-H2S Pipeline

Steel Exposed to High H2S Concentration Solutions at 90 °C. *J. Mater. Sci. Technol.* **30,** 504–510 (2014).

111. Rickard, D. & Luther, G. W. Chemistry of Iron Sulfides. *Chem. Rev.* **107,** 514–562 (2007).

112. Davydov, A., Chuang, K. T. & Sanger, A. R. Mechanism of H 2 S Oxidation by Ferric Oxide and Hydroxide Surfaces. *J. Phys. Chem. B* **102,** 4745–4752 (1998).

113. Antunes, R. A., Costa, I. & Faria, D. L. A. de. Characterization of corrosion products formed on steels in the first months of atmospheric exposure. *Mater. Res.* **6,** 403–408 (2003).

114. Sridhar, N. & Dunn, D. S. In situ study of salt film stability in simulated pits of nickel by Raman and electrochemical impedance spectroscopies. *J. Electrochem. Soc.* **144,** 4243–4253 (1997).

115. Rémazeilles, C. *et al.* Microbiologically influenced corrosion of archaeological artefacts: characterisation of iron(II) sulfides by Raman spectroscopy. *J. Raman Spectrosc.* **41,** 1425–1433 (2010).

116. Williams, D. E., Kilburn, M. R., Cliff, J. & Waterhouse, G. I. N. Composition changes around sulphide inclusions in stainless steels, and implications for the initiation of pitting corrosion. *Corros. Sci.* (2010). doi:10.1016/j.corsci.2010.07.021

117. Baird, T. *et al.* Structural and morphological studies of iron sulfide. *J. Chem. Soc. Faraday Trans.* **92,** 445 (1996).

118. Durnie, W. H., Kinsella, B. J., De Marco, R. & Jefferson, A. A study of the adsorption properties of commercial carbon dioxide corrosion inhibitor formulations. *J. Appl. Electrochem.* **31,** 1221 (2001).

119. de Romero, M., Ortíz, R., Marquez, O. & Romero-Gonzalez, M. Use of FTIR in situ technique to evaluate MIC by SRB. *CORROSION* (2007).

120. Marco, R. De & Veder, J.-P. In situ structural characterization of electrochemical systems using synchrotron-radiation techniques. *TrAC Trends Anal. Chem.* **29,** 528–537 (2010).

121. Zimer, A. M. *et al.* Investigation of AISI 1040 steel corrosion in H 2S solution containing chloride ions by digital image processing coupled with electrochemical techniques. *Corros. Sci.* **53,** 3193–3201 (2011).

122. Nyborg, R. Initiation and Growth of Mesa Corrosion Attack During CO2 Corrosion of Carbon Steel. in *CORROSION 98.* Paper no. 98048 (NACE International, 1998).

123. Cui, N., Ma, H. ., Luo, J. . & Chiovelli, S. Use of scanning reference electrode technique for characterizing pitting and general corrosion of carbon steel in neutral media. *Electrochem. commun.* **3,** 716–721 (2001).

124. Fonseca, L. *et al.* Thermal AFM: a thermopile case study. *Ultramicroscopy* **101,** 153–159 (2004).

125. Sakai, Y., Iijima, Y., Asakawa, D. & Hiraoka, K. XPS depth profiling of polystyrene etched by electrospray droplet impact. *Surf. Interface Anal.* **42,** 658–661 (2010).

126. Ghahari, S. M. *et al.* In situ synchrotron X-ray micro-tomography study of pitting corrosion in stainless steel. *Corros. Sci.* **53,** 2684–2687 (2011).

127. Xu, W. *et al.* In-Situ Synchrotron Studies of the Effect of Nitrate on Iron Artificial Pits in Chloride Solutions: II. On the Effect of Carbon. *J. Electrochem. Soc.* **162,** C243–C250 (2015).

128. Schmuki, P. *et al.* Passivity of Iron in Alkaline Solutions Studied by In Situ XANES and

a Laser Reflection Technique. *J. Electrochem. Soc.* **146,** 2097 (1999).

129. Oblonsky, L. J., Ryan, M. P. & Isaacs, H. S. In situ XANES study of the formation and reduction of the passive film formed on Fe in acetate solution. *Corros. Sci.* **42,** 229–241 (2000).

130. Street, S. R. *et al.* The Effect of Nitrate on Salt Layers in Pitting Corrosion of 304L Stainless Steel. *J. Electrochem. Soc.* **162,** C457–C464 (2015).

131. Smith, S. N. & Joosten, M. W. Corrosion of carbon steel by H2S in CO2 containing oilfieled Environments. *Nace* 1–26 (2006).

132. Yang, L. Multielectrode systems. in *Techniques for Corrosion Monitoring* (ed. Yang, L. B. T.-T. for C. M.) **44,** 187–241 (Woodhead Publishing, 2008).

133. Ferraro, J. R., Nakamoto, K. & Brown, C. W. *Introductory Raman Spectroscopy*. *Introductory Raman Spectroscopy: Second Edition* (Elsevier, 2003). doi:10.1016/B978-0-12-254105-6.X5000-8

134. Stock, S. R. In situ X-ray Measurement Methods. in *Characterization of Materials* 1652–1671 (John Wiley & Sons, Inc., 2012). doi:10.1002/0471266965.com134

135. Koronfel, M. A. Nanoscale Degradation of Metal-on-Metal Implants. (PhD Thesis, Imperial College London, 2018).

136. Willmott, P. *An Introduction to Synchrotron Radiation*. (Wiley, 2011). doi:10.1002/9781119970958

137. Kelly, S. D., Hesterberg, D. & Ravel, B. Analysis of Soils and Minerals Using X-ray Absorption Spectroscopy. in *Methods of Soil Analysis, Part 5 - Mineralogical Methods* 367–464 (2008). doi:10.2136/sssabookser5.5.c14

138. Ravel, B. & Newville, M. ATHENA, ARTEMIS, HEPHAESTUS : data analysis for X-ray absorption spectroscopy using IFEFFIT. *J. Synchrotron Radiat.* **12,** 537–541 (2005).

139. Filik, J. *et al.* Processing two-dimensional X-ray diffraction and small-angle scattering data in DAWN 2. *J. Appl. Crystallogr.* **50,** 959–966 (2017).

140. Basham, M. *et al.* Data Analysis WorkbeNch (DAWN). *J. Synchrotron Radiat.* **22,** 853–858 (2015).

141. Pohl, H. A. Solubility of Iron Sulfides. *J. Chem. Eng. Data* **7,** 295–306 (1962).

142. Nimmo, J. R. Porosity and Pore Size Distribution. in *Reference Module in Earth Systems and Environmental Sciences* 1–10 (Elsevier, 2013). doi:10.1016/B978-0-12-409548-9.05265-9

143. Heift, D. Iron Sulfide Materials: Catalysts for Electrochemical Hydrogen Evolution. *Inorganics* **7,** 75 (2019).

144. Davison, W. The solubility of iron sulphides in synthetic and natural waters at ambient temperature. *Aquat. Sci.* **53,** 309–329 (1991).

145. Boughriet, A., Figueiredo, R. S., Laureyns, J. & Recourt, P. Identification of newly generated iron phases in recent anoxic sediments: 57Fe Mössbauer and microRaman spectroscopic studies. *J. Chem. Soc. Faraday Trans.* **93,** 3209–3215 (1997).

146. Finklea III, S. L., Cathey, L. & Amma, E. L. Investigation of the bonding mechanism in pyrite using the Mössbauer effect and X-ray crystallography. *Acta Crystallogr. Sect. A* **32,** 529–537 (1976).

147. White, S. N. Laser Raman spectroscopy as a technique for identification of seafloor hydrothermal and cold seep minerals. *Chem. Geol.* **259,** 240–252 (2009).

148. Hanesch, M. Raman spectroscopy of iron oxides and (oxy)hydroxides at low laser

power and possible applications in environmental magnetic studies. *Geophys. J. Int.* **177,** 941–948 (2009).

149. Wei, C. *et al.* Approaches for measuring the surface areas of metal oxide electrocatalysts for determining their intrinsic electrocatalytic activity. *Chem. Soc. Rev.* **48,** 2518–2534 (2019).

150. Rickard, D. The solubility of FeS. *Geochim. Cosmochim. Acta* **70,** 5779–5789 (2006).

151. Hem, J. *Some chemical relationships among sulfur species and dissolved ferrous iron*. *U.S. Geol. Surv., Water Supply Paper* (1960). doi:10.3133/wsp1459C

152. Shamso, A., Laycock, N., Abdullah, A. & Ryan, M. Under-Deposit Corrosion: Investigating Dissolution Kinetics Using Artificial Pits. in *CORROSION 2018.* Paper no. 11055 (Houston, TX: NACE International, 2018).

153. Newman, R. C. & Ajjawi, M. A. A. A micro-electrode study of the nitrate effect on pitting of stainless steels. *Corros. Sci.* **26,** 1057–1063 (1986).

154. Srinivasan, J., McGrath, M. J. & Kelly, R. G. A High-Throughput Artificial Pit Technique to Measure Kinetic Parameters for Pitting Stability. *J. Electrochem. Soc.* **162,** C725–C731 (2015).

155. GALVELE, J. R. Pitting Corrosion. *Treatise Mater. Sci. Technol.* **23,** 1–57 (1983).

156. Fang, H., Brown, B., Young, D., Nešic, S. & Nešić, S. Investigation Of Elemental Sulfur Corrosion Mechanisms. in *CORROSION 2011* 13 (NACE International, 2011).

157. Steudel, R. Mechanism for the Formation of Elemental Sulfur from Aqueous Sulfide in Chemical and Microbiological Desulfurization Processes. *Ind. Eng. Chem. Res.* **35,** 1417–1423 (1996).

158. Anderko, A. M. & Shuler, P. J. Modeling the formation of iron sulfide scales using thermodynamic simulation software. in *CORROSION 98.* Paper no. 98064 (Houston, TX: NACE International, 1998).

159. Zheng, Y., Brown, B. & Nesic, S. Electrochemical Study and Modeling Of H2S Corrosion of Mild Steel. in *CORROSION 2013.* Paper no. 2406 (Houston, TX: NACE International, 2013).

160. Powell, C. R., Dillon, K. M. & Matson, J. B. A review of hydrogen sulfide (H2S) donors: Chemistry and potential therapeutic applications. *Biochem. Pharmacol.* **149,** 110–123 (2018).

161. Zheng, Y. Electrochemical Mechanism and Model of H_2S Corrosion of Carbon Steel. *Department of Chemical and Biomolecular Engineering and the Russ College of Engineering and Technology* **1,** (2015).

162. Kvarekval, J., Nyborg, R. & Choi, H. Formation of multilayer iron sulfide films during high temperature CO2/H2S corrosion of carbon steel. *Corros. 2003* (2003).

163. Ma, H. *et al.* The influence of hydrogen sulfide on corrosion of iron under different conditions. *Corros. Sci.* **42,** 1669–1683 (2000).

164. Liu, Y. *et al.* New Approach to Study Iron Sulfide Precipitation Kinetics, Solubility, and Phase Transformation. *Ind. Eng. Chem. Res.* **56,** 9016–9027 (2017).

165. Budavari, S. The Merck index : an encyclopedia of chemicals, drugs, and biologicals. *Merck and Co., Inc.,* (1989).

166. OECD SIDS. *Iron Dichloride CAS No: 7758-94-3 SIDS: Initial Assessment Report*. (2004).

167. Hemmingsen, T., Fusek, F. & Skavås, E. Monitoring of the corrosion process on sulphide film formation with electrochemical and optical measurements. *Electrochim.*

Acta **51,** 2919–2925 (2006).

168. Haisch, T., Mittemeijer, E. J. & Schultze, J. W. On the influence of microstructure and carbide content of steels on the electrochemical dissolution process in aqueous NaCl-electrolytes. *Mater. Corros.* **53,** 740–755 (2002).

169. Zhang, C. *et al.* Electrical Resistivity of Fe-C Alloy at High Pressure: Effects of Carbon as a Light Element on the Thermal Conductivity of the Earth's Core. *J. Geophys. Res. Solid Earth* **123,** 3564–3577 (2018).

170. Jensen, E., Købler, C., Jensen, P. S. & Mølhave, K. In-situ SEM microchip setup for electrochemical experiments with water based solutions. *Ultramicroscopy* **129,** 63–69 (2013).

171. Steegstra, P. Hydrous iridium oxide for in situ pH sensing: electrodeposition, properties and applications. (PhD Thesis, University of Gothenburg, 2013).

172. Chung, H.-J. *et al.* Ultrathin, Stretchable, Multiplexing pH Sensor Arrays on Biomedical Devices With Demonstrations on Rabbit and Human Hearts Undergoing Ischemia. *Adv. Healthc. Mater.* **3,** 59–68 (2014).

173. Dam, V. A. T., Zevenbergen, M. A. G. & van Schaijk, R. Flexible Chloride Sensor for Sweat Analysis. *Procedia Eng.* **120,** 237–240 (2015).

174. Kim, T. Y., Hong, S. A. & Yang, S. A solid-state thin-film Ag/AgCl reference electrode coated with graphene oxide and its use in a pH sensor. *Sensors (Switzerland)* **15,** 6469–6482 (2015).

175. Ng, S. R. & O'Hare, D. An iridium oxide microelectrode for monitoring acute local pH changes of endothelial cells. *Analyst* **140,** 4224–4231 (2015).